SPACEBORNE

RADAR

OBSERVATIONS

A GUIDE FOR MAGELLAN

RADAR - IMAGE ANALYSIS

Spaceborne Radar Observations

A Guide for Magellan Radar-Image Analysis

J. P. Ford
R. G. Blom
J. A. Crisp
C. Elachi
T. G. Farr
R. S. Saunders
E. E. Theilig
S. D. Wall
S. B. Yewell

December 15, 1989

Foreword

The Magellan Mission will provide, for the first time, high-resolution images of almost the total surface of Venus. Past observations with Soviet Venera 15 and 16 spaceborne radar and Arecibo, Puerto Rico, and Goldstone, California, ground-based radar at medium resolution (a few kilometers) over large regions of the planet provided intriguing hints of large-scale morphological features that could be associated with impact, volcanic, tectonic, and erosional phenomena. The high resolution (a few hundred meters) of the Magellan images should allow clear identification of the processes that shaped the surface morphology.

To facilitate interpretation of the Magellan data, it is important to collect and make widely available a comparative data set of images acquired over well-known Earth regions using an imaging system similar to that of the Magellan radar. Fortunately, the data available from three Earth-orbiting radar missions—Seasat (1978); the Shuttle Imaging Radar A (SIR-A, 1981) and Shuttle Imaging Radar B (SIR-B, 1984)—make this possible. These three missions acquired data over a wide variety of regions, including some that reflect processes similar to those that might have shaped the Venusian surface: impact features, volcanic regions with a wide variety of age and type, regions shaped by wind erosion and fluvial erosion, and areas shaped by tectonics.

This publication provides examples of radar images of well-documented Earth regions to help those planetologists who have little familiarity with radar-image interpretation better understand the data. We hope this information will increase the number of scientists involved in the analysis of Magellan data.

The examples are grouped under the following general categories: impact structures, volcanic landforms, eolian features and subsurface imaging, and tectonic landforms. Each includes a thorough analysis of representative radar coverage acquired with Seasat Synthetic-Aperture Radar (SAR), SIR-A, or SIR-B, as well as supporting information from field work or geologic maps; a reference list is provided for readers interested in further in-depth study.

In addition to the examples, some fundamentals of imaging radars and signal interaction with a planetary surface are provided. Particular emphasis is given to the geologic interpretation of radar images, and examples of radar-image anomalies are included to help the interpreter recognize potential image artifacts.

Acknowledgments

Abstract

Geologic analyses of spaceborne radar images of Earth are reviewed and summarized with respect to detecting, mapping, and interpreting impact craters, volcanic landforms, eolian and subsurface features, and tectonic landforms. Interpretations are illustrated mostly with Seasat Synthetic-Aperture-Radar and shuttle-imaging-radar images. Analogies are drawn for the potential interpretation of radar images of Venus, with emphasis on the effects of variation in Magellan look angle with Venusian latitude. In each landform category, differences in feature perception and interpretive capability are related to variations in imaging geometry, spatial resolution, and wavelength of the imaging radar systems.

Impact craters and other radially symmetrical features may show apparent bilateral symmetry parallel to the illumination vector at low look angles. The styles of eruption and the emplacement of major and minor volcanic constructs can be interpreted from morphologic features observed in images. Radar responses that are governed by small-scale surface roughness may serve to distinguish flow types, but do not provide unambiguous information. Imaging of sand dunes is rigorously constrained by specific angular relations between the illumination vector and the orientation and angle of repose of the dune faces, but is independent of radar wavelength. With a single look angle, conditions that enable shallow subsurface imaging to occur do not provide the information necessary to determine whether the radar has recorded surface or subsurface features. The topographic linearity of many tectonic landforms is enhanced on images at regional and local scales, but the detection of structural detail is a strong function of illumination direction. Nontopographic tectonic lineaments may appear in response to contrasts in small-scale surface roughness or dielectric constant. The breakpoint for rough surfaces will vary by about 25% through the range of Magellan viewing geometries from low to high Venusian latitudes. Examples of anomalies and system artifacts that can affect image interpretation are described.

Contents

. . . .

PRECEDING PAGE BLANK NOT FILMED

PAGE _VIII_ INTENTIONALLY BLANK

Appendixes

Synthetic-Aperture Radar Imaging

Introduction

Synthetic-aperture radar (SAR) transmits pulses of electromagnetic energy perpendicular to the line of flight of a moving platform (spacecraft) and measures and records the intensity, time delay, and frequency shift of the echoes. Each pulse spreads across the terrain as a section of a cone, and echoes are generated as the pulse is reflected. Measuring and dividing the echo in time gives cross-track (range) resolution because the earliest echoes come from the closest part of the illuminated terrain, and later echoes come from progressively greater distances.

Relative motion between terrain and spacecraft in the along-track (azimuth) direction induces a position-dependent frequency change, or shift, on the echoes. Echoes from terrain ahead of the spacecraft have a higher frequency and echoes from terrain behind the spacecraft have a lower frequency than the transmitted signal. Doppler measurement of the reflected signal provides terrain location information in the flight-track direction as a function of the frequency shift.

Image resolution elements are thus created by the combined analysis of time delay and frequency shift. Resolution elements are illuminated more than once as the SAR flies along, and the spatial resolution of a large antenna is synthesized by multiple sampling from a smaller antenna; this is the synthetic-aperture technique. Each resolution element is assigned a brightness level corresponding to the strength of the echo from that portion of the terrain. These concepts are illustrated in Figure 1. Further explanation of the technique can be found in Elachi (1980 and 1987).

Imaging Geometry

It is important to define some of the terms that refer to the geometry of radar images, because these terms are sometimes used in different ways. The terms are illustrated in Figure 2. Look angle is that angle between the sensor nadir and the antenna boresight. It is fixed at the sensor and does not vary with terrain slope. Look angle is the complement of depression angle, a term often used in describing airborne imaging-radar geometry. Incidence angle is that angle between the surface normal and the radar beam. Consequently, incidence angle is a function of both the look angle and the slope of the terrain observed. Look angle and incidence angle are equal in value only if the terrain is horizontal and the radar-platform altitude is low enough to make planetary curvature negligible. Look angle and incidence angle are never the same in spaceborne radar images because of planetary surface curvature, which increases the incidence angle slightly.

Figure 3 shows the nominal incidence angle of the Magellan imaging radar as a function of Venusian latitude. Because many of the image examples in this publication are from Seasat or
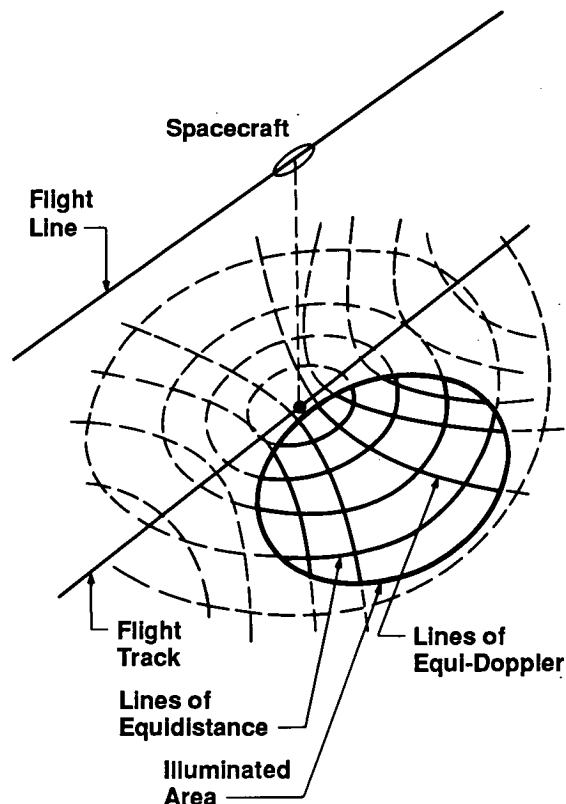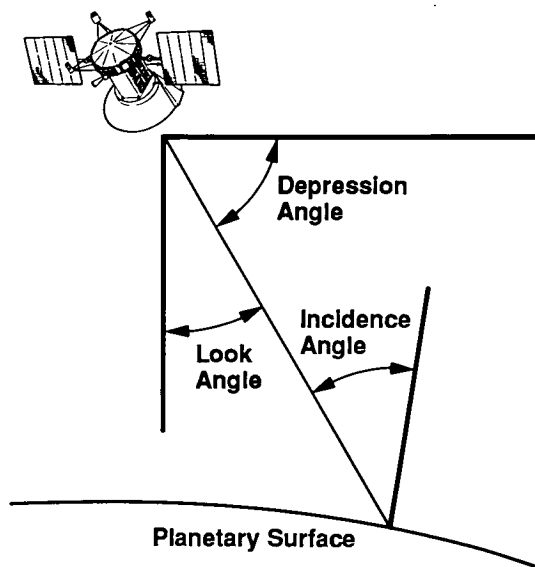

Figure 1. Constant time-delay and Doppler contour lines that form the radar-imaging coordinate system. Image resolution elements are defined by intersections of Doppler resolution elements and time-delay resolution elements. The brightness in each image resolution element is proportional to the backscattered energy. Figure copyrighted 1980 by the AAAS (Elachi, 1980).

Figure 2. Nomenclature for imaging radar geometry. For a horizontal surface, the look angle is slightly less than the incidence angle because of planetary curvature when viewed from orbit.

and the incident radar beam. If a surface is tilted nearly perpendicular to the radar beam, it will reflect the greatest amount of radar energy (i.e., echo) and, in turn, produce a very bright area on the image. Conversely, a surface that slopes away from the radar will produce a weaker echo and therefore a darker area on the image. This effect emphasizes topography, which can be useful for mapping geologic structures.

If a surface slopes away from the radar at a great enough angle, the area will receive no radar illumination and a shadow will result. In Magellan images, shadows will result where surfaces are inclined away from the radar 71 deg or more at the minimum look angle of 14 deg plus 5 deg for planetary curvature, and 44 deg or more at the maximum look angle of 44 deg plus about 2 deg for planetary curvature. The steepness required to produce a shadow increases as the strike of the slope moves farther out of alignment with the radar beam. Most terrestrial slopes are less than the 44-deg minimum indicated above, and so, presuming Venus is similar, it is probable that shadows will be uncommon in Magellan images. Because the Magellan look angle will vary with latitude, the expressions of topography, shadows, and variations in backscatter will also vary with latitude. This topic is covered in later chapters of this publication.

SIR-A, their incidence angles are also indicated on the figure. The effects of incidence-angle variation relative to latitude on feature identification are described and illustrated in several examples in the text; these variations must be kept in mind when interpreting Magellan radar images.

Response to Terrain

The factors that control brightness in radar images are, in the decreasing order of effect, surface slope, surface roughness, and the dielectric constant of the material imaged. On Earth, dielectric constant is mainly a function of moisture content: dry soil has a lower dielectric constant than wet soil, and wet soil is a better radar reflector than dry soil. The values of the dielectric constant of most geologic materials are broadly similar (Campbell and Ulrichs, 1969). Despite the small differences, variations in dielectric constant may have geologic significance (Zisk and Mouginis-Mark, 1980; Jurgens et al., 1988), if the subtle effects can be reliably detected. The effects of slope and roughness are reviewed below.

Slope

Very significant in the interpretation of radar imagery is the relationship between surface slope

Roughness

Brightness variations in SAR images give clues about the surface at a scale much smaller than the spatial resolution of the radar image. When imaged by SAR, a smooth surface such as a playa reflects most of the energy away from the radar and thus is dark on the image. The highest parts of an alluvial fan, on the other hand, have rough surfaces composed of cobbles and boulders. Thus, although cobbles and boulders cannot be resolved on the image, a rough surface can be inferred because of the bright area caused by strong echoes.

The surface-roughness response is wavelength dependent. Long wavelengths are not backscattered by relatively fine-textured surfaces. The longer the wavelength, the coarser the surface must be for backscattering to occur. Because imaging radars operate over a broad range of wavelengths (from 1 to 75 cm), the texture of a given surface can vary from rough

when observed at a short wavelength to smooth when observed at a longer wavelength.

Peake and Oliver (1971) studied the relationship between surfaces of known roughness and radar backscatter. Practical geologic applications relating surface roughness to radar backscatter are described by Schaber et al. (1976) in studies of radar response to alluvial fans and lava flows. Additional useful discussions can be found in Sabins (1987), MacDonald (1980), and MacDonald and Waite (1973). Schaber et al. (1976) found good agreement between surface roughness measurements made in the field and the Rayleigh criterion for the transition from slightly rough to smooth (quasi-specular reflection) behavior. The Rayleigh criterion formula is

$$h < \lambda \ /(8 \cos i) \tag{1}$$

where λ is the radar wavelength, i is the incidence angle, and h is the rms height.

Ulaby et al. (1982), however, found better agreement using the Fraunhofer criterion in a study of bare agricultural fields of known roughness. The Fraunhofer criterion formula is

$$h < \lambda \ /(32 \cos i) \tag{2}$$

The use of slightly different formulas illustrates the difficulty of modeling a complex surface, but the formulas do indicate a range over which the transition from slightly rough to smooth will occur.

Peake and Oliver (1971) also defined a "rough" criterion, which describes surfaces that scatter essentially all of the energy in a diffuse manner. The formula is

$$h > \lambda \ /(4.4 \cos i) \tag{3}$$

These formulas can be used as a guide in the interpretation of radar images, provided the limitations of modeling natural surfaces are kept in mind.

The Magellan radar has a wavelength of 12.6 cm. With the Fraunhofer criterion (Formula (2)) applied to Magellan images, a smooth surface (dark area) will have irregularities less than about 0.4 cm when imaged at the minimum incidence angle of 19 deg (a 14-deg look angle plus the angle added for planetary curvature of
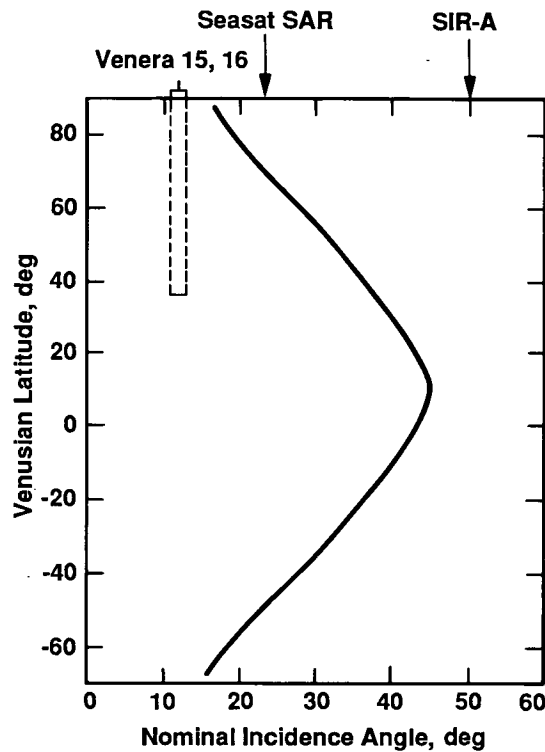
Figure 3. Variation of Magellan nominal incidence angle with Venusian latitude, showing corresponding nominal values at beam centers for Seasat SAR, SIR–A, and Venera 15 and 16. Short dashed lines indicate the latitudinal range of Venera coverage. Negative latitudes denote the southern hemisphere.

the planet), and irregularities less than about 0.6 cm when imaged at the maximum incidence angle of 45 deg. Use of the Rayleigh criterion (Formula (1)) results in values of about 1.7 and 2.3 cm, respectively.

Use of Formula (3) for rough surfaces indicates that a uniformly bright area will result from surface irregularities greater than about 3.0 cm at a 19-deg incidence angle and greater than about 4.1 cm at an incidence angle of 45 deg.

The above discussion demonstrates that while radar-image-brightness levels are a reflection of surface properties, the radar response will vary with a number of factors that can be poorly known or difficult to determine. Also, for a given surface, image-brightness levels can vary as a function of radar geometry and wavelength. For Magellan, the observing wavelength is constant, but image geometry will vary with Venusian latitude. Accurate interpretation of Magellan images may in part hinge on recognition of the factors discussed above and illustrated by the examples that follow.

Magellan Data Characteristics

Introduction

The Magellan Mission will produce a global data set that will be used for geologic analysis and comparative planetology for many years to come. The acquisition of a global data set for Venus is an important part of completing the exploration of the inner planets, which will allow a detailed comparison of Earth, Mars, and Venus. In many ways, the Venusian data will be more detailed and more complete than anything planetologists currently have for Earth, since the largely unmapped ocean floors occupy 70% of our planet. The Venusian data will be of great interest to all geoscientists, allowing tests of many Earth geophysical and tectonic models.

One of the objectives of the Magellan Mission is to produce a data set that will include the first systematic radar map of an entire planet. The data will be in several forms, but SAR images will provide the basis for the mapping.

Mission Description

Magellan will operate from a near-polar elliptical orbit with a period of 3.15 h. Periapsis will be at 10°N with an altitude of 250 km. The look angle at periapsis will be about 50 deg. Mapping will proceed from the north pole, with a look angle of about 14 deg and an altitude of 2100 km, down to 70°S. The incidence angle will continuously change from about 16 deg at the start of a mapping swath to about 45 deg at periapsis and decrease again to about 20 deg at 70°S. The planned coverage of Venus (less the polar coverage) is given in Figure 4. Mapping characteristics are summarized in Tables 1 and 2. More details of the Magellan mission plan can be found in Dallas and Nickle (1987) and the *Magellan Mission Plan* (1988).
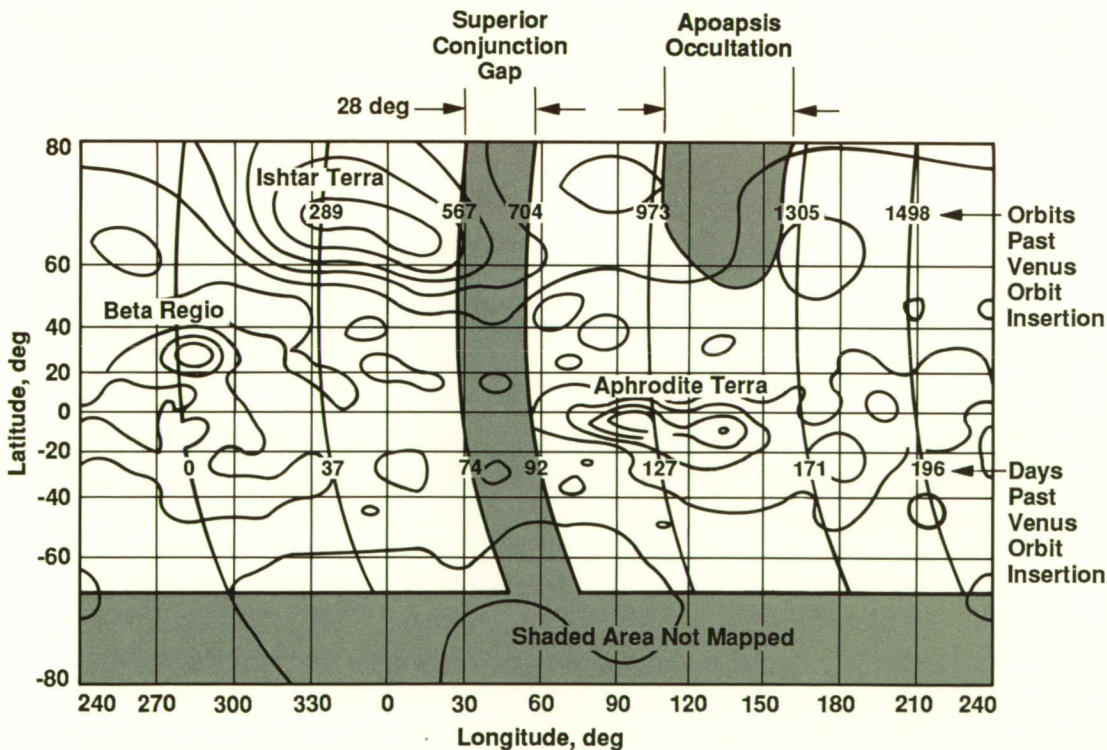
Figure 4. Magellan planned coverage (unshaded area) for Venus: Mercator projection, 1.0-km contours.

Table 1. Magellan mapping characteristics.

Parameter	Value
Mapping frequency, swath/orbit	1
SAR record rate, kbits/s	806.4
Record duration, min/orbit	37.2
Playback rates, kbits/s	268.8 and 115.2
Playback duration, min	90 to 141.5
Tape recorder capacity, bits	3.6×10^9
True anomaly range during mapping, deg	-80 to +80
Altitude range during mapping, km	250 to 2100
Look-angle range during mapping, deg	14 to 50
Swath width, km	20 to 25
Duration of nominal mapping mission, days	243
Latitude range mapped	90°N to 67.2°S
Expected coverage of Venus, %	71 to 79
Planet coverage per day, %	0.4

Table 2. Mapping orbital data for the Magellan launch of May 4, 1989.

Parameter	Value
Period, h	3.15
Periapsis altitude, km	250
Apoapsis altitude, km	8029
Orbital speed at periapsis, km/s	8.4400
Orbital speed at apoapsis, km/s	3.7771
Orbital speed at ± 80 deg true anomaly, km/s	6.9062
Venus sidereal period, days	243.01
Rate of rotation, deg/day	-1.4814
Rate of rotation, deg/orbit	-0.1944
Shift in ground track at equator, km/orbit	20.53
Periapsis latitude	10.0°N
Periapsis longitude at arrival	275.45°

Data-Acquisition Parameters

Because radar-image acquisition, processing, and interpretation differ significantly from the usual optical television-imaging systems used for planetary mapping, it is necessary to understand something about the design of the Magellan radar system.

The data-acquisition parameters of the Magellan synthetic-aperture radar imaging system are given in Table 3 (also, see Johnson and Edgerton, 1985; Johnson, 1989). Several of these parameters interact to control SAR image quality. The most important are spatial resolution, the number of looks, amplitude resolution, signal-to-noise ratio, and incidence angle.

Spatial resolution is specified in range, or cross track, and in azimuth, or along track. Range resolution is determined by the transmitted bandwidth; when projected onto the surface, it is called slant-range resolution and thus becomes a function of incidence angle. Slant-range resolution decreases as incidence angle increases. This effect is seen in the variation of Magellan slant-range resolution with latitude: from 120 to 360 m. Azimuth resolution is determined by the length of the synthetic aperture created by the moving spacecraft. In principle, azimuth resolution can be as small as the antenna. Magellan azimuth resolution will be held at 120 m for most of the mapping swath.

The number of "looks" is the number of independent observations made for each resolution element (see Figure 1 in *Synthetic-Aperture Radar Imaging*). The science requirements for Magellan specify a minimum of four looks. This minimum may be reached around periapsis, but, in general, more looks will be achieved. Increasing the number of looks reduces coherent "noise" or speckle that occurs in coherent imaging (see *Image Anomalies and System Artifacts*).

Amplitude resolution is a measure of how well the image data represent the backscatter, or reflection characteristics, of the surface over a wide range of reflectivity or backscatter strengths. Magellan science requirements specify that image quality must be maintained over a wide range of backscatter strengths. This would require a large number of bits per sample, more than are available. Therefore, a method of data compression called the "block adaptive

quantizer" was developed and built into the flight hardware. This technique preserves the amplitude resolution while allowing the return of a larger quantity of high-resolution data.

Thermal signal-to-noise ratio (SNR) for Magellan is designed to be 8 dB because tests show that this level is approximately at the threshold between no noticeable improvement at higher values and noticeable image degradation at lower levels. The system SNR, about 5 dB in the processed images, is the combination of all noise sources including those from radar hardware, processing, and the radio link.

Incidence angle is the angle between the incoming radar pulse and the normal to the surface. An incidence angle that is constant relative to the mean spherical surface of Venus would have been desirable because a given geologic terrain may appear differently at different incidence angles. In interpreting Magellan images, then, more care and understanding of the effects of the varying incidence angle, which decreases with increasing latitude, are required.

The elliptical orbit of Magellan will place constraints on the maximum incidence angle that can be used for mapping (approximate values are given in Table 4). In general, higher incidence angles result in less distortion in the images, especially in rugged mountainous terrain. The most serious problem arises when the slopes exceed the incidence angle and layover occurs. This was not a severe problem for Venera 15 and 16 even at a 10-deg incidence angle because of the low resolution (1 to 2 km). That is, few slopes of many kilometers extent and steeper than 10 deg occur on planetary surfaces. For smaller slope lengths at the resolution of Magellan images, steeper slopes are resolved, and hence layover at low incidence angles becomes more of a problem. A reasonable upper limit is the angle of repose of dry materials; this is about 30 deg and independent of gravity, so it is the same on all planetary surfaces. Magellan science requirements specify that the radar must be operated at the largest angle of incidence that allows all the other image requirements to be met. More than 70% of the image coverage will be at incidence angles greater than 30 deg.

Parameter	Value
Planned operating altitude, km	250 to 2100
Possible operating altitude, km	225 to 3500
Radar frequency/wavelength, GHz/cm	2.385/12.6
System bandwidth, MHz	2.26
Spatial resolution (slant range), m	120 to 360
Azimuth resolution, m	120 to 150
Number of looks	4 or more
Swath width, km	20 to 25
Antenna diameter, m	3.7
Antenna look angle, deg	13 to 45 from nadir
Incidence angle on surface (nominal), deg	16 to 45
Polarization	HH
Transmitted pulse length, μs	26.5
Pulse-repetition frequency, Hz	4400 to 5800
Transmitted peak power, W	350
Time-bandwidth product	60
SAR data on-board recorded bit rate, kbits/s	750
Quantization, bits	2

Table 3. Magellan SAR imaging system parameters.

Altitude, km	Incidence angle, deg	Range resolution, m	Azimuth resolution, m	Looks
250	50	115	120	5
275	48	120	120	6
500	40	135	120	7
1000	31	170	120	8
1750	20	260	120	12
2100	17	300	120	16

Table 4. Radar performance parameters.

In general, the SAR may be operated at any incidence angle lower than the maximum angle required for mapping. Other incidence angles will be obtained during the extended mission to provide stereoimage coverage. Table 4 shows the SAR performance at the planned mapping incidence angles.

The elliptical orbit of the Magellan space-craft will require frequent adjustment of the radar operating parameters because of changing slant range (400 to 2200 km) and variations in speed (6.9 to 8.3 km/s). The commandable parameters (look angle, 14 to 50 deg; pulse-repetition frequency, 4400 to 5800 Hz; processed band-width, 1300 to 4000 Hz; burst duration, 0.02 to 0.2 s; and burst period, 0.2 to 1.0 s) must be balanced against the many mapping require-ments.

Processing

The Magellan SAR data will require complex digital processing, or correlation, to create images. The digital processor used for Magellan is called the Advanced Digital SAR Processor. This system was developed for use by shuttleborne imaging radar systems such as SIR-C.

The SAR Experiment Data Record (SAR-EDR) is processed by the Magellan SAR Data Processing Subsystem (SDPS). The SAR-EDR contains SAR echo bursts, orbit ephemeris data, antenna pointing information, and engineering data. The output of the SDPS is the Full-Resolution Basic Image Data Record (F-BIDR), which is the averaged composite of approxi-

mately 6000 single-look framelets, each from one SAR burst.

To process a SAR burst into a framelet, the processor performs range compression, azimuth compression, radiometric gain compensation, geometric rectification, and framelet truncation. Range and azimuth compression provide the high spatial resolution. Radiometric compensa-tion converts the data number (dn) values into the normalized backscatter coefficient. Geomet-ric rectification projects the images into the sinusoidal projection and the along-track and cross-track (AT/CT) projection. Framelet truncation removes pixels that do not have the required quality based on processing bandwidth and range swath.

Each burst of data is processed into a one-look image framelet (Figure 5). The framelet along-track dimension is determined by the processed bandwidth, and the cross-track dimension is determined by the collected swath width. Processed bandwidth is the range of Doppler frequency processed on each burst. Data from successive bursts are processed and averaged along track to create multilooks.

Data Products

Magellan data products will fall into three categories: standard products (Appendix B), special products (Appendix C), and cartographic products. Standard image products will include all raw data, correlated image strips, mosaics, and ancillary data. Special products will include images produced for science analysis and reports, and public-information products.

Figure 5. Burst-mode data collection.

Planet Limb → ← Orbit Path

K + 2
K + 1
K

Processing Bandwidth

Antenna Footprint

The Crosshatched Area Represents the One-Look Image Framelet Corresponding to Burst K + 1

Framelet (K + 2) —
Framelet (K + 1) —
Framelet (K) —

L
D
W

L, W, and D Vary as a Function of Orbit True Anomaly
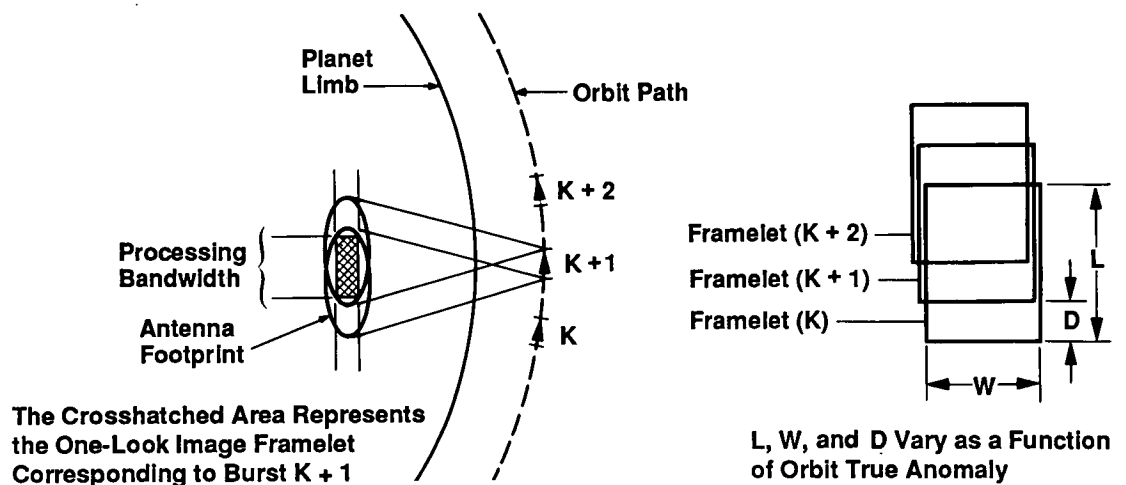
Cartographic products will be intermediate-resolution scaled-map quadrangles in standard projections. A complete description of the Magellan science data products can be found in the *Magellan Science Requirements Document* (1987) and Appendixes B and C.

Full-Resolution Basic Image Data Record

The F-BIDR will be the fundamental image data set and the basis for all the other image products. The complete description of this product can be found in the *Magellan Software Interface Specification* (1988). The F-BIDR is produced by the SDPS. The F-BIDR is available in digital form on magnetic tape (2400-ft reels of 6250-character/ in. computer-compatible tape). It contains a copy of the ancillary data provided in the SAR-EDR, the full-resolution image data, processing parameters used to produce the image, results of analyses of selected raw data and selected single-look images, and the reduced radiometer data. One F-BIDR is created for each orbit, resulting in nearly 1900 records in the nominal mission. One F-BIDR contains approximately 120 Mbytes of image data and approximately 10 Mbytes of ancillary data. The F-BIDR label format is F-BIDR.onum;ver; for example, F-BIDR.001;2 identifies a reprocessed version of the data from mapping orbit number 1, version 2.

The F-BIDR between 70°S and 89°N is in a sinusoidal equal-area projection with a local-reference meridian that corresponds to the intersection of the SAR antenna boresight intercept locus and the equator of Venus. Pixels are resampled and placed along latitude lines and spaced 75 m apart. An overlapping section of each F-BIDR, between 80°N and the north pole, is projected in the AT/CT grid system. The AT/CT projection places image lines along great circles normal to the spacecraft ground track. The orbit plane is determined at 85°N and the image line that includes that latitude becomes the reference meridian for the AT/CT sinusoidal equal-area projection of that orbit.

Pixel values are in units of normalized radar backscatter represented by 8 bits. The pixel values are the decibel (dB) representation of the ratio of the radar cross-section value obtained from the SAR processing and the corresponding value in the backscatter-coefficient model:

$$\sigma_0 = \frac{0.0188 \cos I}{(\sin I + 0.111 \cos^3 I)}$$

The steps are 0.2 dB with a range of values from -25 dB to +25 dB, using data numbers (dn or pixel value) from 1 through 251. A dn of 0 is used as a filler value, and numbers 252 through 255 are data descriptor tags.

Full-Resolution Mosaicked Image Data Record

The F-BIDRs will not be in a format useful for geologic mapping. Consequently, the F-BIDRs will be assembled into Full-Resolution Mosaicked Image Data Records (F-MIDRs) (Figure 6) by the Magellan Image Data Processing Subsystem (IDPS). In the standard processing for the nominal mission, 15% of the planet will be mosaicked into F-MIDRs; this will result in approximately 240 full-resolution mosaics.

To provide coverage for larger areas, the data will be averaged in successive operations in which a mosaic pixel is replaced by the average of nine pixels. The first step of this process is the creation of a 3 × 3 compression of the F-BIDR called the compressed BIDR or C-BIDR. The C-BIDRs are mosaicked into 8192 × 8192 arrays called C1-MIDRs. C2-MIDRs and C3-MIDRs are successive 3 × 3 compressions into 8192 × 8192 pixel arrays. The top 7168 × 8192 pixels are image data and the bottom 1024 × 8192 pixels are annotation. The SAR image field contains a scale grid. The image data field is partitioned into a 7 × 8 array of 1024 × 1024 pixel subframes.

All the data products below 80°N latitude will be in sinusoidal equal-area projection. The F-BIDRs will be available in this projection up to 89°N latitude.

The various MIDR products will be distributed as photographic prints and digital files on CD-ROM. The mosaicked data will fill more than 100 CDs. In general, the photoproducts are spatially filtered to suppress intensity discontinuities at the seams, and the resulting products incorporate a contrast enhancement. The archived digital data are not altered in this way, so any digital standard-product mosaic will have the unfiltered, original dn values.

Figure 6. Magellan image data products.
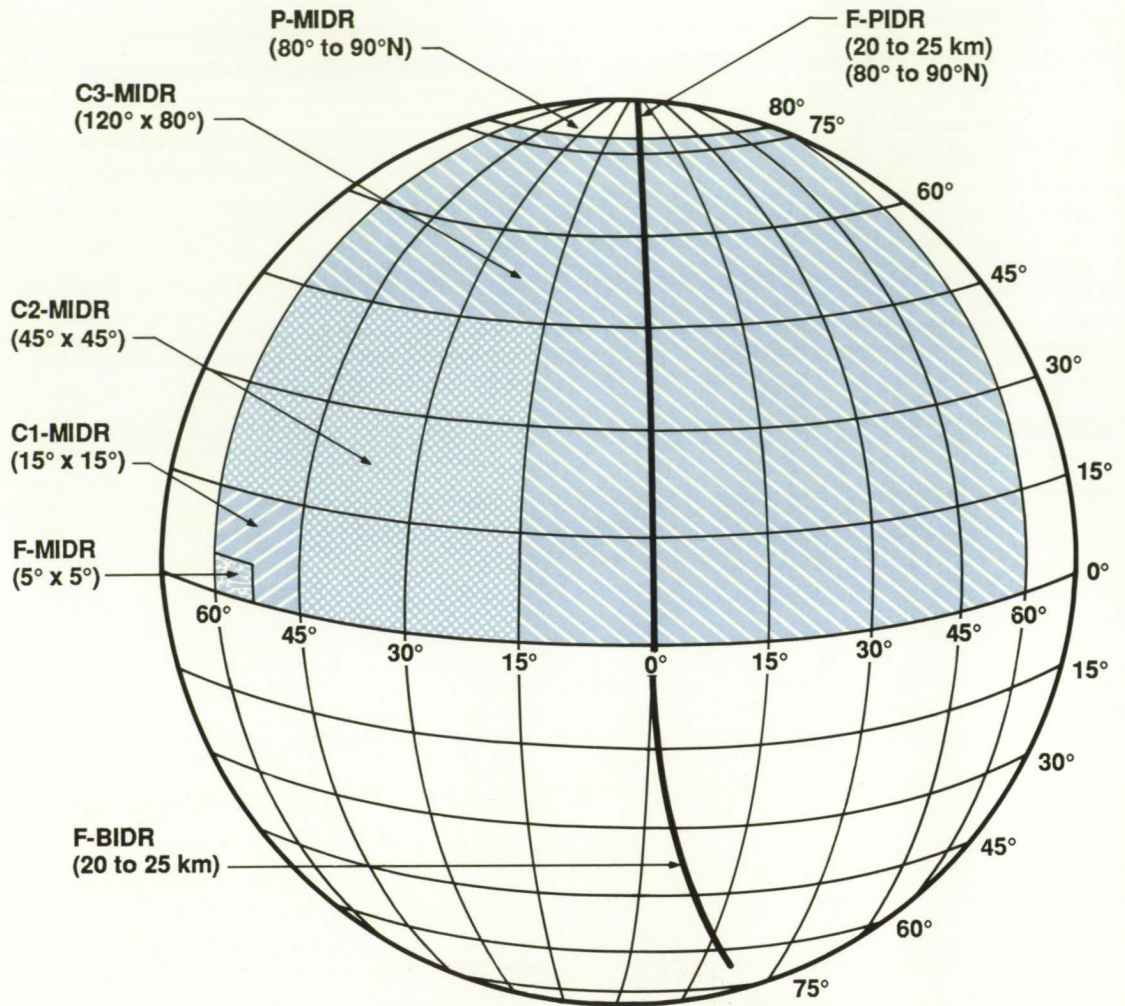
F-BIDR	**Full-Resolution Basic Image Data Record**
F-PIDR	**Full-Resolution Polar Image Data Record**
F-MIDR	**Full-Resolution Mosaicked Image Data Record**
C1-MIDR	**Compressed-Once Mosaicked Image Data Record**
C2-MIDR	**Compressed-Twice Mosaicked Image Data Record**
C3-MIDR	**Compressed-Thrice Mosaicked Image Data Record**
P-MIDR	**Polar Mosaicked Image Data Record**

The polar AT/CT image data between 80°N and 90°N will be incorporated into Full-Resolution Polar Image Data Record (F-PIDR) frames. Each strip is cut into 7168 pixel segments and placed side by side in frames.

Map projections

Magellan is a mapping mission, and therefore maps are emphasized in the data products. Base maps will be produced at various scales using standard projections. These maps will be used to present the results of the geologic analysis of the mission data (Figure 7).

Because Venus, like Earth, is essentially a sphere, map projections developed by cartographers to depict the spherical surface of Earth can be used. The problem is one of producing a curved surface on a flat sheet while minimizing distortion. A globe might appear to be the best map to use, but it cannot be made large enough for most applications, and it is difficult to make measurements on a surface that is not flat. With any flat projection, compromises must be made. Equal-area maps preserve the area from place to place, but distort shapes and scale. Conformal maps preserve the shapes of small features, but distort large regions to some degree.

The Magellan Project will use conformal map projections. The important features of this

True 1:5M Scale 73.4° 27.5°   **True Scale At 90°**   V1   **Polar Stereographic Projection**   75°

V5	V6 Lambert	V7 Conformal	V2 Conic	V3 Projection	V4
V14 V15	V16 V17	V18 V19	V8 V9	V10 V11	V12 V13

75°   50°   25°
180°   240°   300°   0°   60°   120°   180°

25°	V26	V27 True 1:5M	V28	V29	V30	V31	V20	V21	V22	V23	V24	V25	25°
0°	V38	V39 Scale ±22.8	V40	V41	V42	V43	V32	V33	V34	V35	V36	V37	0° -25°

Mercator Projection

180° 210° 240° 270° 300° 330° 0° 30° 60° 90° 120° 150° 180°

V50 V51	V52 Lambert V53	V54 Conformal V55	V44 Conic V45	V46 Projection V47	V48 V49
V59	V60 V61		V56	V57	V58

-25° -50° -75°

True 1:5M Scale -27.5° -73.4°   **True Scale At 90°**   V62   **Polar Stereographic Projection**   -75°

62 Sheets

Figure 7. The Magellan Venus mapping plan.
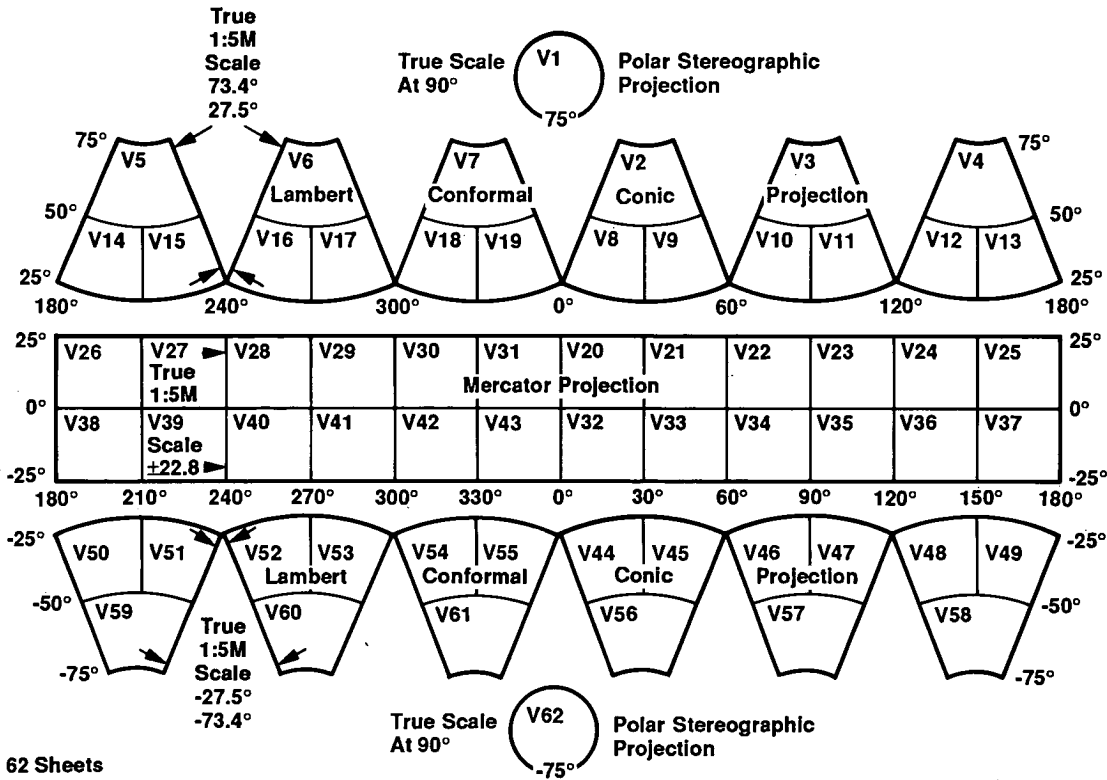
type of projection are the true angles about a given point and the constant scale in all directions about a point. This means that lines of latitude cross lines of longitude at right angles just as they do on the globe.

Three standard conformal map projections will be used for the maps of Venus: Lambert Conformal, Mercator, and Polar Stereographic. The areas covered by these projections are shown in Figure 7. The Mercator projection has parallel, equally spaced meridians of longitude crossed at right angles by horizontal parallels of latitude. The scale is a true 1:5,000,000 at ±22.8 deg latitude. This projection will cover up to the 25°N latitude to minimize the kind of distortion in some maps of Earth that makes Greenland appear so much larger than it is.

The Lambert Conformal Conic Projection will be used between latitudes of 25 and 75 deg, both north and south. A true 1:5,000,000 scale is placed on parallels of 27.5 deg and 73.4 deg,

north and south. On this projection, parallels of latitude are concentric circles while meridians of longitude are equally spaced straight lines that are radii of the parallels, thus cutting them at right angles.

The Polar Stereographic Projection will be used for the polar regions down to 75°N from the north pole and up to 75°S from the south pole. A true 1:5,000,000 scale is at the pole. On this projection, the sphere is projected onto a plane tangent to the pole. The point of projection is from the opposite pole.

The cartographic products will comprise a series of 62 maps at a 1:5,000,000 scale. They are semicontrolled, using the best control grid available at the time of production during the mission. The final control grid will be available for production of additional maps after the primary mission. These maps will be produced by the United States Geological Survey in Flagstaff, Arizona.

11

Impact Structures

. . . .

Introduction

Investigators have speculated on the presence of impact features on Venus (Saunders and Malin, 1976). Earth-based radar observations show features on Venus that are morphologically akin to impact craters (Burns and Campbell, 1985). Radar images obtained by Soviet Venera missions 15 and 16 cover about 25% of the planetary surface and display a large number of craters, many of which resemble impact craters on Mercury, Moon, Mars, and other planetary bodies. However, the resolution of Venera images limits perception to craters with a diameter greater than about 8 km.

The Magellan orbiter includes an imaging radar that will cover from 70 to 90% of the Venusian surface at a resolution an order of magnitude higher than that of the Venera missions. Thus, Magellan will provide extensive regional coverage and a more detailed view of the surface. Closer study of crater origins will be possible and smaller craters may be observed. However, the interpretation of craters and structures of impact origin on synthetic-aperture radar (SAR) images depends not only on resolution, but also on contrasts in surface reflectivity and such imaging characteristics as the illumination geometry and wavelength as well. To understand the types of information about impact craters on Venus that Magellan radar is expected to provide, it is instructive to review existing spaceborne radar-image observations of impact features on Earth where there is good ground-truth data and compare them with impact features on the Venera images.

Imaging Characteristics

The importance of large-scale slope, small-scale surface roughness, and incidence angle in interpreting crater morphology and structure from radar images is examined below by reference to terrestrial examples obtained by Seasat SAR and SIR-A. The observations are compared with images obtained by Venera 15 and 16 and discussed in the context of the Magellan imaging radar. The essential radar parameters of these imaging systems are shown in Table 5. Seasat SAR and SIR-A were operated at a comparatively long radar wavelength (23.5 cm) and high spatial resolution (25 to 40 m), with antenna geometries that produced different nominal incidence angles. The Venera system obtained images at a shorter wavelength (8 cm) and lower resolution (1000 to 2000 m), with a very low nominal incidence angle. Magellan will operate at an intermediate wavelength (12.6 cm) and spatial resolution (120 to 300 m). However, the nominal incidence angle of Magellan will vary significantly with latitude on Venus (Johnson, 1989).

For each system, the specified incidence angle (Table 5) is nominal because it is valid only for a level horizontal surface. On sloping surfaces, the incidence angle decreases at foreslopes or increases at backslopes by the amount of the slope in the direction of the illumination vector. Thus foreslopes are negative and backslopes are positive relative to a nominal incidence angle.

Radar system	Nominal incidence angle, deg	Wavelength, cm	Spatial resolution, m
Seasat SAR	23 ± 3	23.5	~25
SIR-A	50 ± 3	23.5	~40
Venera 15, 16	11 to 13 ± 1.5	8.0	1000 to 2000
Magellan	16 to 45	12.6	120 to 300

Table 5. Spaceborne imaging radar system parameters.

PAGE __12__ INTENTIONALLY BLANK

Figure 8. Variation of radar backscatter with incidence angle for surfaces from rough, through intermediate, to smooth showing the ranges of dominant surface effects.
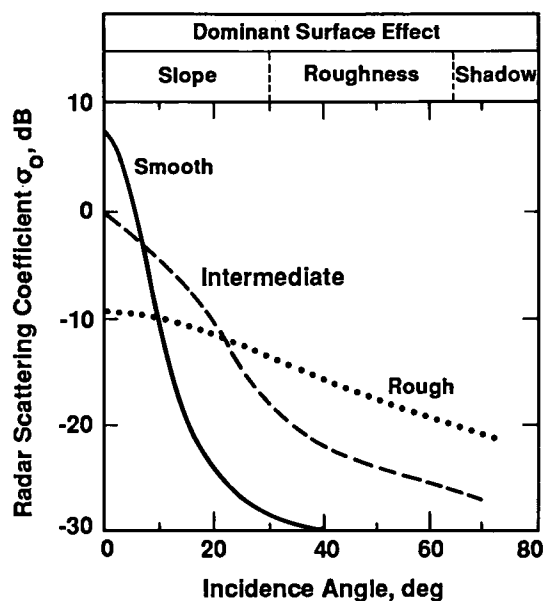
At low incidence angles, up to about 30 deg, backscatter is dominated by large-scale surface slope, on the order of meters. Small changes of slope, and hence incidence angle, produce relatively large changes of backscatter. This yields strongly contrasting gray levels on images. At incidence angles from about 30 to 60 deg, backscatter is dominated mostly by the small-scale roughness of a surface, on the order of the radar wavelength. At this scale, smooth surfaces produce specular reflection and are dark on images; rough surfaces produce diffuse scattering and are bright on images. Intermediate surfaces produce both types of scattering and are gray on images. Backscatter curves for rough, intermediate, and smooth surfaces (Figure 8) show that in the range of incidence angles from 30 to 60 deg, changes in surface roughness have a greater effect on backscatter intensity than changes in incidence angle. At incidence angles greater than about 60 deg, backscatter is weak and surfaces are dark to very dark on images.

A breakpoint between smooth and rough surfaces (and the corresponding dominant radar scattering mechanisms) is loosely implied by the Rayleigh criterion. Because the equation for this criterion does not consider an intermediate category of surfaces between definitely smooth and definitely rough, it was modified by Peake and Oliver (1971) using factors that define upper and lower values for rms surface smoothness or roughness (see *Synthetic-Aperture Radar Imaging*). Field measurements of different types of surfaces have led researchers to experiment with a variety of modifiers (e.g., Schaber et al.,

1976 (geologic surfaces); Ulaby et al., 1982 (agricultural surfaces)). This illustrates one of the difficulties associated with modeling the radar behavior of natural surfaces. Regardless of the modifying factor that is used, it follows from the equations that at any incidence angle a given surface is rougher as the wavelength decreases and, independent of wavelength, a given surface is smoother as the incidence angle increases.

Using the modified Rayleigh criterion for example, Table 6 shows that there is about a 29% increase in rms surface smoothness and a 25% decrease in rms surface roughness through the range of Magellan nominal incidence angles from about 45 to about 16 deg. For the interpretation of Magellan radar images, this has important implications that are discussed further under *Radar halos* in this chapter.

Craters and Structures

Characteristically, an impact crater has a circular rim and a small depth relative to its diameter. Because such craters are radially symmetrical, the landforms are ideal for relating image responses to radar illumination geometry. The geomorphic expression of impact craters is most pronounced and widespread on planetary bodies that have low rates of resurfacing. For example, Mercury and Moon are covered with circular craters, which often overlap. This indicates successive impact events on surfaces that are old and relatively stable. Earth has a comparatively rapid rate of resurfacing. Most terrestrial impact features have had their original morphology modified by erosion; only a few recent features retain a distinct craterform.

Craters range in form from simple, bowl-shaped features to complex structures with central peaks and/or rings (Grieve, 1987). They also exhibit a wide range of degradation states from relatively fresh structures, some with portions of preserved ejecta, to erosional scars known as astroblemes (Dietz, 1961). Simple, bowl-shaped craters are confined to diameters up to about 2 km in sedimentary rocks and about 4 km in crystalline rocks. At greater diameters, up to about 150 km, terrestrial impact structures have a complex form that commonly includes a central uplift. Astroblemes expose a root level of crater substructure from which the overlying craterform has been completely removed by erosion.

Table 6. RMS
surface smoothness
and roughness
breakpoints for the
range of Magellan
nominal incidence
angles (from
modified Rayleigh
criterion).

Incidence angle, deg	Surface	Wavelength, cm		
		23.5 (Seasat, SIR)	12.6 (Magellan)	8.0 (Venera)
16	smooth	< 1.0	< 0.5	< 0.3
	rough	> 5.6	> 3.0	> 1.9
45	smooth	< 1.4	< 0.7	< 0.5
	rough	> 7.6	> 4.0	> 2.6

Currently, 116 terrestrial impact structures have been verified, and a small number of new structures are recognized each year (Grieve, 1987; Grieve and Robertson, 1987). The principal support for an impact origin comes from the physical association of meteorite debris and/or evidence of shock-metamorphic effects. In the absence of such evidence, an impact origin may be suspected for a crater on the basis of its morphology, provided that other nonimpact sources of cratering such as volcanism, tectonism, collapse from underground solution, or wind erosion are evidently less plausible in any given instance.

Measurements indicate that the circularity of terrestrial impact craters is generally higher than that of craters of other origins (Pike, 1974). At low incidence angles, pronounced relief displacement creates a major difficulty in determining the precise position of crater rims on images. It is convenient here to consider the radar responses from crater surfaces in an orthogonal frame of reference. Abrupt contrasts in radar response to changing slope conditions (hence incidence angle) produce sharp tonal boundaries normal to the illumination vector; these contrasts divide a crater into distal, medial, and proximal sectors. This image characteristic provides the basis for analysis and interpretation in the following examples.

Simple Terrestrial Structures

The best currently available radar coverage of simple terrestrial structures includes Barringer (Meteor) Crater, Arizona, U.S.A., and Talemzane (Daiet el Maadna) Crater, Algeria (Figure 9). The craters display similar morphology and an approximate radial symmetry. Each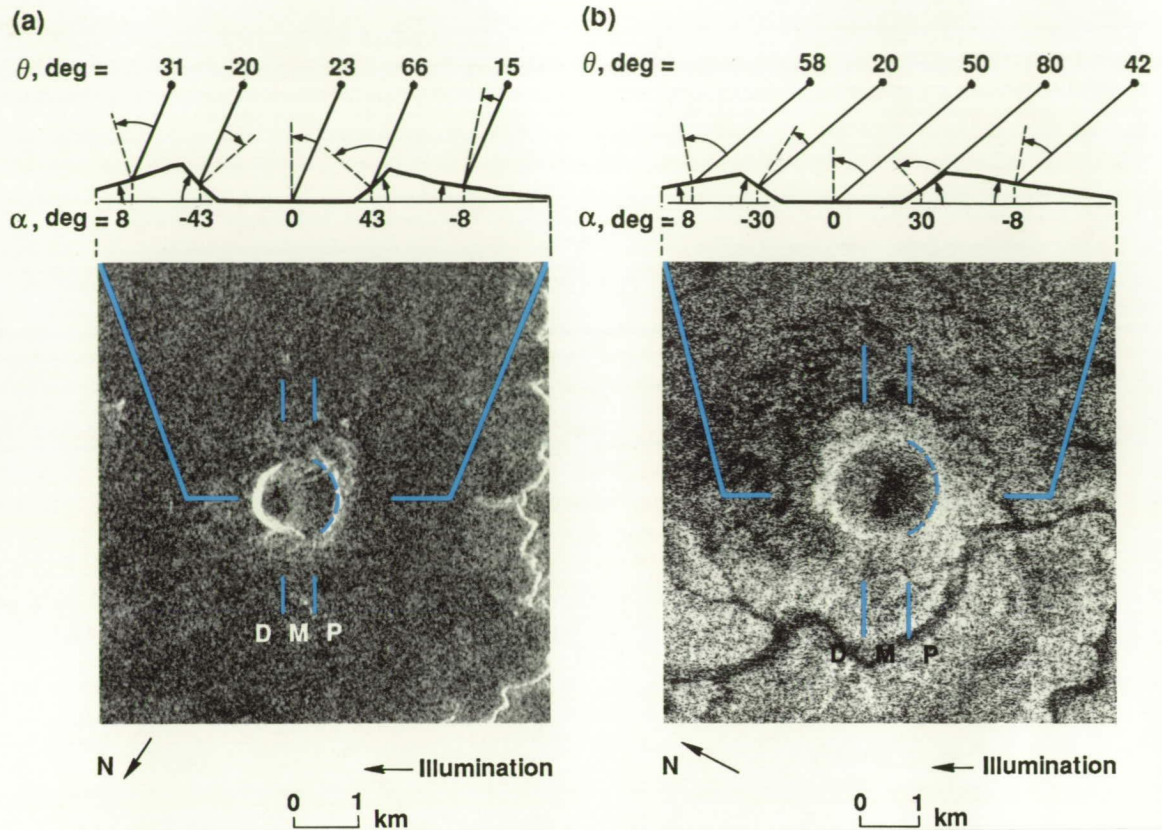 is located in a comparable geologic setting on a plateau underlain by flat-lying sedimentary rocks. Field descriptions of the craters indicate that Barringer is the best preserved and least subdued; thus it is thought to be the younger of the two.

Barringer, U.S.A.

Barringer Crater is located on a plateau underlain by sandstone and dolomitic limestone formations. The crater is essentially bowl-shaped, about 1.2 km in diameter (D) and 180 m deep (d). In plan view, it appears to be square-sided with rounded corners (low roundness, but high sphericity), which may represent some structural control by the regional joint sets. The depth-to-diameter ratio (d/D) is 0.15. The crater has an encompassing rim that rises 30 to 60 m above the surrounding plateau. The rim is locally overturned and ejecta blocks up to 30 m are scattered about the surface close to the rim (Shoemaker and Kieffer, 1974). The crater has a comparatively level floor and a surrounding interior wall composed of talus slopes up to about 43 deg. Bedrock outcrops toward the top are locally vertical or overturned at the rim. The outer surface slopes away from the rim at about 8 to 10 deg. The rim is outlined by tonal contrasts on the Seasat SAR image (Figure 9(a)); the contrasts are pronounced in the distal and proximal sectors, but subdued in the medial sector. The crater floor and the undisturbed plateau surface show medium to dark image tones because they are mostly level and comparatively smooth to the 23.5-cm wavelength (L-band) radar. There is no evidence of a radar halo on the image.

The illumination geometry shown in Figure 9(a) falls mostly in the range where backscatter is dominated by large-scale slope effects, which result in notable relief displacement. For instance, the negative incidence angle on the

Figure 9. Simple, terrestrial impact structures: (a) Seasat SAR image of Barringer Crater, Arizona, U.S.A.; (b) SIR-A image of Talemzane Crater, Algeria. The craters are divided by strips into sectors that are distal (D), medial (M), or proximal (P), relative to the illumination vector.

(a)

θ, deg = 31 -20 23 66 15

α, deg = 8 -43 0 43 -8

D M P

N

← Illumination

0 1 km

(b)

θ, deg = 58 20 50 80 42

α, deg = 8 -30 0 30 -8

D M P

N

← Illumination

0 1 km

Note: The proximal sectors of the crater rims are indicated by dashed lines. The schematics show the average surface slope angles (α) and corresponding radar incidence angles (θ) at five locations across the diameter of each crater in the direction of radar illumination. Negative slope angles represent foreslopes. The negative incidence angle in (a) indicates radar foldover of the crater wall and rim in the distal sector. Note that the contrasting intensities of responses around the halo in (b) are bilaterally symmetrical in the direction of illumination. There is no vertical exaggeration.

crater wall in the distal sector indicates that the upper part of the slope was imaged by the radar before the base. This compresses the slope to the point of foldover, causing saturation on the image and obscuring part of the crater floor. Further contributions to saturation are provided by corner reflections from within the crater. Forward scatter from relatively smooth surfaces on the crater floor and from the proximal sector of the wall are doubly reflected as backscatter from appropriately oriented facets on the wall and rim in the distal sector. Consequently in this sector, the wall and the interior facing portion of the rim appear very bright, rim structure is imperceptible, and the position of the rim on the image is indeterminate.

In the proximal sector, the outline of the crater rim is more clearly marked. The rim structure on the outer slope is bright from inclined surfaces of overturned strata that locally produce specular returns, and from randomly distributed meter- and decameter-size ejecta

blocks on the rim. The crater wall slopes away from the radar illumination in this sector and is dark because of low backscatter at the large incidence angle (~ 66 deg). The rim shows a significantly greater radius of curvature than that in the opposite distal sector.

In the medial sector, the surfaces of the crater wall and the outer slope on each side are aligned essentially parallel to the illumination vector. In this orientation, slope changes produce lower backscatter contrasts. Tonal contrasts are subdued and the edge of the rim is not sharply defined on the image. The flanks of the distal sector appear compressed relative to the flanks of the proximal sector. This lowers the apparent circularity of the crater outline in plan view and imparts a bilateral symmetry in the direction of the radar illumination.

Talemzane, Algeria

Talemzane Crater is located on a plateau underlain by limestone strata. It forms an ap-

proximately circular depression about 1.75 km in diameter and 67 m in depth (d/D ratio = 0.04). It is encompassed by a rim uplifted some 27 m above the surrounding plateau. The crater floor contains an asymmetrical area of fine-grained alluvial sediments to the south. The crater wall slopes all around at angles between 22 and 35 deg. Limestone beds are more steeply inclined or vertical in the upper part of the wall, and in places they are overturned (Lambert et al., 1980). However, the wall is not as steep and the edge of the rim is not as sharply defined as the wall and rim of Barringer Crater. The outer surface slopes away from the rim at 8 to 10 deg. It shows a radar halo on the SIR-A image (Figure 9(b)) that varies systematically in brightness around the rim (McHone and Greeley, 1987). Rocks exposed on this surface are mainly mixed breccias that closely resemble those in the crater. They form a nearly continuous annular blanket that is concentric with the crater and that extends about 400 m from the rim. The size of the fragments ranges up to 10 m and decreases with distance from the rim. The outline of the rim (Figure 9(b)) is marked by less pronounced tonal contrasts than that of the Barringer Crater observed on the Seasat SAR image (Figure 9(a)). Dark image tones on the crater floor and most of the plateau surface north and east of the crater represent low backscatter from level and relatively smooth sandy surfaces.

The illumination geometry shown in Figure 9(b) lies mostly in the range where backscatter is dominated by small-scale surface roughness. Moderate to relatively high incidence angles on the outer slope in the medial and proximal sectors result in bright image tones dominated by the small-scale roughness of the coarse-grained ejecta fragments. This produces the radar-bright halo seen on the image out to about one third of the crater diameter (Figure 9(b)). The halo is comparatively bright in the proximal sector, but appears darker in the distal sector where there is less radar signal return as the incidence angle approaches 60 deg. Note that equivalently rough, blocky, weathered surfaces of undisturbed limestone bedrock on the level surface of the plateau south and west of the crater produce image tones comparable to those in the radar-bright halo. However, the low incidence angle on the distal sector of the wall and on adjacent segments of the uplifted rim results in bright image tones dominated here by large-scale slope.

Additional radar brightness may be provided from energy scattered forward off the crater floor and then backscattered from appropriately oriented facets on the rim.

In the medial sector where the walls are essentially in line with the illumination vector and slope changes provide little contribution to backscatter, the rim and the outer slope appear equally bright on the image because of diffuse backscatter from the rough surface. This roughness-related brightness merges imperceptibly with slope-related brightness on the image toward the distal sector of the crater wall. The transition between dominance of backscatter by surface roughness and dominance by slope is not readily apparent from the image. However, the curvature of the rim appears to be comparable in both proximal and distal sectors and the outline of the crater retains a radially symmetrical form on the image.

Volcanic Maar Craters

Though the morphology of the small craters described above is typical of fresh, simple impact structures on Earth, it is not unique to an origin by impact. Among the various crater types that do not originate by impact, volcanic maar craters have morphologic characteristics that most closely resemble those of small impact craters. Maar craters originate from shallow volcanic eruption and collapse. They have an uplifted rim structure and a circular form in plan view that approaches the circularity of impact craters. In the absence of regional geologic information, the two types of craters can be confused on radar images (Greeley et al., 1987).

Maar craters were imaged by both Seasat SAR and SIR-A in the Pinacate Volcanic Field, Sonora, Mexico. This is a Quaternary basaltic shield of numerous lava flows and cinder cones, as well as eight maar craters and a partially collapsed tuff cone. The craters, which range up to 1.6 km in diameter, expose steeply sloping to vertical interior walls with stratified volcanic rocks (Jahns, 1959; Gutmann and Sheridan, 1978). Though the maars in the Pinacate field display equal or greater depth relative to diameter (d/D ratio) and steeper interior slopes, they show radar responses similar to those of the impact craters discussed above.

Elegante, Mexico

Elegante is the largest maar crater in the Pinacate field and the most nearly circular in outline; also, it has the simplest rim, with a symmetrical outer slope. It is a flat-floored, essentially cylindrical depression approximately 1.6 km in diameter and 244 m deep (d/D ratio = 0.15). The crater walls form a continuous ring of cliffs up to 130 m high with an average slope of about 80 deg. At the base of the cliffs, an apron of talus with a more gentle slope (about 24 deg) extends to the base of the crater. The rim rises approximately 50 m above the surrounding plain and slopes outward from its crest at 9 to 15 deg. It exposes a steeper inner slope, with tuff breccia up to 70 m thick. The tuff breccia thins as it encompasses the crater out to about one-half the diameter. The circular pattern of the rim crest is interrupted to the southeast by a depression known as the Scallop (Gutmann, 1976).

The Seasat SAR and corresponding SIR-A images of Elegante Crater (Figure 10) provide good examples for contrasting the dual-incidence-angle viewing effects and for comparing

Figure 10. Elegante Crater, Pinacate Volcanic Field, Sonora, Mexico: (a) Seasat SAR image; (b) SIR-A image. The crater is divided by strips into sectors that are distal (D), medial (M), or proximal (P), relative to the illumination vector.
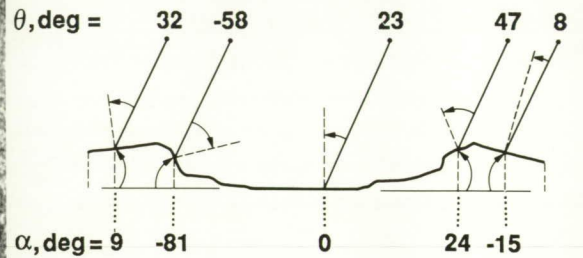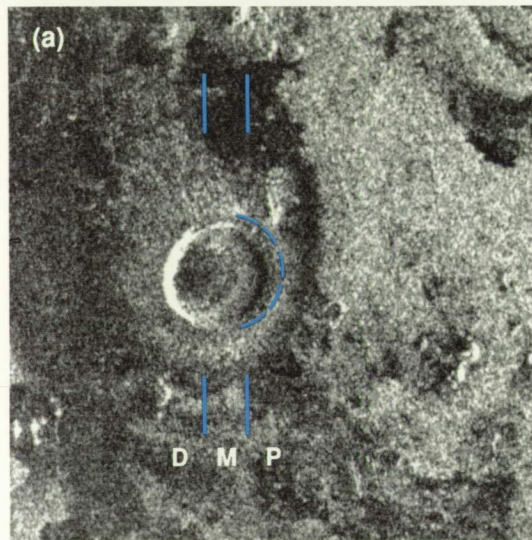
ORIGINAL PAGE
BLACK AND WHITE PHOTOGRAPH
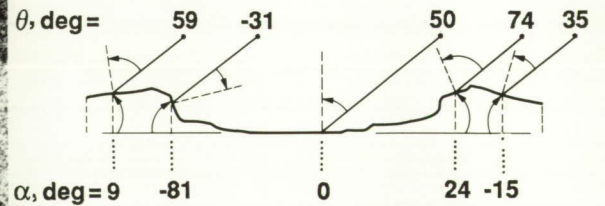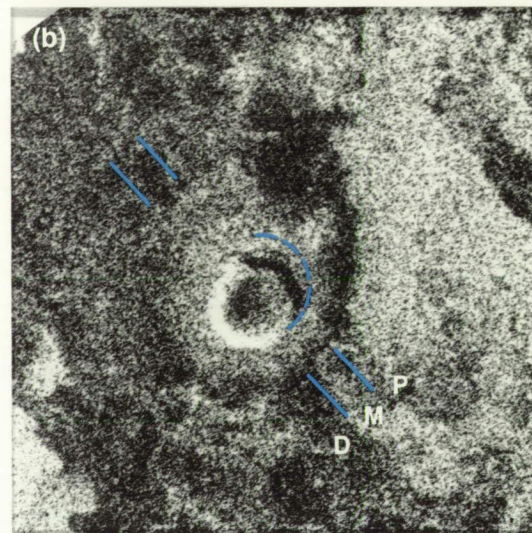
Note: The proximal sector of the crater rim is indicated by a dashed line on each image. The schematic sections are in the direction of the Seasat SAR illumination; the average slope angles (α) and incidence angles (θ) correspond to five locations across the crater diameter. Negative slope angles represent foreslopes. On both images, the radar brightness that extends to the south from the gentle outer slope denotes the steeper erosional slopes of a small breached cinder cone. There is no vertical exaggeration.

these effects to the observations by Seasat SAR at Barringer Crater and SIR-A at Talemzane Crater. Though the Seasat SAR and the SIR-A images of Elegante Crater were obtained from azimuthal directions 40 deg apart, the essentially radial symmetry of the crater renders it virtually isotropic with respect to the illumination azimuth. Thus the contrasts in radar signal intensity around the crater relate mostly to different Seasat SAR and SIR-A incidence-angle effects.

The slope of the crater wall produces negative incidence in both Seasat SAR and SIR-A images; the negative incidence results in foldover and saturation around the distal sector of the wall in both images. The saturation obliterates signal from the inner slope of the upturned rim, and the position of the rim crest in this sector is indeterminate on both images. In the proximal sector, the steep crater wall is in shadow on both images. Here the rim crest is outlined by the subdued tonal contrast between its comparatively steep inner slope and its more gentle outer slope. Foldover in the distal sector and shadowing in the proximal sector combine to distort the radial symmetry of the rim crest on both Seasat SAR and SIR-A images and to produce an apparent bilateral symmetry parallel to the illumination vector.

In the medial sector, the Seasat SAR image (Figure 10(a)) shows the outline of the rim crest, which is normal to the craterward limit of numerous small radial gullies that extend across the outer slope. The gullies are highlighted in this sector, where they are normal or highly oblique to the illumination vector. However, they are obscure in the proximal and distal sectors, where they are parallel or gently inclined to the illumination vector. At the lower resolution of SIR-A (Table 5), the rim crest is unclear and individual gullies are imperceptible on the SIR-A image (Figure 10(b)).

Complex Terrestrial Structures

A small but varied assemblage of complex terrestrial structures including astroblemes was imaged by Seasat SAR and SIR-A. The structures range widely in size and level of preservation, but mostly the craterforms have been removed by postimpact erosion. The best spaceborne radar image coverage of known

structures includes Elgygytkhyn, Chukotka, U.S.S.R, and about 60% of Manicouagan, Quebec, Canada. Elgygytkhyn is the largest terrestrial impact structure that has the erosional remains of the original crater rim. Manicouagan presents topography that has been profoundly modified by glacial erosion.

Elgygytkhyn, U.S.S.R

Elgygytkhyn Crater (also referred to as Elgygytgyn) is located on the upland of the Anadyr' Plateau in eastern Siberia. A possible impact origin was suggested by Zotkin and Tsvetkov (1970). An origin by impact is supported on morphological grounds by the remarkable circularity of the ring of eroded mountain peaks that surround the crater, and the lack of collapse scalloping around the crater margin. These crater features have been shown to be in sharp contrast with caldera morphology as observed on Landsat images. Furthermore, Elgygytkhyn does not display the geomorphic aspect of a caldera (Dietz and McHone, 1976).

The Seasat SAR image of Elgygytkhyn clearly shows the ring of mountains that surrounds the crater; the ring has a diameter of about 18 km (Figure 11). Nevertheless, the rim crest is so deeply eroded that significant contrasts of radar response in different sectors of the crater are not apparent. If a central uplift is associated with the structure, it is obscured entirely by the lake.
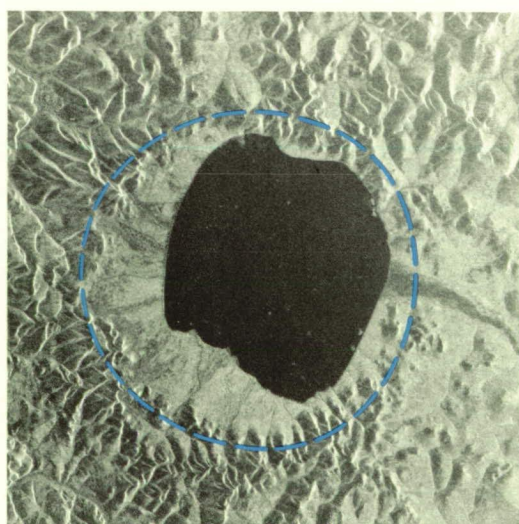

N   ← Illumination

0   10 km

Figure 11. Seasat SAR image of Elgygytkhyn Crater, Chukotka, U.S.S.R. The dashed line indicates the crater rim. The form of the mountains and valleys on the image gives no evidence of significant glacial erosion in the area outside the crater.

19

Manicouagan, Canada

Manicouagan is one of the most intensively studied complex impact structures on Earth. It has concentrically arranged morphological elements that were defined by Floran and Dence (1976) and have more recently been elaborated by other authors. The morphology consists of an inner central region, an inner plateau, and an annular trough, and a group of outer elements that include an inner fractured zone, outer disturbed zone, and outer circumferential depression. These morphological elements represent structural levels much below the original form of the crater (Grieve and Head, 1983). The Seasat SAR image (Figure 12(a)) covers all but the western sector of the Manicouagan structure. However, it displays varying proportions of each of the morphological elements shown on the sketch map (Figure 12(b)).

The three outer morphological elements of the structure are best defined to the west, in the portion not covered by the Seasat SAR image. The distal boundary of the inner fracture zone is perceptible on the image (Figure 12(a)) to the north where it coincides with sharp bends in most streams that flow inward to the annular trough. East of the annular trough, the outer elements have not been defined. An area of distinctive coarse-grained texture on the image east of the trough corresponds to massive crystalline rocks (gabbro). Conjugate sets of linear topographic features denote fracturing in this area. The higher density and closer spacing of these features for about 20 km outward from the trough probably indicate the inner fractured zone.

Concentrically aligned valley segments are prominent from 10 to 50 km east and southeast of the annular trough. The orientation suggests that they are structurally related to the Manicouagan feature. Locally, the concentric valleys are truncated against prominent topographic alignments that radiate outward from the annular trough for tens of kilometers. The radially aligned features denote the extensive fracture halo that is reported to have a diameter of about 150 km (Grieve et al.,1988).

Figure 12. Manicouagan structure, Quebec, Canada: (a) Seasat SAR image; (b) sketch map. Note the annular trough, about 15 km wide and 65 km in diameter, that contains the Manicouagan Reservoir.
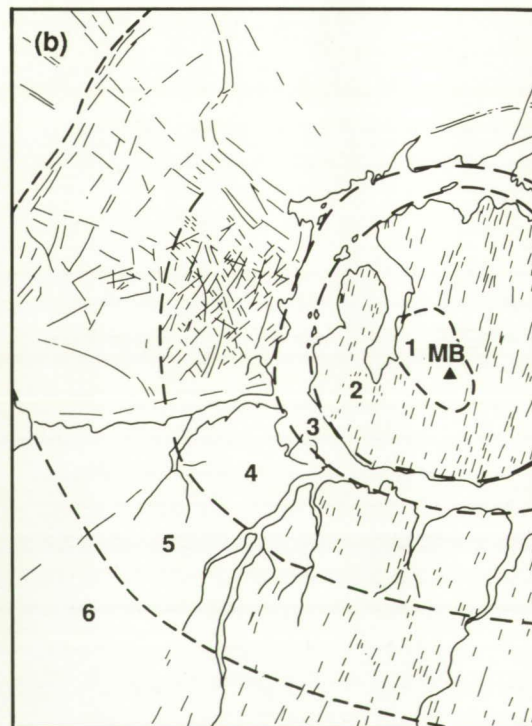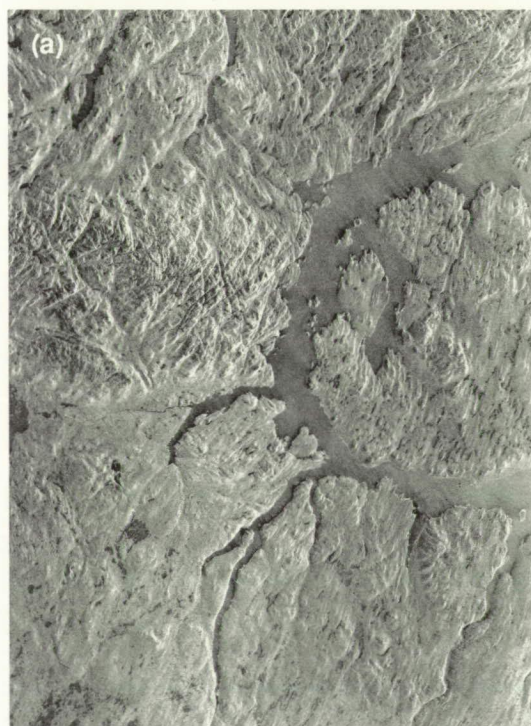
N ⟋   ⟵ Illumination

0 ————— 30 km

Note: The sketch map shows (1) Mont de Babel (MB) in the central peaks, (2) the inner plateau, (3) the annular trough, (4) the inner fractured zone, (5) the outer disturbed zone, and (6) the outer circumferential depression. Note the north-south orientation of glacial topography at the center, the high density of conjugate linear features east of the annular trough, and the extensive radial alignments of valley segments outward from the trough.

20

Venusian Impact Craters

Venera radar images reveal about 150 impact craters with diameters from 8 to 144 km that are distributed over less than 20% of the Venusian surface (Ivanov et al., 1986; Basilevsky et al., 1987). Smaller craters have been reported, but diagnostic features are not resolved. The size–frequency distribution of the craters shows a maximum in the 16- to 32-km-diameter interval. The craters have been classified into morphological types that change progressively with increasing diameter. Most morphological types show contrasts in levels of preservation from fresh through mature to degraded. Apparently this represents a degradational sequence that is independent of crater size (Basilevsky et al., 1987).

Venusian impact craters range from bowl-shaped types, which are the smallest observed on Venera images, through knobby-bottom to central-peak and multiple-ring types, which are the largest. Each of the first three types is represented in the maximum size–frequency interval, though the central-peak type predominates (Basilevsky et al., 1987). Fresh craters have sharp rims and outlines that suggest many of them are radially symmetrical. The diameters of craters in the maximum size–frequency interval range from 10 to 20 times larger than those of Barringer, Talemzane, and Elegante observed by Seasat SAR and/or SIR-A, but because the spatial resolution of Venera images ranges from 70 to 20 times lower than that of Seasat SAR or SIR-A, the scales of perception of the small terrestrial craters and the larger Venusian craters are comparable.

Examples of prominent central-peak-type craters were selected from the Venera 15 and 16 coverage for this analysis. The craters range in diameter from 24 to 34 km (Figure 13) and exhibit fresh to mature morphology with sharp, presumably circular, rims (Basilevsky et al., 1987). Though it is not possible to determine surface slope values from the images, the slope-dominated outlines of the crater walls are analogous in each case. In the distal sectors, the walls appear saturated and compressed due to foldover. Evidently the slope of the walls equals or exceeds the nominal incidence angle here. In the proximal sectors, the crater walls are dark, and the sharp rim crests are drawn toward the illumination vector. In the medial sectors, the

distortion of the crater rims is minimal, but the outlines are weak. These responses impart an appearance of bilateral symmetry to the craters that is further enhanced by the outlines of the central peaks, notably on Rudneva and Zvereva (Figure 13(b) and (c)). Comparable image characteristics were observed on the Seasat SAR images of Barringer and Elegante Craters (Figures 9(a) and 10(a)).

Fresh craters are reported to have radar-bright halos that commonly show bilateral symmetry on the images. The halos are thought to denote surface roughness that is related to ejecta blankets. Mature craters show no apparent halo; this condition is thought to represent terrain modification, perhaps by eolian erosion and deposition (Ivanov et al., 1986). On images of Kemble, Rudneva, and Golubkina (Figure 13(a), (b), and (d)), the radar halos are brightest in the proximal sectors, but comparatively subdued in the distal sectors. A comparable effect was noted on the SIR-A image of Talemzane Crater (Figure 9(b)), where angular fragments of mixed breccia are reported to form a nearly continuous annular blanket that extends up to 400 m from the crater rim (Lambert et al., 1980).

In the case of Zvereva (Figure 13(c)), the proximal sector appears bright, but there is no evidence of a halo in the medial and distal sectors. As this brightness contrast occurs along a mosaic boundary on the image, it is probably a processing artifact.

In addition to obvious impact craters, many circular features have been noted on the Venera 15 and 16 images (Nikolaeva et al., 1986; Basilevsky et al., 1987). While some of these features have morphology suggestive of a volcanic or tectonic origin, a number of circular features are believed to be highly degraded impact craters. Nevertheless, a clear Venusian analogue to the degraded terrestrial Elgygytkhyn Crater has not been reported.

The largest and morphologically most prominent impact crater reported on Venus is a double-ring type named Klenova. It has outer and inner rings with diameters of 144 and 105 km; these rings consist of discontinuous ridges 10 to 20 km wide (Figure 14). The surface inside the inner ring is knobby at the perimeter and smooth toward the 15-km-diameter central hill. The crater is surrounded by a ringlike zone of smooth terrain 40 to 60 km wide. This is probably the ejecta blanket, which

Figure 13. Soviet Venera 15 and 16 radar images of central-peak-type impact craters with sharp rims, radar-bright halos (a), (b), and (d), and a missing halo (c). The craters are divided by strips into sectors that are distal (D), medial (M), or proximal (P) relative to the illumination vector. Identities and diameters (km) are: (a) Kemble, 24; (b) Rudneva, 34; (c) Zvereva, 24; and (d) Golubkina, 28.

(a)

D M P

←— Illumination

(c)

D M P

←— Illumination

(b)

D M P

←— Illumination

(d)

D M P

←— Illumination
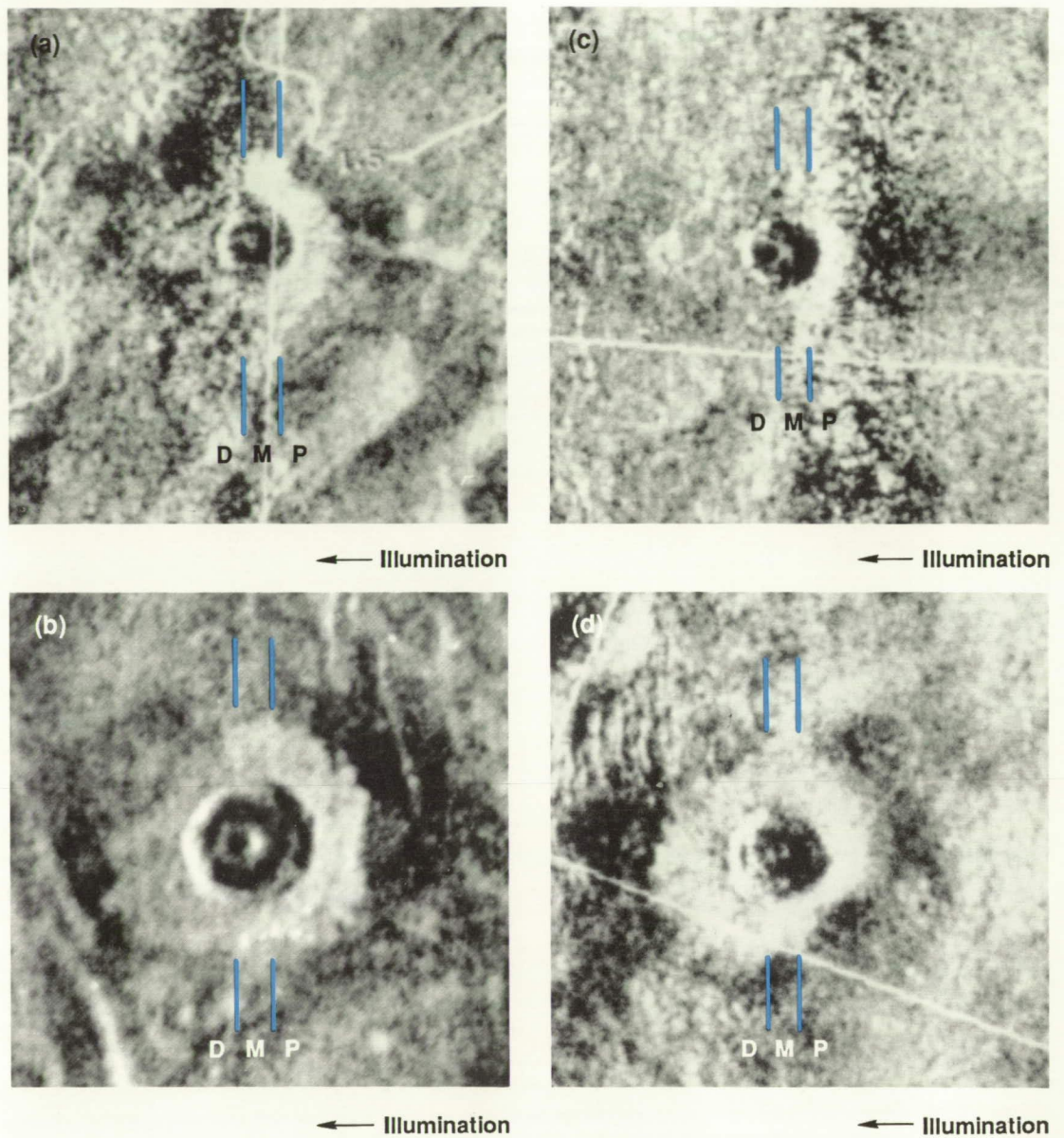
overlies the ridge-and-band pattern of the target terrain (Ivanov et al., 1986; Basilevsky et al., 1987). The overall dimensions of Klenova are comparable to the terrestrial Manicouagan structure (Figure 12). However, the two features expose different structural levels. At the Venera resolution, there is insufficient morphological detail in the image (Figure 14) to make further comparisons.

Discussion

At low incidence angles, Seasat SAR images of terrestrial impact craters and Venera 15 and 16 images of Venusian craters (obtained at a shorter wavelength) show similarities in the radar responses to crater morphology. SIR-A images show notable differences in the responses at high incidence angles. These observations have important implications for the interpretation of Magellan images, which will be obtained through a wide range of incidence angles at a wavelength that is intermediate between that of Seasat SAR and SIR-A at one extreme and Venera 15 and 16 at the other.

Because of orbital considerations, the nominal incidence angle of Magellan radar at the center of the swath will vary from about 45 deg at 10°N latitude to about 16 deg at the north pole and at 70°S latitude (Johnson, 1989). Figure 3 of *Synthetic-Aperture Radar Imaging* shows that at latitudes from 20°N to 10°S, the viewing geometry will approach the SIR-A configuration. North of 60°N and south of 40°S, the viewing geometry will be analogous to that of Seasat SAR. At the latitudinal extremities of imaging in both hemispheres, the viewing geometry will approach the Venera 15 and 16 configuration. Thus, radially symmetrical landforms such as impact craters, central peaks, cones, and other circular features can be expected to show varied outlines on Magellan images at different latitudes.

Impact craters commonly occur as circular features. Degradation or multiple impact may impose a secondary asymmetry on the landforms. It is important on radar images to distinguish between departures from crater circularity that are real and image distortion that relates to the scene illumination.

Crater morphology

At any radar incidence angle, the distortion of a crater outline is minimal across the medial sector, in a direction normal to the illumination. Crater diameters can be measured accurately only in this direction, provided the outline of the rim is distinguishable. This yields the radius of the rim and the center of a circle for comparison to the crater outline on each image. In cases where the slope of the crater wall equals or exceeds the nominal incidence angle, the imaging beam produces foldover, as at Barringer and Elegante on the terrestrial images (Figures 9(a) and 10) and Kemble, Rudneva, Zvereva, and Golubkina on the Venusian images (Figure 13(a) through (d)). In such cases, the outline of the crater corresponds to the circle in the median sector, but is comparatively prolate in the proximal and oblate in the distal sectors. The former is drawn out and the latter is compressed, so the craters appear to show bilateral symmetry parallel to the illumination vector. Where the incidence of the beam does not produce foldover, as at Talemzane (Figure 9(b)), the outline of the crater rim corresponds to the inscribed circle with comparatively little distortion. The variable viewing geometry of Magellan indicates that
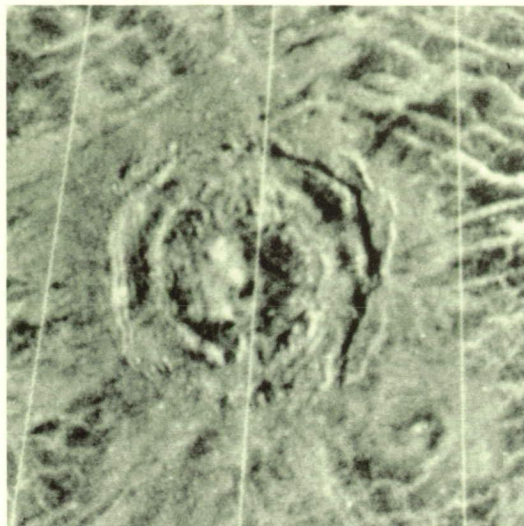
Figure 14. Klenova, shown in this Soviet Venera 16 radar image, is the largest and morphologically most prominent multiple-ring type of impact crater observed on Venus.

← Illumination

impact crater distortion will be greater on images obtained at higher latitudes. Essentially similar morphologic features that appear circular at low latitudes can be expected to show a distinctly different outline at high latitudes. If the outline of a crater at high latitudes is bilaterally symmetrical parallel to the illumination vector, it is likely to be an artifact of the viewing geometry.

Radar halos

The radar brightness of crater halos varies with the rms surface roughness, which is dependent on both the wavelength and the incidence angle (e.g., Table 6). The radar-bright halo on the SIR-A image (23.5-cm wavelength) of Talemzane (Figure 9(b)) represents a surface with rms roughness about three times greater than that of the radar-bright halos on the Venera images (8-cm wavelength) of Kemble, Rudneva, and Golubkina (Figure 13(a), (b), and (d)). However, the halo brightness varies systematically around the craters and shows bilateral symmetry relative to the illumination vector in each case. If the radar-bright halos denote the small-scale roughness of the ejecta blankets, it is likely that either the ejecta are not uniformly rough around the craters, or the slopes of the ejecta blankets provide a sufficient range of incidence angles to produce a notable difference in backscatter intensity from the foreslopes to the backslopes.

At Talemzane Crater, the ejecta are reported to form a nearly continuous annular blanket of mixed breccia that extends out to 400 m from the crater rim (Lambert et al., 1980). In this instance, the symmetrical variation of the halo brightness around the crater probably represents contrasted incidence-angle effects on the image (Figure 9(b)).

Assuming the slopes around Kemble, Rudneva, and Golubkina craters are radially symmetrical, the relations between symmetry, brightness, and the illumination vector suggest in each case that there may be no significant difference in roughness around the ejecta blanket. The brightest responses from the proximal sector of the halos suggest foreslopes where the incidence angle approaches zero and the backscatter is dominantly specular; consequently, the radar return has the greatest intensity here. Less intense responses from the backslopes probably indicate a contrasting incidence-angle effect. It has been proposed that the bright halos may result from fresh ejecta material with a comparatively high Fresnel reflectivity at the low Venera incidence angles (Jurgens et al., 1988). However, this does not account for the symmetrical reduction in brightness observed around the halos from the foreslopes to the backslopes.

Given the variable viewing geometry of the Magellan radar system, it follows that systematic changes must occur with Venusian latitude in the rms values that define the breakpoints between radar-smooth and radar-rough surfaces. From Table 6 and Figure 3 of *Synthetic Aperture Radar Imaging*, it is evident that the breakpoint of rms smoothness at high incidence angles in the low to middle latitudes will be rougher by about 28% at low incidence angles in the polar latitudes. Similarly, the breakpoint of rms roughness at polar latitudes will be smoother by about 25% at the low to middle latitudes. This limits the ability to compare directly the rms surface-roughness characteristics of ejecta blankets or other types of surfaces to narrow latitudinal ranges on the planet. At widely separated latitudes, rms surface roughness comparisons must allow for the contrasting effects of different incidence angles. Further-

more, the criteria used to evaluate rms surface roughness breakpoints assume that reflection occurs at a free-space boundary without modification by fine-grained, unconsolidated deposits at the surface. The conditions that permit radar penetration of such fine-grained deposits and the perception of subsurface roughness cannot be discriminated in images obtained at a single radar wavelength. Corresponding pairs of images obtained at widely different wavelengths are needed to verify radar penetration (Blom, 1988). Thus, in addition, the distinction between surface reflections and possible subsurface returns will not be feasible in the Magellan images.

Resemblance to volcanic maars

The similarities in the radar responses of small terrestrial impact craters and volcanic maar craters of comparable dimensions indicate difficulty in distinguishing the different origins of these craters from the images. On Earth, the regional setting of the craters in volcanic or sedimentary terrains can provide helpful discriminatory information. (However, this distinction cannot apply on Venus, where there is no comparable sedimentary cover.)

In all the terrestrial craters mentioned above, the radar responses have been related to field observations of slope, surface roughness, and structure. In Venusian examples, where direct field observations cannot be made, slope characteristics can be approximated from the image responses by analogy with terrestrial examples, and roughness characteristics can be related to the observing wavelength and the incidence angle (Table 6).

Spatial resolution

Large terrestrial impact structures with diameters up to 150 km retain little or none of their original crater form. At the high resolution of Seasat SAR, they show details of the structurally related morphologic elements. Correspondingly large Venusian impact features at the Venera resolution show only the broadest morphologic outlines. The spatial resolution of the Magellan radar system is coarser than Seasat SAR or SIR-A, but finer than Venera by about an order of magnitude (Table 5). Magellan images will provide the morphologic detail necessary to verify an impact origin or to identify a plausible alternative for large and

degraded Venusian craters comparable to those observed on Venera images.

Magellan images should enable the discrimination of craters with diameters below the limits of reliable Venera resolution (about 8 km) and possibly as small as 2 km, if they exist. This in turn would provide a more definitive indication of the ability of comparatively small bolides to penetrate the Venusian atmosphere. However, the difficulties in discriminating an impact origin from a volcanic origin for small terrestrial craters on higher resolution Seasat SAR and SIR-A images have been described above. Similar difficulties will probably apply in discriminating the origin of small Venusian craters. In any event, the extended coverage of Magellan radar, up to 90% of the Venusian surface, will yield a more comprehensive understanding of the size–frequency distribution of impact craters on Venus.

Volcanic Landforms

Introduction

The present knowledge of Venusian volcanism is restricted by existing coverage to the distribution and large-scale morphology of features greater than several kilometers. Near-global coverage of Venus by Magellan will allow the planet-wide distribution of volcanic land-forms to be mapped. Improved discrimination will allow a better assessment of most landforms, including enigmatic features such as ovoids (coronae), arachnoids, and small domes. The global distribution of volcanic centers, the style of volcanism, and the relations of volcanism to tectonic features should help define the mechanisms of heat loss from the interior of Venus, including the potential for hot-spot volcanism, lithospheric conduction, and plate recycling (Solomon and Head, 1982). Following a brief review of recent findings relevant to volcanism on Venus, this chapter discusses the different scales of volcanic morphology that may be interpreted from Magellan observations and presents examples of radar data on terrestrial volcanic features.

On Earth, the evolution of individual volcanic centers is studied to gain insight into the compositional and thermal history of a magma source. Inferences about the size and depth of magma chambers are drawn from caldera geometry. In a regional context, the orientation of dikes, volcanic vents, and volcanic centers in rift zones provides information about tectonic stresses and their changes over time. Magma composition and the distribution and types of volcanic landforms are associated with varied plate tectonic settings such as convergent (subduction zones/volcanic arcs), divergent (spreading centers) or transform plate boundaries, hot spots, or intracontinental rifts.

On a local scale, lava-flow morphology may provide information on the relative ages, composition, rheology, and effusion rates of lava flows (e.g., Hulme and Fielder, 1977; Malin, 1980; Wilson and Head, 1983; Fink and Zimble-man, 1986; Baloga and Pieri, 1986). The size and distribution of pyroclasts from explosive eruptions can be used to infer the eruption parameters. Figure 15 shows the main types of

QUALITY OF MAGMA	SMALL ◄——— QUANTITY OF MAGMA ———► LARGE					TYPE OF ACTIVITY
FLUID, VERY HOT, MAFIC	LAVA FLOWS *	LOW SHIELDS — Pisgah	SHIELD VOLCANOES — Kilauea, Pinacate, Iceland	BASALTIC PLAINS — Craters of the Moon	FLOOD BASALTS — Iceland CRB	EFFUSIVE
	TEPHRA AND SPATTER CONES *	COMPOSITE VOLCANOES — Mount Shasta			STRATO-VOLCANIC CHAIN	
INCREASING GAS CONTENT AND SILICA	EXOGENOUS DOMES AND THICK FLOWS — Mount Shasta, Valles Caldera, Medicine Lake	NONE KNOWN				MIXED
	MAARS AND TUFF CONES — Pinacate, Kilauea, Iceland					
VISCOUS COOL, SILICIC	DIATREMES	CALDERAS AND IGNIMBRITE SHEETS — Valles Caldera, Central Andes		VOLCANO-TECTONIC DEPRESSIONS		EXPLOSIVE

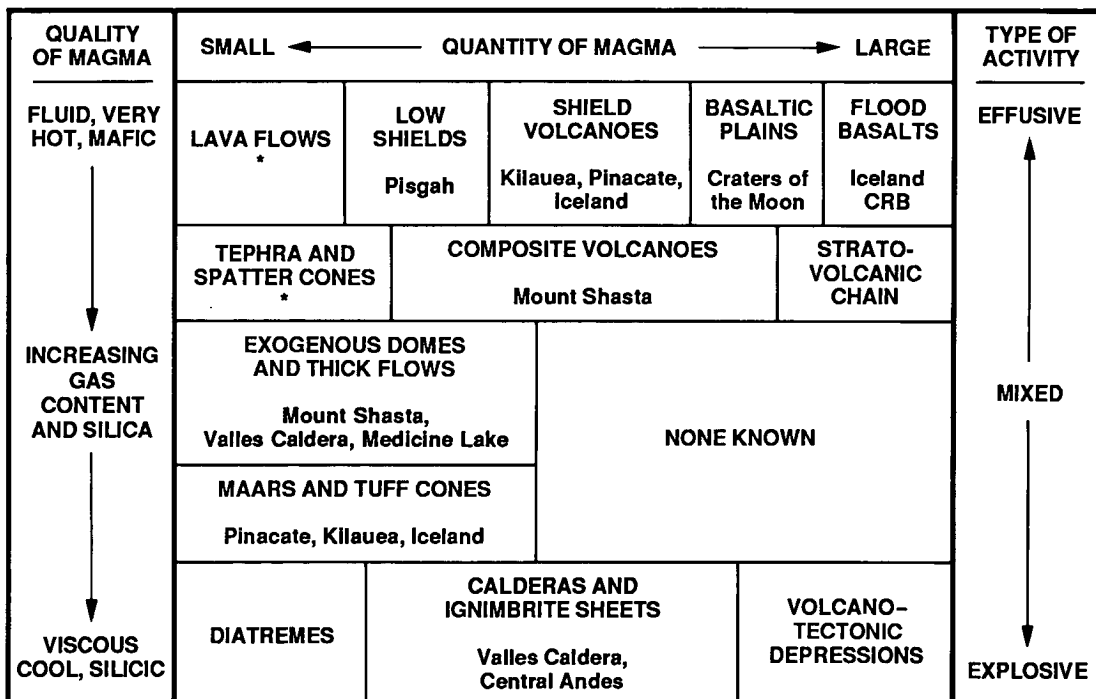*Examples in most of the areas discussed

Figure 15. The types of volcanic landforms as a function of the style of eruption and the physical properties and quantity of magma erupted (modified from Rittmann, 1962, and Greeley, 1977). Each area discussed in the text contains several different types of volcanic features and is listed under the appropriate categories in the diagram.

volcanic landforms as a function of basic controlling parameters and notes the terrestrial examples discussed in this chapter.

The interpretation of volcanic features depends partly on understanding the planetary environmental effects on the processes involved. Although Venus is similar to Earth in mass, density, and diameter (Appendix A), the dense Venusian atmosphere results in high surface temperatures (650 to 750 K) and pressures (4 to 10 MPa) that affect eruption temperatures, cooling rates, and exsolution of volatiles. Although a complete understanding has not been reached, theoretical studies by Wilson and Head (1983) and Head and Wilson (1986) predict no significant systematic differences in eruption rates or durations, lava-flow geometry, or differences in the relations between eruption temperatures and liquidus temperatures from those in terrestrial flows of similar composition. Because of the high atmospheric pressure, explosive eruptions would be rare on Venus unless magmatic volatile contents are greater than about 2.5 weight %, and the size and distribution of pyroclastic material would differ from similar deposits on Earth (Garvin et al., 1982; Head and Wilson, 1986).

The presence of volcanic materials on Venus is implied both by radar and by surface geochemical data (Barsukov and Basilevsky, 1986; Basilevsky and Head, 1988). A variety of volcanic landforms was revealed on high-resolution radar images of parts of the planet; the images were obtained by Earth-based observations (1- to 3-km resolution) and by Venera 15 and 16 SAR (1- to 2-km resolution). Radar-bright and radar-dark lobate patterns on these images have been interpreted as lava flows and occur within plains units and around large, gently sloping domical landforms (Saunders and Malin, 1977; Campbell et al., 1984; Barsukov et al., 1984a, 1984b, and 1986). Radial lobate features, the presence of summit craters, and altimeter measurements of low slopes suggest that the domical features are shield volcanoes, some of which are associated with highland areas interpreted as possible rift systems (Saunders and Malin, 1977; McGill et al., 1981; Schaber, 1982;

Campbell et al., 1984; Barsukov and Basilevsky, 1986). Long, lobate radar-bright features within plains provinces could be high-effusion-rate, low-viscosity flood basalts (Masursky et al., 1980; Barsukov and Basilevsky, 1986; Stofan et al., 1987). Results from gamma-ray spectrometer and X-ray fluorescence experiments on Soviet landers support these conclusions and suggest that the upland rolling plains are chemically consistent with alkaline basalt and the flat lowlands are comparable to tholeiitic basalt (Surkov et al., 1983 and 1984). The slopes of Aphrodite Terra also have a composition similar to tholeiitic basalt (Surkov et al., 1986 and 1987). Small domes (< 20 km diameter) occurring in plains units may be volcanic in origin. Within Ishtar Terra, two circular depressions surrounded by radial lobate patterns resemble calderas (Masursky et al., 1980; McGill et al., 1983; Barsukov et al., 1984b).

Morphologic Scales and Radar Observation Parameters

The nature of landforms produced by volcanism is largely governed by the volatile content and viscosity of the magma and the quantity of material erupted. The style of volcanism can be determined from the type of vent, the nature and lateral extent of the deposits, and the resultant landforms. The composition and particularly the volatile content of magma are crucial in determining the style and size of explosive eruptions and distribution of the resultant products. Volcanic landforms and surfaces in radar images can be classified according to a scale that includes megamorphic, mesomorphic, and micromorphic features.

Megamorphic features are at scales of kilometers or hundreds of kilometers. Examples include individual shield volcanoes and the products of high-volume eruptions. Observations by the Pioneeer Venus Orbiter and the Venera 15 and 16 missions have yielded information at this scale. The relation of such features to faults, rift valleys, and possible plate boundaries or hot spots should be apparent at the kilometer scale. Deposits from large-scale eruptions should also be distinguishable at this scale; however, flood basalts and pyroclastic flows produce similar landforms, making it

necessary to use surface micromorphology to distinguish the two.

The overall distribution of image tones and patterns provides interpretive data for megamorphic features, which should be readily detectable on Magellan images because at this scale the features are at least an order of magnitude larger than the Magellan spatial resolution (120 to 300 m). The geometric distortion inherent in radar images will vary with the latitude of the Magellan observations and must be considered when making measurements of volcano width, height, volume, and slope—especially with regard to symmetry. Geometric distortion will be most pronounced at the higher latitudes. Altimetry measurements can be used to constrain general topographic distortions and steepness of slopes.

Mesomorphic features are at scales from meters to hundreds of meters. In this range, volcanic features include lava flows, pyroclastic deposits, and constructs such as cinder cones, maar craters, collapse craters, lava ridges, channels, tubes, fissures, flow margins, and certain types of vents. Such landforms can be used to interpret the style of eruption, the flow emplacement mechanism, and the lava rheology (e.g., Hulme, 1974; Moore and Schaber, 1975; Moore et al., 1978; Fink, 1980; Basaltic Volcanism Study Project, 1981; Theilig and Greeley, 1986). Some mesoscale volcanic features may be near the limits of resolution of Magellan's SAR data.

Detection of mesoscale volcanic features on radar images depends on resolution, look angle, and azimuth angle, the first two of which will vary with latitude for Magellan SAR images (see Figure 3 of *Synthetic-Aperture Radar Imaging*). The look angle for Magellan will vary from about 50 deg in the equatorial regions to about 14 deg near the poles. At small look angles, gentle slopes (< 30 deg) on cinder cones, flow margins, and ridges result in incidence angles approaching 0 deg, causing specular reflections and bright returns (Elachi et al., 1980; Farr et al., 1981). This also causes the entire echo from a slope to return at the same time so that the slope is collapsed to a thin line in the azimuth direction. Foreshortening at small look angles may make geometric relations difficult to establish, and, in some cases, it may not be possible to determine relative relief. At large look angles, steeper slopes, such as those in crater interiors or in collapse depressions, cause strong radar returns if oriented toward the radar (Farr et al., 1981; Greeley et al., 1987).

The azimuth angle is important in the detection of mesoscale topographic features on SAR images. Linear features such as ridges, leveed channels, lava tubes, fissures, and flow margins are more easily detected if oriented nearly perpendicular to the radar illumination. Detection of subresolution-size elements may occur if they are strong scatterers because of extreme roughness, because they act as corner reflectors, or because they have slopes normal to the incident radiation (Schaber et al., 1980; Greeley et al., 1985; Blom, 1988). Alternatively, combined reflection from numerous slopes, such as parallel ridges, may cause a higher return for an extended area even if individual components cannot be discerned (Malin et al., 1978).

Micromorphic features are represented by surface roughness at the centimeter to meter scale, which is below the spatial resolution of most imaging radars. However, for surfaces with low slopes and similar electromagnetic properties, radar backscatter and image brightness levels can be related to the average small-scale surface roughness in each image resolution cell. For extended volcanic surfaces, this allows estimation of the texture in lava flows, the grain size in pyroclastic deposits, and the extent of modification by nonvolcanic processes on weathered surfaces. Average small-scale roughness is used to classify volcanic surfaces and deduce their origins (Macdonald, 1953; Swanson, 1973; Peterson and Tilling, 1980). The simplest classification of lava-flow types—into pahoehoe, aa, and block (Macdonald, 1953)—is based on the surface expression of flow rheology and mechanical history (Walker, 1970; Peterson and Tilling, 1980; Kilburn, 1981). Factors such as effusion rate and topography combine with the lava rheology to determine whether a given flow will be pahoehoe or aa, or whether a transition will occur in the middle of a flow.

In Magellan images, brightness should be proportional to centimeter- to meter-scale surface roughness. The 12.6-cm wavelength of the Magellan SAR is shorter than that used by Seasat and the SIR-A and -B missions, and consequently it will be sensitive to smaller-scale

average surface roughness. The reverse will be true in comparing Magellan data with the 8-cm wavelength Venera 15 and 16 data. The effect of wavelength on backscatter has been discussed by Dellwig (1969), Schaber et al. (1980), Farr and Engheta (1983), Blom et al. (1986 and 1987), and Greeley and Martel (1988). As backscatter varies with incidence angle (Figure 16), the changes in Magellan incidence angle with latitude (see Figure 3 of *Synthetic-Aperture Radar Imaging*) and with topographic slope variations will cause variations in image brightness regardless of surface type. Hence, incidence angles must be taken into account when mapping surfaces that have similar small-scale surface roughness.

The average small-scale surface roughness may decrease with time through weathering and depositional processes (Wells et al., 1985; Farr and Anderson, 1987). Possible modification of a flow surface must be taken into account when interpreting the original eruption conditions on Venus. However, weathering conditions and depositional processes on Venus are not well known. Chemical weathering (Nozette and Lewis, 1982) caused by the hot atmosphere

probably occurs, but the absence of water may lower the rate of such reactions. Low-speed winds that could form eolian deposits (Greeley et al., 1982; Williams and Greeley, 1982) have been observed at the surface of Venus (Keldysh, 1977). Similarly, explosive volcanic activity would deposit pyroclastic material on near-vent surfaces (Head and Wilson, 1986); however, it is not known if such activity occurs on Venus. Although a correlation may exist between decreased radar backscatter and increased surface smoothing, a direct correlation with age cannot be made in the absence of knowledge about the original surface texture and the weathering process.

## Observations of Terrestrial Volcanic Areas

Here we present volcanologic and radar remote sensing data for several well-known areas. Specific examples are given and literature is cited on the applications of the principles discussed above to the interpretation of radar images of basaltic flood deposits, complex basaltic plains, shield volcanoes, composite volcanoes, and products of large-scale explosive eruptions. Spatter/tephra cones, lava flows, and ash deposits are discussed in several of the examples.

Flood basalts

High-volume, low-viscosity flood basalts are common on the terrestrial planets and may form most of the Venusian plains. Two examples of this style of volcanism are provided: a young quasi-flood basalt in Iceland and Miocene flows of the Columbia Plateau.

Iceland. Iceland is a complex volcanic plateau with examples of flood basalts, shield volcanoes, calderas, tephra cones, pyroclastic deposits, and lava flows of different compositions and surface textures. Analogous plateaus have been postulated for the western Aphrodite Terra on Venus (Head and Crumpler, 1987; Crumpler and Head, 1988). The tectonic setting of Iceland, a hot spot on the axis of a midocean ridge, is favorable for high rates of magma supply and eruption. This area is included here because it provides one of the few Holocene examples of flood basalts; however, other volcanic landforms are also discussed.

Figure 16. Backscatter coefficient measurments made by Johnson Space Center airborne scatterometer over Pisgah Lava Field using C-band (6.3-cm wavelength) and HH polarization.
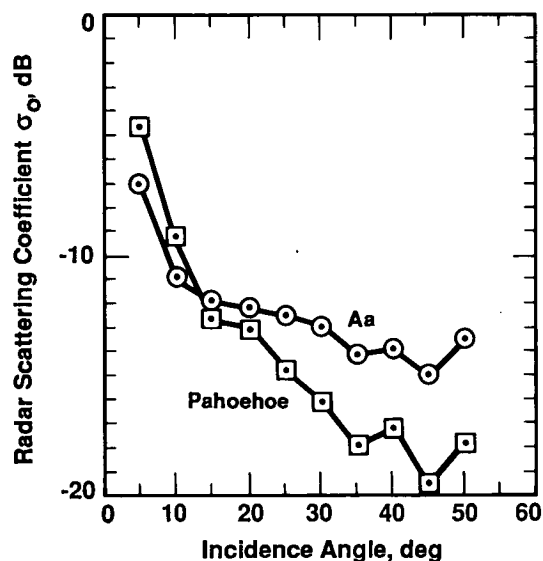
Note: The aa lava has a flatter curve than the pahoehoe because the rough surface scatters more diffusely. Because of this effect, the aa will appear darker than pahoehoe at incidence angles less than about 15 deg.

Many volcanic units, faults, linear features and drainage networks can be distinguished on Seasat images of Iceland (McDonough and Martin-Kaye, 1984). Figure 17 displays the central portion of the Icelandic east rift zone where eruptive products are primarily tholeiitic basalt. The oldest rocks in the area are Tertiary Flood Basalts that underlie the dissected basalt plateau and Tertiary–Pleistocene Old Gray Basalts (Figure 18). A widespread occurrence of the Pleistocene Palagonite Formation results from subglacial basaltic eruptions of voluminous proportions (number (1) in Figure 18). Young Gray Basalts are interglacial eruptive products that were not palagonitized. A swarm of fissures and normal faults (Sigurdsson and Sparks, 1978) at Sveinagja is oriented 6 to 13 deg from the illumination direction of Figure 17. Lobate flow margins west of Kollottadyngja are prominent on the image probably because they are nearly perpendicular to the illumination. Three areas of Holocene volcanism described below include the Askja Caldera, the Trolladyngja Volcano, and the Myvatn area.

The Askja area has undergone basaltic fissure eruptions, the formation of a central volcano, late-stage shallow silicic volcanism, caldera collapse, and late-stage basaltic flows (e.g., Sparks et al., 1981). An historic, 11-km^2 caldera contains a lake (Oskjuvatn) and forms an oblong radar-dark area because of forward specular reflection off the smooth lake surface. The small caldera is nested within an older 45-km^2 caldera that is visible as a broad, radar-bright crescent northwest of Oskjuvatn. High reflectivity from the floor of the older caldera comes from an aa flow that is partly mantled by pumice and ash (Malin et al., 1978).

The most prominent lava flows are radar-bright, late-stage basalts on the north, west, and south sides of the younger caldera. Despite differences of small-scale surface roughness, Mackenzie and Ringrose (1986) found that pahoehoe flows (typically 15 m wide and 50 m long) within the main aa flow of 1961 cannot be discriminated in the Seasat image. Strong returns from the aa were thought to be due to rough surfaces combined with a highly irregular local relief. Strong returns from the pahoehoe were related to the undulating nature of the smoother surfaces, which produced specular returns from appropriately oriented facets. It

was noted that both effects occur at a scale much below the image resolution.

Both aa and pahoehoe were found to be rougher and brighter in radar than pumice deposits, which, in turn, are rougher than ash deposits. An inverse relation was found between the radar return and the amount of pumice and ash covering a lava flow. Malin et al. (1978) and Evans (1978) discriminated the surface roughnesses of nine radar backscatter units using parallel- (HH) and cross- (HV) polarized L-band airborne SAR with look angles from 0 to 45 deg.

A different style of volcanism occurred at Trolladyngja (Figure 19). Magma was fed from a deep source, beginning with initial fissure basalt eruptions and followed by the buildup of a shield volcano. The fissures on the southwest side of Trolladyngja are oriented within 10 deg of the illumination direction. With one exception denoted by (2) in Figure 18, the fissures are not visible on the image. The 500-m-diameter crater at the summit is visible. Trolladyngja and the adjacent shield volcanoes (e.g., Ketildyngja, Kollottadyngja, Urderhals) show an asymmetric appearance on the radar image with bright compressed foreslopes and dark stretched backslopes. This results from the approximate equivalence of both the Seasat SAR look angle and the slope angles of the shields. Thus, the incidence angle at the foreslopes is about 0 deg; at the backslopes, the incidence angle is equivalent to the look angle plus the ground slope.

The Barthardalshraun Lava Flow originated both from Trolladyngja and from a set of fissures to the south. It is over 100 km long and 10 m thick and is considered a quasi-flood basalt. Because it was topographically confined by river channels (note the narrowness of the flow to the north in Figures 17 and 18), it is not as thick as typical flood lava deposits (Greeley and Sigurdsson, 1980). The flow is composed of an older bright unit on and to the north of Trolladyngja and a younger unit with lower reflectivity south of the shield. The age relations of the two flows are not obvious from their radar reflectivities. However, cross-cutting relations relative to the two flows indicate a younger age for the Urderhals Volcano.

Figure 17. Seasat SAR image of east-central Iceland covers prominent shield volcanoes and shows lava flows and flow edges, dissected flood basalts, and the Askja Caldera. The major features of interest are outlined in Figure 18.
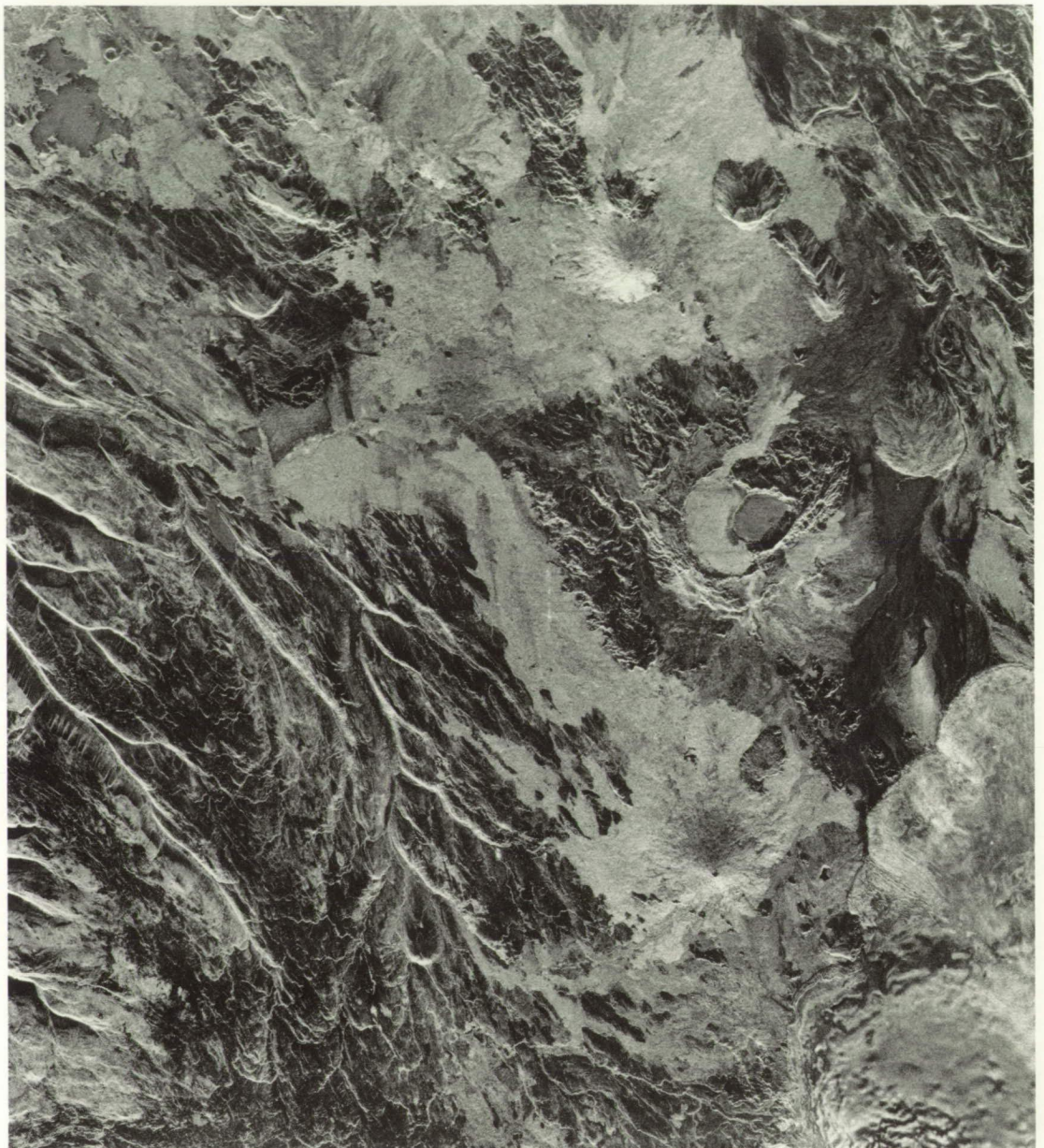
N   0   20 km   ↑ Illumination

Radar-dark, roughly parallel streaks that cut across the Barthardalshraun Lava Flow ((3) in Figure 18) probably do not represent primary flow morphology. They appear as low-albedo features in aerial photographs and could represent tephra or deposits of eolian origin that subdue the surface roughness of the underlying flows.

Some of the individual 100- to 200-m-wide lava flows on the slopes of Trolladyngja are darker than the surrounding terrain (Figure 19(a)), perhaps because they are pahoehoe flows that are smoother than the surrounding aa field. Festoonlike transverse ridges observed in the field by Greeley and Sigurdsson (1980) were used by Theilig and Greeley (1986) to estimate the interior viscosity of the flow when the ridges formed. Although the transverse ridges are 100 m apart and up to 5 m high, they are not resolved in the Seasat image. Either the ridges are below the resolution of the image or the radar backscatter may not vary sufficiently from the surrounding terrain to provide a detectable contrast.

The Myvatn area appears in the upper left corner of Figure 17. Two basaltic tephra rings with central craters and a small rhyolite flow are distinguishable near Myvatn (Saemundsson, 1977) and shown in Figure 20. The tephra rings are about 1 km in diameter with pyroclastic deposits dipping 7 to 42 deg outward (Thorar-
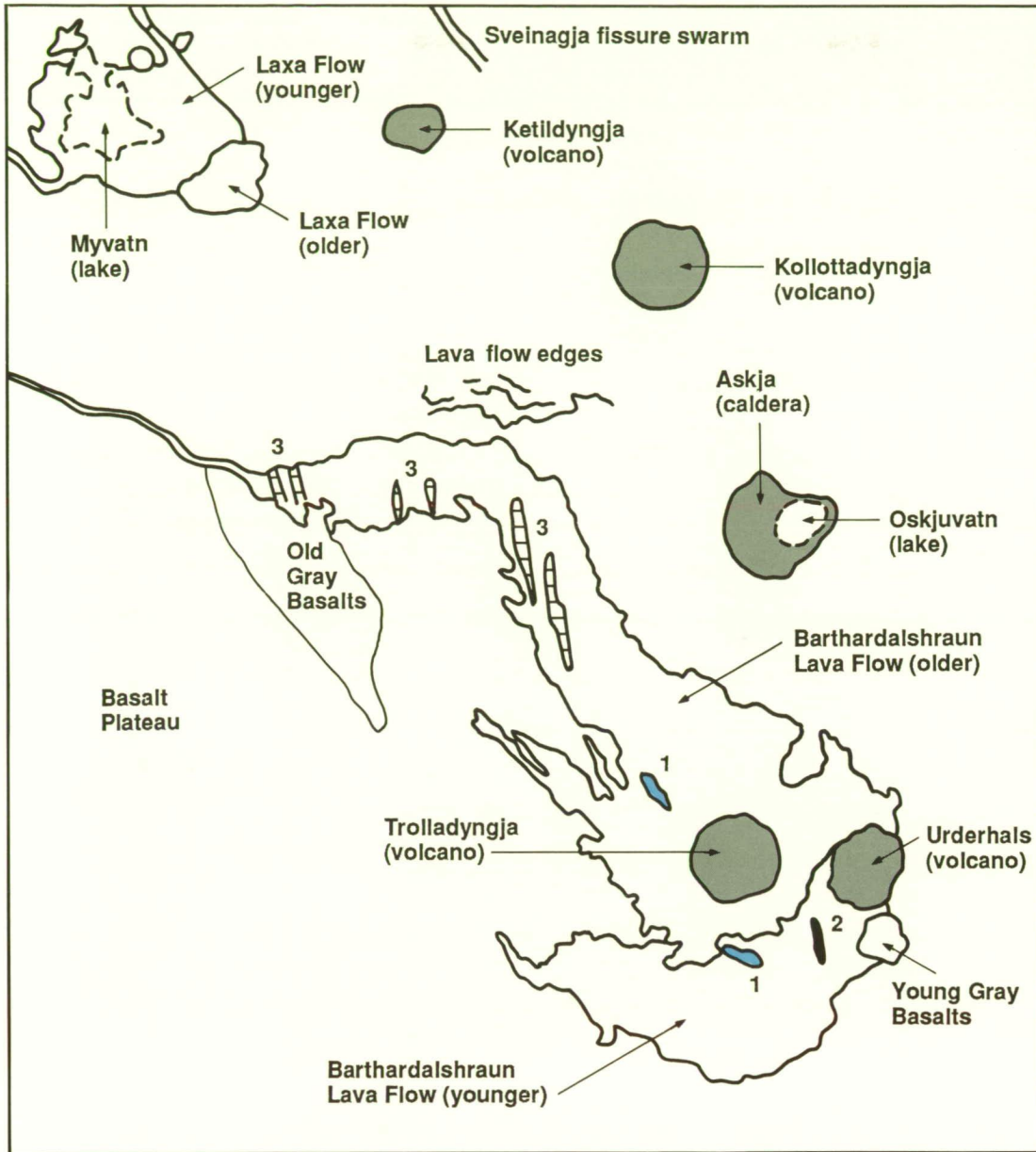
Figure 18. Sketch map of major volcanoes, lava flows, flow edges, and notable features shown in Figure 17. Small-scale features are (1) Palagonite Formation (Moberg), (2) fissure source of younger Barthardalshraun Flow, and (3) dark streaks on older Barthardalshraun Flow. Details of the Myvatn area (upper left) are given in Figure 20. Names of features and geologic units are from Kjartansson (1965).

insson, 1960). Numerous 2-m- to 300-m-diameter craters occur in the Myvatn area, but are not visible on the Seasat image.

The 3500-year-old Laxa pahoehoe flow that surrounds Myvatn is brighter in the radar image than the approximately 2000-year-old Laxa aa unit (Figures 17 and 20). A row of craters in the center of the older flow is visible in Figure 17 as a line of low reflectivity. The source of the older flow is the Ketildyngja volcano (Thorarinsson, 1953; Preusser, 1976). The youngest lava flow in the vicinity is the brightest in the image. Age relations and sources for these flows cannot be ascertained from the radar image.

Columbia Plateau, Northwest U.S.A. The Columbia Plateau in the northwestern United States is one of the larger flood-basalt provinces on Earth, with a total areal extent on the order of 2×10^5 km^2. The Miocene Columbia River Basalts (CRB) erupted from north-northwest trending linear vents and attained a maximum thickness of about 5 km. The Grande Ronde Basalt, which constitutes approximately 85% of the total volume of the CRB, was erupted over a 2-My period (Reidel et al., 1982). On the eastern plateau, both the basalts and the thick Quaternary loess deposits that overlie them have been eroded by cataclysmic floods.

*Figure 19.
Trolladyngja
Volcano: (a)
enlargement of part
of the Seasat image
shown in Figure 17;
the box indicates the
location of (b), an
aerial photograph
(courtesy of Ronald
Greeley, Arizona
State University).
Because of
geometric distortion,
Figures (a) and (b)
cannot be compared
directly. Darker
areas in both images
probably represent
pahoehoe. In (b),
the summit is snow
covered.*
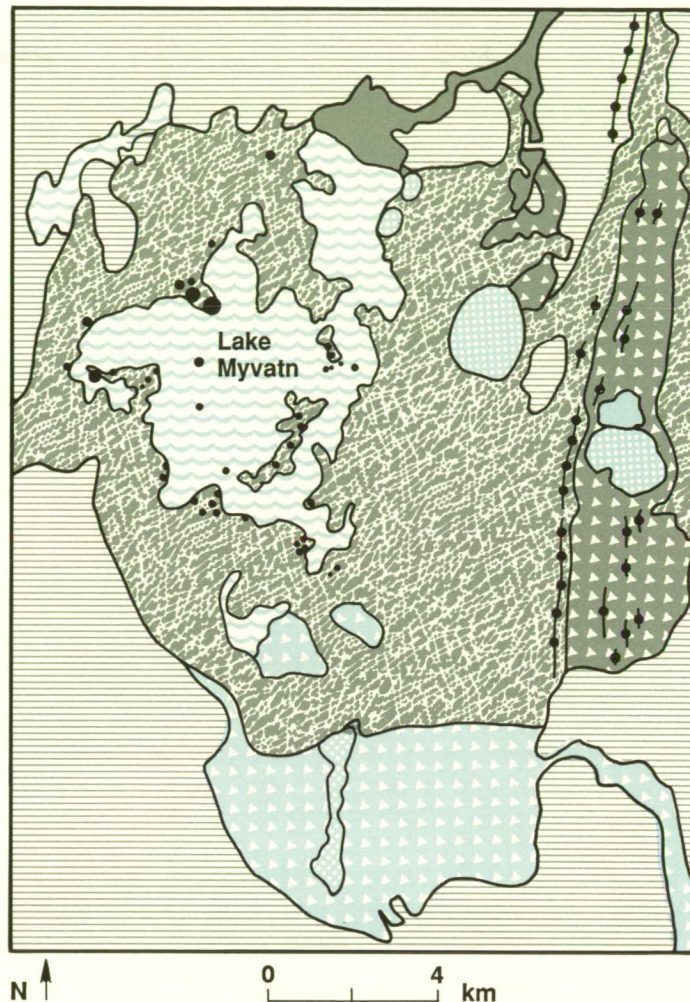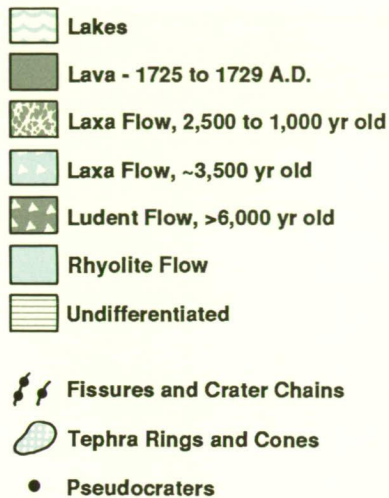

N ↑   0   10   km   ➚ Illumination

N ↑   0   2   km

34
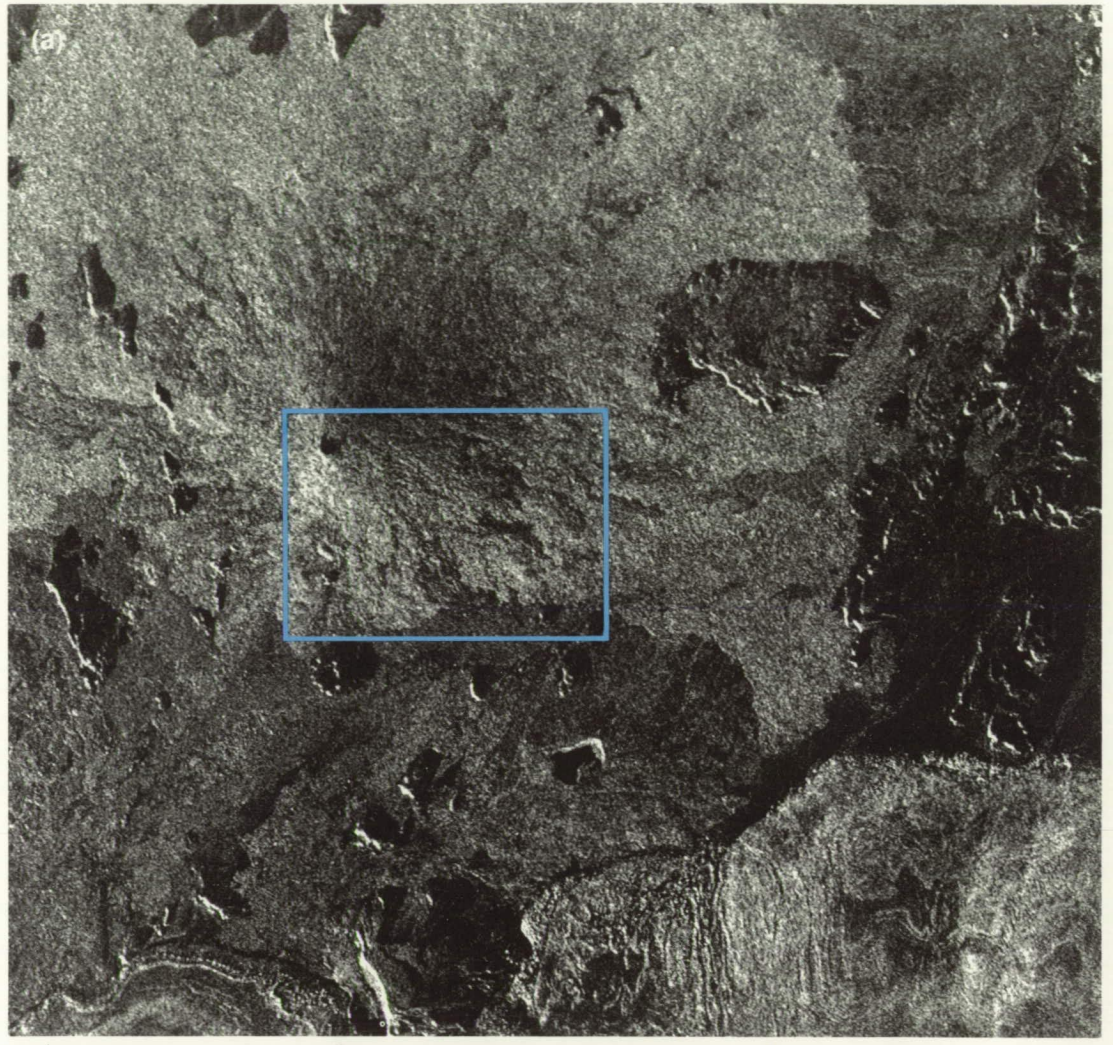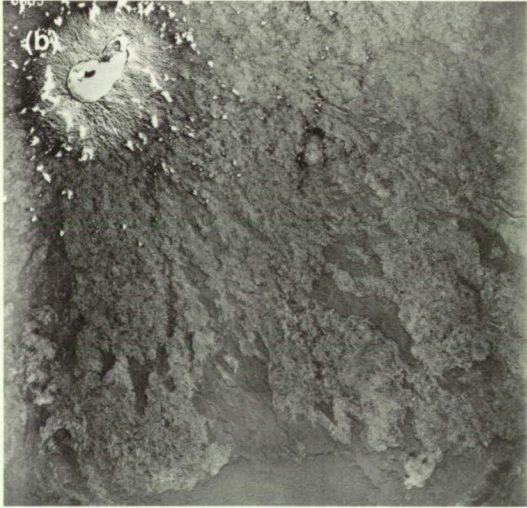
Figure 20. *Geologic sketch map of Myvatn area (modified from Thorarinsson, 1967, as presented by Preusser, 1976).*

Legend:
- Lakes
- Lava - 1725 to 1729 A.D.
- Laxa Flow, 2,500 to 1,000 yr old
- Laxa Flow, ~3,500 yr old
- Ludent Flow, >6,000 yr old
- Rhyolite Flow
- Undifferentiated
- Fissures and Crater Chains
- Tephra Rings and Cones
- Pseudocraters

Lake Myvatn

N   0   4   km

The basalts of the western plateau have been deformed into the Yakima Fold Belt, a series of asymmetric anticlines separated by broad, relatively undeformed synclines (Reidel et al., 1984). A Seasat SAR image covers a portion of the Yakima Fold Belt, bounded to the west by the Cascade Range (Figure 21). Two anticlinal structures are visible in the image but, because the illumination direction is roughly coincident with the trend of the anticlinal ridges, incidence-angle effects are minor. The style of deformation of CRB is not uncommon on the terrestrial planets. The anticlinal ridges of the Yakima Fold Belt are similar in morphology and dimension to first-order ridges in wrinkle-ridge assemblages that occur in mare basalts on the Moon and smooth plains material interpreted to be flood basalts on Mars and Mercury (Watters, 1988). Analogous features may also exist on Venus and are suggested on Venera 15 and 16 radar images by long, narrow, high-relief features near Metis Regio (Watters, 1988).

Basaltic plains: Craters of the Moon, U.S.A.

Basaltic-plains volcanism is characterized by low shield constructs, tube-fed flows, and multiple flow units erupted from point sources aligned along fissures (Greeley, 1982). The Craters of the Moon (COM) Lava Field is one of the most recent fields composing the Snake River Plain, Idaho, which is the type locality for basaltic plains volcanism.

The Snake River Plain is an arcuate topographic depression 50 to 100 km wide extending approximately 650 km across the southern part of Idaho. The central and eastern parts of the Snake River Plain consist of a broad, flat plain composed of Quaternary lava flows. Fissures are associated with rift zones trending perpendicular to the axis of the eastern part of the Snake River Plain. The Great Rift of the Idaho Rift System is a 3-km-wide zone of en echelon fissures trending N35°W and is the primary source for the COM Lava Field (Prinz, 1970). COM provides an opportunity to study a variety of basaltic lava

Figure 21. Seasat SAR image of part of the Yakima Fold Belt. Two anticlinal structures, the Ahtanum ridge (1) and the Toppanish ridge (2), appear as narrow, relatively high-relief landforms. Mount Adams (3), composed of overlapping cones erupted from several vents along a fissure trending north-northwest, is part of the Cascade Range (Harris, 1980). (Image courtesy of Tom Watters.)
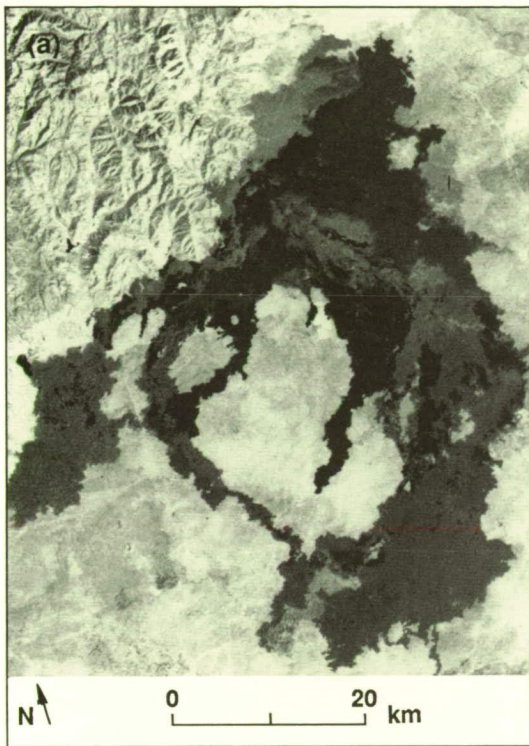

N ↑   0   20 km   → Illumination
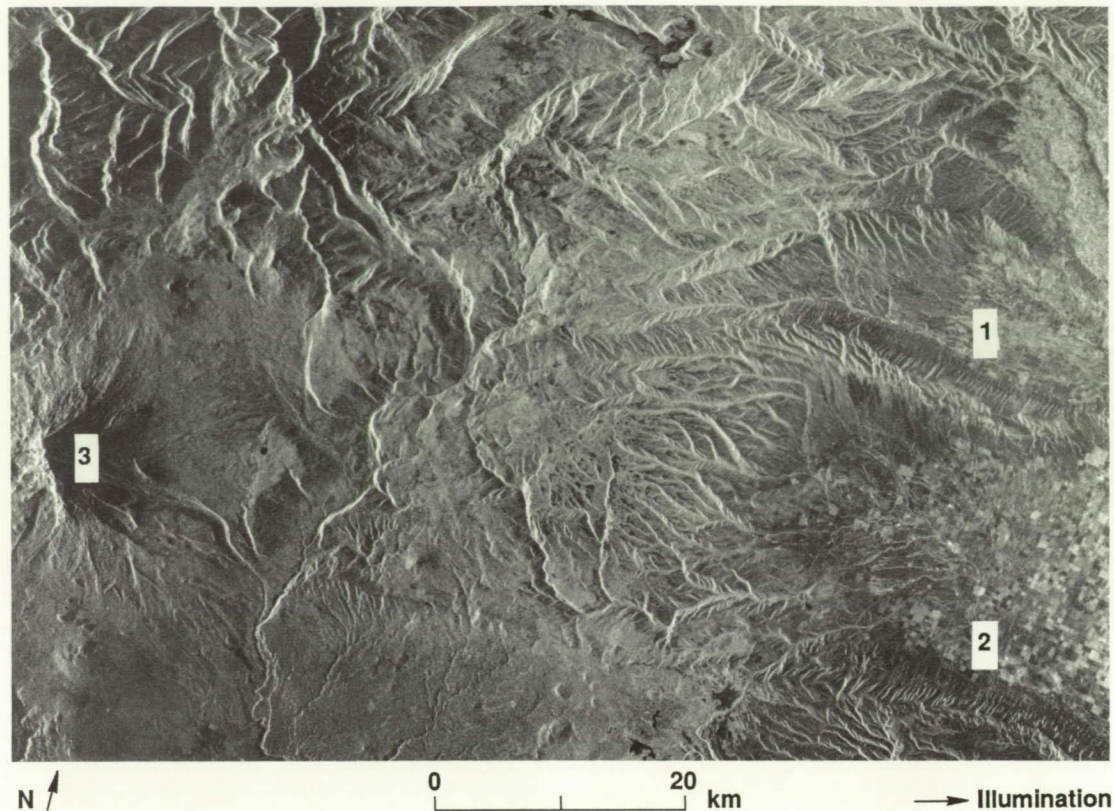
flows and vents (Figure 22(a)). Over 60 flows and flow units cover 1,600 km^2 with more than 30 km^3 of lava to form the largest predominantly Holocene lava field in the conterminous United States. This field consists of pahoehoe, aa, and block lava flows erupted during eight periods from 15,000 to 2,000 years ago (Kuntz et al., 1983, 1986a, 1986b, and 1988) (Figure 22(b)). Vents within the field include 55 cinder cones and 14 fissures, many with spatter cones (Papson, 1977). Discontinuous deposits of loess, eolian sand, and alluvial fan material are interbedded with the lava flows.

Jet Propulsion Laboratory (JPL) aircraft and Seasat SAR images (Figures 23(a) and (b), respectively) provide comparative backscatter information on the COM Lava Field at look angles ranging from 10 to 50 deg. The variation in gray levels in these images is related to the type and age of the lava flows and to the look angle of the radar (Elachi et al., 1980). Young flows are typically free of loess, soil, and vegetation and have higher backscatter. The extremely rough surfaces of aa flows consisting of blocky surface texture and irregular topography with several meters of relief result in these flows being the strongest radar scatterers in Figure 23(a). The effect of look angle on lava-
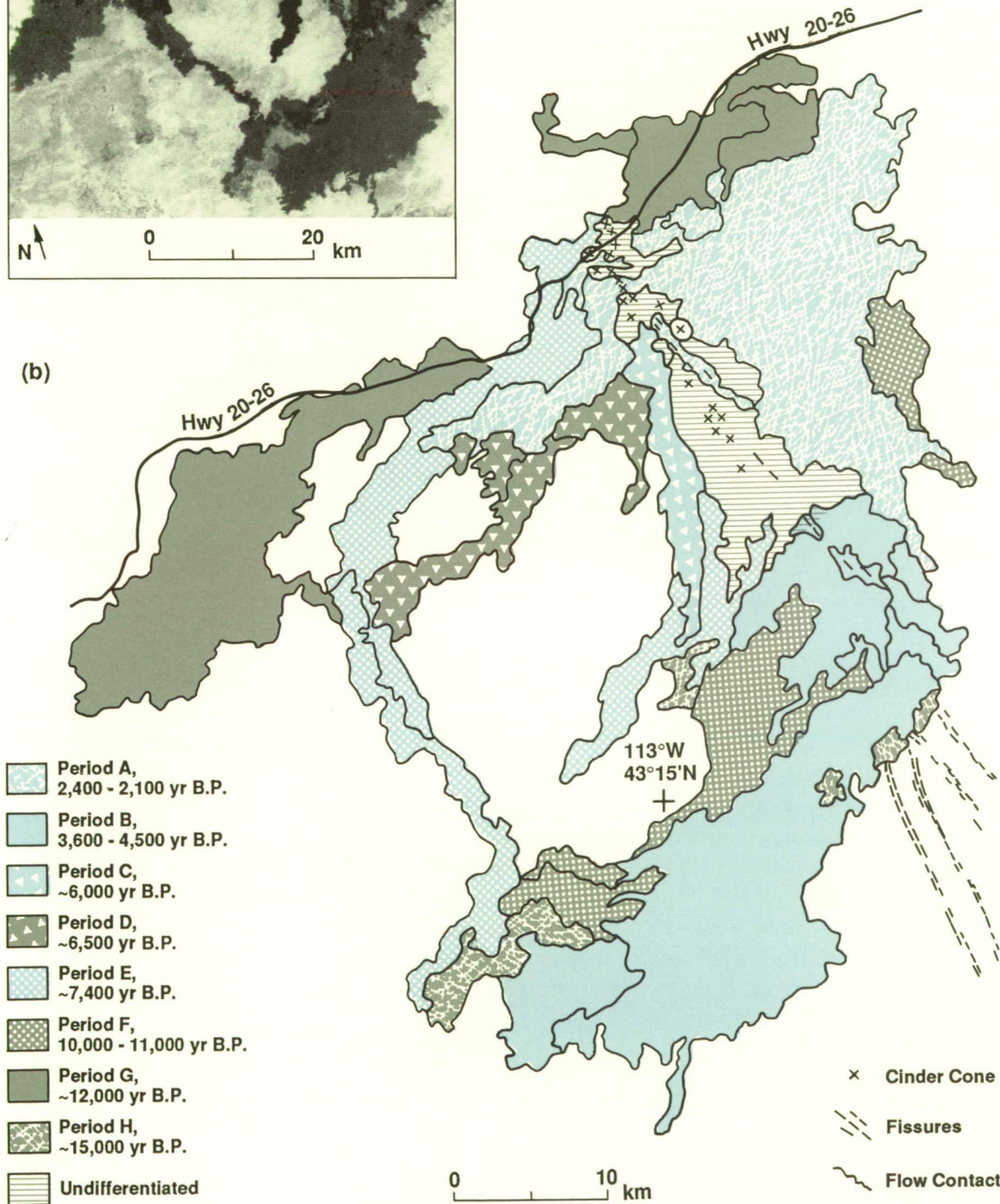
type identification can be demonstrated by comparing a pahoehoe flow with an aa flow in the two images (Figures 23(a) and (b)). The pahoehoe appears in the aircraft image (45-deg look angle) as a mottled unit darker than the nearby aa flow, but in the Seasat image (20-deg look angle), the pahoehoe flow appears uniform and brighter than the aa. This behavior is related to the dominant scatter mechanism (see Figure 8 in *Impact Structures*) at different look angles as demonstrated by backscatter curves for pahoehoe and aa flows (Figure 16). Within or below the range of 15 to 25 deg, specular reflection from the smoother pahoehoe surface produces a stronger radar return, whereas the rough aa surface scatters energy and less is returned to the receiver. At greater look angles, the opposite is true; the smooth surface reflects energy away and the rough surface scatters relatively more energy back to the receiver.

Mantling of older flows by loess and volcanic ash attenuates the initial surface roughness and produces lower backscatter (Rothery and Lefebvre, 1985). Because small-scale surface roughness has been preferentially smoothed by mantling and weathering processes, Blom et al. (1986) found that flows of different ages but similar initial surface texture could be

Figure 22. Craters of the Moon Lava Field: (a) Landsat image; (b) generalized map of the lava flows within the Craters of the Moon field (modified from Kuntz et al., 1986b).

(a)

N

0   20 km

(b)

Hwy 20-26

Hwy 20-26

113°W
43°15'N

Period A,
2,400 - 2,100 yr B.P.

Period B,
3,600 - 4,500 yr B.P.

Period C,
~6,000 yr B.P.

Period D,
~6,500 yr B.P.

Period E,
~7,400 yr B.P.

Period F,
10,000 - 11,000 yr B.P.

Period G,
~12,000 yr B.P.

Period H,
~15,000 yr B.P.

Undifferentiated

0   10 km

×   Cinder Cone

Fissures

Flow Contact

37
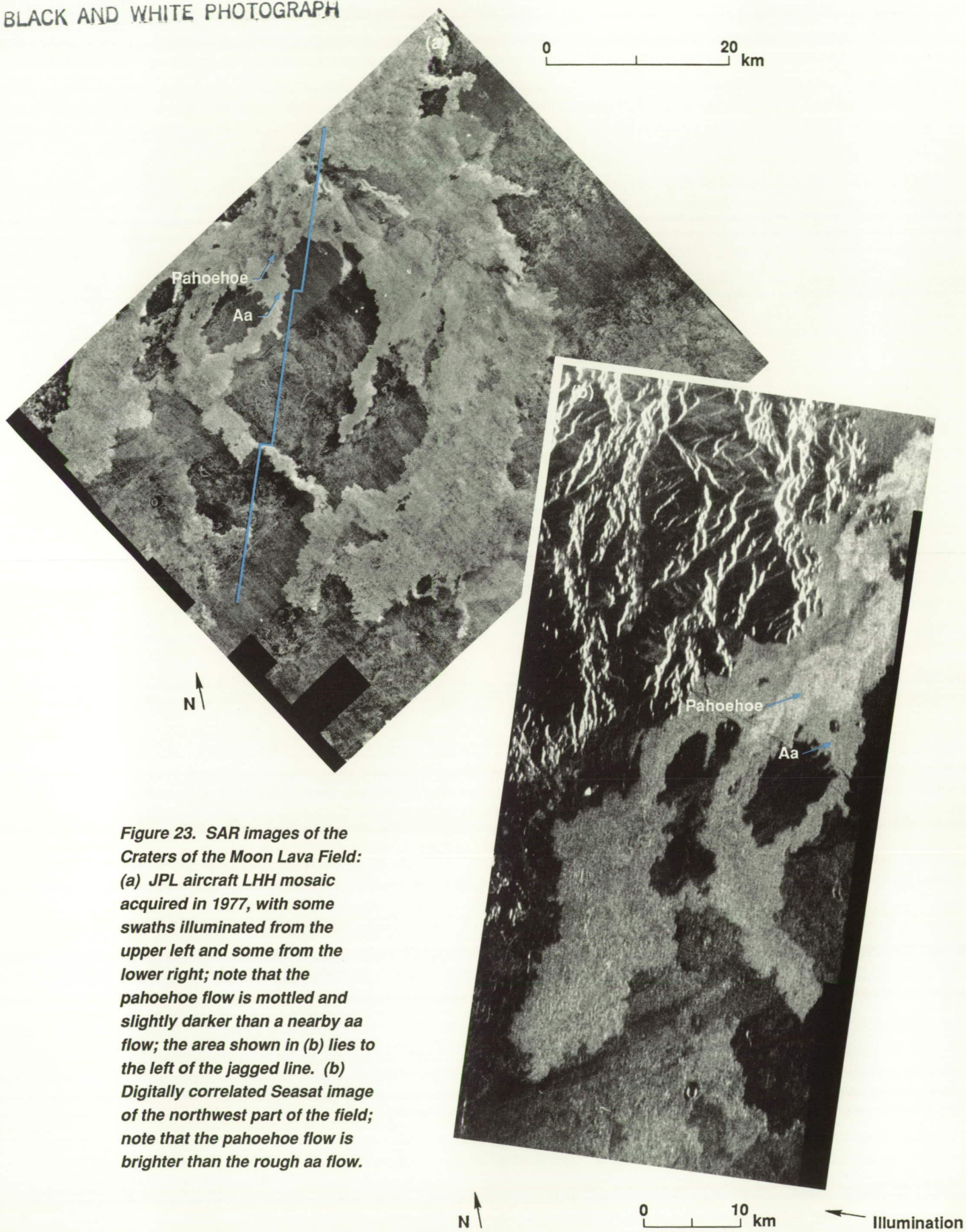
Figure 23. SAR images of the
Craters of the Moon Lava Field:
(a) JPL aircraft LHH mosaic
acquired in 1977, with some
swaths illuminated from the
upper left and some from the
lower right; note that the
pahoehoe flow is mottled and
slightly darker than a nearby aa
flow; the area shown in (b) lies to
the left of the jagged line. (b)
Digitally correlated Seasat image
of the northwest part of the field;
note that the pahoehoe flow is
brighter than the rough aa flow.

discriminated based on backscatter coefficients derived from scatterometer data. Caution must be exercised, however, when attempting to estimate lava flow age from radar backscatter, because the original surface textures may not be the same and flows may weather differently. Within the Craters of the Moon, aa flows weather more slowly than pahoehoe because the surface is rubbly and very permeable, allowing water and sediment to be transported into the interior of the flow rather than collect on the surface (Lefebvre, 1975).

Two major vent types, cinder cones and fissure vents, are present in the COM Lava Field. Fissures are almost parallel to the radar illumination direction and are not visible in the SAR images. Spatter ramparts built along some of the fissure vents are several meters high and consist of agglutinate. These features cannot be seen in L-band data but are distinguishable in X-band, probably as a result of scattering of the smaller radar wavelength by the centimeter-scale agglutinate spatter or alternatively because of increased spatial resolution (Greeley and Martel, 1988). Other geomorphic features that can be distinguished include buttes, lava lakes, and lava tubes that have coarse rubble at their margins (Elachi et al., 1980).

L- and C-band (19- and 6.3-cm wavelength, respectively) HH scatterometer data can be used as a surrogate for Magellan S-band (12.6-cm wavelength) SAR data. A scatterometer data set from COM has been used to investigate the identification and interpretation of lava flow types and ages based on backscatter coefficients obtained at different incidence angles (Theilig et al., 1988). Results of this study suggest that young pahoehoe flows are more distinct at smaller look angles, whereas older, modified pahoehoe flows can be discriminated only at larger angles. Intermediate age surfaces are difficult to separate at most look angles.

Shield volcanoes

Several examples of shield volcanoes are included to illustrate the associated variety of morphologic features and eruptive products. These examples include Kilauea Volcano, Pinacate Volcanic Field, Medicine Lake Highland, Fantastic Lava Beds, and Pisgah Lava Field. The latter example can be classified as a low shield volcano and is similar in morphology

and origin to small volcanoes in the Snake River Plain, Idaho.

Kilauea Volcano, U.S.A. The Shuttle Imaging Radar-B (SIR-B) imaged the southeastern part of the island of Hawaii at look angles of 28 and 48 deg in October 1984. Kilauea Crater and the rain-shadowed Kau Desert to the southwest are shown in Figure 24. The most prominent features in these images are the caldera of Kilauea Crater, several normal faults in the Kau Desert, aa lava flows, and pyroclastic deposits. A good summary of the geology of the area is given in Holcomb (1987). The SIR-B images allow a direct comparison of the effects of look angle on the ability to identify and map lava flows and volcanic features where other system characteristics (e.g., signal-to-noise ratio (SNR), digitization, and altitude) and geometric characteristics (e.g., azimuth) are held relatively constant.

Identification of vents within the SIR-B coverage is dependent on the size and morphology of the feature. Kilauea Crater, about 3 km in diameter, is easily visible in both images because the southeast rim is highlighted and the northwest rim is partly shadowed. Pit craters, such as Halemaumau, at the southwestern edge of Kilauea Crater, and those along the Chain of Craters extending to the southeast, are also visible. Some of these steep-sided depressions are as small as 200 to 300 m. Cinder cones, spatter ramparts, and fissures are smaller and could not be readily identified. In general, topographic features with less than about 10 m of relief cannot be resolved in the SIR-B coverage (Gaddis et al., 1989).

Fault scarps are detected in the images as either dark or bright curvilinear features, depending on their orientation. The Koae Fault System is a series of scarps up to 10 m high, trending east-west, and facing north; they appear as thin bright linear features south of the Kilauea Caldera. In contrast, south of the Koae faults and parallel to the coast, the 350-m-high fault scarp of Hilina Pali faces southeast so that the angle of incidence is large and it appears dark (Gaddis et al., 1985). Both radar images are equally good for discriminating these features.

Figure 24. SIR-B images of the central parts of the swaths over Hawaii, including the Kau Desert and Kilauea Crater: (a) image obtained at 28-deg look angle; (b) image at 48-deg look angle. Note differences in the response of vegetated areas to the right of Kilauea Crater. These images have not been corrected for scale-factor differences.
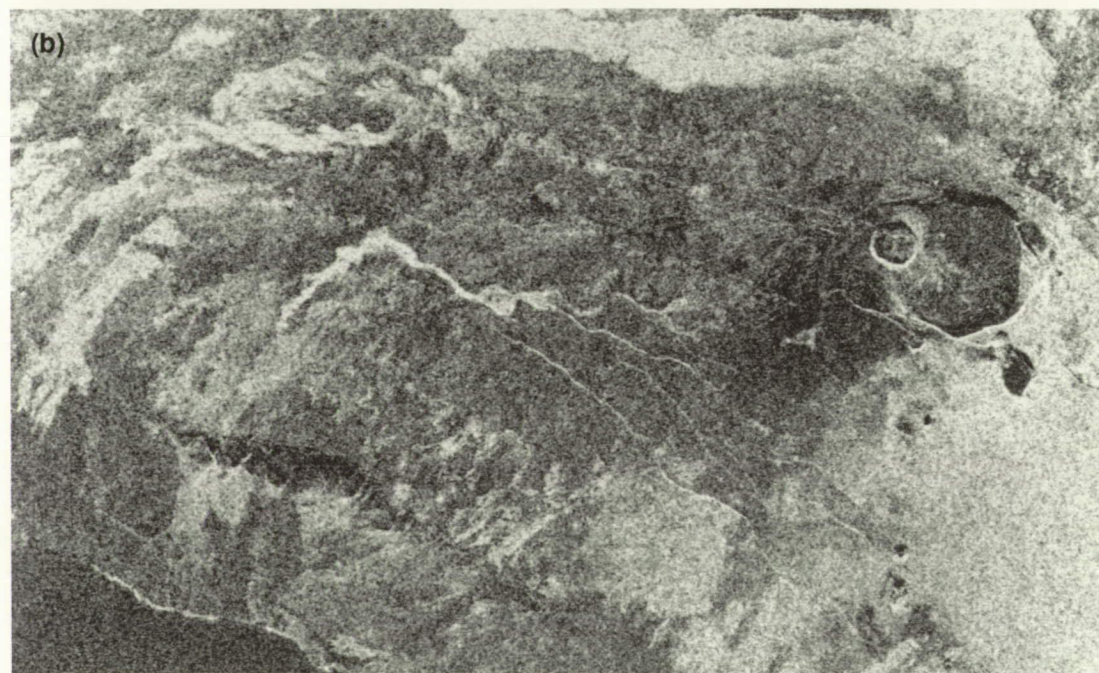
N   0   5 km   Illumination

Both effusive and explosive eruption products can be mapped on the images, with different degrees of success. The larger look angle (48 deg) appears best for discriminating aa flows of differing roughness. This may be because backscatter from rough surfaces tends to be similar at small angles. Farr and Massonnet (1985), Derryberry et al. (1985), and Gaddis et al. (1989) have evaluated the potential for using the SIR-B images for mapping flows of different types and ages and have found that young aa flows are brightest, followed by older aa flows, which are similar to some young pahoehoes, with older pahoehoes being the darkest of the lava flows. Low backscatter from smooth pahoehoe surfaces is comparable to that of adjacent pyroclastic deposits and could be misinterpreted. Slightly greater discrimination

among the pahoehoe flows is evident in the image acquired at the 28-deg look angle than in that at the 48-deg look angle (Gaddis et al., 1989). Derryberry et al. (1986) used various empirical and theoretical scattering models to estimate radar scattering coefficients, σ_0, for aa and pahoehoe surfaces in the SIR-B images.

Explosive volcanic deposits are also observable on the images. The Keanakakoi ash of 1790 covers a large area to the south of Kilauea Crater (Wentworth, 1938; Powers, 1948; Malin et al., 1983; Holcomb, 1987). This ash obscures underlying lava flows and, because it consists of fine-grained material, it is smooth and therefore dark in the radar images (Gaddis et al., 1985 and 1989). In contrast, the explosive eruption of Halemaumau in 1924 produced coarser material near the vent (Wentworth, 1938; Powers, 1948) and is visible as a bright halo around the crater in the radar images (Gaddis et al., 1985).

Based on SIR-B image data alone, the general volcanic history and style of Kilauea could be ascertained; however, similar low radar returns from both ash flows and pahoehoe lava flows could lead to misinterpretation of the dominant eruptive style and flow emplacement conditions (Gaddis et al., 1989). Erroneous identification of smooth pahoehoe flows as fine-grained ash flows would suggest a greater occurrence of pyroclastic activity than actually occurred. Determination of lava flow dimensions also is affected by the inability to delineate pahoehoe flows, particularly lava flows that change from pahoehoe to aa. The inability to resolve mesoscale vent structures obscures part of the history and evolution of the Kilauea summit area and may contribute to underestimating the importance of effusive activity.

Pinacate Volcanic Field, Mexico. The Pinacate Volcanic Field in northwestern Sonora, Mexico, is a broad, complex basaltic shield composed of three separate shield structures. From the Pleistocene through late Holocene approximately 240 to 290 km^3 of hawaiite magma and 13 km^3 of pyroclastic deposits were erupted to form more than 650 lava flows, 500 cinder and agglutinate cones, and 9 maar or maarlike craters (Donnelly, 1974). The flows are 5 to 15 km long, 1 to 10 m thick, and predominantly aa. Encroachment by eolian and alluvial deposits, particularly to the south and west, has formed a mantle that thins toward the interior of

the field. Figure 25 shows Seasat and SIR-A images of the Pinacate Volcanic Field. The relationship of radar units within the SIR-A image to geologic and geomorphic units has been studied by Greeley et al. (1985).

A map of the distribution of lava flows can be made from backscatter contrasts between adjacent flows in either image because the response is not look-angle sensitive. Backscatter curves for these flows remain relatively parallel with increasing look angle, unlike the Fantastic Lava Beds, where the curves converge at high angles (Blom, 1988). Hence, the relative brightness differences between the flows is about the same in the two images. Although backscatter variations between lava flows can be related to the degree of modification by weathering and mantle deposits, a direct correlation to flow age cannot be made (Greeley et al., 1985). Older flows not mantled by eolian sediments can have higher backscatter than younger, mantled lavas. Identification of at least one heavily modified, radar-dark lava flow is enhanced by strong radar returns from blocky flow margins. Multiple scattering from the blocky edges results in the high signal return from the flow margins over a range of orientations relative to viewing direction, not just from radar-facing slopes. Since the surrounding desert is relatively smooth and therefore dark on the image, there is no confusion between lava flows and the surrounding area.

Numerous cinder and agglutinate cones occurring throughout the Pinacate Volcanic Field can be seen on both the Seasat and SIR-A images. They are slightly easier to detect in the Seasat image; however, the small look angle results in geometric distortion, and cone shapes are more reliably determined in the larger-angle SIR-A image. Hence, in studies where shapes of volcanic features are important (such as assessing wind direction during eruption, or directed blasts), large look angles are superior.

The Pinacate Volcanic Field provides an excellent example of maar craters. Formed by phreatic or phreatomagmatic explosions and enlarged by postexplosion collapse (Jahns and Fielder, 1952; Gutmann, 1972), these features

Figure 25. Pinacate Volcanic Field in Sonora, Mexico: (a) SIR-A image; (b) Seasat image. In this case, detection of lava flows is not a function of look angle. Cinder cones are more easily detected in the Seasat image, but are distorted. Note slight differences in perceived shapes of craters in the two images. Bright rings outline maar craters.
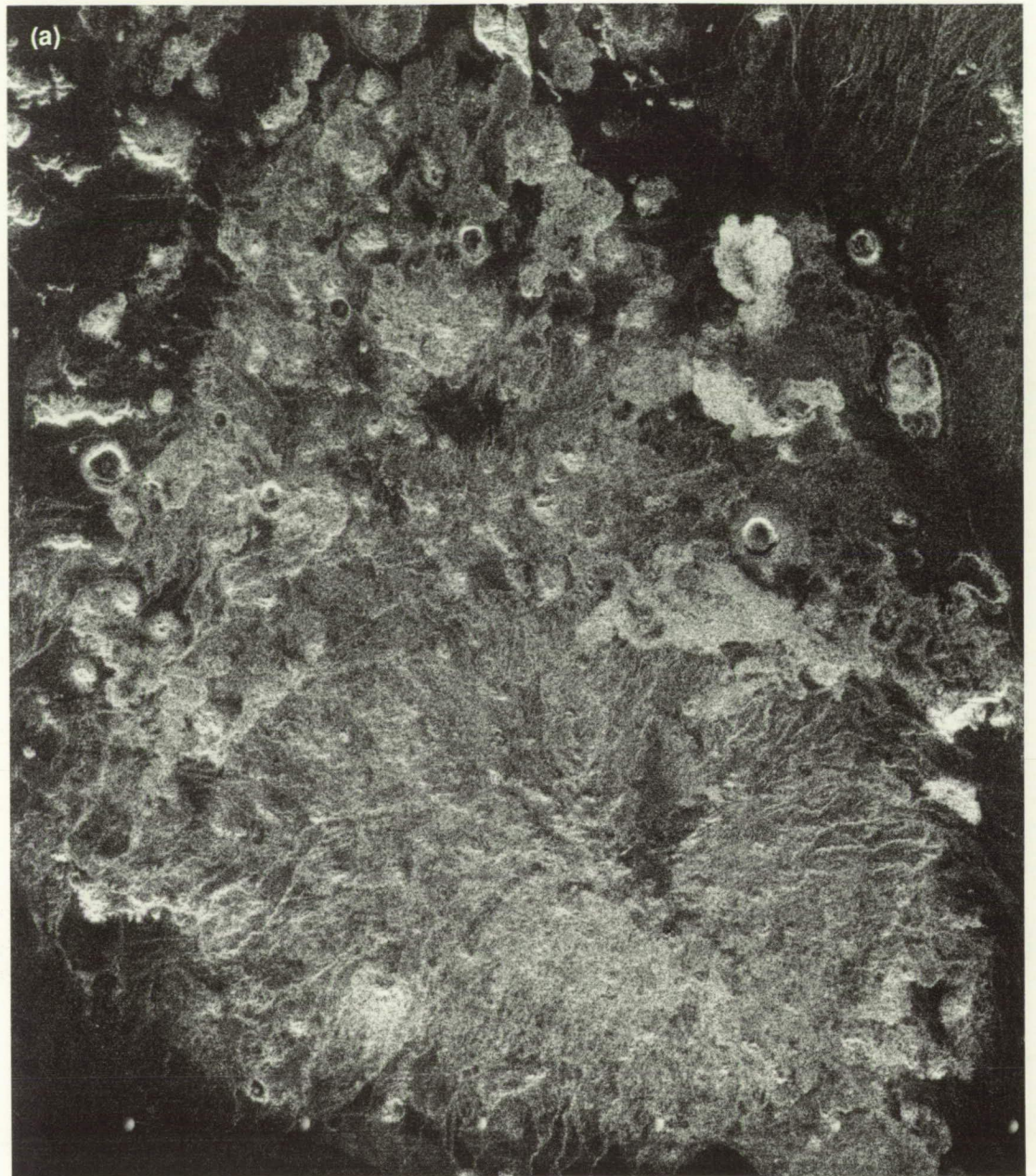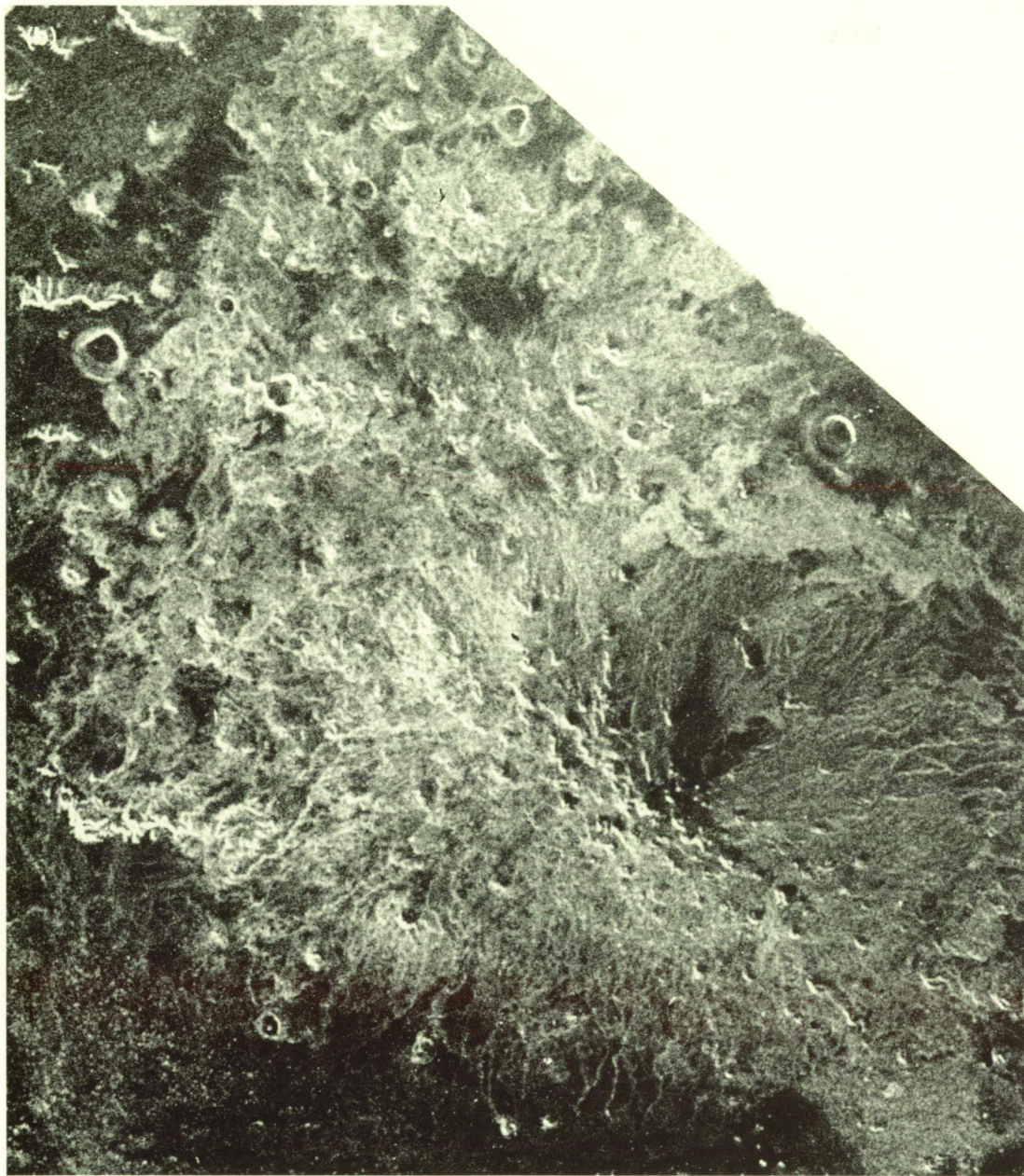

N ↖   0 ————————— 10 km   ↑ Illumination

are raised-rim craters 0.6 to 1.5 km in diameter and 30 to 250 m deep. Their distinct radar-bright ring pattern is related to rim morphology (Greeley et al., 1985 and 1987). Because they are geomorphically similar to impact craters, it is important to be able to distinguish the two types of landforms. Radar response from maar craters is discussed in more detail and compared with that from impact craters in the chapter *Impact Structures*.

Medicine Lake Highland, U.S.A. Medicine Lake Highland is a forested shield volcano located in northern California, about 55 km east of Mount Shasta. The central part of the volcano collapsed to form a caldera, and ring fractures around its periphery became the sites of eruptions of viscous andesitic lavas and cones. Later, more silicic dacites, rhyodacites, and rhyolites erupted on the edges and floor of the caldera. The composite, scoriaceous dacitic and rhyolitic flows of Glass Mountain on the east rim of the caldera and the blocky dacite of Medicine Lake Flow on its floor are examples of these late-stage silicic flows. Concurrent with the summit eruptions, parasitic basaltic aa flows erupted on the flanks of the volcano to the north in the Lava Beds National Monument area (e.g., Callahan Flow) and to the south (e.g., Burnt Lava Flow).

N ↖   0 |——————|——————| 10 km   ↗ Illumination

Numerous cinder cones and lava tubes also formed at this time (Anderson, 1941). The variety of features in this area allows study of radar response to volcanic landforms as a function of magma composition.

The following is summarized from Farr et al. (1981). Cinder cones are detectable on the radar image (Figure 26) because of their topographic expression and the presence of a summit crater (e.g., Caldwell Butte, to the east of the Callahan Flow). Since their slopes are near the Seasat look angle of about 20 deg, the illuminated slope is severely foreshortened and the geometry of the cone is distorted. Lava tubes are visible in the Seasat image as bright curvilinear features (e.g., Modoc Crater Lava Tube in Hatheway, 1971). The strong return from the lava tubes is caused by collapsed sections of roof that leave rough rubble enclosed by steep walls.

Lava flows can be detected on the basis of topographic expression and brightness differences. The more silicic flows are thicker and have a greater topographic expression than the basaltic flows. The Medicine Lake, Glass Mountain, and Little Glass Mountain Flows show highlighted flow fronts up to 30 m high, and both Glass Mountain and Little Glass Mountain exhibit multiple overlapping flow

43

Figure 26. Seasat SAR image of Medicine Lake Highland.
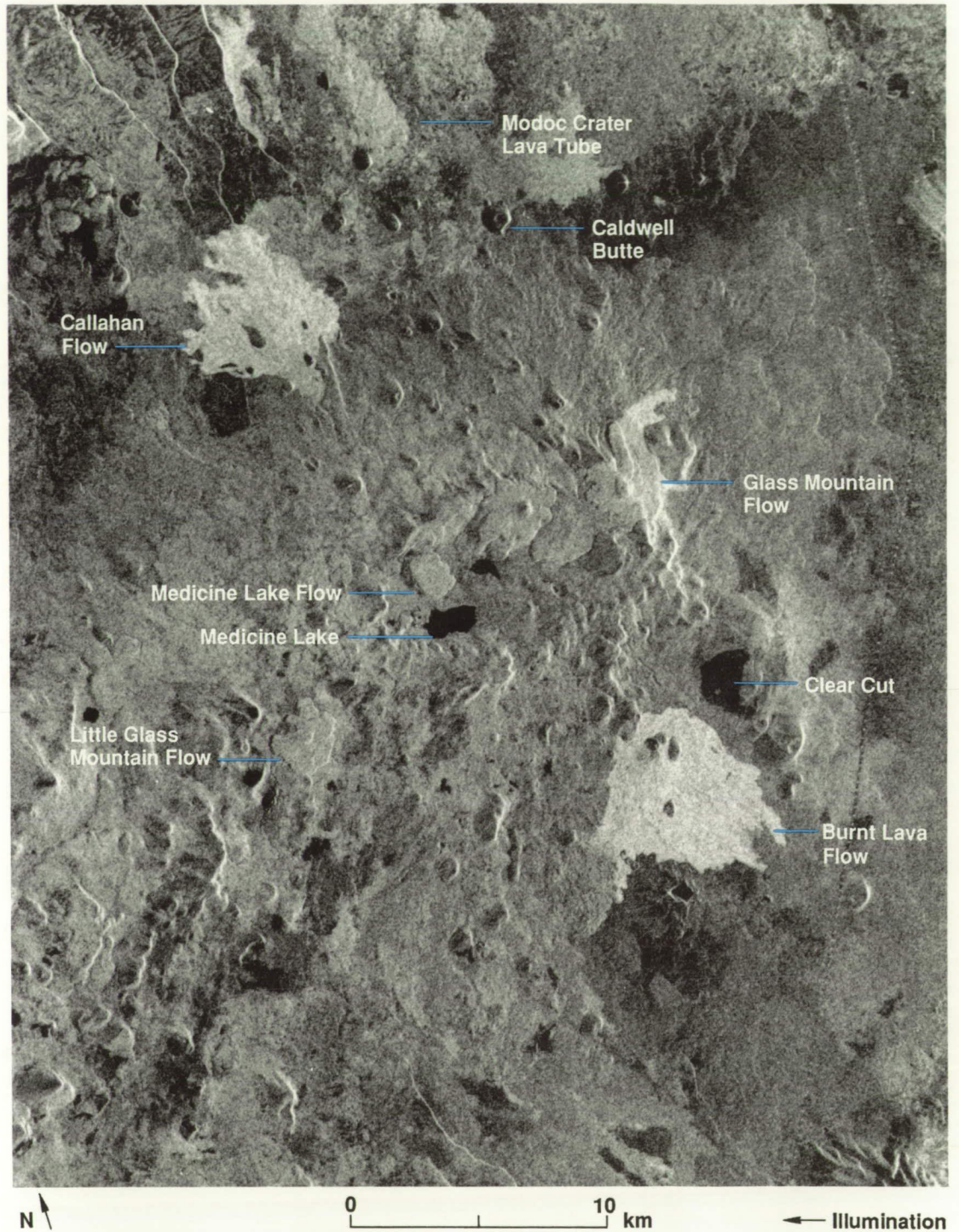
fronts. The Medicine Lake Flow with block surface texture is of intermediate brightness because the block faces are oriented nearly vertically, providing few faces perpendicular to the look angle of the Seasat system. The basaltic Callahan and Burnt Lava Flows lower on the volcano tend to be brighter because of high backscatter from their craggy aa surfaces. These flows also form distinct flow lobes. Flows in Lava Beds National Monument exhibit a variety of brightnesses that may be due to differing

amounts of weathering or tephra cover, which tend to smooth the original surface texture (Donnelly-Nolan and Champion, 1987).

Fantastic Lava Beds, U.S.A. The three spaceborne radar images in Figure 27 illustrate the effect of a variable look angle on the ability to discriminate volcanic features. These images are of the Fantastic Lava Beds in Lassen National Park, northern California, a forested area with a young lava flow (most recent eruption, ca. 200 years ago), ash dunes, a flat ash field, and a

(a)

(b)

(c)

(d)

N ↗   ↖ Illumination

Lakes

Ash

Lava

Ash Dunes

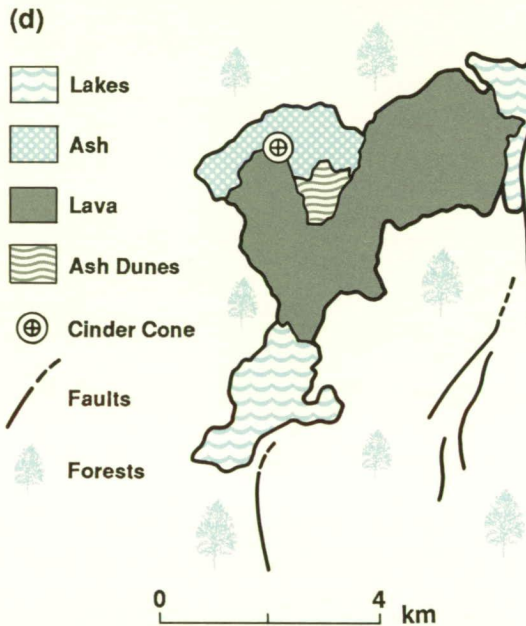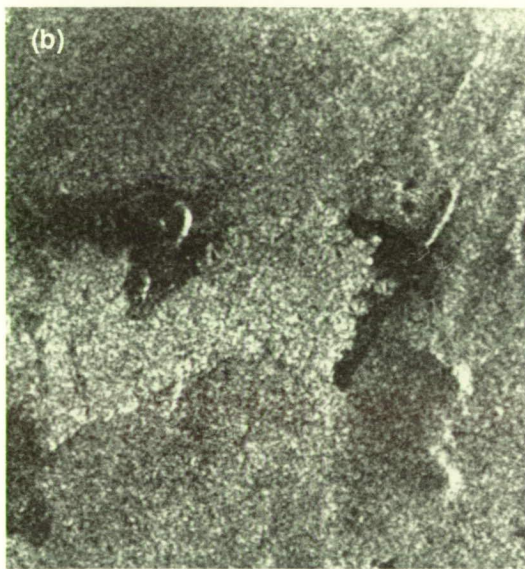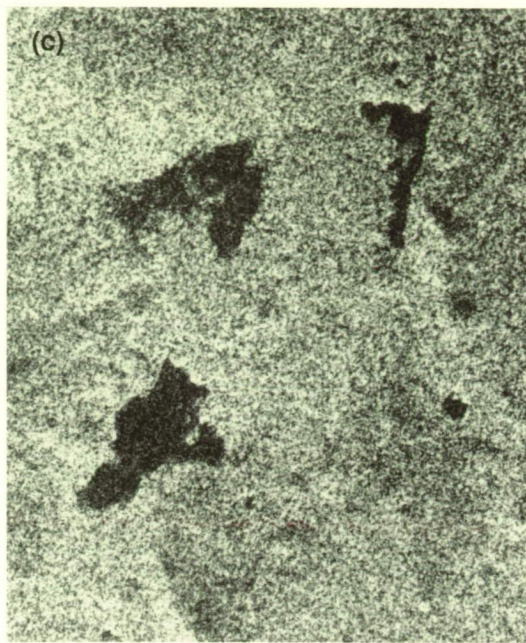⊕ Cinder Cone

Faults

Forests

0   4 km

Figure 27. Spaceborne radar images of Fantastic Lava Beds in Mt. Lassen National Park, California. Most features of interest are distinguishable in the 20-deg-look-angle Seasat image (a). Feature discrimination systematically decreases as look angle increases to about 30 deg in the SIR-B image (b) and to about 47 deg in the SIR-A image (c). Major features are indicated in the sketch map (d).

cinder cone. No significant changes to the area occurred over the years intervening between the Seasat (1978), SIR-A (1981), and SIR-B (1984) images. The principal variable is the look angle at which the area was observed. Illumination direction has generally not been found to be important in the observation of distributed targets such as lava flows and natural forests, because these features usually lack strong directional elements.

Each image has been digitally contrast-enhanced (the SIR-A original negative was digitized) to best display available information. In the small-look-angle Seasat image, it is possible to identify nearly all geologically important features. Confusion in this image might arise only in discriminating lakes and barren ash, both of which have smooth (dark) surfaces. As look angle increases, the ability to separate these surfaces decreases. At the SIR-A look angle, there are only two significant image brightness levels representing all materials: the forests and lava are bright while the ash dunes, lakes, and ash beds are dark and cannot be discriminated.

Look-angle-induced geometric distortion of features with significant topography can also be evaluated with these images. In the SIR-A image, the cinder cone is difficult to detect because it is dark and the rim of the crater at the top of the cone is black, contrasting little with

45

(a)

Scatterometer Track

Cinders

Third Eruptive Phase Lavas (Pahoehoe)

Second Eruptive Phase Lavas (Aa)

First Eruptive Phase Lavas (Pahoehoe)

Fault, Dashed Where Inferred

Mantled Surface

Pisgah Crater

U
D

U
D

N

0   4 km
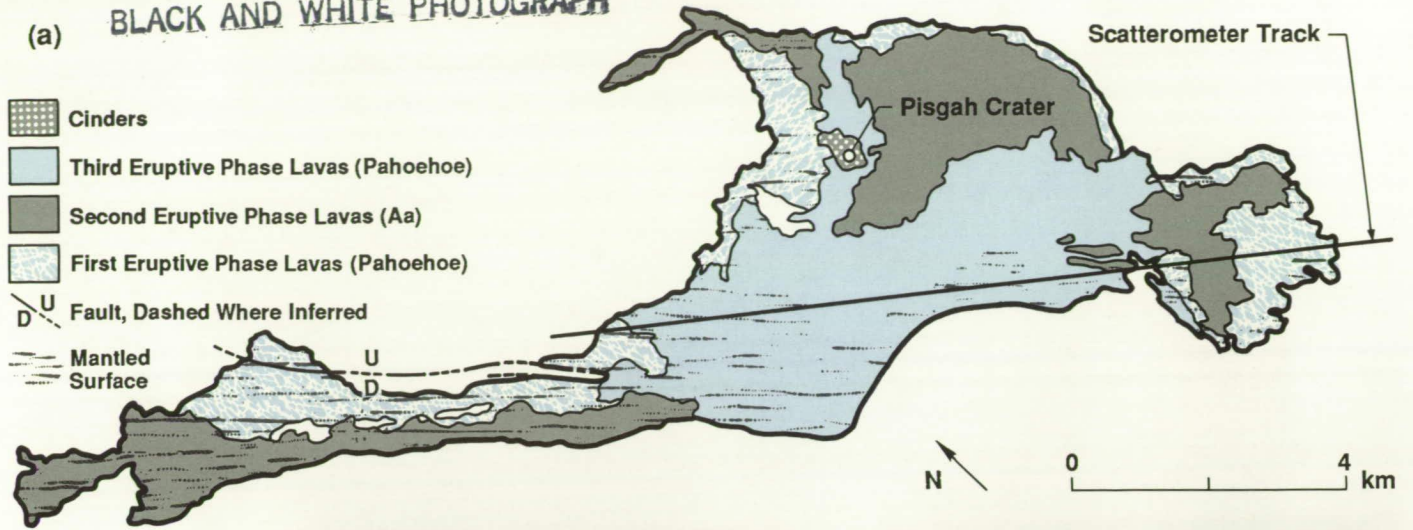
Figure 28. Pisgah Lava Field: (a) geologic map (modified from Wise, 1966, and Dellwig and Moore, 1966); (b) mosiac of two SAR L-band, HH-polarized images obtained by a NASA/ JPL airborne radar system in 1985; (c) Seasat image. On the Seasat image, the bright linear feature northeast of the Pisgah Lava Field is a railroad track and the linear arrangements of bright point returns represent power lines that cross the area.

(b)

N   0   4 km   Illumination

(c)

N   0   4 km   Illumination
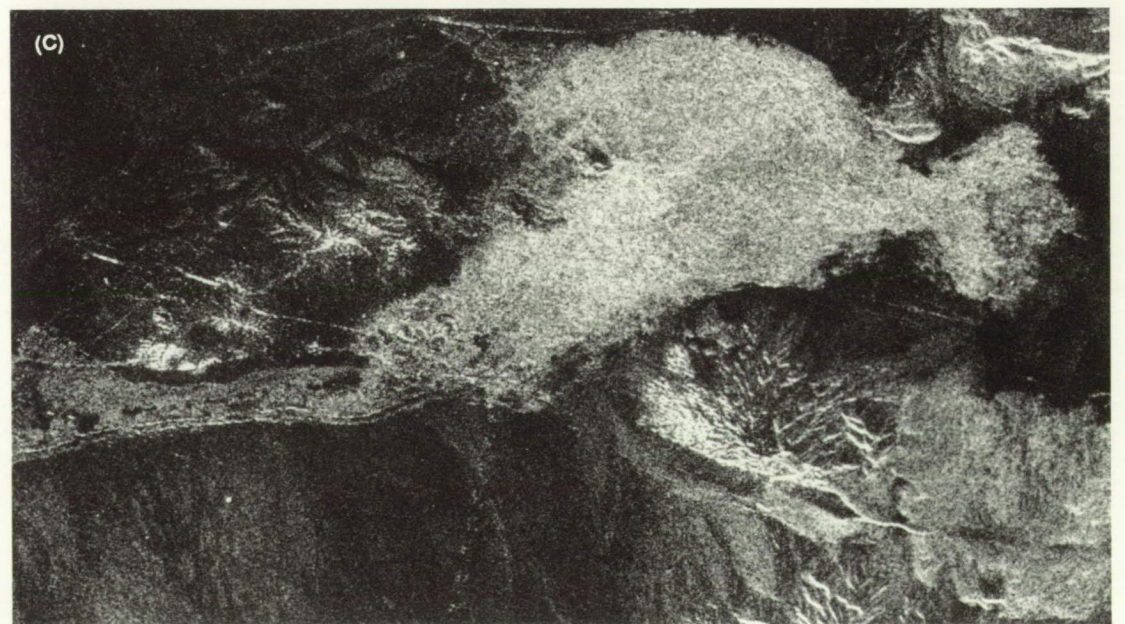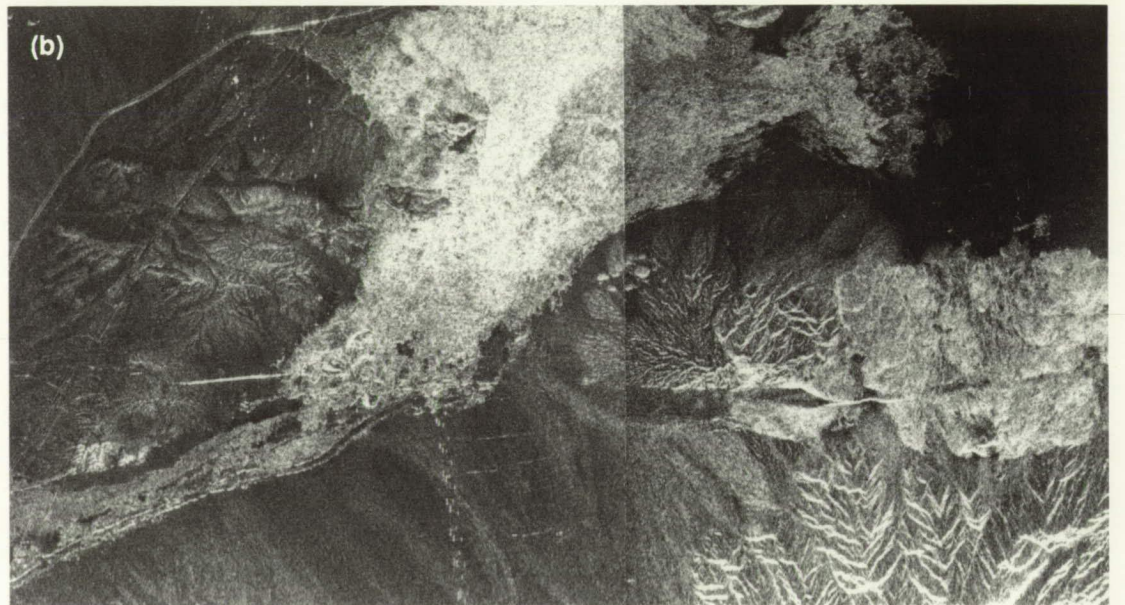
the cone itself. Prior to digital enhancement of this image, the cinder cone could not be detected. Despite the difficulty of detection, distortion of the cone shape is minimal. The cinder cone is distorted in the Seasat image due to the small look angle combined with the steepness of the cone slope. The cinder cone is easily detected, however, because of bright specular reflections from the outer edge and inner rim of the crater atop the cone where the incidence angle is near zero. In the Seasat image, more surface materials are discriminable and the cinder cone is more obvious. Distortion induced by imaging geometry must always be kept in mind when precise knowledge of the shapes of features is critical.

In view of the above observations, if one were assigned the task of assessing the level and recency of volcanic activity in this area, completely different conclusions based on separate analyses of the Seasat, SIR-A, and SIR-B images could be supported. A single radar image from one look angle in the absence of other supporting data may therefore be inadequate for geologic assessment of a region such as this. In the analysis of Magellan images then, the possibility that different types of surfaces may have the same backscatter at a given look angle should be kept in mind.

Pisgah Lava Field, U.S.A. Pisgah Lava Field, a low shield volcano, is located in the Mojave Desert about 61 km east-southeast of Barstow in San Bernardino County, California. Lava erupted onto alluvial-fan and playa-lake deposits to form a compound flow 22.5 km long and 6.4 km across at its widest point. The geology of the Pisgah Lava Field and the surrounding area (Figure 28(a)) was mapped by Wise (1966) and described by Dellwig (1969). Three eruption episodes produced lava flows from vents in the vicinity of Pisgah Crater (Wise, 1966). These units were mapped on the basis of phenocryst variations and, as such, do not necessarily correspond to different surface textures; however, some correlation exists. Phase 1 and 3 lavas are predominantly pahoehoe, whereas Phase 2 lavas, particularly east of the vent, are partly aa. The dominant mesoscale morphology within all three units is a ridge-and-valley topography composed of tumuli and pressure ridges up to 10 m high.

Alluvial and eolian processes have modified the margins of the lava field. Eolian deposits, derived from alluvium to the northwest and transported by the dominant winds in this area, are concentrated on the western side of the flow. Windblown material is deposited in the low areas between tumuli and ridges and, locally, is almost 2 m deep (Dellwig, 1969). Subsequent drainage has ponded against the lava and deposited fluvial sediments that bury the edge of the lava field and fill depressions within the flow adjacent to Lavic Dry Lake.

Sunshine Cone Lava Field is associated with a north-northwest trending fault zone south of the Pisgah flows (Gawarecki, 1964). This field consists of two eruptive units and is slightly older than the Pisgah flows (Wise, 1966).

The Pisgah area has been a test site for remote sensing studies since the early 1960s, and radar investigations have been conducted by Dellwig and Moore (1966), Moore et al. (1968), Dellwig (1969), Farr and Engheta (1983), and Theilig et al. (1988). Experiments to determine an empirical relationship between radar backscatter, surface roughness, and eolian roughness also have been conducted at Pisgah (Greeley et al., 1988).

Aircraft and Seasat L-band HH radar images of the Pisgah area are shown in Figures 28(b) and (c), respectively. In the images, the Pisgah and Sunshine Cone Lava Fields are brighter than the surrounding alluvial material. Variations in backscatter exist across the lava surfaces and, for the Pisgah flows, correspond predominantly to mantled versus unmantled areas. Lower backscatter from mantled surfaces is particularly noticeable on the long extension of the lava field to the northwest and at the southeast end of the flow bordering Lavic Dry Lake. The fact that the mantled areas are still brighter than the surrounding alluvial terrain suggests that only the small-scale roughness (< 1 cm) has been masked or that the radar penetrates the sediments (Elachi et al., 1980). Alternatively, backscatter and specular reflection from the unburied ridges

and mounds may produce a large radar return from the mantled areas.

Other variations in radar brightness on the flow can be related to geologic boundaries between the products of the three eruptive episodes, but the correlation is inconsistent. In both images, the Phase 2 aa unit is slightly brighter than the surrounding areas but cannot be differentiated from the pahoehoe surface southwest of Pisgah Crater. Elachi et al. (1980) noted that specular reflection from the low slopes of ridges and mounds in the hummocky pahoehoe could be responsible for the high returns from that area.

Pisgah Crater, a cinder cone standing 98 m high and having a diameter of 488 m at the base, is the most prominent feature on the lava field. It is composed of cinders and small bombs interbedded with a few layers of agglutinate. The cone is visible in both radar images (Figure 28(b) and (c)) because specular reflection from slopes normal to the incident wave creates large tonal variations. In addition, the cone appears elongated in the Seasat image because of geometric distortion caused by foreshortening.

Airborne L- and C-band (19- and 6.3-cm wavelength, respectively) HH radar scatterometer data of the Pisgah Lava Field have been analyzed to determine the ability to discriminate lava flows, based on backscatter coefficients obtained at different incidence angles (Theilig et al., 1988). Mantled surfaces have the lowest backscatter at all angles for both wavelengths and can be distinguished easily from unmantled surfaces. The difference between the energy returned from bare versus mantled lava tends to increase with incidence angle. Phase 3 pahoehoe is not easily separated from Phase 2 aa at any angle. The difference in backscatter values between the two units is greater in C-band than in L-band; this suggests that surface roughness is similar for both surfaces at the 20-cm scale but varies at the 6-cm scale.

Composite volcano: Mount Shasta, U.S.A.

Mount Shasta, which rises about 3,000 m above the surrounding California terrain, is the largest composite volcano of the High Cascade Range (Figure 29). Volcanic activity began about 500,000 years ago, but most of the volcano was emplaced within the last 250,000 years. At least four overlapping cones composed of pyroxene andesite flows, block and ash flows, lahars, and dacite domes constitute most of Mount Shasta (Christiansen and Miller, 1976). The most recent cones, Shastina and Hotlum, were built within the last 10,000 to 12,000 years, after the last major glacial episode. Only the southern slopes and parts of the eastern and western slopes of the volcano are heavily modified by erosion. Today, five small glaciers are present on the mountain.

Mount Shasta, a nearly circular topographic feature, was imaged at three different look angles by SIR-B, and thus provides an excellent example of how look angle and illumination direction affect the appearance of a particular feature. SIR-B images at look angles of 28, 51, and 57 deg (Leberl et al., 1986) illustrate how a similar volcano on Venus would appear in the Magellan data at mid- to high latitudes and at equatorial latitudes (Figure 29). The most striking effect is that of greater geometric distortion with decreasing look angle. Many volcanic landforms can be identified at all three look angles. Moderate to high reflectivity from flow surfaces and the highlighting of mesoscale lava levees and steep flow margins contribute to the detection of thick andesitic lava flows on the northwest and southeast flanks of the volcano. A north-south line of cones and domes is seen as indistinct mounds on the images. Again, geometric distortion at smaller look angles is evident, particularly on the side of the volcano facing away from the radar. The effect of illumination direction is exhibited by the variable appearance of canyons, which are more distinct when oriented normal to the illumination. The dark halo around the summit of Mount Shasta marks the area above the treeline.

Explosive volcanism

Theoretical studies suggest that large-scale explosive volcanism is unlikely on Venus because of inhibited vesiculation and absence of water. However, the possibility cannot be discounted in view of the limited data available. Two examples of landforms produced by this style of volcanism are discussed below.

48

Valles Caldera, U.S.A. The Valles Caldera within the Jemez Mountains volcanic complex is a classic example of a resurgent cauldron as defined by Smith and Bailey (1968). Situated at the western margin of the Rio Grande Rift, the volcanic complex overlies Paleozoic and Mesozoic sedimentary rocks to the west and is interbedded with Cenozoic continental sediments to the east. Volcanic activity began with the building of a broad highland of basalts, andesites, dacites, and rhyolites erupted between about 13 and 3 Ma (Doell et al., 1968; Gardner and Goff, 1984). Large-scale explosive eruptions between 1.4 and 1.1 Ma produced the numerous rhyolitic ash flows comprising the Bandelier Tuff (Smith and Bailey, 1966). As large volumes of material were evacuated, the roof of the magma chamber collapsed along ring faults and formed calderas. The most recent of these is the 20- by 25-km-wide Valles Caldera. Following collapse, increased pressure in the magma chamber uplifted the caldera floor about 1 km to form Cerro Redondo, a resurgent dome. Later eruptions were localized along faults with the final activity between 0.9 and 0.15 Ma, producing a discontinuous circle of tephra cones, domes, and lava flows in the moat between Cerro Redondo and the caldera walls (Smith and Bailey, 1966; Self et al., 1986 and 1988).

Many of the volcanic elements of this area are depicted in the Seasat SAR image and the accompanying sketch map (Figure 30). Structural features and their tectonic implications are discussed in *Tectonic Landforms*. The megamorphology of the broad shield extending away from the central caldera is evident in the radar image. Valles Caldera, the resurgent dome Cerro Redondo, and the postcaldera ring of cones, domes, and lava flows can all be distinguished in the radar image. The western fault of a graben that formed across the resurgent dome during uplift is visible because of specular reflection from the radar-facing slope. Alluvial deposits on the caldera floor are smooth to L-band radar and form distinct dark patches in the northern and western parts of the depression. The Toledo Embayment, a poorly defined semicircular scarp adjacent to the northwest rim of Valles Caldera, marks a possible remnant caldera or tectonic collapse, modified by subsequent erosion and eruptions (Self et al., 1986). On the Banco Bonito Flow—located on the southwest side of the Valles Caldera—mesoscale, parallel, festoonlike ridges are highlighted along radar-facing slopes.

The gently sloping surface of the Bandelier Tuff has low relief and is exhibited best to the south and west. Deep canyons formed by subsequent erosion cut these surfaces and are highlighted by reflection from radar-facing canyon walls. Because of the small look angle, canyons appear asymmetric, particularly to the north and south where they are approximately perpendicular to the radar look direction. To the east and west, the canyons parallel the illumination and appear shallower and less well defined.

Ignimbrite sheets, central Andes, South America. Ignimbrite sheets are indicative of large explosive volcanic eruptions. Examples of unmodified ignimbrite plains are not common on Earth and the initial morphology of these deposits is not completely known. Older Cenozoic pyroclastic flows in the central Andes, South America, have been imaged by SIR-B and provide examples of modified ignimbrites with a distinctive erosion pattern. The following discussion is based on a study by Fielding et al. (1986).

Cenozoic volcanism has covered much of the Puna/Altiplano, a high plateau in the central Andes, with dacitic to rhyolitic ignimbrites and andesitic composite volcanoes. Large pyroclastic flows were emplaced predominantly during two major periods between 10 and 7 Ma and between 5 and 3 Ma (Kussmaul et al., 1975; Coira et al., 1982). Minor eruptions producing small ignimbrite sheets have occurred within the last 3 Ma (Schwab and Lippolt, 1976).

Ignimbrite sheets are strong scatterers and appear bright on the SAR images (Figure 31). Weathering of these pyroclastic deposits results in variable scales and shapes of roughness that enhance radar backscatter. Ignimbrite deposits in Figure 31(a) and (b) are roughly similar in age to ignimbrites in Chile that have a reticulate network of low ridges about 10 to 30 cm in height and up to a meter in width (Guest, 1969). These ridges are close to the scale of the radar

Figure 29. SIR-B images of Mount Shasta at look angles of (a) 28 deg, (b) 51 deg, and (c) 57 deg, corresponding to expected Magellan data from mid- to high and equatorial latitudes of Venus. Geometric distortion increases with decreasing look angle. Most lava flows and domes are detectable on all three images. (d) Generalized geologic map of Mount Shasta (modified from Wagner and Saucedo, 1987).
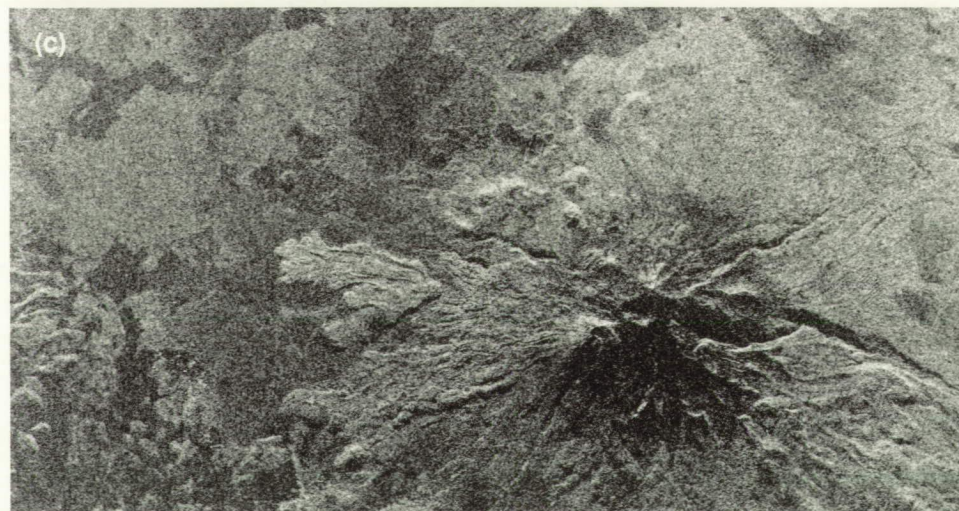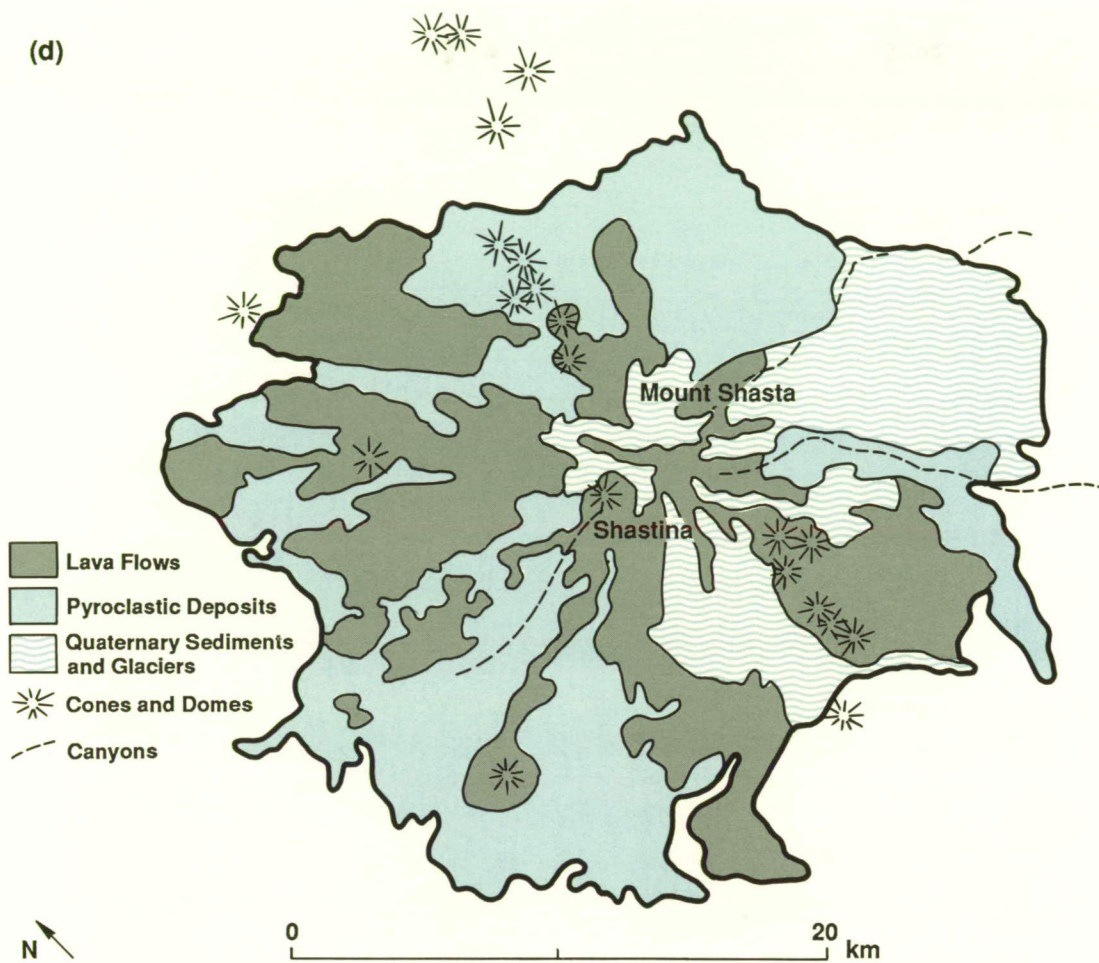
Equivalent
Latitude
on Venus

Mid to High

Equatorial

N

Illumination

0   20
                        km

50

(d)

Mount Shasta

Shastina

Lava Flows

Pyroclastic Deposits

Quaternary Sediments
and Glaciers

Cones and Domes

Canyons

N

0   20 km

wavelength and could contribute to the high backscatter. Older ignimbrites (Figure 31(c)) are characterized by meter-sized blocks and resistant ledges a few centimeters to a few meters in size. These features form facets that, if oriented perpendicular to the radar beam, reflect energy back to the receiver.

Parallel bright and dark lines characterize these deposits on the SAR images and represent a distinct erosional pattern composed of quebradas—linear steep-sided gullies and canyons. The friable nature and thermal disaggregation of ignimbrites enhance the ability of the wind to abrade these deposits. Flowing water contributes to the erosion process but probably follows preexisting channels incised by the wind. Steep gully walls are responsible for the alternating dark and bright bands within the SAR images, with the bright lines representing specular reflection from radar-facing slopes. In the examples used here, the SAR look direction is almost perpendicular to the quebrada trends. If oriented parallel to the radar illumination, they may not be detectable.

Summary

Magellan radar observations will increase our understanding of volcanism on Venus and provide new insight into the evolution of geologic processes on Earth's sister planet. Diverse volcanic processes on Earth produce distinct types of volcanoes and associated features that can be detected on SAR images and interpreted in terms of styles of eruption and

Figure 30. Jemez Mountains volcanic complex in the Rio Grande Rift, New Mexico: (a) Seasat mosaic of the region. The megamorphology of Valles Caldera surrounded by a shield-like apron of pyroclastic deposits is visible in the image. (b) Generalized map of volcanic units (modified from Ross et al., 1961). The extent of this map is indicated at the margins of the image.

N

0   20 km

Illumination

106°45' 106°30' 106°15'

(b)

36°00'

Valles Caldera

• Cerro Redondo   Los Alamos

35°45'

35°30'

Pleistocene
- Alluvium
- Postcaldera Rhyolite
- Bandelier Tuff

Pliocene
- Early Volcanics and Volcanic Sediments
- Tertiary Sediments

Pre-Tertiary
- Mesozoic, Paleozoic, and Precambrian Rocks, Undifferentiated
- Contact
- Normal Fault, Dotted Where Concealed

N

0   15 km
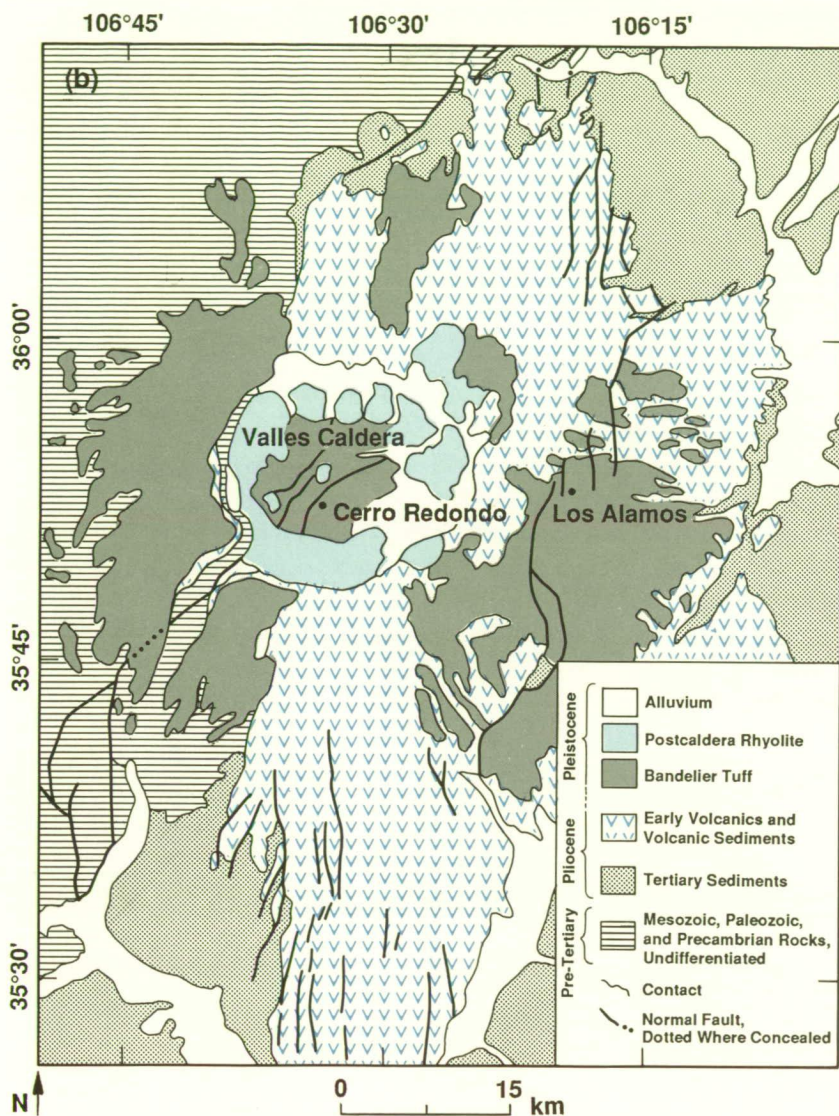
emplacement, rheology, and tectonic setting. For example, it is possible to discriminate plains units emplaced as flood basalts (e.g., Columbia River Basalts) from units emplaced as a series of overlapping tube-fed flows (e.g., Craters of the Moon) or low shields (e.g., Pisgah Lava Field). The presence of flank lava flows serves to discriminate Askja-like calderas (Iceland) from large-scale explosive silicic ones such as the Valles Caldera.

Geometric distortion that is high at low look angles decreases noticeably as the look angle increases above about 35 deg (e.g., Mount Shasta, Fantastic Lava Beds, Pinacate Lava Field). However, there are inconsistensies in the relations between feature discrimination and look angle that remain unexplained (e.g., systematic decrease in feature discrimination with increasing look angle at the Fantastic Lava Beds as compared to no noticeable contrast in feature discrimination with increasing look angle at the Pinacate Lava Field).

The global coverage of Magellan will provide a basis for comparative planetology at multiple spatial scales and further our understanding of relations between volcanism, tectonism, and thermal evolution at the planetary scale. In addition, altimetry data will help define

*Figure 31. SIR-B
images of ignimbrite
sheets: (a) and (b)
in Bolivia; (c) in
Argentina. High
backscatter from the
rough erosional
surfaces
characterizes the
ignimbrite deposits.
Linear light and dark
bands represent a
pattern that may be
characteristic of the
eolian erosion of
ignimbrites along
cooling or tectonic
joints. A dark saw-
tooth band in (b)
marks the contact
between two
ignimbrite sheets.*

N ↗   ← Illumination

0 _____ 5 km
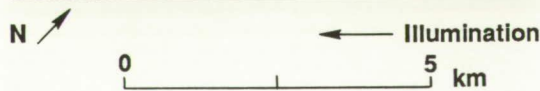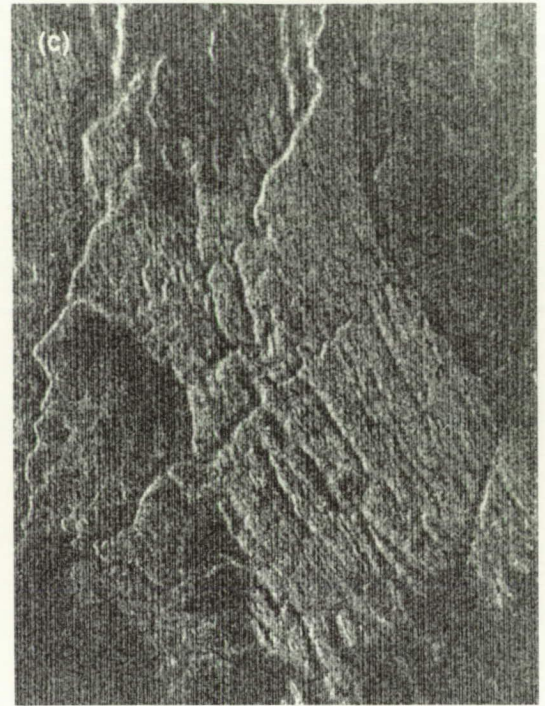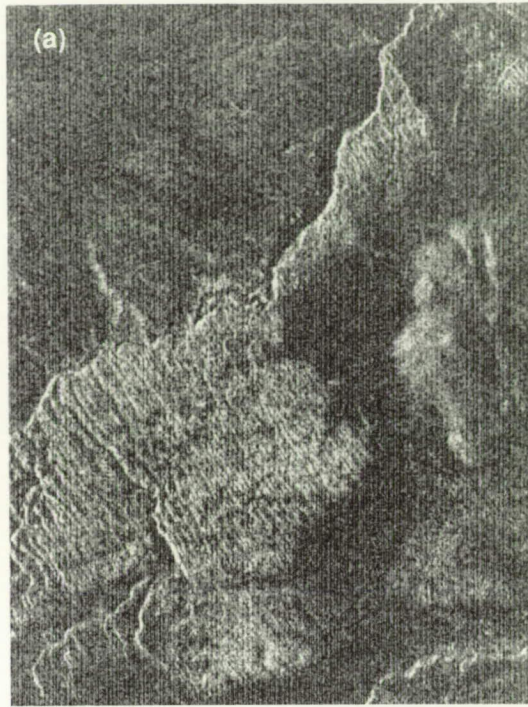
the morphology of megascale features such as
shield and composite volcanoes.

The increased resolution afforded by
Magellan SAR will allow the identification of
mesoscale features and reveal more information
about the morphology of individual flows, vents,
and related constructs. It will also allow analysis
and interpretation of small-scale surface rough-
ness characteristics. This information will help
elucidate the evolution and relative ages of
individual volcanic centers, characterize the
styles of volcanism, constrain the composition of
the deposits, and evaluate evidence for postem-
placement weathering. However, experience
with terrestrial examples in high-resolution
spaceborne SAR images has shown limitations in
the ability to discriminate certain eruptive
products (e.g., ash vs. pahoehoe at Kilauea; aa
vs. pahoehoe at Askja Volcano) and the age
relations and source of multiple lava flows (e.g.,
Myvatn, Iceland). These examples should stand
as a reminder of limits that may exist in the inter-
pretability of Magellan images.

Sand Dunes and Subsurface Imaging

Introduction

This chapter reviews the radar imaging characteristics of eolian deposits and the phenomenon of subsurface radar imaging. The combination of these topics in a single chapter arises from the fact that wind-blown material is the most common radar-transparent material at Earth's surface. One of the criteria for radar penetration is fine-grained homogeneous cover material, and eolian sorting readily achieves this. Some eolian deposits have scattering properties that are highly directional and thus impose geometric constraints on the imaging system if they are to be detected.

Eolian Deposits

Eolian deposits (such as sand dunes and sand sheets) cover a large percentage of the surface of both Earth and Mars (McKee, 1979; Cutts and Smith, 1973; Breed et al., 1979), and may occur on Venus (Greeley and Iversen, 1985). Should eolian deposits occur, detection and study of them would provide insight into the geologic processes on Venus. Since it is necessary to image the surface with radar, and since terrestrial eolian materials have peculiar radar backscatter characteristics, it is important to understand these characteristics to enable interpretation of possible eolian features on Venus.

The following review summarizes studies of radar images and scatterometer data of terrestrial sand dunes reported in the literature (Blom and Elachi, 1981 and 1987). The essential conclusions of these studies are quite simple, but they have significant implications for the detection and study of possible eolian terrains in radar images of Venus.

While the geometry and other characteristics of eolian landforms on Venus are likely to be different from terrestrial examples, the radar response is likely to be similar. This is due to the fact that wind-transported material is fine grained by nature, which means essentially that

all eolian surfaces are smooth at radar wavelengths. The possible eolian landforms to be encountered on Venus are not discussed here as this is a different problem than that addressed. Experimental and theoretical results about potential eolian material and landforms on Venus can be found in Greeley et al., 1980 and 1984; Greeley and Marshall, 1985; and White, 1981.

Terrestrial sand dunes are quasi-specular reflectors at all wavelengths studied (75 cm through 2.25 cm, Blom and Elachi, 1987). These wavelengths bracket the Magellan wavelength of 12.6 cm. Because of this quasi-specular behavior, a radar echo from a dune is possible only when a dune face several wavelengths on a side is nearly perpendicular to the imaging radar. If such is not the case, dunes are imaged as a dark area and the true nature of the landscape is not disclosed in the radar image. Radar echoes from sand dunes are highly directional and sensitive to the imaging geometry of the radar system. To illustrate the effects that can be encountered, the following examples show extreme changes in the appearance of dunes as a function of the look angle and illumination direction of the radar.

Look-angle effects

Airborne 3.0-cm wavelength (X-band) and Seasat and SIR-A 23.5-cm wavelength (L-band) images of the southern portion of the Algodones Dunes (southeastern California) are shown in Figure 32. Both of the spaceborne images have been digitally contrast stretched (the SIR-A original negative was digitized). This portion of the dune field consists of large barchanoid dunes enclosing areas of desert floor (interdune flats). In the Seasat image and the low-look-angle airborne image, the sand dunes are quite bright, texturally distinctive, and easily distinguished from the darker image tone of the desert floor. In the larger-look-angle airborne and SIR-A images, however, the dunes are black and the desert floor remains dark, though brighter than the dunes. Thus the dunes themselves are not detectable at the larger look angle, and there is a

Figure 32.
Algodones Dunes,
California: (a) SIR-A
and (b) airborne
images were
acquired at look
angles greater than
the angle of repose
for dunes; (c) Seasat
and (d) airborne
images were
acquired at look
angles less than the
angle of repose. In
the Seasat and low-
look-angle airborne
images, sand dunes
are visible because
of quasi-specular
reflection from
favorably oriented
dune slopes, where
the incidence angle
is zero. In the SIR-A
and large-look-angle
airborne images, the
dunes are dark
because the look
angle is greater than
the angle of repose.
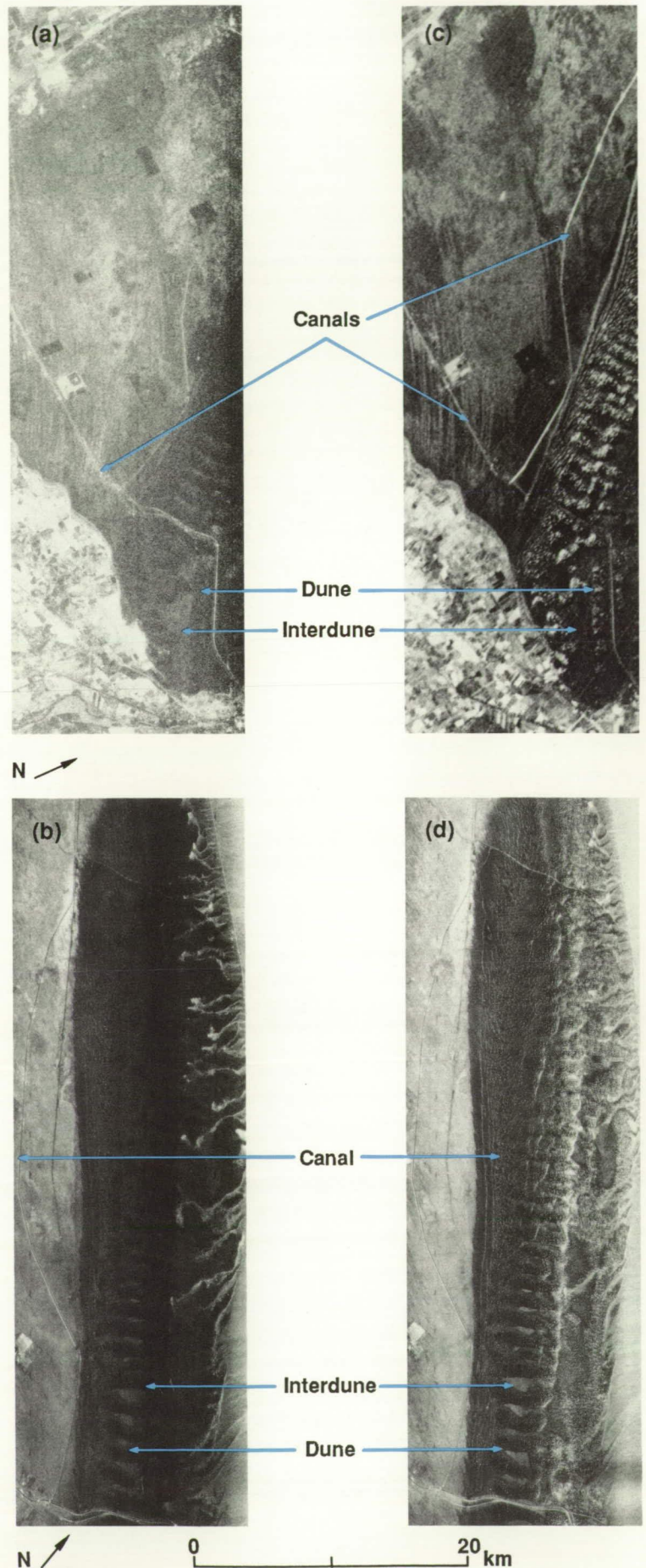
contrast reversal between the two surfaces when viewed at these different look angles; this reversal is independent of wavelength. The large dunes would probably be undetected if an analysis were based on only the larger-look-angle images.

The seemingly unusual backscattering behavior of sand dunes is due to the fact that dunes consist of a set of smooth surfaces with a nonzero slope. The dunes are bright in the low-look-angle images because of quasi-specular reflection from smooth dune faces that are near-normal to the radar beam, where the incidence angle at the dune face is zero. Because terrestrial eolian sand has an angle of repose of about 33 degrees, no dune slopes exceed this value. Therefore, radar backscatter from a dune is possible only at look angles less than 33 degrees where a dune slope may be normal to the incident beam. If this is not the case, the echo is specularly reflected away from the radar antenna, and the black image tone seen in the high-look-angle images results. Thus, to image terrestrial dunes with radar, a necessary (but not sufficient) condition is a look angle less than 33 deg. (Note that, in the case of spaceborne SARs, the effective look angle is slightly increased by planetary curvature.) Venusian dunes may have a different slope geometry, but they will almost certainly have radar-smooth surfaces. Hence, the look-angle constraints may be different, but the mechanism by which dunes are detected will be the same.

To reinforce this important point, consider the scatterometer data shown in Figure 33. The graphs show backscatter plotted as a function of look angle, and show the surface response as the look angle changes. Scatterometer data can be used to predict the appearance of various surfaces in radar images as a function of frequency and geometry. Here, horizontally polarized transmit and receive data at wavelengths of 75.0, 19.0, and 6.3 cm are shown. Also, vertically polarized transmit and receive 2.25-cm wavelength scatterometer data are plotted (horizontally polarized data at this wavelength are not available). These wavelengths bracket the Magellan and Venera radar wavelengths, and also the Seasat and SIR systems used to image the Earth. When examin-
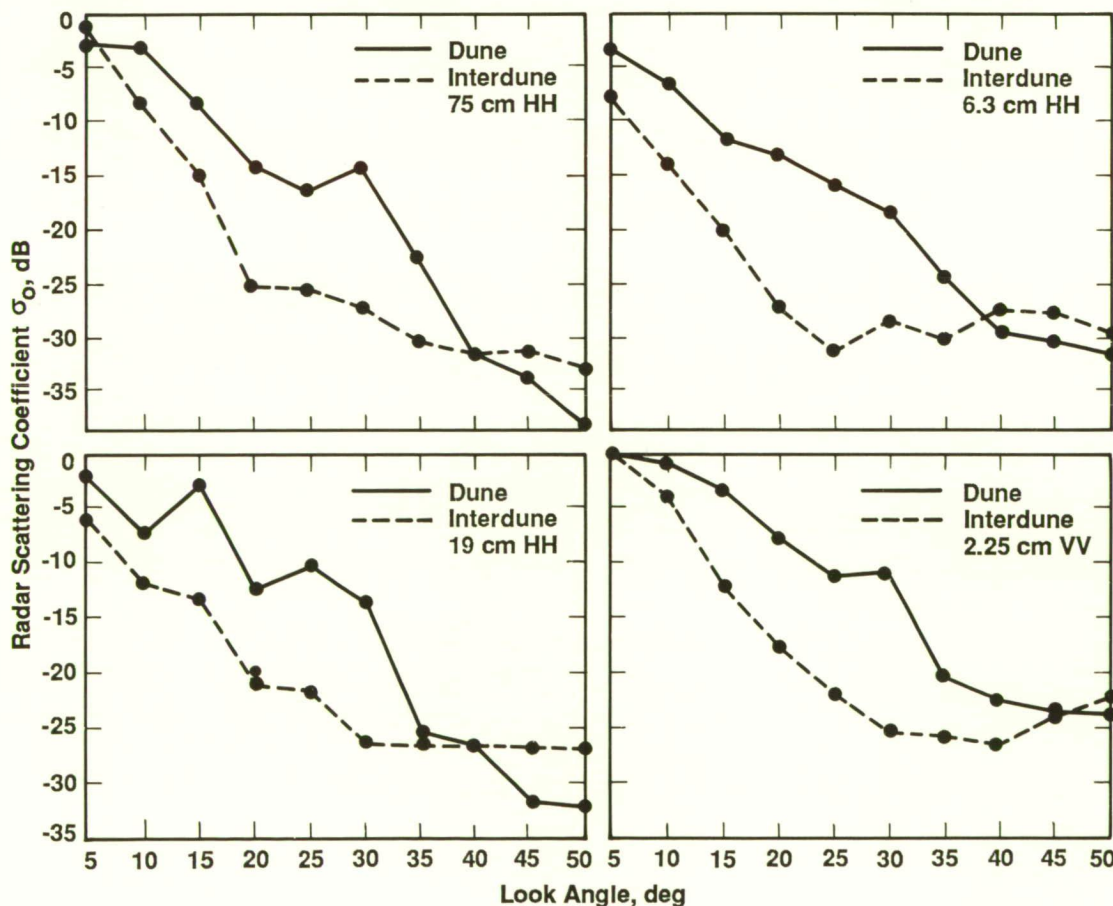
Figure 33. Scatterometer data for a large dune and interdune flat (desert floor), Algodones Dunes, California, at four wavelengths from 75 cm to 2.25 cm. Dunes are darker than interdune flats at larger angles and brighter at small angles, as in Figure 32. Backscattering characteristics of the dunes are not functions of the observing wavelength. Minor differences in curve shapes for different wavelengths are due to varying fields of view for different scatterometers.

57

ing the plots, keep in mind that the Magellan radar will have a look-angle variation with latitude that nearly equals the plotted range.

Figure 33 shows that dunes are brighter than desert floor at small look angles and darker than desert floor at higher look angles, duplicating the response seen in the radar images of Figure 32. This behavior is independent of wavelength. Hence, the detection of sand dunes requires a radar with a look angle less than the angle of repose. Note that dune response is not sensitive to wavelength over the region considered here since the backscatter curves have similar characteristics. Should Venusian dunes have geometric characteristics similar to those of terrestrial dunes, images of them at high latitudes would be comparable to the low-look-angle images in Figure 32, while low-latitude dunes would look like those in the high-look-angle images in Figure 32 (see Figure 3 of *Synthetic-Aperture Radar Imaging*). It would therefore be very difficult to image such dunes using the Magellan radar at low latitudes, and a false impression of a latitudinally varying distribution of dunes might be given.

Illumination-direction effects

Dunes are also directional features, and so must be oriented approximately perpendicular to

the radar beam, or no backscatter will occur. Thus, the morphology of the dunes as revealed by the radar could be misleading in regard to dune form and wind regime. These effects are illustrated in Figure 34, which shows a Skylab visible-wavelength image and two Seasat radar images—from different illumination directions—of the Mohawk Dunes in Arizona. The dunes have a network pattern in the Skylab photograph. Each Seasat image reveals only half of this network pattern. Each radar image, by itself, could easily lead to a misunderstanding of the true dune forms and the wind regime responsible.

Conclusions

Terrestrial eolian features are quasi-specular radar reflectors and hence impose stringent geometric constraints on any radar system, if they are to be detected. Radar look angles must be less than the angle of repose for dunes, and the radar illumination direction must be approximately perpendicular to the dune trends. Should eolian features exist on Venus, their detection will likely impose similar constraints on the radar system.

The radar system configuration must include the ability to view the area from more than one illumination direction. Dune response to radar is

Figure 34. Mohawk Dunes, Arizona: (a) Skylab photograph; (b) Seasat ascending image; (c) Seasat descending image. In the Seasat images, only one set of the intersecting dunes shows in each image because of the orientation of the radar illumination. The spacing of the linear dune crests is about 130 m.
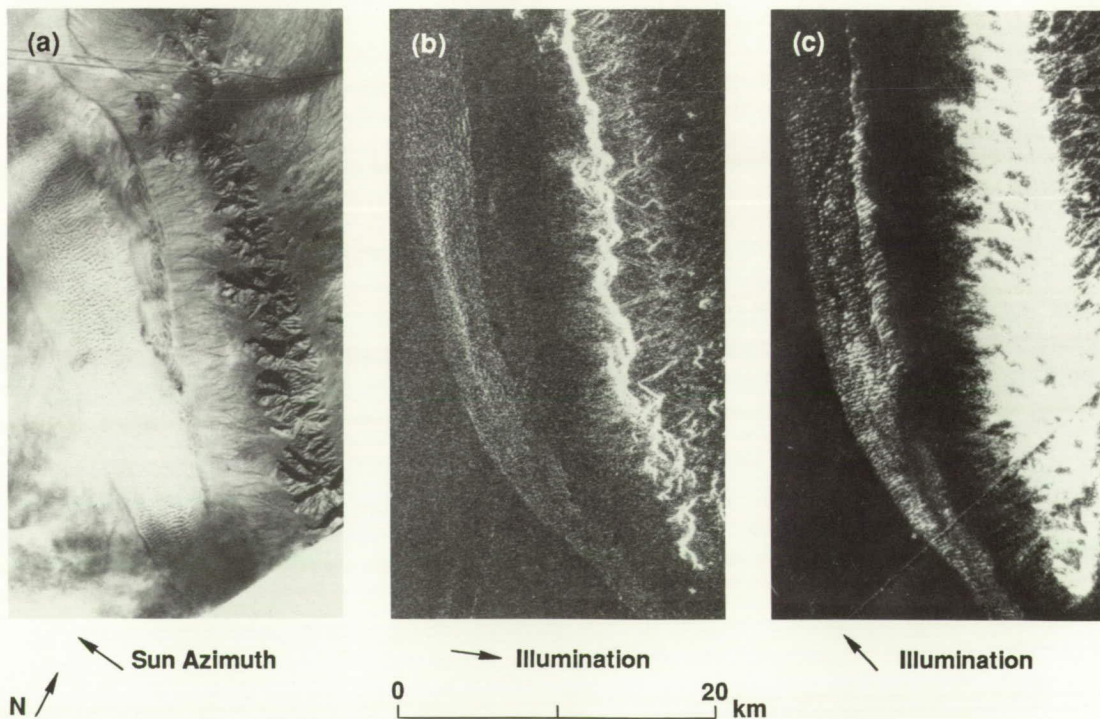
not sensitive to wavelengths over the region studied (75 to 2.25 cm).

In the interpretation of Magellan images, then, inferences about the presence or absence of eolian landscapes and their forms must be made very cautiously, with both the characteristics of the response of eolian material to radar and the viewing geometry constraints imposed by the Magellan orbit kept in mind.

Subsurface Imaging

Although the imaging of shallow subsurface features by radar has occurred on Earth, it is a rare phenomenon. Subsurface imaging may also occur in Magellan images of Venus. It is therefore useful to review the circumstances under which subsurface imaging can occur and the resulting response on the radar image. Since it is difficult or impossible to determine, based on a radar image alone, that imaged features are surface or subsurface, surficial processes that created now-buried landforms might be misinterpreted as current geomorphic processes. For example, if only SIR-A radar images of the Egyptian Sahara were available, the obviously fluvial landforms seen in the radar images might be mistakenly identified as the result of current geologic processes. In this environment, the overlying cover of eolian deposits is largely transparent to the SIR-A radar.

The possibility of subsurface radar imaging through dry surficial materials has been long known, but only recently demonstrated. Shuttle Imaging Radar-A images of Egypt and Sudan, acquired in November 1981, revealed a largely unknown fluvial landscape beneath an eolian cover (McCauley et al., 1982). In this case, subsurface radar imaging occurred on a regional scale. Figure 35 from Elachi et al. (1984) shows the dramatic contrast in landscapes perceived by radar and optical sensors in the Sahara. Imaging of subsurface features through dry fine-grained material has now been documented for Seasat, SIR-A, and SIR-B radar images of very arid areas (McCauley et al., 1982; Blom et al., 1984; Elachi et al., 1984; Berlin et al., 1985 and 1986; McCauley et al., 1986).

Necessary conditions

The conditions under which subsurface radar imaging can occur must be met simultaneously. (These conditions are reviewed in a geologic context by Blom et al., 1984.) The conditions are:

(1) The cover material must be radar smooth, fine grained, homogeneous, and not too thick. (At a 23.5-cm wavelength, 2 m of penetration have been documented; 4 to 6 m may be possible under conceivable conditions.)

(2) The cover material must be extremely dry. (Moisture content must be less than about 1%; this criterion is most difficult to satisfy on Earth.)

(3) The subsurface must be rough enough to generate backscatter.

Simultaneous satisfaction of these conditions on Earth is unusual; however, the sand sheets in hyperarid regions such as the Sahara are ideal. On Earth, the most limiting factor is the moisture constraint—few locations are as dry as the Sahara. (See "Response to Terrain" in *Synthetic-Aperture Radar Imaging*). On Venus, the surface temperature eliminates the moisture constraint, and fine-grained areas, if they exist, present the possibility of regional subsurface imaging as in the Sahara.

Variables in interpretation of Magellan images

Effects of grain size. For a radar signal to penetrate a medium without substantial attenuation, the particle size of the medium must be small relative to the wavelength, and the cover material must be homogeneous. Roth and Elachi (1975) found that losses from the scattering of radar signals were considerable for grain sizes larger than about one-fifth of the wavelength, whereas these losses were small for grain sizes less than about one-tenth of the wavelength. Because wavelength shortens upon penetration of a denser medium, the size of the particles in the cover material must be less than 0.8 cm to prevent scattering losses for an S-band system such as Magellan. Roth and Elachi (1975) also indicated that the presence of only a few particles exceeding the one-fifth-wavelength-size criterion for each radar resolution cell results in scattering sufficient to largely obscure subsurface features. Therefore, only those environ-

Figure 35. A 50 × 100 km area at the Egyptian/Sudanese border: (a) Landsat MSS (multispectral scanner) band 6 image; (b) SIR-A image. The Landsat image shows a landscape dominated by eolian processes. The Selima Sand Sheet blankets the underlying material to a few meters in thickness. Presently active dunes are visible as diagonal streaks near the image center. In contrast, the SIR-A image reveals a subsurface landscape carved by fluvial processes. The confluence of two large river channels is in the center of the SIR-A image. The dunes in the Landsat image have no expression on the SIR-A image.

N ↗   0 |_____|_____| 20 km   ↑ Illumination
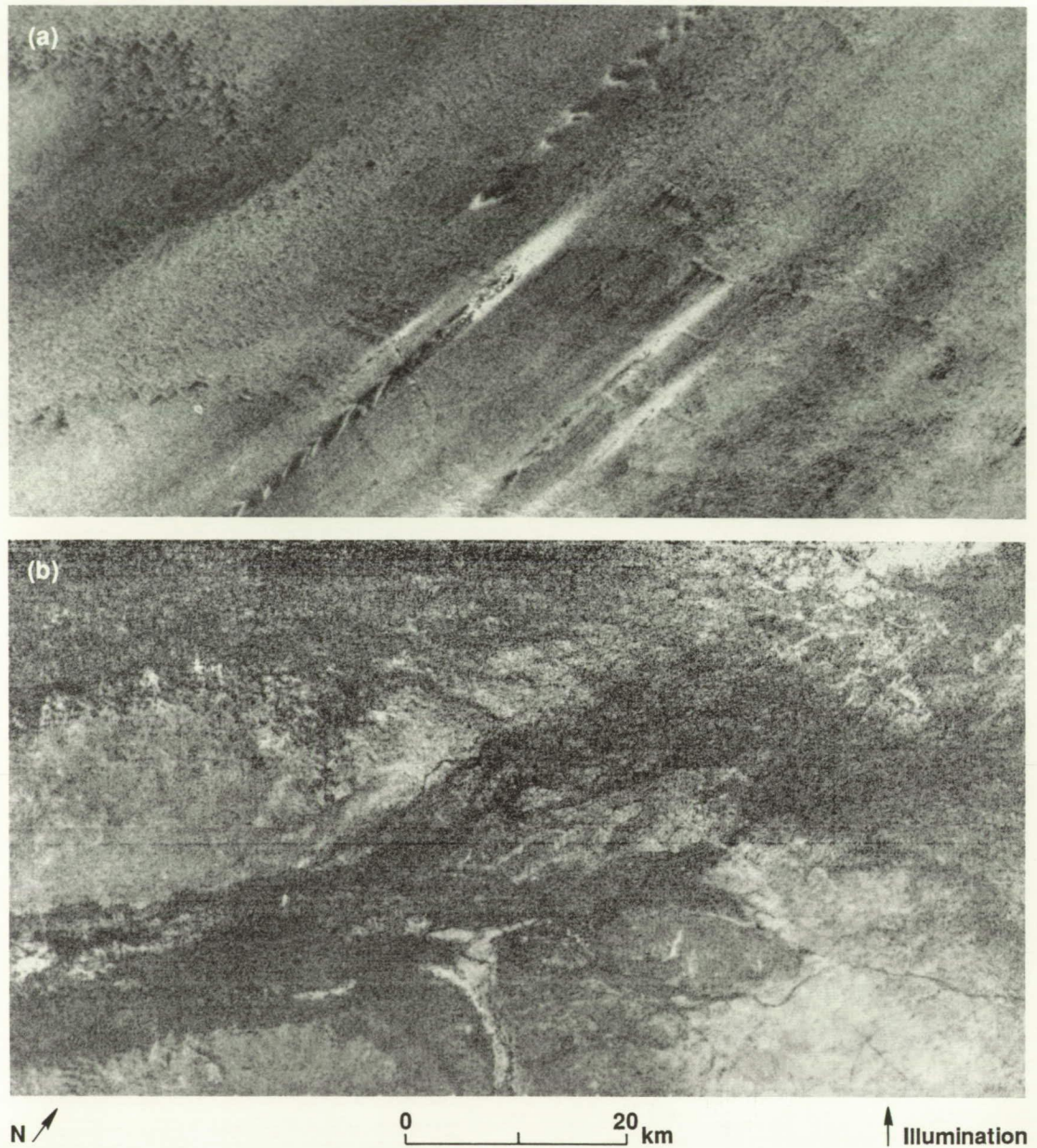
ments where geologic processes produce homogeneous fine-grained cover materials are favorable for the detection of subsurface features by radar. Landscapes dominated by eolian processes are most suitable for subsurface imaging. Grus from equigranular granitic rocks, volcanic ash, and fine-grained impact ejecta are other likely possibilities.

Look-angle considerations. Because the Magellan look angle will vary with latitude (see Figure 3 of *Synthetic-Aperture Radar Imaging*), a discussion of the effects of this variation on subsurface imaging is warranted.

The first consideration is summarized from Elachi et al. (1984). With respect to Magellan images, the important conclusion reached is that the rate of decrease in backscattered signal strength with increasing incidence angle is less for subsurface features than for the same features exposed at the surface. The cause is refraction at the surface interface, which reduces both the incidence angle and wavelength. Because radar backscatter curves have, typically, a steeper slope at smaller incidence angles, the consequence of a reduced incidence angle is an appreciable increase in echo strength. The wavelength reduction also increases potential echo strength because it allows satisfaction of the Rayleigh roughness criterion with a smoother subsurface reflector. Elachi et al. (1984) showed

that under extreme conditions, a subsurface feature can yield an actually stronger echo than that from the same feature exposed at the surface.

A second consideration is the possible interaction of the radar signal with a fine-grained cover over a rough substrate where cover thickness and slope vary. The following example refers to an eolian terrain, but it is applicable to other fine-grained material as well.

A terrain of low sand dunes on a flat sand sheet allows imaging of the surface dunes at small look angles and the subsurface features at larger look angles. The reasoning follows. Because sand dunes can be imaged only at look angles less than the angle of repose, dry dunes are seen only on images taken at small look angles, although a specular echo always occurs from their surfaces. A rough subsurface, however, will backscatter at all look angles. Hence, if the dunes and sand sheet are not too thick and otherwise favorable for subsurface imaging, the dunes would be imaged at small look angles and partially mask the subsurface image; at larger look angles, the rough subsurface would be seen but not the dune cover.

In Figure 36, the incoming high-look-angle radar beam (1) strikes the smooth sand sheet and is specularly reflected forward (thin arrowed line); no energy returns to the radar, and a dark image area results. In this case, the sand is too thick for the energy that penetrates the surface to be scattered from the subsurface. Energy that strikes the sand dune (2) is partially reflected forward off the smooth dune face and partially refracted into the sand. As this energy continues down, it strikes the rough substrate and is diffusely scattered. If the overburden is not too

thick, some of this energy could return to the surface and be received at the radar, resulting in intermediate brightness. At (3), rough material is exposed at the surface and a strong diffuse echo occurs, resulting in a bright image. In the next four cases ((4), (5), (6), and (7)), the incoming signal is at a lower look angle. In (4), the signal is specularly reflected off the face of the sand dune, and, because of the geometry, a strong signal is returned. Some of the signal penetrates the sand and is diffusely scattered off the rough substrate; this much weaker subsurface signal may also be recorded. Case (5) shows that even with a low look angle, geometry unfavorable to image formation can occur in sand dunes. Radar energy is here specularly reflected away from the sensor, and the backsides of the dunes are not imaged. Also, the combination of the dune and sand sheet is too thick here, and the signal that penetrates is not strong enough to reach the substrate. In case (6), some energy is partially reflected away at the sand sheet, and the rest is refracted and then diffusely scattered off the rough substrate. Here, the subsurface will be imaged, if the sand sheet is not too thick. Case (7) shows that the exposed rough surface is also a diffuse scatterer at low look angles, and a bright image results. In these different situations, the surface, subsurface, both, or neither may be detected in the resulting images.

Application to Magellan images

While geological processes on the surface of Venus are not well known at this time, recent reports by Pettengill et al. (1988) and Jurgens et al. (1988) indicate two factors of interest here. First, there are areas where the dielectric constant is very high compared to that of
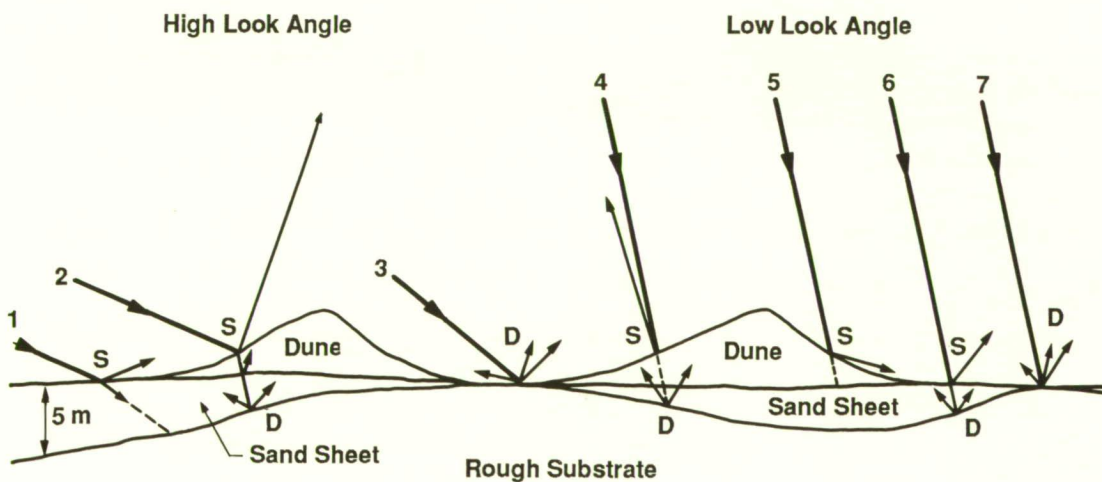

Figure 36. Possible circumstances under which the surface and subsurface could be variously detected in the same image (S = specular scattering, D = diffuse scattering).

61

ordinary rocks sampled in the laboratory by Campbell and Ulrichs (1969). The Venusian values are also much higher than those for Moon and Mars, for which much better knowledge of the surface is available. Second, the analysis of Pettengill et al. (1988) indicates that Venus is probably not substantially covered with soil or dust relative to the coverings on Mars and Moon. They state, "...most of the Venus surface is overlain, at most, by only a few centimeters of soil or dust..." If generally true, this would indicate a cover medium that would permit subsurface imaging because the "dust" may be radar transparent. Jurgens et al. (1988) suggest that some dark areas in their radar images of Venus may be mantled by fine-grained ejecta from impacts. Such fine-grained material, if it exists, might also be radar transparent, but subsurface features beneath it would not be detected because the other criteria are not satisfied.

Because of the high surface temperature on Venus, there will be no moisture to raise the dielectric constant, although both Jurgens et al. (1988) and Pettengill et al. (1988) demonstrate that there are areas of very high dielectric

constant. They suggest the phenomenon may be the result of a concentration of electrically conducting materials such as iron sulfides. Such areas have anomalously high radar reflectivity.

The point of emphasis is that a single radar image does not contain information sufficient to determine whether the radar is detecting surface or subsurface features. For example, if only SIR images of the Sahara were available, the fluvial features observed by McCauley et al. (1982) could have been misinterpreted as features of the current landscape, rather than those of a relict subsurface landscape. For an analysis of such terrain, multi-look-angle and multiwavelength radar images would be most desirable (the latter because penetration is a function of wavelength, and a short wavelength radar would penetrate less), but complementary visible and near-infrared images (such as those of the Landsat Thematic Mapper) would suffice because they view only the surface. Such images are not possible from an orbit around Venus because of the cloud cover. In interpreting the Magellan images, the possibility that subsurface rather than the surface features are revealed must always be kept in mind.

Tectonic Landforms

Introduction

Venus and Earth are regarded as sister planets because they are comparable in diameter, density, and proximity to the Sun (Appendix A). However, they have evolved along different paths and are known to have widely contrasting surfaces and atmospheres. Accordingly, the tectonic character of Venus is vitally important to comparative studies of planetary evolution among the terrestrial planets. On Earth, the concept of plate tectonics, which embodies segmentation, spreading, and recycling of the lithosphere through time, has provided the necessary intellectual framework for studying global tectonic history (Cox and Hart, 1986). Plate boundaries are highly mobile and much of Earth's surface is comparatively young. Observations over the past 25 years have indicated that planetary bodies with a diameter less than one half that of Earth (e.g., Mars and Mercury) are characterized by unsegmented, globally continuous lithospheres that expose an extensive record of early bombardment and early volcanism. The surfaces of these bodies are relatively old and stable.

Venus is thought to be a dynamic planet with a surface that is comparatively young (Basilevsky and Head, 1988). The density of impact craters observed by Soviet Venera 15 and 16 imaging radar in the northern hemisphere of Venus suggests that the age of the surface could range from about 4.5 Ma (Schaber et al., 1987) to about 1 Ga (Basilevsky et al., 1987; Ivanov et al., 1986), depending on the modeling assumptions used. However, the Venera images cover only 25% of the planet, and the cratering history of Venus is not known with confidence.

The global tectonic environment of Venus is uncertain. Low-resolution radar reflectivity and altimetry measurements in the Pioneer Venus experiment enabled the recognition of lowlands, rolling uplands, and highlands on a near-global scale (Masursky et al., 1980; Pettengill et al., 1980). Long, global-scale zones of disturbance have provided evidence of limited lithospheric extension in the Equatorial Highlands (Aphrodite Terra) (Schaber, 1982). Examination of the topography in western Aphrodite Terra led Head and Crumpler (1987) to suggest that the area displays the characteristics of oceanic divergent plate boundaries and is the site of crustal spreading on Venus.

Earth-based radar observations have provided comparatively high-resolution images of geologic structures in local areas. Banded terrain (ridge and groove) reported by Campbell et al. (1983) to represent tectonic folds and faults was interpreted by Kotelnikov et al. (1984) to indicate horizontal deformation.

Tectonic terrains mapped in northern and midlatitudes from the Venera 15 and 16 imaging missions (Basilevsky et al., 1986) reveal (1) large areas of plains that show flowlike features, streaks, grooves, and low ridges; (2) intersecting sets of ridges and grooves (parquet) known as tesserae; (3) subparallel ridges and grooves that extend over long, relatively narrow belts, but may occupy broad zones; and (4) concentric patterns of ridges and grooves (coronae) called ovoids. Basilevsky et al. (1986) concluded that terrestrial-style plate tectonics does not exist and also that ancient terranes are not observed. Using Venera image data, Crumpler et al. (1986) showed the presence of fold and fault structures in patterns suggestive of orogenic belts. More recently, an interconnected transpolar disruption zone about 60,000 km in length has been reported by Kozak and Schaber (1989). Though this feature is similar in scale to Earth's interconnected oceanic ridge system, it is reported to be markedly different in other respects.

Radar reflectivity, altimetry, and image data obtained to the present have suggested both horizontal and vertical movements on the surface of Venus. The general tectonic style in the area imaged by the Venera missions is quite different from that on present-day Earth and the smaller terrestrial planets. Few features on Venus

compare directly to the essential plate tectonic elements on Earth. High-resolution images (100 to 200 m) and global coverage are needed to determine the overall character, distribution, and tectonic origin of landforms on Venus, and to distinguish volcano–tectonic features from impact craters. The advent of Magellan radar coverage will provide continuing impetus to the search for a paradigm that explains the evolution of the Venusian surface.

Tectonic Styles

Tectonic landforms are underlain by structural features produced by crustal deformation. The landforms result from differential erosion acting on structures produced by endogenic processes of regional extent. Different styles of regional deformation tend to reflect pronounced contrasts in tectonic settings. However, similarities among certain types of deformation packages, such as compressional folds and thrusts or large-scale strike-slip faults, enable us to extrapolate from well-studied areas to lesser-known ones. Spaceborne images offer a synoptic basis for observing and interpreting regional structural relations from tectonic landforms.

Radar imaging of Earth's tectonic landforms is restricted to surface features of the continental crust. Plate tectonic features of the oceanic crust, such as ridges, oceanic transforms, and trenches, are underwater and not perceptible to radar. Radar images reviewed here are arranged according to tectonic style, with illustrations taken from prominent fold belts, accreted terranes, a boundary transform zone, and comparatively stable continental plate interiors. These images were obtained by Seasat SAR and Shuttle Imaging Radar (SIR).

Fold belts

Numerous fold belts are distributed in linear zones that coincide with mountain chains in the continental crust. In the nineteenth century, the deposition and deformation observed in the central Appalachian fold belt of eastern North America provided the basis for the concept of the geosyncline (Hall, 1859). Like many orogenic belts, the Appalachians have a long and complex history that includes several widely separated episodes of deformation. In the framework of plate tectonics, the Appalachians provide the type example for the closing and reopening of an ocean (Wilson, 1966). The thrust sheets that characterize Appalachian tectonics are mainly décollements in which older sequences have overridden younger rocks. Imbricate thrust slices are bounded at the surface by high-angle reverse faults that change to low-angle thrusts at depth. Some effects of the continental collision between the African and North American plates that accompanied the closing of the Iapetus (pre-Atlantic) ocean in the Alleghenian (Permian) orogeny are illustrated in the deformation of the valley-and-ridge portion of the fold belt. Thrust slices are exposed at the surface in the south. In the central portion, the thrusts are buried by kilometers of moderately to strongly folded layered rocks (Gwinn, 1964). The contrasted topographic expression of thrust faults and folded terrane is clearly demonstrated in the different landscapes of the southern (Figures 37 through 40) and central (Figures 41 and 42) portions of the Appalachian Valley and Ridge Province.

Southern Appalachian Valley and Ridge Province, U.S.A. In the southern Appalachians, the valley-and-ridge geomorphic province is dominated by reverse faults that flatten at depth to form low-angle bedding plane thrusts and by folds not connected to the basement. To the north, the Cumberland Plateau is underlain by relatively undeformed, gently dipping strata. Seasat SAR coverage of a portion of the province is shown in Figures 37 and 38. The Pine Mountain Thrust carried a thin sheet of rocks northwestward over the relatively undeformed Cumberland Plateau for a distance estimated at 6.4 km (Harris and Milici, 1977). The terrane is divided by major thrust faults into northeast-trending slices, with strata folded and faulted in a regular fashion. The topographic trend parallels the structural strike. The unconnected structure of the basement has been inferred from magnetic and gravitational data (Watkins, 1964). Subsequent work has demonstrated the existence of large crystalline detachments (Cook et al., 1979; Harris et al., 1981).

Structural mapping is feasible from the Seasat SAR images where the structures
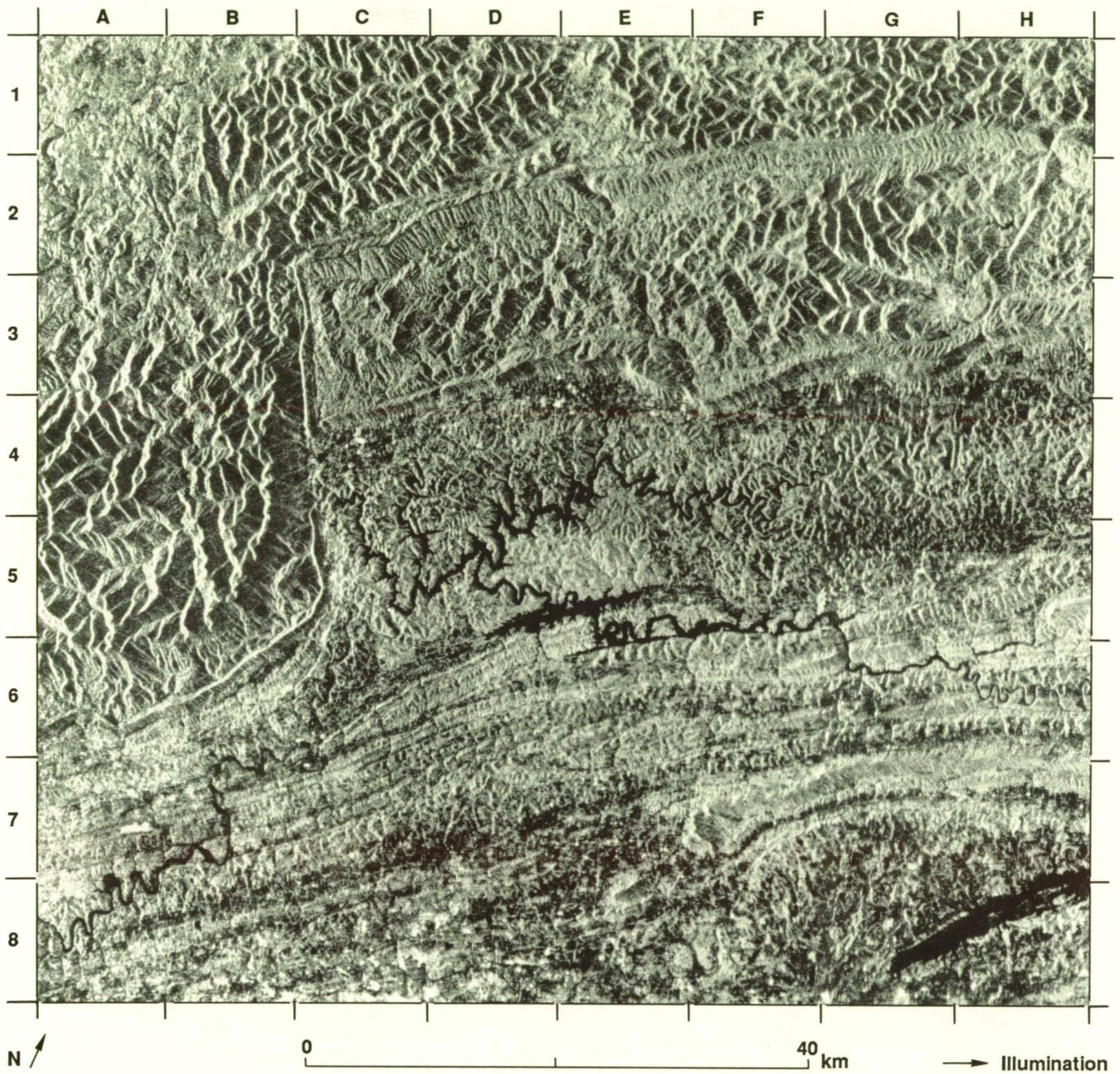
Figure 37. Seasat SAR image of thrust-faulted, valley-and-ridge terrane showing the Pine Mountain Thrust Sheet, southern Appalachians, U.S.A. Imaging azimuth is 67.5 deg.

N

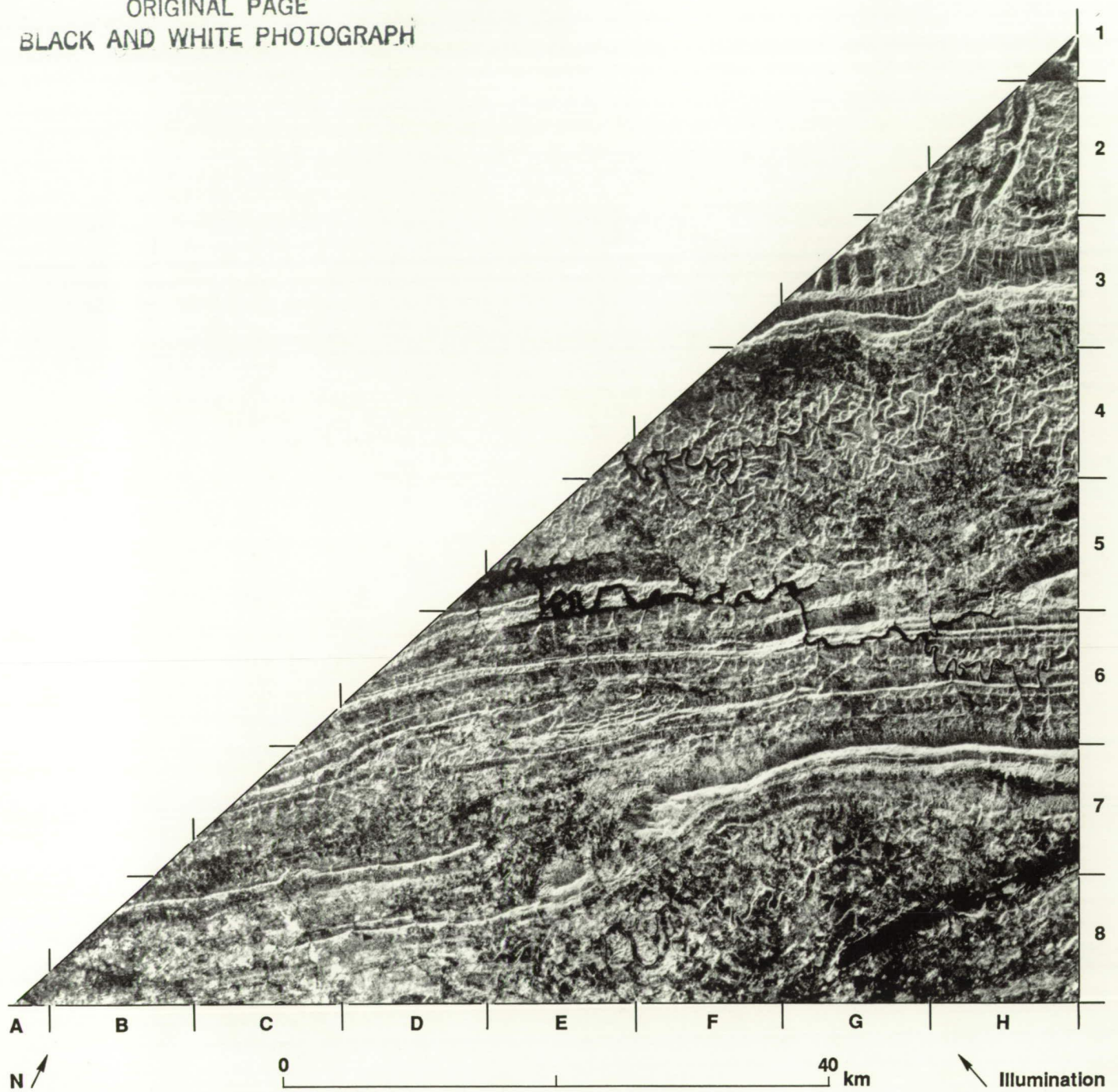0   40 km

⟶ Illumination

Figure 38. Seasat
SAR image
corresponding to
part of the valley-
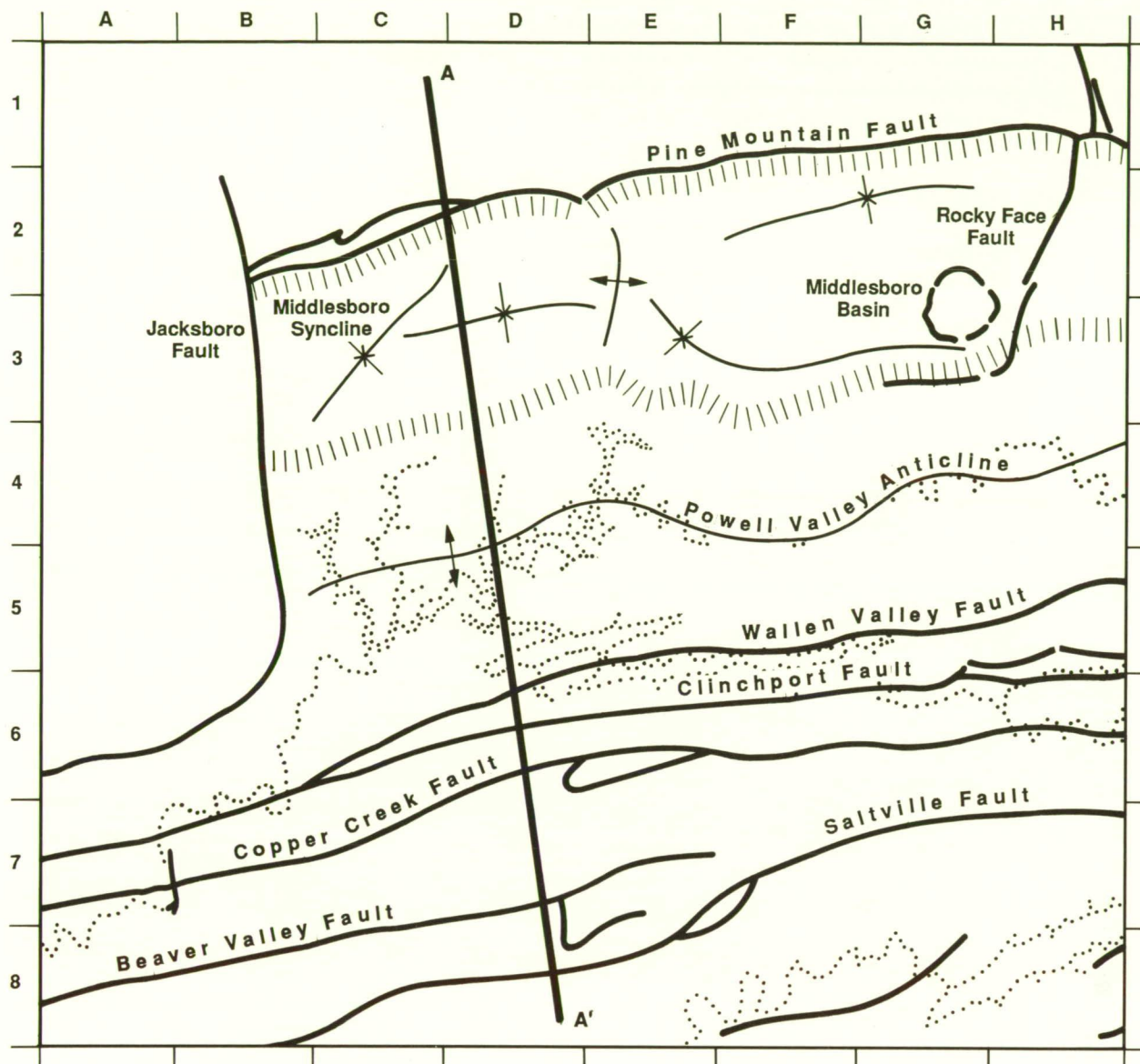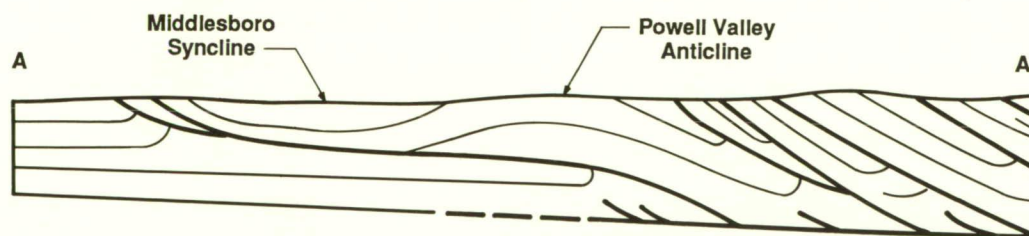and-ridge terrane in
Figure 37. Imaging
azimuth is 292.5 deg.

Figure 39. Simplified structural sketch map and schematic cross section of the area covered by Seasat SAR in Figure 37 (modified from Harris and Milici, 1977).

67

(Figure 39) can be inferred from the geomorphology. In this terrane, the majority of erosional features that are responsible for extensive linear changes of tone and texture on the images are structurally controlled (Ford, 1980).

Pine Mountain is a major linear feature that exposes a northwest facing scarp (Figure 37, C2 to H1). The extensive linear to curvilinear trace of Cumberland Mountain shows a southeast facing scarp (C4 to H3), the base of which marks the north limb of the Powell Valley Anticline. A broad synclinal structure is apparent from the pattern of small flatirons that face each other across the dip slopes of the Pine and Cumberland Mountains (Middlesboro Syncline). Additional structures evident within this block include the Rocky Face Fault (H1 to H2) and the fault-bounded Middlesboro Basin (G2/G3 to H2/H3). The basin structure (about 6 km in diameter) has been described as a probable meteorite scar or astrobleme (Englund and Roen, 1962) and later confirmed as such from the discovery of shatter cones in the central uplift portion of the structure (Dietz, 1966).

Many extensive topographic lineaments correspond with major faults. The Jacksboro and Pine Mountain Faults are among the more pronounced examples that give a distinctive outline to the terrane in this scene. The high-angle truncation of the Pine Mountain Thrust Sheet by the Jacksboro Fault suggests a wrench or tear origin for this fault. Repetition of distinctive linear topography in the successive parallel to subparallel ridges and valleys denotes repetition of the underlying lithologies by faulting (Figure 39). It also denotes the effects of differential erosion on beds of differing hardness. Corresponding repetition of distinctive image textures on the Seasat SAR images allows the faults to be located. The low-angle truncation of the Wallen Valley Thrust by the Clinchport Thrust is clearly evident in Figure 37 at the base of the junction between B6 and C6. The intersection of these thrust faults marks a hinge between regional directions of structural strike— about N50°E to the west and N60°E to the east. Offset ridges and abruptly truncated ridges typically indicate high-angle faulting (for

example, the termination of Beaver Ridge at the right side of D7).

Minor geomorphic lineaments consisting of linear valley segments and stream channels less than 10 km long are widespread. Few of these features have been mapped as faults or fracture traces, though some are adjacent to or aligned with major fault structures. The Seasat SAR images (Figures 37 and 38) show short, aligned, and en echelon valley segments up to 3 km long that parallel the Rocky Face Fault and extend far north and south of its mapped trace. A linear north-trending magnetic gradient in the basement lies parallel to this fault and extends south across the Powell Valley Anticline. This gradient has been interpreted as reflecting a pre-Appalachian structural grain in the basement (Watkins, 1963 and 1964) . The close coincidence of the small topographic lineaments aligned with the Rocky Face Fault and observed on the Seasat SAR images probably reflects this subsurface structural grain.

Discontinuous short lineaments mapped from the SAR images are aligned with the Jacksboro Fault and extend tens of kilometers southeast of its surface trace. Gravity and magnetic discontinuities that are also aligned in this direction have been cited as evidence for subsurface extension of the Jacksboro Fault in the basement (Watkins, 1964). The lineaments mapped from the SAR images may represent fracture traces associated with the compressive stresses that gave rise to the Jacksboro Fault.

Strong local brightness variations occur within corresponding areas of the two images (Figures 37 and 38). Some surfaces that appear bright in one illumination azimuth are dark or obscure in the other. Examples are clearly evident along the ridge-and-valley terrane. Where the ridges and valleys are illuminated parallel to the strike (Figure 37) there is little image contrast between them. Correspondingly, there is pronounced highlighting of the ridges and clear discrimination of the intervening valleys where these features are illuminated across strike (Figure 38). This example illustrates one of many conditions under which radar response is strongly directional. The valleys have level to gently undulating surfaces with slopes that are mostly less than 7 deg. The ridges and mountains have steep slopes, commonly 20 to 35 deg and up to a maximum of about 40 deg. Bright image tones generally
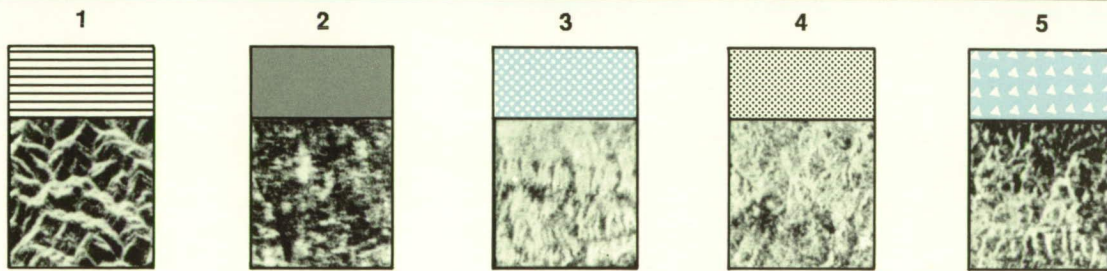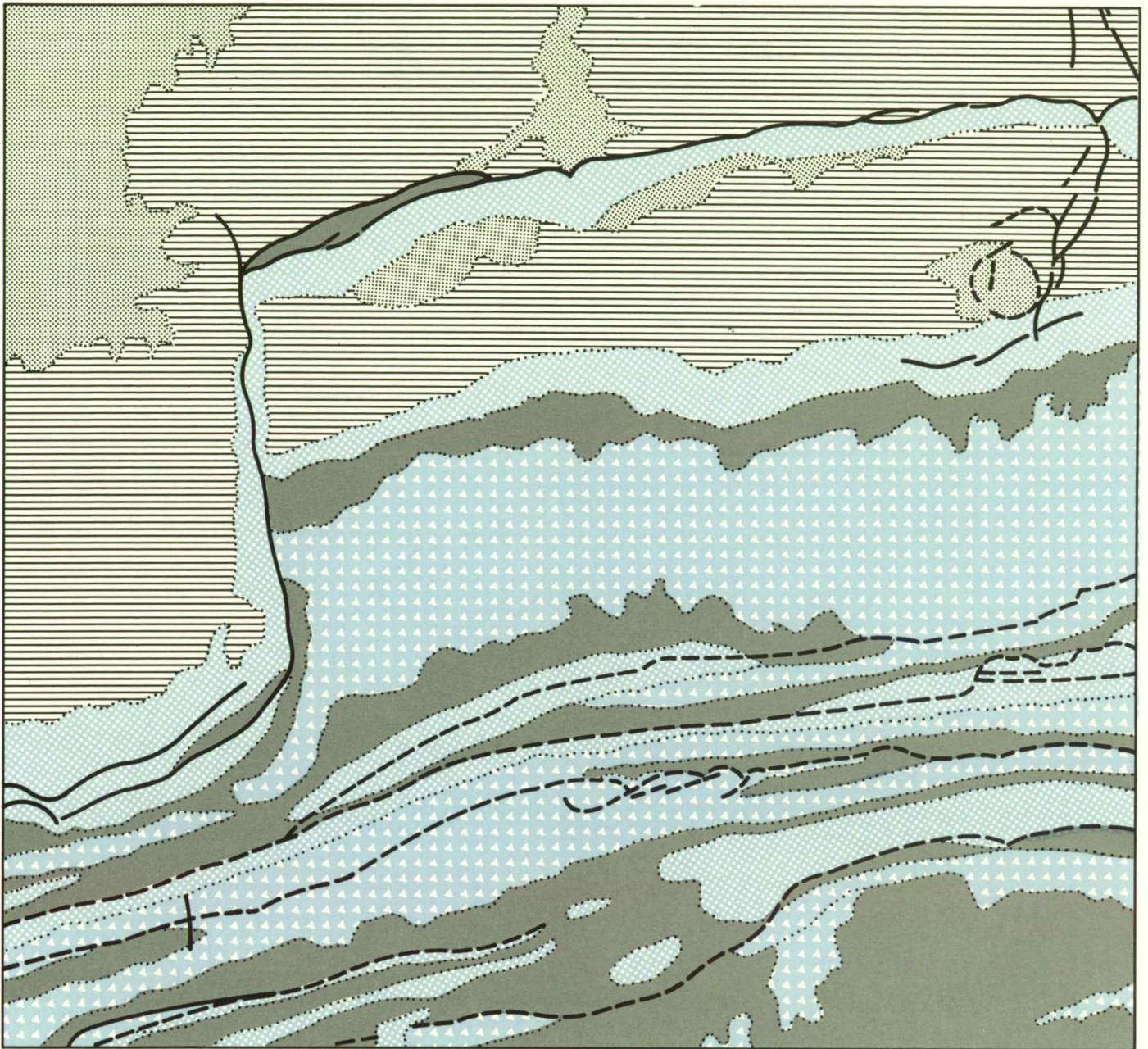
Figure 40. Image texture map from the Seasat SAR image in Figure 37. Texture units correspond to major lithologic associations: (1) sandstone/shale/siltstone (massive), (2) clay–shale/limestone, (3) conglomerate/sandstone/shale, (4) sandstone/shale/ siltstone (thin-bedded), (5) dolomite/chert/crystalline limestone (Ford, 1980).

Figure 41.
Seasat SAR
image of
folded
valley-and-
ridge terrane
in central
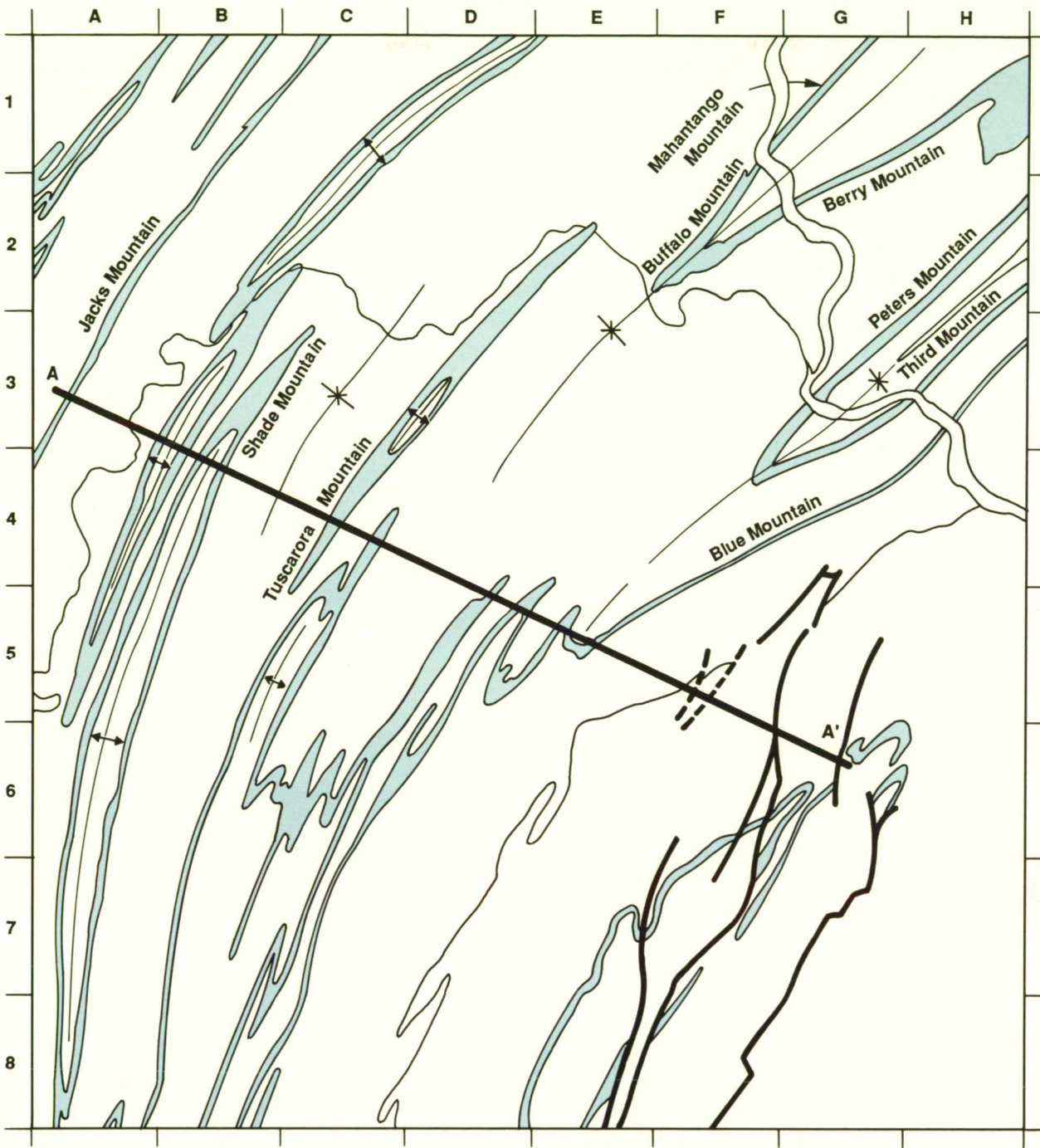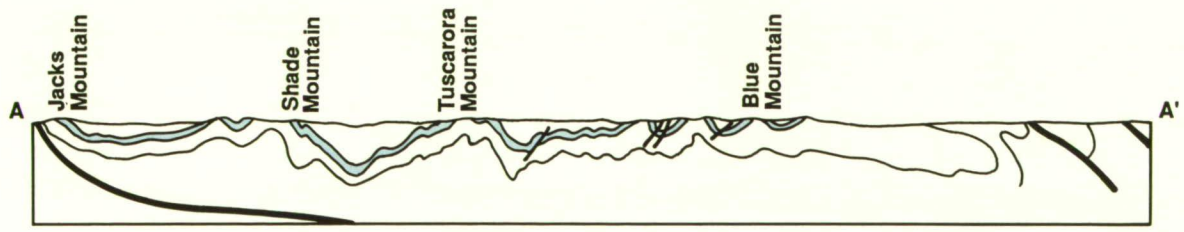Pennsylvania.

N

◄── Illumination

0   40 km

Figure 42. Simplified structural sketch map and schematic cross section of the area covered by Seasat SAR in Figure 41.

Ridge-Forming Strata, Including Tuscarora, Pocono, and Pottsville Formations

Anticlinal Axis With Plunge Direction

Synclinal Axis

0   40
|_____| km

71

Figure 43. Location and plate-tectonic setting of Sibi Trough, Pakistan. Bold lines denote plate boundaries. Arrows show relative motion between plates. Toothmarks indicate direction of thrusting. (Modified from Jacob and Quittmeyer, 1979.)
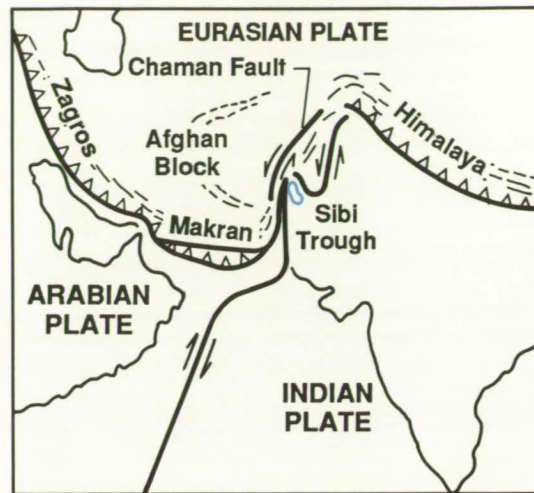
represent strong radar backscatter from sloping surfaces or foldover of slopes that face toward the illumination vector (foreslopes). Some dark tones represent weak returns from backslopes. Foreslopes in one illumination azimuth appear as backslopes in the other. On a scale large enough to be independent of this effect, however, distinctive image textures can be discriminated in corresponding areas on the two images.

In many areas of the Valley and Ridge Province, lithologic mapping is facilitated by studying the topography (Swingle, 1973). Image textures that are broadly representative of topography can be discriminated and mapped from the Seasat SAR images (Figure 40). The types of topography reflected in the image textures correlate reasonably well with distinct bedrock associations and bulk lithologic sequences, though they do not identify individual lithologies or stratigraphic units.

Central Appalachian Valley and Ridge Province, U.S.A. In the central Appalachians, the Valley and Ridge Province exposes a sequence of long narrow ridges and wide open valleys that extend in broad arcuate form over 600 km. A Seasat SAR image of this terrane in central Pennsylvania is shown in Figure 41. Major ridges are situated 5 to 15 km apart and extend for tens of kilometers in length. Structurally, the terrane consists of numerous elongate subparallel plunging anticlines and synclines

with fewer thrusts than those in the southern Appalachians (Figure 42).

The exact nature of the structures can be inferred in the image (Figure 41) from the bedding attitudes in successive ridges and from the shape of the noses formed by the convergence of the paired limbs. Owing to the steep dips of the limbs, most anticlines appear as narrow slender features with long sharp noses (e.g., Shade Mountain, Figures 41 and 42, C3 through A8). The noses denote axial plunge directions. With more gently dipping limbs, most synclines appear as wide, more open features that have shorter and more rounded noses (e.g., Mahantango-Buffalo and Berry Mountains, F2 and G1 to H1). Major ridges are held up by resistant sandstones and conglomerates of the Tuscarora, Pocono, and Pottsville Formations. Minor ridge offsets indicate high-angle cross-cutting faults. The ridges are homoclinal, each representing a single limb of a larger structure. Incipient breaching of an anticline beneath Tuscarora Mountain is evident in Figure 41 at D3. In one instance, a ridge (Third Mountain) is situated centrally in the core of a plunging syncline (H2).

Sibi Trough, Pakistan. Profound and large-scale deformation of the lithosphere has occurred in localities where there is a history of collision and suturing of continental plates. This is exemplified in south Asia by the collision and suturing of India and Eurasia in the mid-Tertiary (Molnar and Tapponnier, 1975 and 1977; Peltzer and Tapponnier, 1988). Where the collision was oblique, such as occurred in western Pakistan adjacent to Afghanistan, it has given rise to great structural complexity. Major strike-slip faults terminate and interact with thrusts and reverse faults in zones of convergence. Such interactions are well marked in Pakistan, where the Chaman transform zone connects the Makran and Himalayan convergence zones (Figure 43). Combined eastward thrusting and sinistral strike-slip along north-south oriented faults have been interpreted to indicate northwest motion of the Indian subcontinent relative to the Afghan Block (Lawrence et al., 1981).

The SIR-A image (Figure 44) covers the Sibi Trough in western Pakistan. This area is located about 100 km east of the Chaman Transform. The trough is situated at the western extremity of the Indian subcontinent in a zone of
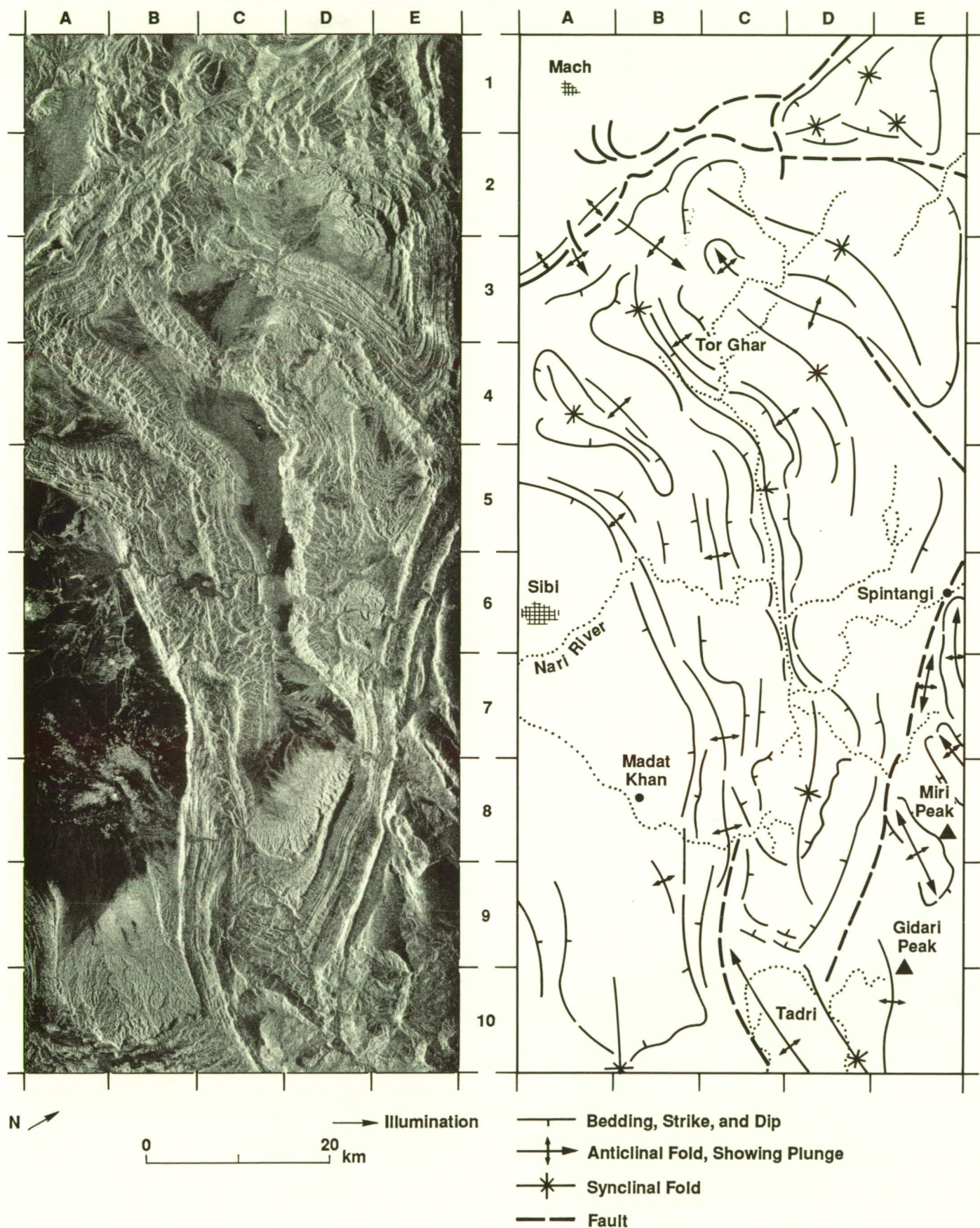
N

0   20 km

→ Illumination

── Bedding, Strike, and Dip

Anticlinal Fold, Showing Plunge

Synclinal Fold

─ ─ Fault

Figure 44. SIR-A image of Sibi Trough,
Pakistan, with simplified structural sketch map.

73

compression. The tectonic effects of collision are marked here by thrusts and by folds that show abrupt changes of orientation over short distances. Broad synclinal basins are separated by narrow, tightly folded anticlines. Bedding patterns on the image outline the strike and dip of the rocks. Moderate to gently inclined strata in the limbs of synclines show patterns of flatirons from which the dip directions are inferred (e.g., Figure 44, B4 to C7). Narrow outcrop patterns indicate steeply dipping to vertical or overturned beds. Bright radar returns from the antidip slopes of tightly folded anticlinal limbs are pronounced about 10 km northwest of Sibi and at Tor Ghar (A5 to B5 and B3 to C4). A few kilometers west of Spintangi, vertical to overturned beds that extend southeast for about 20 km appear as a narrow saturated band on the image.

North and east of the Sibi Trough, older rocks are exposed in the cores of doubly plunging folds. In contrast to the Sibi Trough, the folds to the north and east show broad anticlines with narrow, tightly folded synclines. Deformation was Late Tertiary to Recent. Separation of this area from the Sibi Trough is distinctly marked along a fault trace that extends on the image from D9 to E6. Examples of the broad anticlines are apparent from Galusha Hill, near Spintangi, to Gidari Peak (E6 to E9). Faults oriented approximately north-south in the upper left of the image (A3 to D1) mark the western limit of left slip in the Chaman transform zone.

Accreted terranes

The Paleozoic and Early Mesozoic rock sequences of much of western North America, including about 95% of Alaska, have widely divergent lithotectonic origins and, in many places, are juxtaposed along fault boundaries. They have been interpreted as slabs of crust added to the preexisting continent by piecemeal accretion during Late Mesozoic and Cenozoic time (Coney et al., 1980; Churkin et al., 1982;

Jones et al., 1983 and 1987). The crustal slabs are referred to as terranes. Most of the terrane boundaries are known or suspected faults, but the recognition of an accretionary origin resulted from the observation of pronounced discontinuities in lithology and paleobiology combined with striking contrasts in paleomagnetism across fault boundaries.

The potential for discriminating accretionary tectonic landforms on images with Magellan characteristics and comparison with corresponding images having Venera characteristics has been investigated by Arvidson et al. (1988). Seasat SAR mosaics of an area of eastern interior Alaska with simulated Magellan and Venera image characteristics were evaluated and compared for relevant geologic information content. The simulated parameters included spatial resolution, number of looks, system signal-to-noise ratio, and incidence angle. The major contrast between the simulations is the spatial resolution, which is 10 to 15 times higher for Magellan than for Venera.

Eastern interior Alaska, U.S.A. Seasat SAR mosaics of an area of accretionary terranes in eastern interior Alaska are shown with simulated Magellan resolution (~120 m) in Figure 45 and with simulated Venera resolution (~2000 m) in Figure 46. Tectonized highlands are located in four distinct regions from north to south. They include (1) the southern foothills and the Philip Smith Mountains of the Brooks Range (Figures 45 and 46, C1/D1 to C2/D2), (2) the Kokrines Hills-Ray Mountains-Hodzana Highland (A4 to C2), (3) the Yukon-Tanana Upland (B4/C4 to C5/D5), and (4) the northern foothills and mountains of the Alaska Range (B6 to C5 and C6). The highlands are underlain by a wide range of complexly deformed, predominantly Precambrian through Lower Paleozoic metasedimentary and metaigneous rocks (Beikman, 1980, and sources quoted therein). The generalized lithology and the distribution of lithotectonic terranes in the area covered by the SAR image simulations are shown in Figure 47.

Both the Magellan and the Venera image simulations (Figures 45 and 46) show the dominance of steep slopes up to 30 deg and local relief up to 1000 m in the highland areas. The radar sensitivity to slope distorts the topography in a strongly directional fashion and obscures most of the other surface characteristics in the

highland areas. Though it is possible on both simulations to observe broad tectonic fabrics imprinted on the highlands on a scale of tens of kilometers, only the Magellan simulation shows sufficient detail to distinguish structures and drainage networks on a scale of hundreds of meters. For example, the mountains in the north have a blocky structure with dominantly east-trending facets and smooth valleys up to 10 km wide that widen southward in the direction of drainage. They follow linear and broadly arcuate traces with a symmetry that appears to be structurally controlled. The outline suggests a broad structural antiform with an east-west axis, accompanied by plutonic intrusion. The U-shaped form of the wide valleys seen at the simulated Magellan resolution strongly suggests glacial erosion. These valley forms are not evident at the simulated Venera resolution.

The structural relations among major accretionary terranes recognized in the area are shown in Figure 48. Though the Angayucham and the Tozitna Terranes are bounded by major faults and separated by the intervening Ruby Terrane, they contain grossly similar oceanic rock associations that give rise to broadly comparable landforms. Thus, discrimination between the Angayucham and Tozitna Terranes is not possible on either of the image simulations (Figures 45 and 46) owing to the absence of well-defined topographic characteristics or unambiguous boundaries. Numerous radar lineaments that correspond with previously mapped faults, some of which extend for over 100 km, are seen in the Magellan simulation. However, the lineaments in many cases do not correspond with terrane boundaries.

In addition to accretionary terranes, the area includes postaccretionary Cretaceous plutons, which are widely distributed from the Ray Mountains through the Hodzana Highland to the Brooks Range, and younger relatively unde-formed sedimentary basins, especially in the Yukon Flats and Tanana Lowlands (Figure 47, C3 to E3 and B5 to C5). These postaccretionary features cannot be discriminated from the accretionary terranes based only on their topography in images.

The basic observations for recognizing accretionary terranes are mostly not susceptible to measurement or verification by radar or other forms of remote sensing. Specifically, confusion arises in identifying accretionary terranes on the images because (1) different terranes that have grossly similar lithologies may appear to be texturally similar (compare Angayucham and Tozitna Terranes), (2) the traces of low-angle thrust faults that mark some terrane boundaries are commonly not distinguishable in images, (3) the fault traces that are distinguishable do not necessarily represent terrane boundaries, and (4) the distinction between lithotectonic terranes of accretionary origin and younger nonaccretionary plutons or sedimentary rock bodies of postaccretionary origin cannot be made from image data alone. In view of the above observations, there is little possibility of detecting and correctly identifying lithotectonic accretionary terranes on radar images of Venus.

Continental boundary transforms

Plate tectonics involves major strike-slip faulting. Some of the longest strike-slip faults occur as boundary transforms between plates that move parallel to the boundary. A remarkable feature of such faults is their disregard of gross physiographic features such as mountains and plains and their pronounced linearity across such features over extended distances. A review of the principles, concepts, and tectonic implications of strike-slip faults has been given by Sylvester (1988). Because the San Andreas Fault is the most extensively studied strike-slip fault, it has been the source of many ideas relating to strike-slip tectonics. The San Andreas Fault is a ridge/ridge transform that extends for a distance of about 1000 km and marks the boundary between the North American and the Pacific Plates. It represents a deep discontinuity in Earth's crust that extends down to the lithosphere. At the surface, it forms a nearly continuous extension of roughly parallel fractures distributed in a band that varies in width from a few tens of meters up to 10 km (Crowell, 1975). Strike-slip faulting produces distinctive geomorphic features at regional and local scales that stand out on spaceborne radar images.

Figure 45. Seasat
SAR mosaic of
eastern interior
Alaska at simulated
Magellan resolution.

A · B · C · D · E

153° · 150° · 147° · 144°

1 · 2 · 3 · 4 · 5 · 6

68° · 67° · 66° · 65° · 64°

0 · 200 km

Illumination

Figure 46. Seasat SAR mosaic of eastern interior Alaska at simulated Venera resolution.
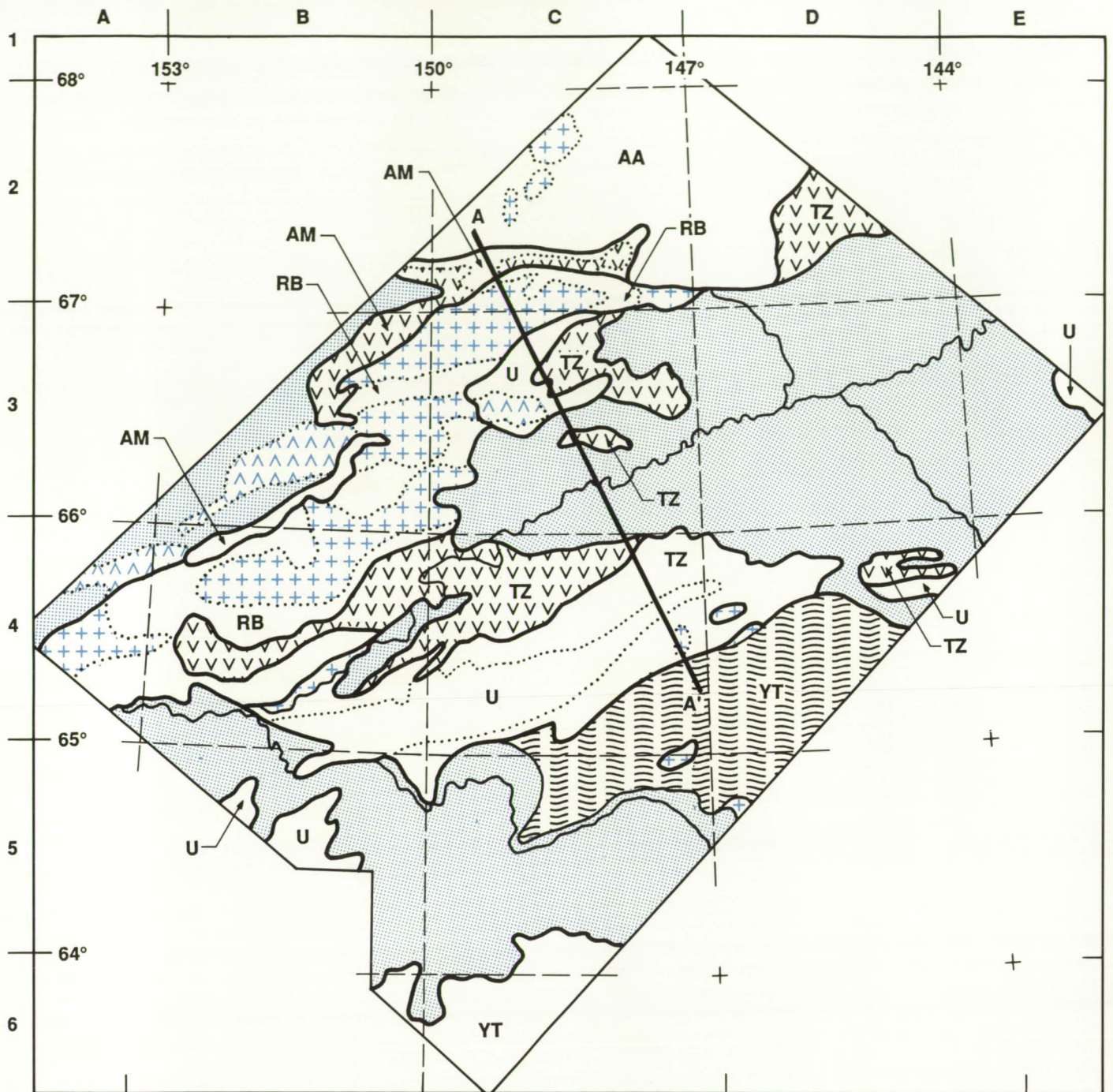
Lithology

⬚ (stippled)	Cenozoic and Upper Cretaceous Sedimentary Deposits
∧∧∧∧	Tertiary and Cretaceous Volcanic Rocks, Felsic
∨∨∨∨	Jurassic to Permian Volcanic Rocks, Mafic
++++	Cretaceous Plutonic Rocks, Felsic
(blank)	Paleozoic Sedimentary and Metasedimentary Rocks
≋≋≋	Paleozoic and Precambrian Metasedimentary and Metaigneous Rocks

Terranes

AA	Arctic Alaska
AM	Angayucham
RB	Ruby
TZ	Tozitna
YT	Yukon-Tanana
U	Undifferentiated

0   200 km

Figure 47. Generalized lithology and distribution of lithotectonic terranes in the area covered by Seasat SAR simulations (Figures 45 and 46). Bold lines denote terrane boundaries. Nonaccretionary rock bodies are shown in blue. Complex and fragmentary terranes are not differentiated. (Modified from Arvidson et al., 1988.) A schematic cross section is given in Figure 48.

Figure 48. Schematic cross section (from Figure 47) showing Angayucham (AM) and Tozitna Terranes structurally above Ruby Terrane (RB) (modified from Churkin et al., 1982; Jones et al., 1986).

Southern California, U.S.A. The Seasat SAR image mosaic in Figure 49 shows segments of the major crustal blocks and structural features that make up the landscape in southern California. Most of the landforms in this area are the direct result of tectonic processes. Major fault structures that give rise to prominent topographic features on the image are shown in Figure 50. The dominant structure is the San Andreas Fault. In this scene, it extends for about 320 km from the junction of the Garlock Fault (Figure 49, A2), across the east-west trending Transverse Ranges (A3 to C4), to its termination east of the Salton Sea (D6). The fault separates the Los Angeles Basin, Coastal Ranges, and Salton Trough to the west and south from the Mojave Desert Block to the east.

The Garlock Fault separates the Mojave Desert Block from the Sierra Nevada and the Basin Ranges (including Death Valley and Panamint Valley) to the north. This major fault, which extends from the San Andreas Fault to the south end of Death Valley (A2 to D2), has been described as an intracontinental transform (Davis and Burchfiel, 1973). Seismic studies suggest that it is a relatively shallow structure that transforms to a horizontal shear zone at a depth of about 10 km (Serpa, 1987).

The linear to curvilinear traces of the San Andreas and the Garlock Faults form large-scale topography that is strongly enhanced on the radar mosaic (Figure 49). The San Andreas Fault trace bends notably at localities where other faults intersect it at a high angle (e.g., A2 and C5). Extensive northwest-southeast oriented linear features in the central Mojave area denote the traces of strike-slip faults within the Mojave Desert Block. These faults are part of a complex regional network of right shear that connects the

Death Valley region with the San Andreas Fault system (Dokka and Travis, 1989).

West of the San Andreas Fault, the image shows extensive linear topography and alignment of landforms over distances upward of 20 km. These features mark the traces of faults in the San Jacinto and the Elsinore Fault zones (Figure 50). The San Jacinto Fault zone is thought to represent a major component of braided subparallel faults that occur toward the termination of the San Andreas Fault system. The fault system is transformed at its south end to a spreading rift as the structure passes southeast into the Salton Trough and the Gulf of California spreading center (Crowell, 1979; Elders et al., 1972; Robinson et al., 1976). Further west, the Elsinore Fault zone displays a narrow linear trough that extends for about 40 km toward Lake Elsinore. The right-stepping fault strands at this locality have given rise to a pull-apart basin (Mann et al., 1983) in which the lake is situated (Figure 49, box 1).

When opposing blocks in a fault system move in strike-slip, long thin slivers of rock may subside between parallel or en echelon fault strands to form closed depressions, or they may rise to produce pressure ridges. Thus active strike-slip faulting is expressed by the presence of comparatively small-scale youthful geomorphic features aligned along a fault zone and by offset drainage channels across the fault. Conclusive evidence for strike-slip faulting is provided by offset scarps that face in opposite directions across a fault plane. Associated small-scale geomorphic features such as closed depressions, troughs, sag ponds, and various types of linear ridges and valleys have been described and defined by many workers (e.g., Sharp, 1954; Wesson et al., 1975; Crowell, 1979;

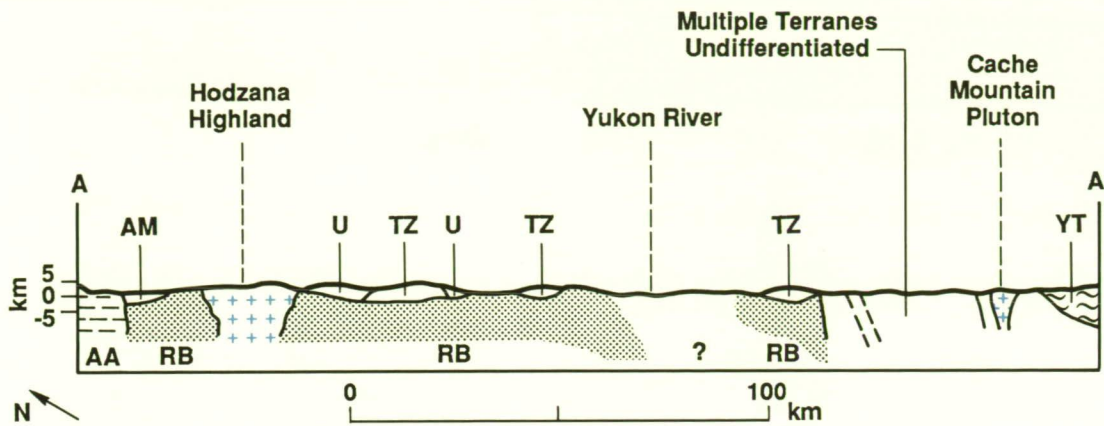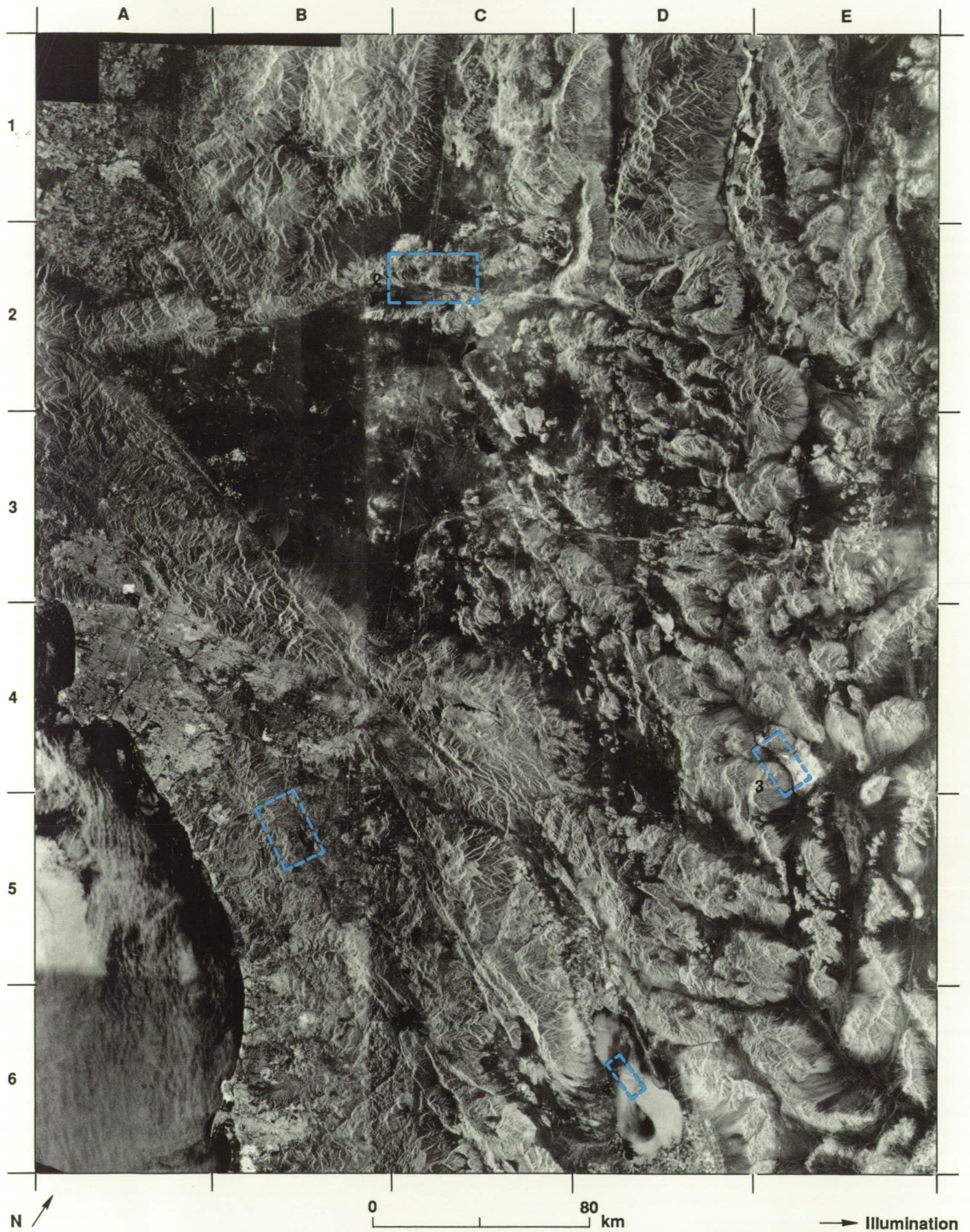*Figure 49. Seasat SAR mosaic of southern California. Areas within boxes 1 through 4 illustrate comparatively small-scale, fault-related features described in the text.*
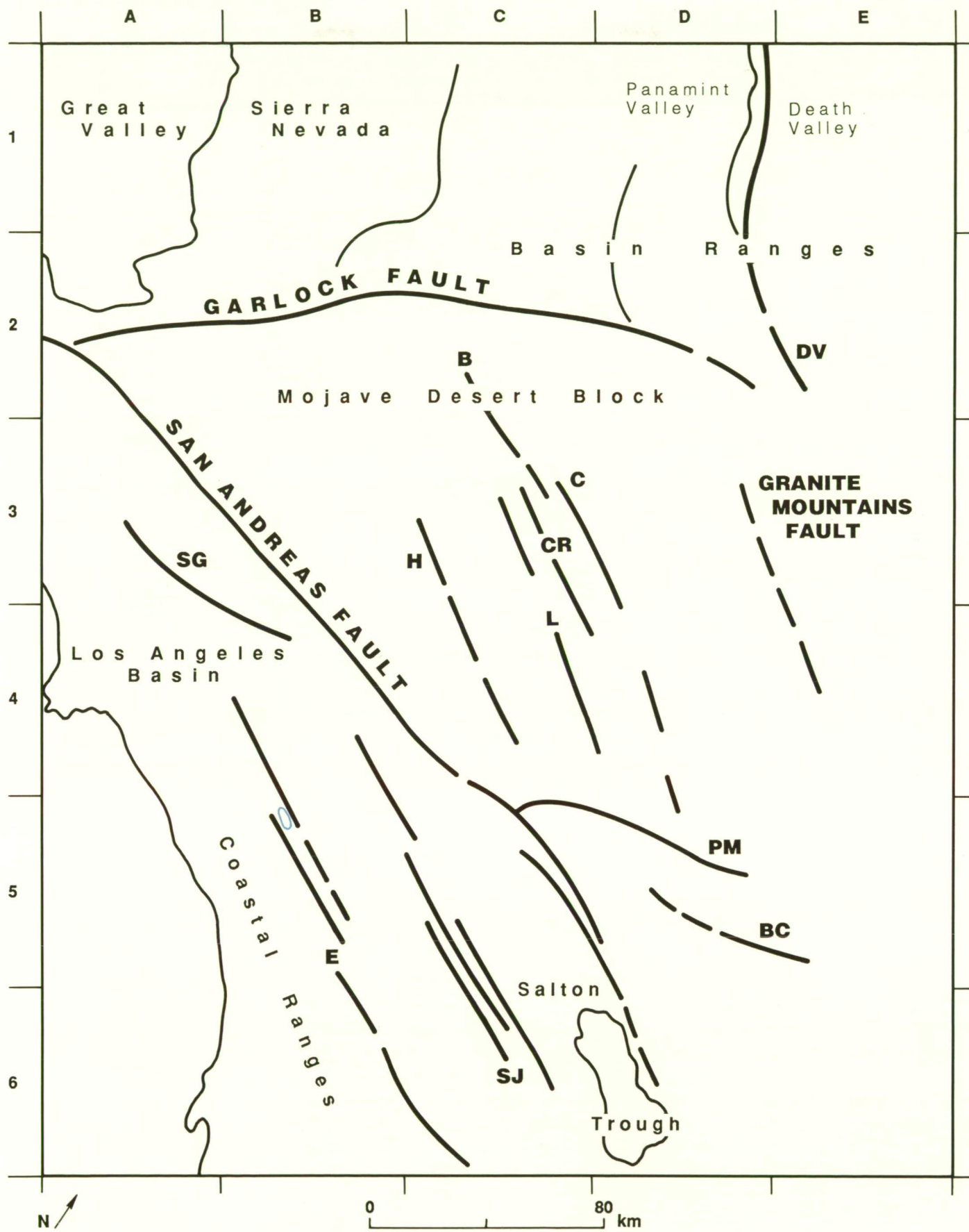
Figure 50. Sketch map of major crustal blocks and strike-slip faults in southern California. Faults and fault systems include Blackwater (B), Blue Cut (BC), Calico (C), Camp Rock (CR), Death Valley (DV), Elsinore (E), Helendale (H), Lenwood (L), Pinto Mountain (PM), San Gabriel (SG), San Jacinto (SJ).

Figure 51. Segment of Garlock Fault (Figure 49, box 2) showing small-scale, youthful geomorphic features aligned along the fault zone. Offset drainages indicate left-lateral displacement on the fault.
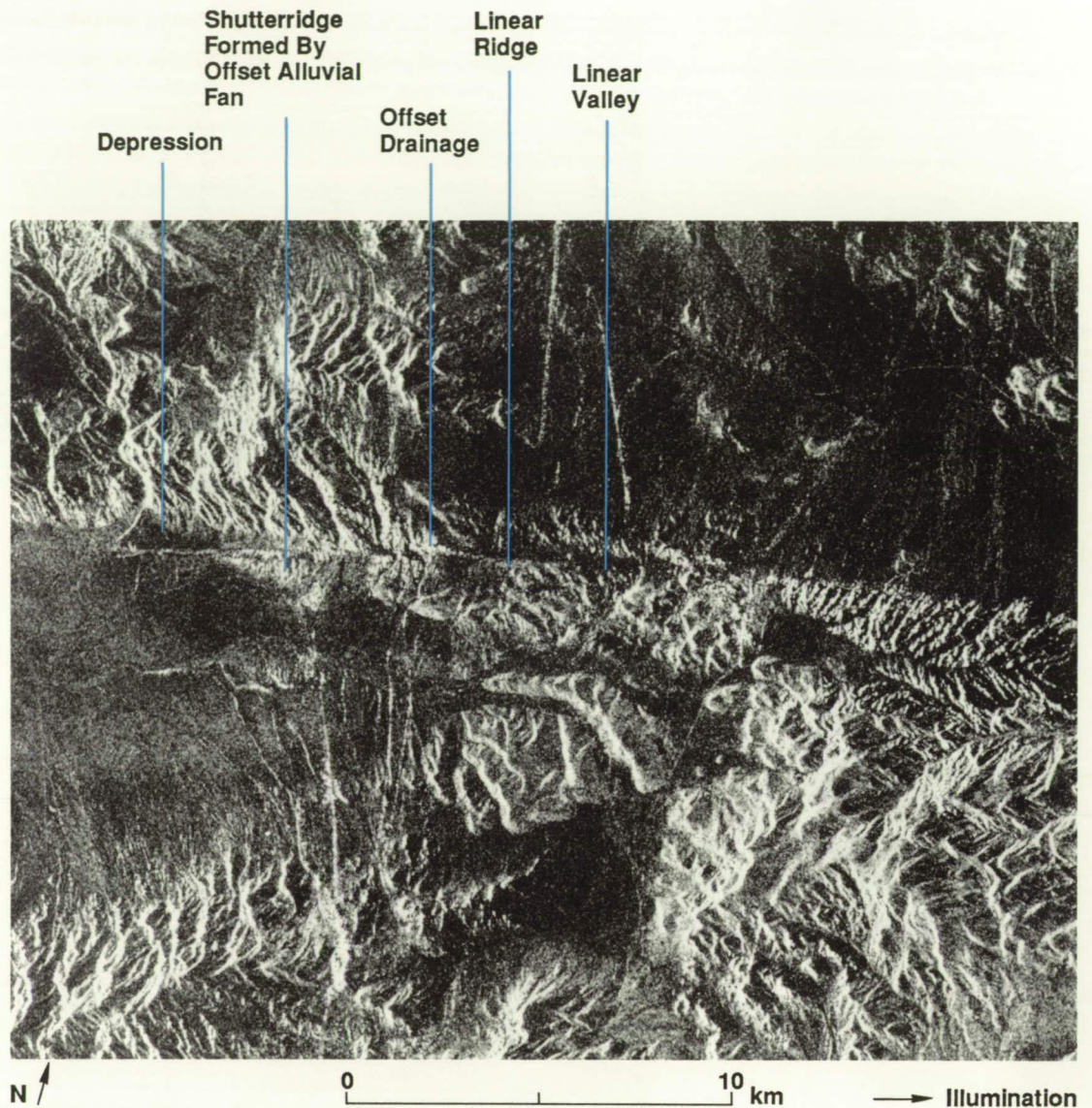
Hester and Hallinger, 1987). Notable examples of closed depressions, shutterridges, and other linear ridges and valleys along a portion of the Garlock Fault are evident in Figure 51 from their spatial relations and morphotectonic outlines. In addition, the direction of horizontal displacement can be determined from the direction of stream valley offsets across the fault, which is left lateral in this instance.

From the above discussion, it is clear that a variety of different tectonic landforms are enhanced on radar images because radar systems are very sensitive to slope characteristics. However, where relief is low and slopes are negligible, imaging radars are sensitive both to the small-scale roughness of a surface and to its complex dielectric constant. Small-scale roughness is a measure of average microrelief at a scale of centimeters. Rough surfaces yield

diffuse backscatter that appears bright on images. Smooth surfaces produce dominant forward scatter and appear dark on images. Nevertheless, in this context "rough" and "smooth" are relative terms and they vary with the observing wavelength. A surface that is "rough" at a short wavelength is "smooth" at a longer wavelength (see *Synthetic-Aperture Radar Imaging*).

The dielectric constant of most rocks lies within a narrow range; however, it varies as a function of moisture content in porous rocks, sediments, and soils. Porous surface materials with a comparatively low dielectric constant when dry have a much higher dielectric constant when they contain moisture; this results in considerably brighter radar returns. Radar sensitivity both to surface roughness and to moisture content have enabled the perception of nonrelief features of tectonic origin. Compari-
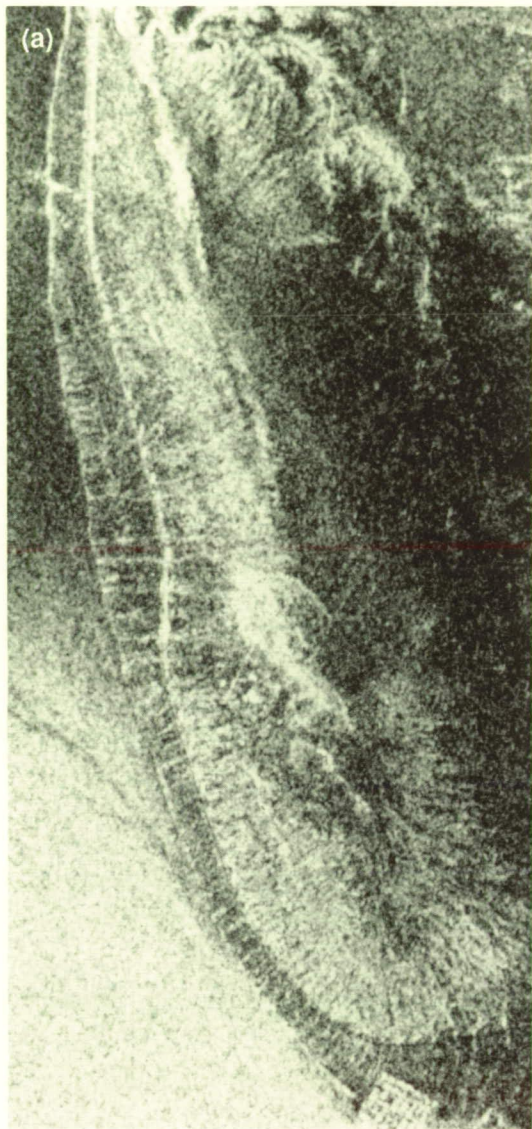
Figure 52. Durmid Hills east of the Salton Sea (Figure 49, box 3): (a) Seasat SAR image obtained at 23.5-cm wavelength in August, 1978; (b) corresponding airborne radar image obtained at 2.4-cm wavelength in November 1985 by Aero Service for the U.S. Geological Survey. The tonal lineament marking the trace of the San Andreas Fault on the Seasat SAR image is not perceptible at the shorter wavelength of the airborne radar.

N ↗   ⟶ Illumination   ↖ Illumination

0 _____ 4 km
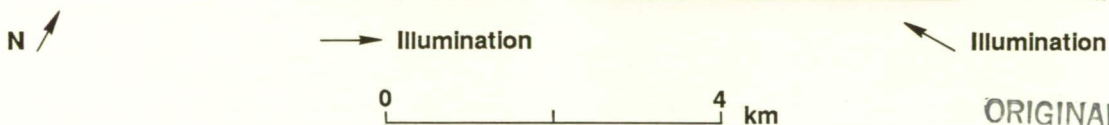
sons of Seasat SAR images obtained at 23.5-cm wavelength (L-band) with corresponding airborne radar images obtained at wavelengths of 2.8 cm (X-band) and 0.8 cm (Ka-band) provide examples.

The Seasat SAR image of the Durmid Hills east of the Salton Sea (Figure 49, box 3) shows a pronounced tonal lineament marked by bright radar returns to the southwest and radar darkness to the northeast (Figure 52(a)). Slopes in this area are 2 deg or less. The tonal lineament is not apparent on a corresponding airborne radar image obtained with higher spatial resolution at a shorter wavelength (Figure 52(b)). Sabins et al. (1980) reported that the Seasat lineament marks the trace of the San Andreas Fault and corre-

sponds to a fault boundary between outcrops of the Borrego Formation to the southwest and Lake Cahuila deposits to the northeast. The Borrego surface is highly dissected by numerous closely spaced gullies and littered with gravel- and boulder-size fragments of sandstone. The surface is rough at both the long wavelength of Seasat SAR and the shorter airborne radar wavelength. This results in diffuse backscatter and bright image tones in each image in Figure 52 (cf. Sabins et al., 1980, Figure 10, which shows corresponding bright image tones at 0.8-cm wavelength (Ka-band)).

The Lake Cahuila deposits overlie and mostly conceal the Borrego Formation. Because the surface of these deposits is a smooth layer of

Figure 53. Bristol Dry Lake (Figure 49, box 4): (a) airborne radar image obtained at 2.4-cm wavelength in July 1975 by Goodyear Aerospace (courtesy of Ray Sugiura); (b) corresponding Seasat SAR image obtained at 23.5-cm wavelength in August 1978. The tonal lineament extending northwest-southeast across the lake bed in the 2.4-cm-wavelength image is not perceptible in the 23.5-cm-wavelength image.

Illumination

↑N

0   10 km

Illumination
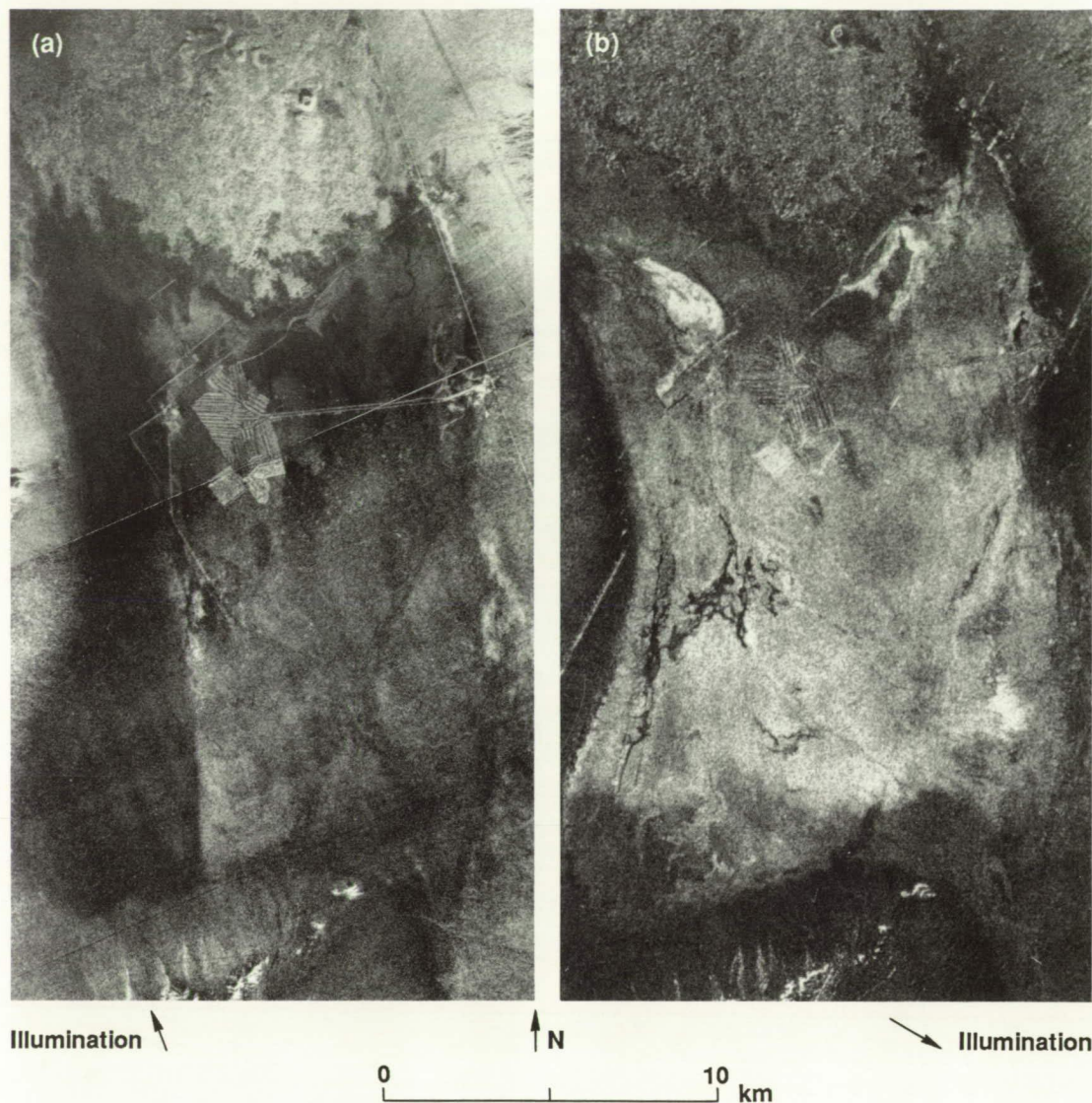
unconsolidated sand and silt, gullies are comparatively scarce. The small-scale relief of the surface is smooth at the Seasat SAR wavelength. This produces low backscatter and darkness on the image. However, at shorter airborne radar wavelengths of 2.8 cm or less, the Cahuila surface is rough and appears radar-bright on images (e.g., Figure 52(b), and Figure 10 of Sabins et al., 1980).

In this example, the 23.5-cm radar wavelength (Seasat SAR, L-band) discriminates juxtaposed surfaces that have different small-scale roughness characteristics, thereby revealing the trace of the San Andreas Fault in an area where there are no clear scarps, depresssions, linear ridges, or offset drainages. This type of surface discrimination is clearly wavelength dependent and not feasible at the 2.4- or 0.8-cm wavelengths of the airborne radar systems (X- or Ka-band). In the field, the fault trace is rela-

tively obscure. The absence of Cahuila deposits southwest of the fault has not been explained; it may represent nondeposition, or it may be the result of selective postdepositional erosion.

An airborne radar image obtained at 2.4-cm wavelength south of the Bristol Mountains (Figure 49, box 4) shows a pronounced northwest-southeast tonal lineament across the playa deposits in Bristol Dry Lake (Figure 53(a)). This tonal lineament does not appear on a corresponding 23.5-cm-wavelength Seasat SAR image (Figure 53(b)). The sediments consist of silt, clay, salt, and minor amounts of fine sand. The playa surface is covered by a dry crust less than 1 cm thick that has a puffy appearance. Sediments beneath the crust are moist to locally wet.

Sugiura and Sabins (1980) reported no significant differences in the sediment characteristics on either side of the lineament on the airborne radar image, and they found no evi-

dence for faulting of the sediments. They observed, however, that the sediments had a comparatively higher moisture content on the south side of the lineament and suggested that the lineament expresses a buried fault that controls ground water movement beneath the playa. Previous mapping has indicated the presence of a buried fault in the locality that coincides with the airborne radar lineament across the playa (Kupfer and Bassett, 1962).

The presence of the lineament on the 2.4-cm-wavelength image (Figure 53(a)) may denote a higher sensitivity of the shorter-wavelength radar in discriminating subsurface moisture conditions (hence dielectric constant). However, the two images in Figure 53 were obtained over an interval of 3 years, and the specific moisture content of the playa deposits at the instant of image acquisition in each case is not known. Consequently, any attempt to compare relative moisture sensing capabilities using these data will remain inconclusive.

Continental interiors

On the basis of plate tectonic theory, major deformation of Earth's crust takes place at active plate boundaries. However, crustal deformation has also occurred well into the interior of continental plates. Such deformation takes a variety of forms including continental rifting and associated volcanic eruption, magma inflation, plutonic intrusion, and widespread crustal upwarping or downwarping called epeirogeny. Each of these types of tectonic deformation is characterized by distinctive regional and local landforms.

Continental rifts. Rifts occur where the entire thickness of the lithosphere has ruptured under extension (Burke, 1980). Rifts are common in the oceanic crust. To a lesser extent, they occur in the continental crust, but only there can they be observed by radar imaging techniques. Active continental rifts take the form of long narrow troughs of regional extent. Such troughs are bounded by normal faults and are commonly associated with volcanic constructs. Linear fault-bounded valleys are characteristic landforms in zones of rifting. As an example, the Rio Grande Rift is a zone of active extension about 850 km long that stretches from central Colorado to southern New Mexico and widens from about 10 km in the north to over 150 km in the south. It is a major structural feature that

consists of a series of en echelon north-trending grabens and half-grabens (Woodward, 1977). The grabens are referred to as basins that separate the Great Plains from the Colorado Plateau, the Rocky Mountains, and the Basin and Range physiographic provinces (Figure 54). The regional outline of the structure is marked by offset segments along northeast-oriented lineaments. The rift has been divided into northern, central, and southern segments, each of which has its own structural style and history (Chapin, 1979).

A portion of the central segment that includes the Jemez Volcanic Field is shown in the Seasat SAR image, Figure 30(a) of *Volcanic Landforms*. Most of the marginal faults that bound the rift are poorly exposed. The image shows the best exposures of marginal faults on the west side of the rift, in the form of prominent linear east-facing escarpments. Extensive northeast- and east-northeast-oriented lineaments in the image transect the rift and intersect at the
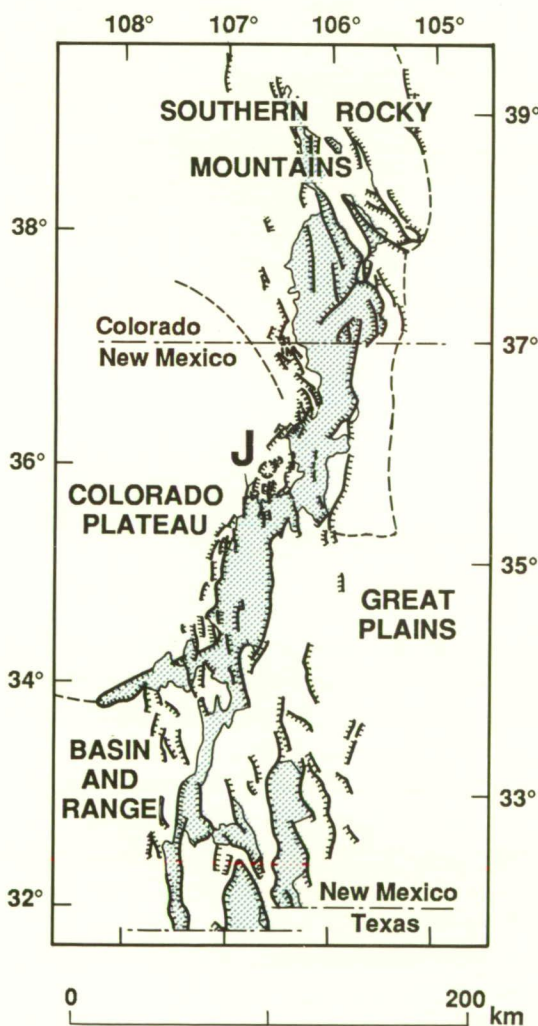

Figure 54. Relations of Rio Grande Rift (stippled) to surrounding physiographic provinces. Faults are shown by lines with hachures that denote the downthrown side. The central portion of the rift marked "J" denotes the Jemez Volcanic Field and adjacent area shown in Figure 30(a) of Volcanic Landforms (sketch from Golombek et al., 1983).

Valles Caldera. These lineaments provided the structural control for emplacement of the Jemez magma system.

Continental shields. Earth's major continental plates each display one or more shields that consist of extensive, ancient, crystalline rocks. Such shields form continental nuclei to which other slabs of continental crust have accreted episodically. Though shield areas vary in their geologic details, the rocks in all shield areas are very ancient (synonymous with Precambrian), deeply beveled by erosion, and widely separated in space and time from those in present-day mountain chains. Large areas of the ancient continental shields, known generally as basement, are overlain unconformably by sequences of younger rocks that reveal numerous episodes of epeirogenic uplift or subsidence, accompanied by corresponding episodes of erosion or sedimentation, respectively. Structural deformation and plutonic intrusion provide further evidence of intracontinental tectonism. The morphotectonic relations displayed by rock bodies in such continental interior areas serve in part to allow investigators to infer the geologic history. In this tectonic setting, however, crustal rocks are neither as thick nor as complexly deformed as they are in continental collision zones.

The SIR-A image in Figure 55 covers an area of basement terrane in the Guiana Shield of northern South America. The scene is located in Amazonas, Venezuela. Structures are indicated by the erosional characteristics of the land, the drainage, and the outcrop patterns. In this context, four radar map units are evident in the image. Because of continuous forest cover, these units do not provide any direct information about their lithologic identity. The four units mapped in Figure 55 consist of (1) topographically subdued basement, (2) prominent upland, (3) cross-cutting intrusive rock, and (4) topographically featureless lowland.

Basement rocks crop out at low elevations (map unit 1). The erosional topography in Figure 55 shows conjugate sets of linear features (e.g., at A7 to A8 and B7). These features represent joints, fractures, or faults whose orientation, spacing, and linear extent denote the structural trends in the basement. In this area of the Guiana Shield, the basement consists predominantly of granite, granite gneiss, and migmatite.

In areas of prominent upland (map unit 2), the basement is overlain by younger rocks that have a thick tabular form. These rocks are probable equivalents of arenites in the Roraima Formation. The erosional remnants of the Roraima Plateau appear in the image as small mesas (B2/B4 to A6 and E6) and as residual inselbergs distributed throughout the lower third of the image. Joints and fracture traces in the basement are pronounced in the vicinity of the inselbergs, and locally they govern the erosional outlines of the mesas. The mesa scarps and the slopes of the inselbergs show very bright radar outlines where they face toward the radar illumination and radar darkness where they face away. This indicates that the slopes exceed the complement of the SIR-A nominal incidence angle (40 deg). Resistant ridges in the area from C1 to D2 reveal the outlines of a doubly plunging synclinal structure. Ridge offsets along the structure denote normal faults that produced a horst across the southern end.

Cross-cutting relations are evident from the circular to elliptical outlines of an intrusive rock body in the basement (map unit 3, B5 to C5). This feature has a diameter from 7 to 10 km and is of unknown composition (Martin-Kaye and Lawrence, 1983). Other intrusive features with a comparable size and outline that have been mapped in Brazil within 150 km of the circular feature (Projeto Radambrasil, 1975 and 1976) include bodies of basic igneous rock and one occurrence of carbonatite (Seis Lagos).

Lowland areas that are topographically featureless (map unit 4) include weakly resistant alluvial deposits or basins with poorly consolidated sediments overlying the basement (e.g., A1 to E1 to E4).

Canyons. Continental lowland areas that have been subjected to comparatively rapid epeirogenic uplift become incised by streams that cut canyons in the landscape as it rises. As stream downcutting tends to follow paths of structural and lithological weakness, a drainage network develops that outlines the local and regional patterns of fracturing and faulting. Canyons often expose layered rocks that have markedly differing resistance to erosion. Consequently, the profile across a canyon may alternate abruptly between precipitous to vertical slopes (held up by strong resistant rocks such as massive limestone or sandstone) and gentle slopes (underlain by weak, thin-bedded rocks

N

→ Illumination

0   20

Siapa River

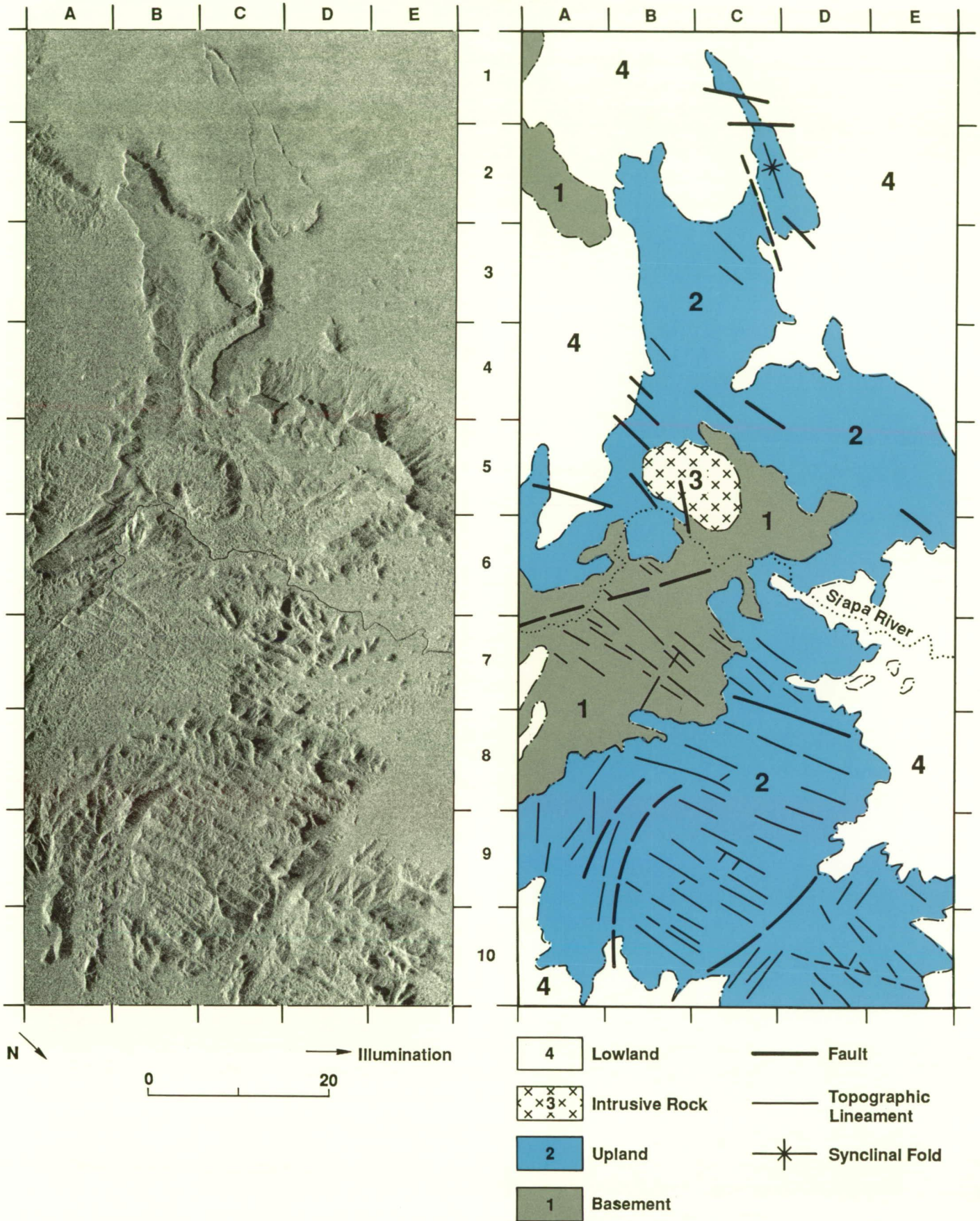| 4 | Lowland | ▬ | Fault |
3	Intrusive Rock	—	Topographic Lineament
2	Upland	✳	Synclinal Fold
1	Basement		

Figure 55. SIR-A image of Guiana Shield in the vicinity of Rio Siapa, Amazonas, Venezuela, with simplified structural sketch map. Map units 1 through 4 are described in the text.

87

such as shale and siltstone). While the individual layered rock units exposed in a canyon wall rarely exceed 100 m in thickness, local relief of 1000 m or more from the base to the rim of a canyon is not uncommon.

The vertical succession of abruptly contrasted slopes that is characteristic of profiles across canyons produces strong differences in radar backscatter under certain circumstances (Elachi and Farr, 1980). The differences in backscatter vary with the incidence angle and the direction of illumination as illustrated here by images obtained with the Seasat SAR and SIR systems.

A Seasat SAR image of a portion of the Grand Canyon, Arizona, is shown in Figure 56. In this locality, the canyon is about 16.2 km wide and 1.3 km deep. With the low nominal incidence angle of Seasat SAR (23 deg), foreslopes are compressed to thin lines of saturation. However, backslopes along the canyon wall show contrasting bands of bright and dark. These bands correspond to alternating gentle and steep slopes, respectively (Berlin et al., 1982). Each band denotes a sequence of layered rocks that has strongly contrasting erosional characteristics relative to those in the adjacent bands. The bands provide generalized surface-slope information, but they cannot be used to measure stratigraphic thickness or to identify lithology. Individual bands can be traced and matched in the image along segments of the canyon wall for about 20 km (C2 to D1) and across the canyon (D3). Different levels of the plateau surface above the canyon are evident on each side of the Coconino Rim (A5 to C2).

Shuttle radar images of the Pakaraima Mountains, Guyana, South America, and the Central Kalimantan Plateau, Borneo, Australasia (Figure 57(a) and (b)) show the drainage of the Mazaruni and the Mahakam Rivers and their tributary canyons, respectively. In each of the two localities, relief in the canyons is upward of 400 m, and dissection has exposed rock layers that have differing resistances to erosion. For purposes of comparison, image (a) was obtained at a nominal incidence angle of 50 deg by SIR-A and image (b) at a nominal incidence of 42 deg by SIR-B. With this moderate to high range of nominal incidence angles, foreslopes appear bright and backslopes are partly in radar shadow, depending on their orientation relative to the illumination vector. Appropriately oriented

backslopes of canyons in the center of Figure 57(b) show alternating light and dark bands along the canyon walls; these bands denote corresponding alternations of gentle and steep slopes (compare Figure 56). More extensive landform degradation is evidenced in Figure 57(a), with three successive erosional levels of the plateau above the canyon at the bottom center of the figure. In both images, the canyons appear to be regularly spaced and to follow predominantly linear traces. Abrupt changes in the orientation of a canyon coincide with the dominant fracture pattern in each case. Abrupt bends in the major drainage channels indicate control of these features by the same sets of intersecting fracture patterns.

Summary and Discussion

Seasat SAR and Shuttle Imaging Radar have demonstrated the ability of spaceborne radar systems to obtain high-resolution image coverage of a wide range of landforms on Earth. From these images it is possible to interpret regional and local tectonic relations. With similar system capabilities, Magellan radar images are expected to provide evidence for tectonic or other origins of the landforms on Venus.

Tectonic landforms occur notably in linear to curvilinear belts that stretch for hundreds of kilometers and include major crustal elements such as ridges and trenches in the oceanic crust and mountain chains and rifts in the continental crust. Examples of tectonic landforms in the Appalachian Mountain fold belt (Figures 37, 38, and 41), the North American–Pacific plate boundary transform (Figure 49), and the Rio Grande Rift (Figure 30(a), *Volcanic Landforms*) show that tectonically deformed features are predominantly linear in outline at both regional and local scales.

The high sensitivity of imaging radars to slope at moderate to low incidence angles enhances the perception of linear topography on images. It reveals broad spatial patterns that are essential to structural and tectonic interpretation. As radar responses are strongly directional, the ability to discriminate linear features on images varies with the orientation of the features relative to the illumination vector. Landforms that appear prominent on images where they are transverse to the illumination (Figure 38) may be
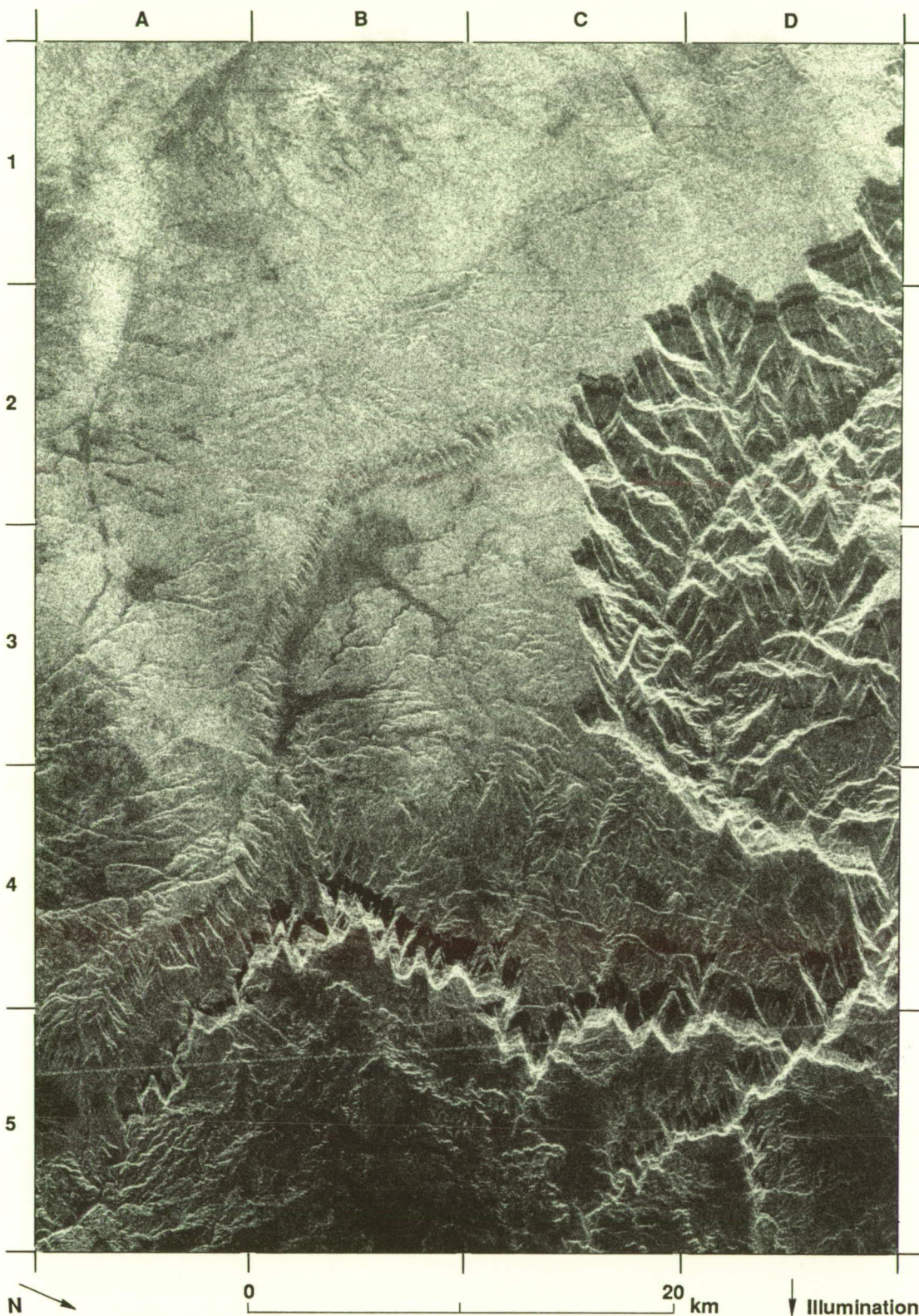
Figure 56. Seasat SAR image of Grand Canyon, Arizona, shows contrasted bands of bright and dark radar responses from backslopes along the canyon walls.

obscure to indistinguishable on images where they are parallel to the illumination (Figure 37). Variations in nominal incidence angle can make the difference between enhancement (Figure 57) or obliteration (Figure 56) of sloping surfaces on images. Linear fault traces should be examined carefully because other linear features such as dipping strata, dikes, or linear jointing patterns may be expressed in a similar manner on images. In the absence of relief, nontopographic lineaments may appear in response to local contrasts of small-scale surface roughness or dielectric

Figure 57. Canyons imaged by (a) SIR-A in the Pakaraima Mountains, Guyana, South America, and (b) SIR-B in the Central Kalimantan Plateau, Borneo, Australasia, appear regularly spaced and show preferred linear orientations that reflect regional conjugate fracture patterns in the underlying rocks.

N ↙   N ↘   ↓ Illumination

0 _____ 40 km
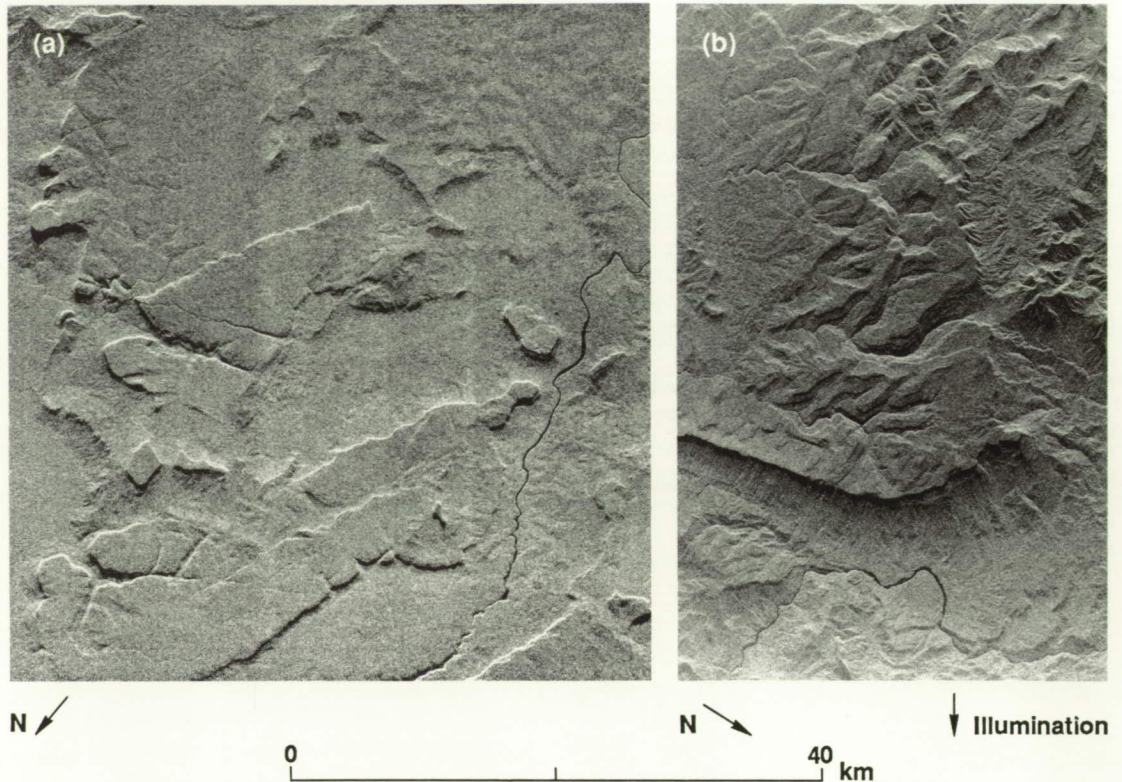
constant (Figures 52 and 53). The possibilities for alternative interpretations of image data can significantly influence the image analyst. Such possibilities are to be anticipated in the interpretation of Magellan radar images.

Landform interpretation from radar images is governed at a local scale by the spatial resolution of the images and at a regional scale by the areal coverage available. Contrasts in feature perception at different simulated resolutions were demonstrated for accreted terranes in eastern interior Alaska (Figures 45 and 46). Magellan radar is expected to discriminate surface features at a scale of hundreds of meters. To obtain the desired regional coverage of Alaska (Figure 45) and Southern California (Figure 49), it was necessary to mosaic adjacent Seasat SAR image swaths. The Magellan coverage of Venus will be mosaicked in a similar fashion. This will allow the preparation of maps showing regional and local landform patterns and global tectonic networks, if they exist. However, as on Earth, it is not possible to erect an unambiguous model for the tectonic evolution of Venus based only on detection and interpretation of landforms at the surface.

Magellan radar images are expected to provide substantial advances in detecting and interpreting the Venusian landscape. This will be accompanied by radar altimetry measurements of topographic relief. Details of the landform patterns derived from these complementary data sets will provide a basis for modeling the tectonic evolution of Venus on a global scale. Age measurements and precise timing of tectonic events are essential elements of such modeling. Impact craters may be used in estimating an average surface age for Venus, though the validity of applying either terrestrial or lunar cratering rates to estimates of cratering rates on Venus is not known and may be questionable.

On Earth, the precise timing needed to document plate tectonic events was determined from geophysical measurements, independent of surface imaging or altimetry data and unrelated to rates of cratering. Reversals of the magnetic field have provided a sequence of intervals, resulting in time markers that vary in duration from tens to hundreds of thousands of years. By comparison, impact cratering may yield a few intervals and time markers on the order of hundreds of millions of years duration. Thus, for Venus, we probably should not expect to develop a definitive model of tectonic evolution from the analysis of images and altimetry data alone.

Image Anomalies and System Artifacts

Introduction

In this chapter, characteristics of SAR images that distinguish them from images taken with other sensors are presented first. Analysts trained in conventional photointerpretation must be aware of them to avoid misinterpretation. Next, artifacts contributed to a SAR image by the limitations or incorrect operation of a sensor or processing system are considered. These artifacts may create image anomalies that can lead to misinterpretation of the data. Many of the examples given are images of cultural targets; this is due partly to an observational bias in the existing data caused by the prevalence of such targets on Earth and partly to the fact that the simple geometries of cultural targets make artifacts easier to see. Where possible, similar effects in images of natural targets are shown.

Unique Characteristics of SAR Images

The three basic characteristics of the returned radar echo measured by a typical SAR sensor are backscatter (usually represented as normalized radar backscattering cross section), time delay, and Doppler shift. The first of these characterizes the target radiometrically, while the latter two allow the returned radar signal to be positioned properly in an image.

In the SAR processing system, a relationship is assumed between the Doppler-shift/time-delay coordinates and the along-track/cross-track coordinates. The latter correspond to linear dimensions along the target, the so-called "ground range." The resulting displayed perspective is that of a photographic camera located in a plane roughly perpendicular to the flight track and containing both target and SAR, but in a direction 90 deg from the SAR as seen from the target.

However, there are limits to this analogy. First, radar backscatter is controlled by properties of the target that are fundamentally different from those that control visible-light reflectance.

Second, some target characteristics can make the geometric conversion to ground range incorrect. The result is misplacement of the target's image when the conversion is made to ground range, which can create difficulties in interpretation.

Radiometric effects

The obvious radiometric difference between SAR images and most other images is the grainy texture known as speckle (Dainty, 1984). Most digital camera systems are designed to be radiometrically quantization-noise limited. This means that the quantization level in the analog-to-digital conversion is set to encompass all or most of the analog noise. Therefore, the dominant noise in the resulting image is digital quantization, and any individual pixel represents a deterministic estimate of the reflectance of the target, limited in accuracy only by the digitization interval. On the other hand, speckle is generally the dominant noise in SAR images. Pixel intensities within such images represent only a statistical measure of the target backscatter.

Speckle appears in any coherent imaging system when an extended (i.e., nonpoint) target is imaged. It is a result of the coherent addition at any given time of returns from many individual scatterers within a resolution element. The coherent sum of these returns is a function of the sensor position. If the sensor is moved a small distance, the composite amplitude will be an independent sample of the target backscatter. In principle, each of these independent samples gives additional data about the target, but their differences are generally regarded as an artifact or treated as a noise source. Speckle is Rayleigh-distributed when the receiver is linear (as for Magellan), and the distribution can be wide. Interpretability can often be increased by narrowing this distribution at the expense of spatial resolution. To this end, SAR images are usually presented as pixels made up of an incoherent sum of several of these independent samples, or "looks," of the target. A four-look image, for example, will have a 3-dB variation among pixels that observe the same target. This

noise can be reduced by incoherently averaging those pixels (i.e., increasing the number of looks), but if the target is not spatially homogeneous, the process of spatial averaging leads to a loss in resolution of whatever inhomogeneity exists. For example, averaging 10 resolution cells in a four-look image would reduce speckle noise to about 0.5 dB, but would reduce the resolution by an order of magnitude. Whether this loss is worth the corresponding reduction in speckle depends on the specific image and the intent of the investigation.

To illustrate this tradeoff, Figure 58 shows a Seasat SAR image of the SP Lava Field, a basaltic flow area that is part of the San Francisco Volcanic Field in Arizona. The image includes SP Mountain, a 1.2-km-diameter cinder cone, at its center (marked as "1" on the sketch map). The SP flow (2) extends from it about 7 km. Several smaller cinder cones lie to the east and south of SP Mountain, most of which are breached. In particular, cinder cone (3) is topped by a large crater, (5) contains a smaller round

crater, and (4), (6), and (7) have linear or arcuate vents at their peaks. The feature (8) has a roughly concentric ridge surrounding it to the north (Schaber et al., 1980).

The image is displayed at one, two, four, eight, and sixteen looks in parts (a) through (e) of the figure, respectively. Note that the first visual effect produced by increasing the number of looks is a blurring of the speckle; central craters, especially those at (3), (4), and (7), are more distinct. As the number of looks further increases to eight, however, loss of resolution begins to dominate, and central craters are less well resolved. The vent at (7) disappears completely at greater than eight looks. In this example, the two- and four-look images seem to offer the best presentation of the targets, but the choice clearly depends on both the target and the purpose of the investigation. Ford (1982) conducted a survey of geologic analysts, the results of which showed that although the optimal number of looks depends on the target type and resolution, a majority of the analysts

Figure 58. Seasat image of SP Lava Field, Arizona. Images (a), (b), (c), (d), and (e) have 1, 2, 4, 8, and 16 looks with resolution of 86, 120, 172, 240 and 344 m, respectively. The sketch map (f) shows features described in the text.

C-2
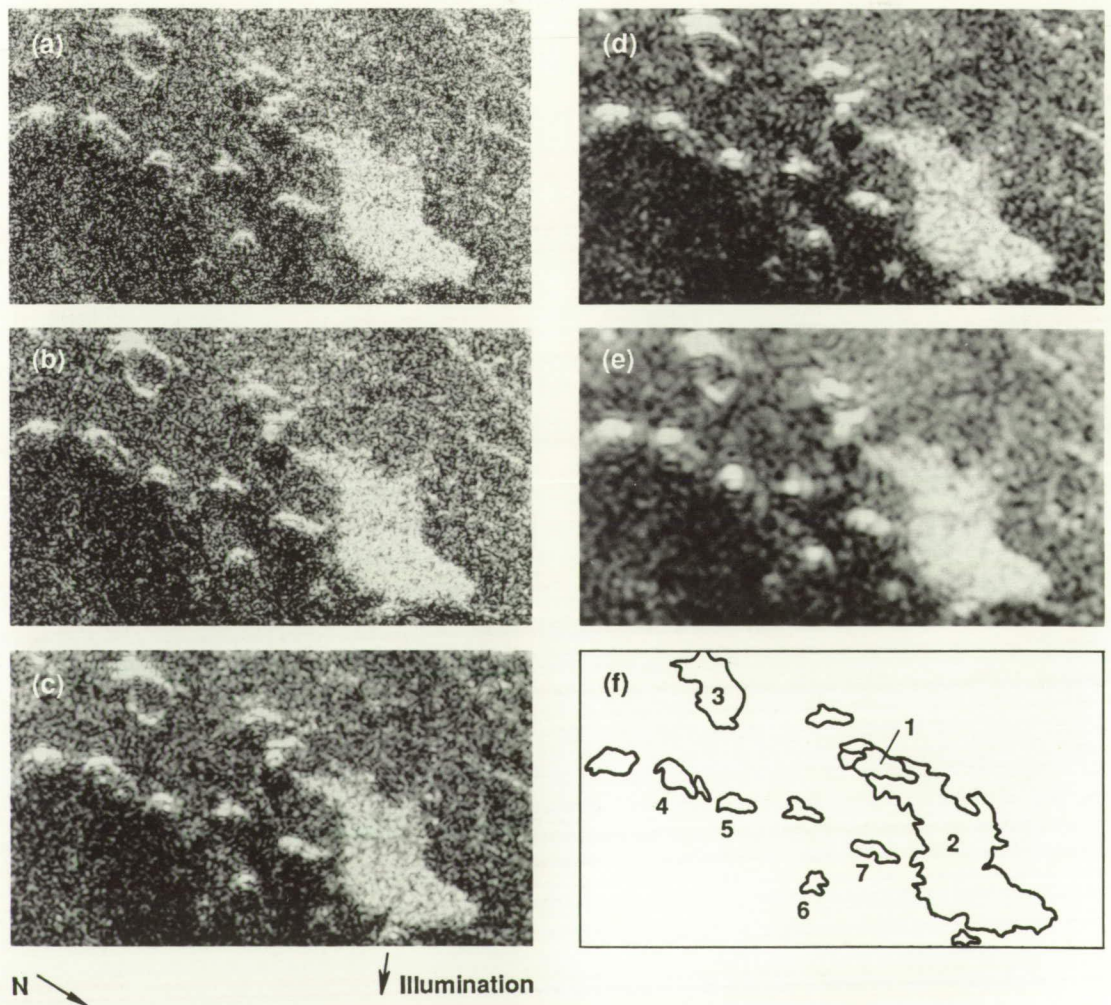
preferred two-look images. Seasat SAR, SIR-A, and SIR-B standard-product images were processed at four looks.

An exceptionally strong return is generated by any target that directs radiation preferentially toward the sensor (Figure 59). Examples of such targets are (1) those whose orientation is such that they specularly reflect the radar signal back to its source, and (2) dihedral and trihedral corner reflectors. Corner reflectors are formed by alignments of two or three mutually perpendicular reflective planes. They will return radiation preferentially in the direction from which it came over a broad range of incidence angles. Trihedral (three-plane) corner reflectors are often used terrestrially as fiducial marks because they are exceptionally bright in SAR images. Dihedral (two-plane) corner reflectors

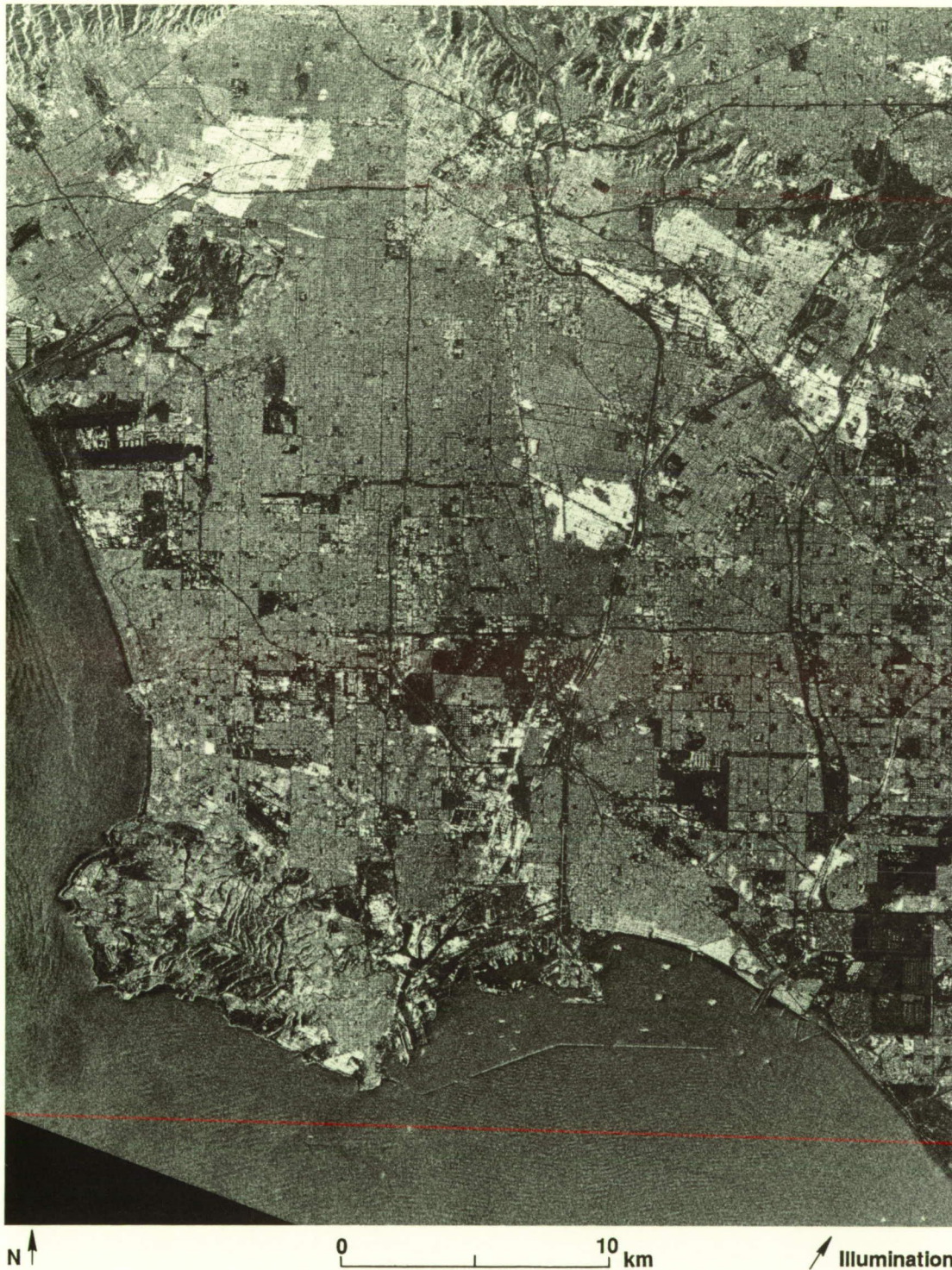*Figure 59. Seasat image of the Los Angeles Basin. The pronounced brightness in some areas is the result of the chance parallel alignment of streets and adjacent buildings with the flight path.*

N↑

0   10 km

⟋ Illumination

function in a similar way but over a narrower angular range. Strong radar returns are commonly generated by natural approximations to dihedral corner reflectors formed by two perpendicular planar (or near-planar) surfaces. These include segments of crater rims, scarp faces, embankments and river channels, and cultural structures such as buildings, fences, and roadbed berms. They must be oriented with both planes perpendicular to the plane of zero Doppler shift. The effect in the image is to emphasize such features; if the features are curved, those portions that lie along-track are emphasized. In the Seasat image (Figure 57), streets aligned parallel to the flight track form corner reflectors with the adjacent building fronts to produce a return that is much brighter than that from areas where this alignment does not occur.

Conversely, care must be taken to anticipate possible causes of data saturation—a common artifact in most types of imaging systems. Natural targets have a wider variation in backscatter than the dynamic range of most SAR systems, at least when operating at a single gain state. Targets whose backscatter exceeds the available dynamic range (either before or after compression) will not be faithfully represented in the resulting image. Slopes with preferential orientation and foreshortened mountains are examples of targets that may saturate the system and thus create images that are difficult to analyze. Crater rims, for example, would be expected to show a brightening at those parts of the rim normal to the illumination, as discussed above. The strength and form of this brightening can be used to infer details about the roughness or slope of the crater rim, if the brightening is not limited by saturation. In Figure 60(a), taken by SIR-B of a crater on the Iraqi–Jordanian border, brightening on the far rim is evident despite the low signal-to-noise ratio of the image. The same crater as imaged by SIR-A, which had a significantly smaller dynamic range, is shown in Figure 60(b). In the latter case, saturation has obscured the effect and a different conclusion might be reached about the nature of the rim if the artifact were not recognized.

Geometric artifacts

Geometric artifacts can be introduced by failure of the geometric conversion algorithm to account properly for target characteristics when converting the Doppler/range data into ground-range coordinates. The conversion from time delay into a cross-track ground coordinate assumes that targets farther away from the SAR antenna are also farther away from nadir. The assumption is generally true for larger look angles and moderate topography. Failure to meet this assumption can result in an effect known as layover or foldover, which occurs where foreslopes exceed the nominal (i.e., horizontal-terrain) incidence angle.

The geometry for layover is illustrated by the sketches in Figure 61. Two positions of a transmitted wavefront are shown, with radii $R_1 < R_2$. Note that in Figure 61(a) the point labeled (b) on the top of a mountain is farther both from the SAR nadir and from the SAR itself than point (a) at the base of the mountain. The simple mapping of time delay into ground range will properly place the mountain in the image. Note also that cameralike perspective is created as the distance between points (a) and (b) is foreshortened. In Figure 61(b), however, the mapping is not performed correctly because of the smaller look angle. Point (a) is now closer to the SAR than point (b). In the related ground-

Figure 60. Images of a crater on the Iraqi–Jordanian border: (a) SIR-B—note rim brightening in far range; (b) SIR-A—data saturation masks the effect observed in (a).

Illumination

Illumination

N

0   2 km

(a)

SAR

R₁ R₂

b

a
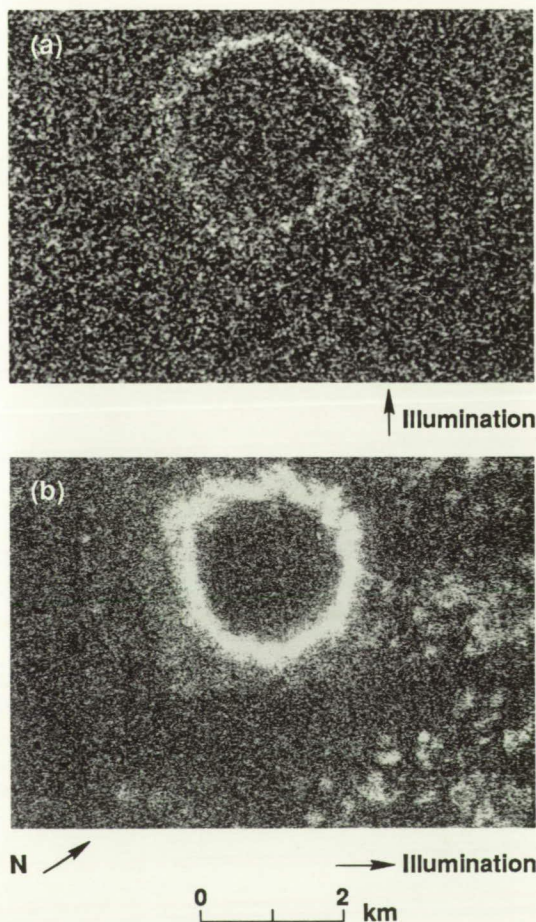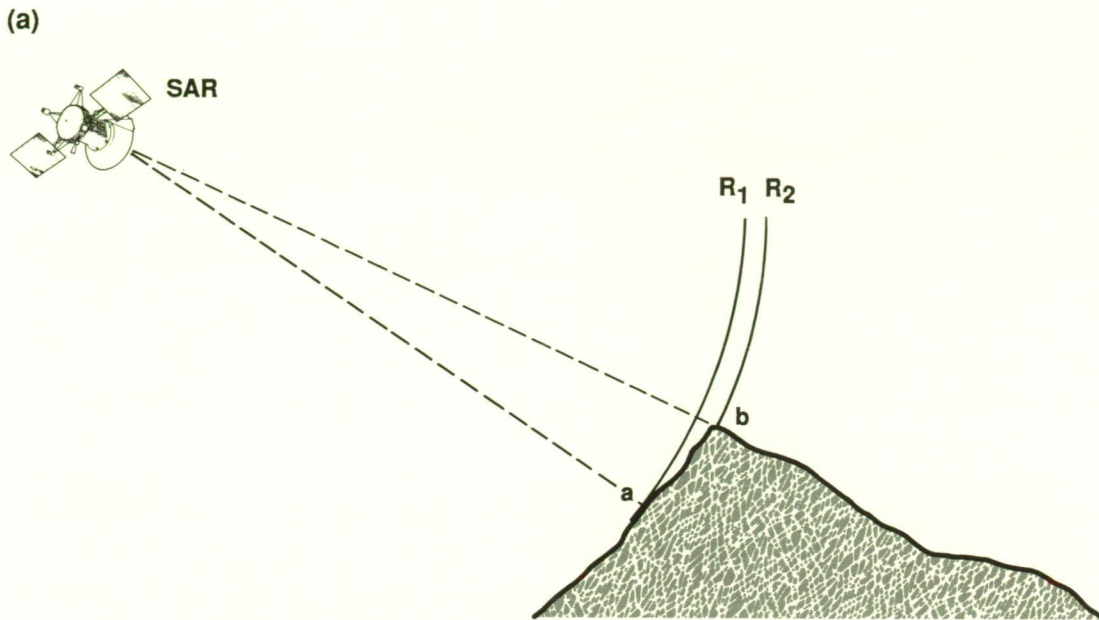
Figure 61.
Transformation from
slant range to
ground range: (a)
the assumed
transformation is
accurate and
features are properly
placed; (b) the
incidence angle is
smaller, the
transformation is
inaccurate, and
layover results.

(b)

SAR

R₁ R₂

b
c

a
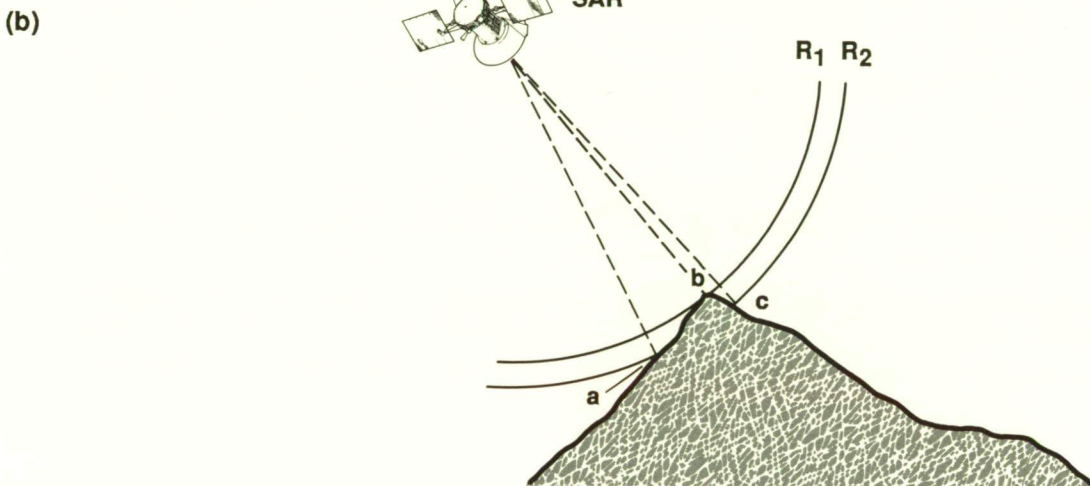
range image, point (a) will be misplaced with respect to point (b), and the mountain slope will be displayed in reverse, relative to the illumination vector. Note also that points (a) and (c) will be overlaid in the image. Without additional data, this misplacement is not only irrecoverable, but not identifiable except from local knowledge. Clearly, layover is more likely to occur when using low-incidence angle SAR in rugged terrain. Figure 62 is a Seasat image of a section of the Alaska Range near Mount McKinley. This 23-deg-incidence-angle image shows a ridge and a peak laid over into the glacier-covered valley below. Only from knowledge of the topography can the misrepresentation shown here be corrected (Kwok et al., 1987).

Figure 63(a) is another example of pixel misplacement in range. It shows an image of Golden Gate Bridge in San Francisco, California, taken by the JPL airborne SAR aboard the NASA CV-990. The bridge lies almost parallel to the flight direction. Not one but three bridges can be seen in the image. These are not ambiguities (which will be discussed later), but three separate returns from the bridge: one direct, one bounced from the water surface, and one bounced from the water twice. Figure 63(b) illustrates the three return paths. Since the three time delays were different, the mapping into ground range placed the three returns in three different range positions. With Magellan, multiple bounces may occur from targets similar

Figure 62. Seasat image of a portion of the Alaska Range showing layover of a ridge and peak adjacent to a glacier-filled valley.
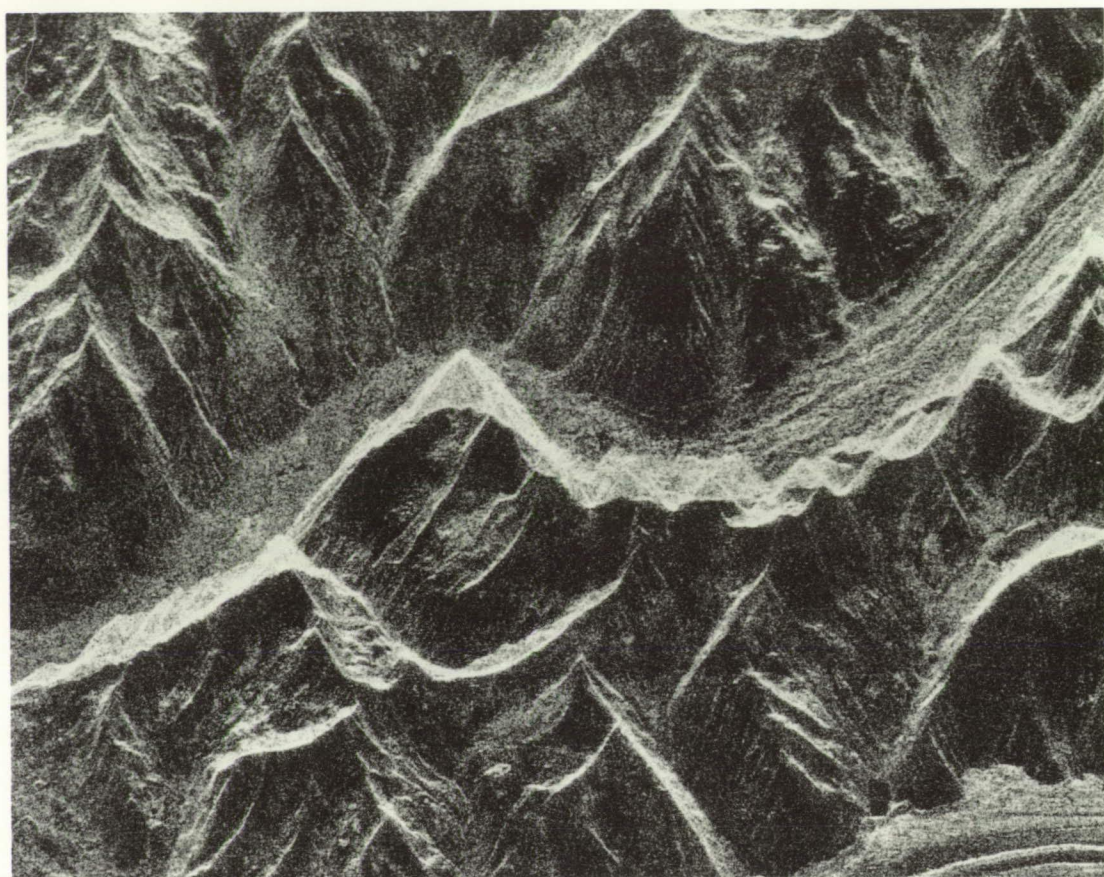
N ↘   0 |___|___| 2 km   ↓ Illumination

in morphology to the cultural target described here. Such targets will be misplaced in ground-range images. Although these effects can be removed by using dual antennas and interferometric techniques (Zebker and Goldstein, 1986), Magellan will not have such capabilities.

The second geometric dimension measured by SAR is Doppler shift. The Doppler shift of the target is used together with target range delay to properly locate the target image. Again, a simple geometric relationship and constant relative motion are assumed. However, since both target and sensor have, in general, motions of their own, the transformation requires knowledge of their relative velocities. Imperfect knowledge of the relative velocity or nonuniform motion of the imaged field will result in misplacement of targets in the image. In Figure 64, which is an enlargement taken from another JPL aircraft SAR image, Golden Gate Bridge lies approximately parallel to the flight track along a line of constant azimuth. The bridge is correctly placed assuming that its Doppler shift is identical to that of the Earth. Cars on the bridge (indicated by arrows), however, are misplaced

because their velocities relative to the sensor are different from that of the bridge.

SAR Processing Errors

Ambiguities

In the azimuth (along-track) direction, a target's return is sampled at the pulse-repetition frequency (PRF). Since the target return is not a band-limited signal, it is not possible to sufficiently sample it (and even if it were, it is not generally efficient to do so). The resulting signal thus may contain high-frequency data that masquerade as data at lower frequencies. Such data are called "aliased" and appear in the correlated image as ghosts of the target repeated at some distance in azimuth. These are referred to as "azimuth ambiguities." In normal processing, azimuth ambiguities are suppressed by limiting the processing bandwidth to an appropriate fraction of the PRF so that the signal-to-ambiguity ratio is maximized. In Magellan, for example, total ambiguities are specified to be at least 15 dB lower than the properly placed

(a)

N ←

0   2
|___|___| km

↑ Illumination
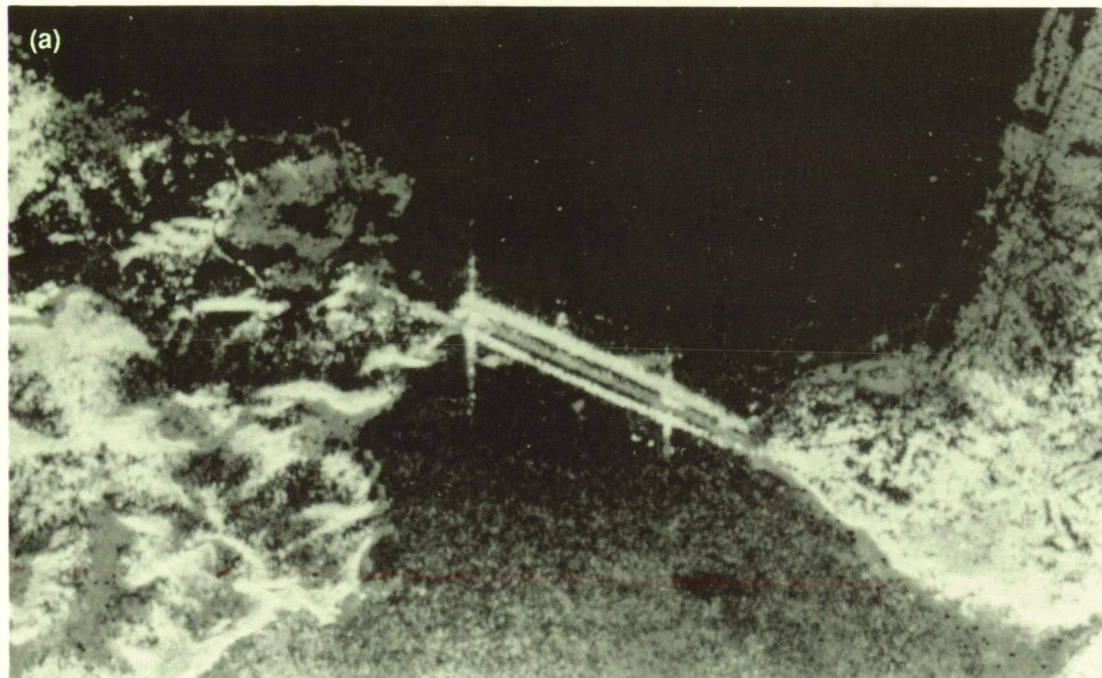
Figure 63. Pixel misplacement in range: (a) JPL aircraft SAR image of Golden Gate Bridge, San Francisco (note the tripled image of the bridge); (b) the three possible paths for signal return (modified from Zebker and Goldstein, 1986.)

(b)

Direct Path

Intermediate Path

Longest Path

Golden Gate Bridge, End View

Ocean
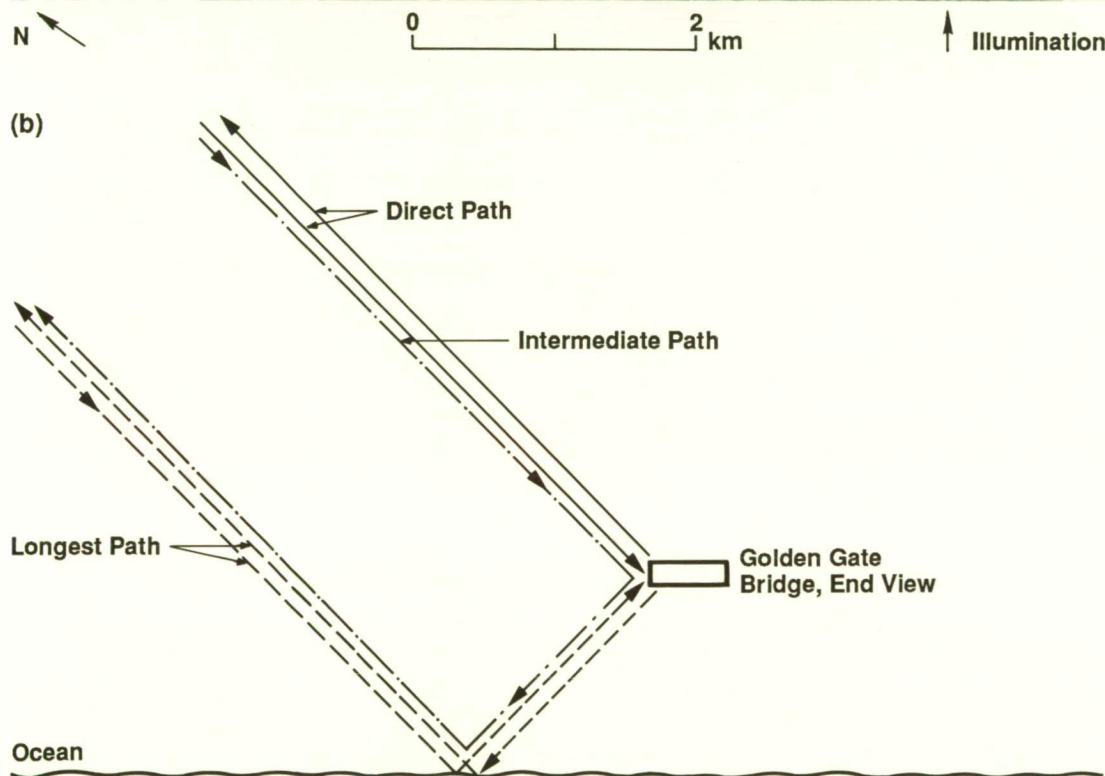
return. Therefore, they should not be observable unless the target is exceptionally bright against a low background or the processing bandwidth is improperly set. However, in such naturally repetitive scenes as mountain ranges or drainage systems, azimuth ambiguities can easily be misinterpreted. Figure 65 is a SIR-B image taken southeast of Juneau, Alaska; improper processing has decreased the signal-to-ambiguity ratio in a mountainous area. Note that in the left half of the image the ambiguities blend in with the rugged terrain and are difficult to distinguish from the natural scene, but in the right half they are obvious at the coastline.

Range ambiguities result from echoes from the extreme far range that have a round-trip time long enough to place them in the receive window intended for the succeeding pulse (or, conversely, echoes from near range with a round-trip short enough to place them in the receive

97

Figure 64. JPL aircraft SAR image of Golden Gate Bridge, San Francisco. Traffic going across the bridge is mispositioned because of its movement with respect to the bridge.

N ←   0   1 km   ↑ Illumination
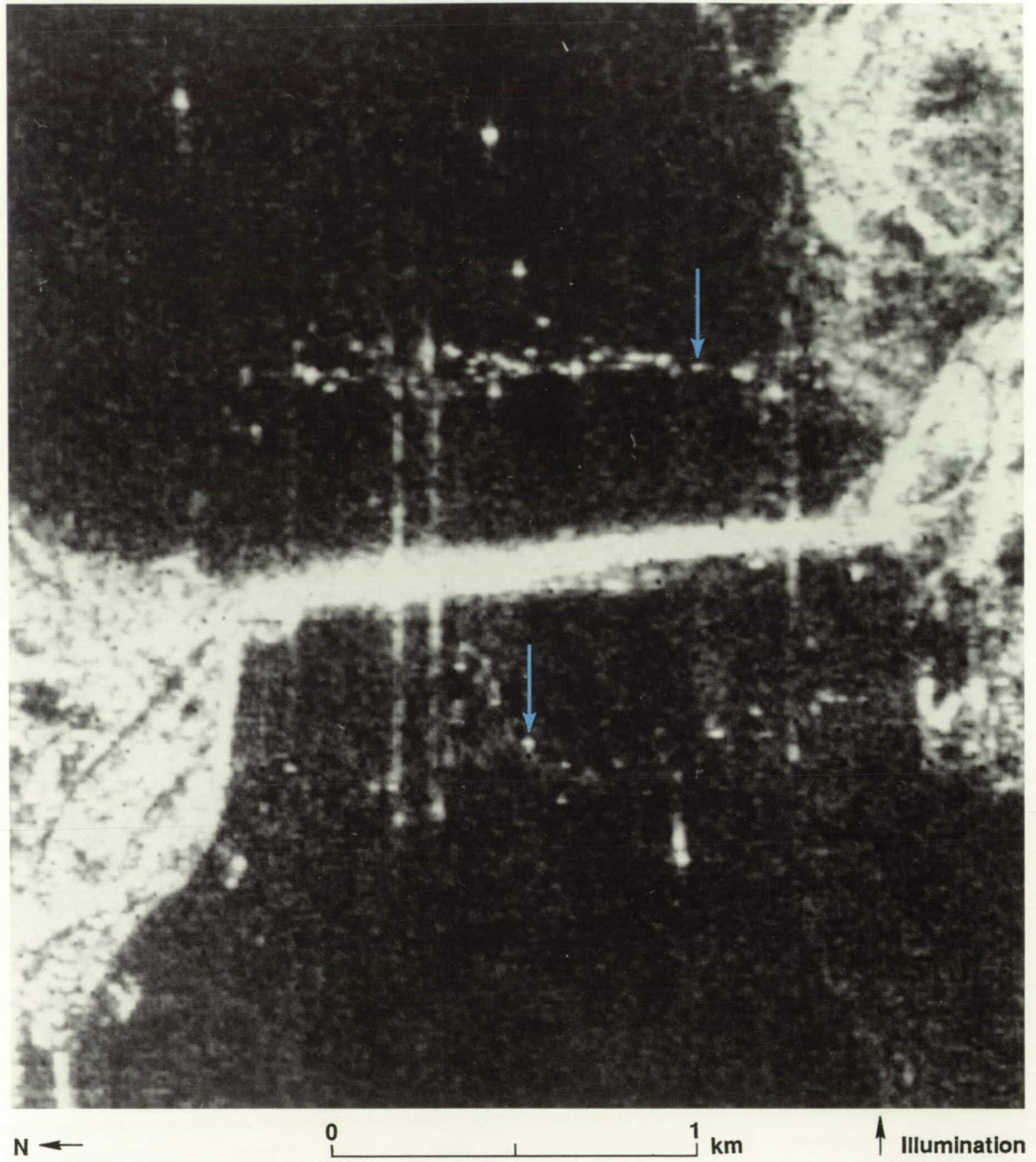
Figure 65. SIR-B image of a mountainous area near Juneau, Alaska, shows azimuth ambiguities because of improper processing.

N ↓   0   20 km   ↓ Illumination

98
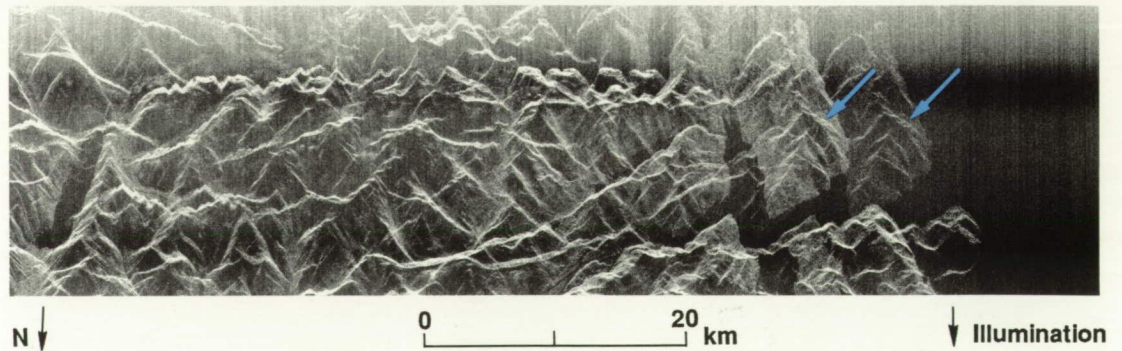
window intended for the preceding pulse). These echoes are also incorrectly placed in the image. The effect in the image is similar to that shown in Figure 63, but the additional extra time delay is not due to a characteristic of the target. Sidelobes in the antenna gain pattern, incorrect swath illumination, uncompensated roll of the sensor, and terrain effects all increase the possibility of range ambiguities.

Range-gate misalignment effects

One principal advantage of SAR is that it provides its own illumination source. There is, however, the associated complexity of integrating target illumination and echo reception: the receiver must be timed to acquire the echo from the same surface area illuminated by the antenna radiation pattern; this period is the receiver's "range gate." Since the latter alignment is one of geometry and the former one of timing, the relationship between the two changes with sensor altitude. Often the range gate must be changed during data acquisition to accommodate altitude changes. Near periapsis, the Magellan radar will change range gates many times per second. In situations where the sensor altitude is imperfectly known, the alignment of the antenna pattern and range gate may be likewise imperfect.

Two different kinds of artifacts can result from this procedure. First, a fade to black at one edge of the image can occur if the range gate and antenna pattern are not properly aligned, because the edge of the image will be determined by the edge of the range gate. Second, and much more likely to be misinterpreted, a repetition of data can result from a cross-track shift in ground-range coordinates; this shift occurs if the range gate is shifted and proper account is not taken of that fact when the data are correlated. Figure 66 illustrates this latter effect in a Seasat image of the Appalachian Mountains in Kentucky. A range-gate shift occurred in this image, and both the unshifted and shifted data occupied the same synthetic aperture. The feature indicated by arrows is prominent, but all data in the same azimuth band on the image are repeated.

Many of the artifacts illustrated in this chapter can be traced to characteristics unique to a particular system. The Magellan SAR has many unique design features made necessary by the elliptical orbit, the shared high-gain antenna, the limited data rate, and other aspects of the mission. Likewise, the Magellan data processing system has its unique aspects, such as multilook registration using spacecraft navigation and mosaicking. The SAR principles that underlie the system are familiar, but these new features will without doubt create their own brands of artifacts.
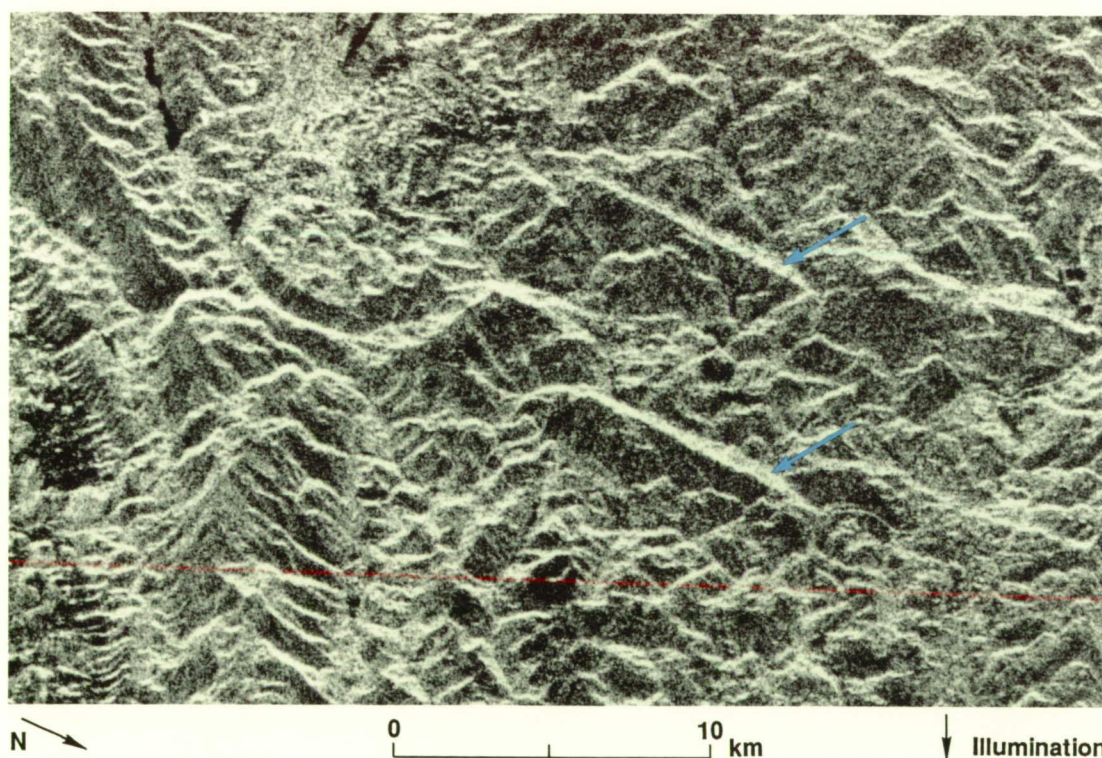
Figure 66. Seasat image of the Appalachian Mountains in Kentucky. A range-gate shift caused features in the image to double.

N

0   10 km

Illumination

99

References

Anderson, C.A., 1941, "Volcanoes of the Medicine Lake Highland, California," *Univ. Calif. Pub. Geol. Science,* v. 25, p. 344–422.

Arvidson, R.E., M. Schulte, R. Kwok, J. Curlander, C. Elachi, John P. Ford, and R.S. Saunders, 1988, "Construction and analysis of simulated Venera and Magellan images of Venus," *Icarus,* v. 75, p. 163–181.

Baloga, S., and D. Pieri, 1986, "Time-dependent profiles of lava flows," *J. Geophys. Res.,* v. 91, p. 9543–9552.

Barsukov, V.L., and A.T. Basilevsky, 1986, "The geology of Venus," NASA TM-88567, translation of "Geologiya Venery," *Priroda,* v. 6, p. 24–35.

Barsukov, V.L., A.T. Basilevsky, G.A. Burba, N.N. Bobinna, V.P. Kryuchkov, R.O. Kuzmin, O.V. Nikolaeva, A.A. Pronin, L.B. Ronca, I.M. Chernaya, V.P. Shashkina, A.V. Garanin, E.R. Kushky, M.S. Markov, A.L. Sukhanov, V.A. Kotelnikov, O.N. Rzhiga, G.M. Petrov, Yu.N. Alexandrov, A.I. Sidorenko, A.F. Bogomolov, G.I. Skrypnik, M.Yu. Bergman, L.V. Kudrin, I.M. Boksht-ein, M.A. Kronrod, P.A. Chochia, Yu. S. Tyuflin, S.A. Kadnichansky, and E.L. Akim, 1986, "The geology and geomorphology of the Venus surface as revealed by the radar images obtained by Veneras 15 and 16," *Proc. Lunar Planet. Science Conf. 16th,* in *J. Geophys. Res.,* v. 91, supp., p. D378–D398.

Barsukov, V.L., A.T. Basilevsky, R.O. Kuzmin, A.A. Pronin, V.P. Kryuchkov, O.V. Nikolaeva, I.M. Chernaya, G.A. Burba, N.N. Bobinna, V.P. Shaskina, M.S. Markov, and A.L. Sukhanov, 1984a, "Geology of Venus from the results of analysis of radar images taken by Venera 15 and Venera 16 probes —preliminary data," *Geokhimiya,* v. 12, p. 1811–1820.

Barsukov, V.L., A.T. Basilevsky, A.A. Pronin, R.O. Kuzmin, V.P. Kryuchkov, O.V. Nikolaeva, I.M. Chernaya, G.A. Burba, N.N. Bobinna, V.P. Shashkina, V.A. Kotelnikov, O.N. Rzhiga, G.M. Petrov, Yu. N. Alexandrov, Yu.I. Sidorenko, V.M. Kovtunenko, R.S. Kremnjev, A.F. Bogomolov, M.N. Menshikov, N.V. Zjerikhin, Yu.S. Tyuflin, E.L. Akim, M.S. Markov, and A.L. Sukhanov, 1984b, "The first results of geological-geomorphological analysis of the radar images of the surface of Venus obtained by spacecrafts Venera 15 and 16," (in Russian), *Akad. Nauk. SSSR Doklady,* v. 279, p. 946–950.

Basaltic Volcanism Study Project, 1981, *Basaltic Volcanism on the Terrestrial Planets,* New York: Pergamon Press, 1286 pp.

Basilevsky, A.T., and J.W. Head, III, 1988, "The geology of Venus," *Ann. Rev. Earth Planet. Science,* v. 16, p. 295–317.

Basilevsky, A.T., B.A. Ivanov, G.A. Burba, I.M. Chernaya, V.P. Kryuchkov, O.V. Nikolaeva, D.B. Campbell, and L.B. Ronca, 1987, "Impact craters of Venus: A continuation of the analysis of data from the Venera 15 and 16 spacecraft," *J. Geophys. Res.,* v. 92, no. B12, p. 12,869–12,901.

Basilevsky, A.T., A.A. Pronin, L.B. Ronca, V.P. Kryuchkov, A.L. Sukhanov, and M.S. Markov, 1986, "Styles of tectonic deformation on Venus: Analysis of Venera 15 and 16 data," *Proc. Lunar Planet. Science Conf. 16th,* in *J. Geophys. Res.,* v. 91, no. B4, supp., p. D399–D411.

Beatty, J.K., B. O'Leary, and A. Chaikin, eds., 1981, *The New Solar System,* New York: Cambridge University Press and Sky Publ., 224 pp.

Beikman, H.M., compiler, 1980, *Geologic Map of Alaska*, Washington, D.C.: U.S. Geological Survey, scale 1:2,500,000.

Berlin, G.L., G.G. Schaber, R.C. Kozak, and P. Chavez, Jr., 1982, "Cliff and slope topography of part of the Grand Canyon, Arizona as characterized on a Seasat radar image," *Remote Sensing of Environment*, v. 12, p. 81–85.

Berlin, G.L., M.A. Tarabzouni, A. Al-Nasser, K.M. Sheikho, and R.W. Larson, 1986, "SIR-B subsurface imaging of a sand-buried landscape: Al Labbah Plateau, Saudi Arabia," *I.E.E.E. Trans. Geoscience and Remote Sensing,* v. GE-24, p. 595–602.

Berlin, G.L., M.A. Tarabzouni, K.M. Sheikho, and A. Al-Nasser, 1985, "SIR-A and Landsat MSS observations of eolian sand deposits on the Al Labbah Plateau, Saudi Arabia," *Proc. Nineteenth Int. Symp. on Remote Sensing of Environment*, Ann Arbor, Michigan: Environmental Research Institute of Michigan, p. 311–321.

Blom, R.G., 1988, "Effects of variation in look angle and wavelength in radar images of volcanic and aeolian terrains, or now you see it, now you don't," *Int. J. Remote Sensing*, v. 9, p. 945–965.

Blom, R.G., P. Cooley, and L.R. Schenck, 1986, "On the relationship between age of lava flows and radar backscatter," *I.E.E.E. Int. Geoscience and Remote Sensing Symp.*, p. 1119–1127.

Blom, R.G., R.E. Crippen, and C. Elachi, 1984, "Detection of subsurface features in Seasat radar images of Means Valley, Mojave Desert, California," *Geology*, v. 12, p. 346–349.

Blom, R.G., and C. Elachi, 1981, "Spaceborne and airborne imaging radar observations of sand dunes," *J. Geophys. Res.*, v. 86, p. 3061–3073.

Blom, R.G., and C. Elachi, 1987, "Multifrequency and multipolarization radar scatterometry of sand dunes and comparison with spaceborne and airborne radar images," *J. Geophys. Res.*, v. 92, p. 7877–7889.

Blom, R.G., L.R. Schenck, and R.E. Alley, 1987, "What are the best radar wavelengths, incidence angles, and polarizations for discrimination among lava flows and sedimentary rocks?—A statistical approach," *I.E.E.E. Trans. Geoscience and Remote Sensing,* v. GE-25, p. 208–213.

Breed, C.S., M.J. Grolier, and J.F. McCauley, 1979, "Morphology and distribution of common 'sand' dunes on Mars: Comparison with the Earth," *J. Geophys. Res.*, v. 84, p. 8183–8204.

Burke, K.C., 1980, "Intracontinental rifts and aulacogens," *Geophys. Study Group, N.R.C. Continental Tectonics,* Washington, D.C.: National Academy of Sciences, p. 42–49.

Burns, B.A., and D.B. Campbell, 1985, "Radar evidence for cratering on Venus," *J. Geophys. Res.*, v. 90, p. 3037–3047.

Campbell, D.B., J.K. Harmon, A.A. Hine, and J.W. Head, 1983, "Venus - Identification of banded terrain in the mountains of Ishtar Terra," *Science*, v. 221, p. 644–647.

Campbell, D.B., J.W. Head, J.K. Harmon, and A.A. Hine, 1984, "Venus: Volcanism and rift formation in Beta Regio," *Science,* v. 226, p. 167–170.

Campbell, M.J., and J. Ulrichs, 1969, "Electrical properties of rocks and their significance for Lunar radar observations," *J. Geophys. Res.,* v. 74, p. 5867–5881.

Chapin, C.E., 1979, "Evolution of the Rio Grande Rift—A summary," *Rio Grande Rift: Tectonics and Magmatism*, R.E. Ricker, ed., Washington, D.C.: American Geophysical Union, p. 1–15.

Christiansen, R.L., and C.D. Miller, 1976, "Volcanic evolution of Mt. Shasta, California," *Geol. Soc. Amer. Abstracts with Programs,* v. 8, p. 360–361.

Churkin, M., Jr., H.L. Foster, R.M. Chapman, and F.R. Weber, 1982, "Terranes and suture zones in east central Alaska," *J. Geophys. Res.,* v. 87, no. B5, p. 3718–3730.

Coira, B., J. Davidson, C. Mpodozis, and V. Ramos, 1982, "Tectonic and magmatic evolution of the Andes of northern Argentina and Chile," *Magmatic Evolution of the Andes, Earth-Science Rev.,* v. 18, p. 303–332.

Coney, P.J., D.L. Jones, and J.W.H. Monger, 1980, "Cordilleran suspect terranes," *Nature,* v. 288, p. 329–333.

Cook, F.A., D.S. Albaugh, L.D. Brown, S. Kaufman, J.E. Oliver, and R.D. Hatcher, 1979, "Thin-skinned tectonics in the crystalline southern Appalachians: CO-CORP seismic reflection profiling of the Blue Ridge and Piedmont," *Geology,* v. 7, p. 563–567.

Cox, A., and R.B. Hart, 1986, *Plate Tectonics: How it Works,* Palo Alto, California: Blackwell Scientific Publications, 392 pp.

Crowell, J.C., ed., 1975, *San Andreas Fault in Southern California,* Sacramento, California: California Division of Mines and Geology, Special Report 118, 272 pp.

Crowell, J.C., 1979, "The San Andreas fault system through time," *J. Geol. Soc. London,* v. 136, p. 293–302.

Crumpler, L.S., and J.W. Head, 1988, "Bilateral topographic symmetry patterns across Aphrodite Terra, Venus," *J. Geophys. Res.,* v. 93, p. 301–312.

Crumpler, L.S., J.W. Head, and D.B. Campbell, 1986, "Orogenic belts on Venus," *Geology,* v. 14, p. 1031–1034.

Cutts, J.A., and R.S.U. Smith, 1973, "Eolian deposits and dunes on Mars," *J. Geophys. Res.,* v. 78, p. 4139–4154.

Dainty, J.C., ed., 1984, *Laser Speckle and Related Phenomena,* New York: Springer-Verlag, 342 pp.

Dallas, S.S., and N.L. Nickle, 1987, "The Magellan Mission to Venus. Advances in Astronautical Sciences," *Part 1, Aerospace Century 21,* AAS 86-331, v. 64.

Davis, G.A., and B.C. Burchfiel, 1973, "Garlock fault: An intracontinental transform structure, Southern California," *Geol. Soc. Amer. Bulletin,* v. 84, p. 1407–1422.

Dellwig, L.F., 1969, "An evaluation of multifrequency radar imagery of the Pisgah Crater area, California," *Modern Geology,* v. 1, p. 65–73.

Dellwig, L.F., and R.K. Moore, 1966, "The geological value of simultaneously produced like- and cross-polarized radar imagery," *J. Geophys. Res.,* v. 71, p. 3597–3601.

Derryberry, B.A., V.H. Kaupp, H.C. MacDonald, W.P. Waite, L.R. Gaddis, and P.J. Mouginis-Mark, 1985, "Introductory analyses of SIR-B radar data for Hawaii," *I.E.E.E. Int. Geoscience and Remote Sensing Symp. Digest,* p. 370–375.

Derryberry, B.A., W.P. Waite, V.H. Kaupp, H.C. MacDonald, L.R. Gaddis, and P. Mouginis-Mark, 1986, "Hawaiian lava flows and SIR-B results," *I.E.E.E. Int. Geoscience and Remote Sensing Symp.,* p. 497–501.

Dietz, R.S., 1961, "Astroblemes," *Scientific Amer.,* v. 205, p. 50–58.

Dietz, R.S., 1966, "Shatter cones at the Middlesboro Structure, Kentucky," *Meteoritics,* v. 3, p. 27–29.

Dietz, R.S., and J.F. McHone, 1976, "Elgygytgyn: Probably world's largest meteorite crater," *Geology,* v. 4, p. 391–392.

Doell, R.R., G.B. Dalrymple, R.L. Smith, and R.A. Bailey, 1968, "Paleomagnetism, potassium-argon ages, and geology of rhyolites and associated rocks of the Valles Caldera, New Mexico," *Geol. Soc. Amer. Memoir,* v. 116, p. 211–248.

Dokka, R.K., and C.J. Travis, 1989, "Late Cenozoic strike-slip faulting in the Mojave Desert, California," *Tectonics* (in press).

Donnelly, M., 1974, *Geology of the Sierra del Pinacate Volcanic Field, Northern Sonora, Mexico, and Southern Arizona, U.S.A.,* Ph.D. dissertation, Stanford University.

Donnelly-Nolan, J.M., and D.E. Champion, 1987, *Geologic Map of Lava Beds National Monument, Northern California,* U.S. Geological Survey Misc. Inv. Map I-1804, scale 1:24,000.

Elachi, C., 1980, "Spaceborne imaging radar: geologic and oceanographic applications," *Science,* v. 209, p. 1073–1082.

Elachi, C., 1987, *Introduction to the Physics and Techniques of Remote Sensing,* Wiley Series in Remote Sensing, New York: John Wiley and Sons, 413 pp.

Elachi, C., R. Blom, M. Daily, T. Farr, and R.S. Saunders, 1980, "Radar imaging of volcanic fields and sand dune fields: Implications for VOIR," in *Radar Geology: An Assessment,* JPL Publication 80-61, Pasadena, California: Jet Propulsion Laboratory, p. 114–150.

Elachi, C., and T.G. Farr, 1980, "Observation of the Grand Canyon wall structure with an airborne imaging radar," *Remote Sensing of Environment,* v. 9, p. 171–174.

Elachi, C., L.E. Roth, and G.G. Schaber, 1984, "Spaceborne radar subsurface imaging in hyperarid regions," *I.E.E.E. Trans. Geoscience and Remote Sensing,* v. GE-22, p. 383–388.

Elders, W.A., R.W. Rex, T. Meidav, P.T. Robinson, and S. Biehler, 1972, "Crustal spreading in Southern California," *Science,* v. 178, p. 15–24.

Englund, K.J., and J.B. Roen, 1962, *Origin of the Middlesboro Basin, Kentucky,* U.S. Geological Survey Prof. Paper 450-E, Article 184, p. E20–E22.

Evans, D.L., 1978, *Radar Observations of a Volcanic Terrain: Askja Caldera, Iceland,* JPL Publication 78-81, Pasadena, California: Jet Propulsion Laboratory, 39 pp.

Farr, T.G., and R.S. Anderson, 1987, "Simulation of surface modification processes in arid regions: Applications to remote sensing and the study of climate change," *Geol. Soc. Amer. Abstracts with Program.,* v. 19, p. 659.

Farr, T.G., C. Elachi, M. Daily, and R. Blom, 1981, "Imaging radar observations of volcanic features in Medicine Lake Highland, California," *I.E.E.E. Int. Geoscience and Remote Sensing Symp. Digest,* p. 872–877.

Farr, T.G., and N. Engheta, 1983, "Quantitative comparisons of radar image, scatterometer, and surface roughness data from Pisgah Crater, California," *I.E.E.E. Int. Geoscience and Remote Sensing Symp. Digest,* p. 2.1–2.6.

Farr, T.G., and D. Massonnet, 1985, "The use of multi-incidence angle radar images for geologic mapping," *Proc. Int. Symp. on Remote Sensing of Environment, 4th Thematic Conf., Remote Sensing for Exploration Geology,* Ann Arbor, Michigan: Environmental Research Institute of Michigan, p. 553.

Fielding, E.J., W.J. Knox, Jr., and A.L. Bloom, 1986, "SIR-B radar imagery of volcanic deposits in the Andes," *I.E.E.E. Trans. Geoscience and Remote Sensing,* v. GE-24, p. 582–589.

Fink, J.H., 1980, "Surface folding and viscosity of rhyolite flows," *Geology,* v. 8, p. 250–254.

Fink, J.H., and J.R. Zimbelman, 1986, "Rheology of the 1983 Royal Gardens basalt flows, Kilauea Volcano, Hawaii," *Bulletin Volcanol.,* v. 48, p. 87–96.

Floran, R.J., and M.R. Dence, 1976, "Morphology of the Manicouagan ring-structure, Quebec, and some comparisons with lunar basins and craters," *Proc. Lunar Science Conf. 7th,* p. 2845–2865.

Ford, J.P., 1980, "Seasat orbital radar imagery for geologic mapping: Tennessee—Kentucky—Virginia," *Amer. Assoc. Petroleum Geologists Bulletin,* v. 64, p. 2064–2094.

Ford, J.P., 1982, "Resolution versus speckle relative to geologic interpretability of spaceborne radar images: A survey of user preference," *I.E.E.E. Trans. Geoscience and Remote Sensing,* v. GE-20, p. 434–444.

Ford, P.G., 1986, "Pioneer Venus Hypsometry," paper submitted to the Magellan Project in response to Critical Design Review Action Item 33 regarding topographic model of Venus (JPL internal document).

Gaddis, L.R., P.J. Mouginis-Mark, V.H. Kaupp, H.C. MacDonald, and W.P. Waite, 1985, "Preliminary geologic analysis of SIR-B radar data for Hawaii," *I.E.E.E. Int. Geoscience and Remote Sensing Symp. Digest,* p. 364–369.

Gaddis, L., P. Mouginis-Mark, R. Singer, and V. Kaupp, 1989, "Geologic analyses of Shuttle Imaging Radar (SIR-B) data of Kilauea Volcano, Hawaii," *Geol. Soc. Amer. Bulletin,* v. 101, p. 317–332.

Gardner, J.N., and F. Goff, 1984, "Potassium-argon dates from the Jemez Volcanic Field: Implications for tectonic activity in the north-central Rio Grand Rift," in *New Mexico Geol. Soc. Guidebook 35th Field Conf.,* Rio Grande Rift, Northern New Mexico, p. 75–81.

Garvin, J.B., J.W. Head, and L. Wilson, 1982, "Magma vesiculation and pyroclastic volcanism on Venus," *Icarus,* v. 52, p. 365–372.

Gawarecki, S.J., 1964, "Geologic reconnaissance report of the Pisgah Crater, California area," *Earth Resources Survey Program Technical Letter NASA - 2,* unpublished report, 12 pp.

Golombek, M.P., G.E. McGill, and L. Brown, 1983, "Tectonic and geologic evolution of the Española Basin, Rio Grand Rift: Structure, rate and extension, and relation to the state of stress in the western United States," *Tectonophysics,* v. 94, p. 483–507.

Greeley, R., 1977, "Volcanic morphology," in *Volcanism of the Eastern Snake River Plain, Idaho: A Comparative Planetary Geology Guidebook,* R. Greeley and J.S. King, eds., NASA CR 154621, Washington, D.C.: National Aeronautics and Space Administration, p. 5–22.

Greeley, R., 1982, "The Snake River Plain, Idaho: Representative of a new category of volcanism," *J. Geophys. Res.,* v. 87, p. 2705–2712.

Greeley, R., P.R. Christensen, and J.F. McHone, 1987, "Radar characteristics of small craters: Implications for Venus," *Earth, Moon, and Planets,* v. 37, p. 89–111.

Greeley, R., P.R. Christensen, J.F. McHone, Y. Asmerom, and J.R. Zimbelman, 1985, *Analysis of the Gran Desierto-Pinacate Region, Sonora, Mexico, via Shuttle Imaging Radar,* NASA CR 177356, Washington, D.C.: National Aeronautics and Space Administration, 44 pp.

Greeley, R., and J.D. Iversen, 1985, *Wind as a Geological Process on Earth, Mars, Venus, and Titan,* Cambridge: Cambridge University Press, 333 pp.

Greeley, R., N. Lancaster, R. Sullivan, R.S. Saunders, E. Theilig, S. Wall, A. Dobrovolskis, B.R. White, and J.D. Iversen, 1988, "A relationship between radar backscatter and aerodynamic roughness: Preliminary results," *Geophys. Res. Lett.*, v. 15, p. 565–568.

Greeley, R., and J.R. Marshall, 1985, "Transport of Venusian rolling 'stones' by wind?" *Nature*, v. 313, p. 771–773.

Greeley, R., J.R. Marshall, and R.N. Leach, 1984, "Microdunes and other eolian bedforms on Venus: Wind tunnel simulations," *Icarus*, v. 60, p. 152–160.

Greeley, R., and L. Martel, 1988, "Radar observations of basaltic lava flows, Craters of the Moon, Idaho," *Int. J. Remote Sensing*, v. 9, p. 1071–1085.

Greeley, R., and H. Sigurdsson, 1980, *Pristine Morphology of a Quasi-Flood Basalt Flow: The Barthardalshraun of Trolladyngja, Iceland*, NASA TM-82385, Washington, D.C.: National Aeronautics and Space Administration, p. 245–246.

Greeley, R., B.R. White, R. Leach, R. Leonard, J. Pollack, and J.D. Iversen, 1980, *Venus Aeolian Processes: Saltation Studies and the Venusian Wind Tunnel*, NASA TM-82385, Washington, D.C.: National Aeronautics and Space Administration, p. 275–277.

Greeley, R., S. Williams, J.D. Iversen, R. Leach, B.R. White, and J. Pollock, 1982, "Windblown sand on Venus: Preliminary laboratory simulations," *EOS*, v. 63, p. 1021.

Grieve, R.A.F., 1987, "Terrestrial impact structures," *Ann. Rev. Earth Planet. Science*, v. 15, p. 245–270.

Grieve, R.A.F., and J.W. Head, 1983, "The Manicouagan impact structure: An analysis of its original dimensions and form," *J. Geophys. Res.*, v. 88, supp., p. A807–A818.

Grieve, R.A.F., and P.R. Robertson, 1987, *Terrestrial Impact Structures*, Geological Survey Canada, Map 1658A, scale 1:63,000,000.

Grieve, R.A.F., C.A. Wood, J.B. Garvin, G. McLaughlin, and J.F. McHone, eds., 1988, *Astronauts Guide to Terrestrial Impact Craters*, LPI Technical Report 88-03, Houston: Lunar and Planetary Institute, 89 pp.

Guest, J.E., 1969, "Upper tertiary ignimbrites in the Andean Cordillera of part of the Antofagasta Province, northern Chile," *Geol. Soc. Amer. Bulletin*, v. 80, p. 337–362.

Gutmann, J.T., 1972, *Eruptive History and Petrology of Crater Elegante, Sonora, Mexico*, Ph.D. dissertation, Stanford University.

Gutmann, J.T., 1976, "Geology of Crater Elegante, Sonora, Mexico," *Geol. Soc. Amer. Bulletin*, v. 87, p. 1718–1729.

Gutmann, J.T., and M.F. Sheridan, 1978, "Geology of the Pinacate Volcanic Field," in *Guidebook to the Geology of Central Arizona*, D.M. Burt, and T.L. Pewe, eds., Arizona Bureau of Geology and Mining Technology, Special Paper 2, p. 47–59.

Gwinn, V.E., 1964, "Thin-skinned tectonics in the Plateau and northwestern Valley and Ridge Provinces of the Central Appalachians," *Geol. Soc. Amer. Bulletin*, v. 75, p. 863–900.

Hall, J., 1859, *Natural History of New York, 3, Paleontology*, New York: Appleton.

Harris, S.L., 1980, *Fire and Ice: The Cascade Volcanoes*, Seattle, Washington: The Mountaineers, 316 pp.

Harris, L.D., A.G. Harris, W. de Witt, Jr., and K.C. Bayer, 1981, "Evaluation of southern eastern overthrust belt beneath Blue Ridge-Piedmont Thrust," *Amer. Assoc. Petroleum Geologists Bulletin*, v. 65, p. 2497–2505.

Harris, L.D., and R.C. Milici, 1977, *Characteristics of Thin-Skinned Style Deformation in the Southern Appalachians, and Potential Hydrocarbon Traps*, U.S. Geological Survey Prof. Paper 1018, 40 pp.

Hatheway, A., 1971, *Lava Tubes and Collapse Depressions*, Ph.D. dissertation, Univ. of Arizona.

Head, J.W., and L.S. Crumpler, 1987, "Evidence for divergent plate boundary characteristics and crustal spreading on Venus," *Science*, v. 238, p. 1380–1385.

Head, J.W., and L. Wilson, 1986, "Volcanic processes and landforms on Venus: Theory, predictions, and observations," *J. Geophys. Res.*, v. 91, p. 9407–9446.

Hester, R.L., and D.E. Hallinger, eds., 1987, *The San Andreas Fault—Cajon Pass to Palmdale*, Pacific Section, Amer. Assoc. of Petroleum Geologists, Volume and Guidebook No. 59, 179 pp.

Holcomb, R.T., 1987, *Eruptive History and Long-Term Behavior of Kilauea Volcano*, U.S. Geological Survey Prof. Paper 1350, p. 261–350.

Hulme, G., 1974, "The interpretation of lava flow morphology," *Geophys. J. Royal Astron. Soc.*, v. 39, p. 361–383.

Hulme, G., and G. Fielder, 1977, "Effusion rates and rheology of lunar lavas," *Phil. Trans. Royal Soc. London*, v. A285, p. 227–234.

Hunt, G.R., and P. Moore, 1981, *Jupiter*, New York: Rand McNally, 96 pp.

Ivanov, B.A., A.T. Basilevsky, V.P. Kryuchkov, and I.M. Chernaya, 1986, "Impact craters on Venus: Analysis of Venera 15 and 16 data," *Proc. Lunar Planet. Science Conf. 16th*, in *J. Geophys. Res.*, v. 91, no. B4, supp., p. D413–D430.

Jacob, K.H., and R.L. Quittmeyer, 1979, "The Makran Region of Pakistan and Iran: Trench-arc system with active plate subduction," in *Geodynamics of Pakistan*, A. Farah and K.A. DeJong, eds., Quetta, Pakistan: Geological Survey of Pakistan, p. 305–316.

Jahns, R.H., 1959, "Collapse depressions of the Pinacate Volcanic Field, Sonora, Mexico," *Southern Arizona Guidebook 2*, Arizona Geological Society, p. 165–184.

Jahns, R.H., and R.G. Fielder, 1952, "Collapsed volcano," *Engineering and Science*, v. 15, p. 13–16.

Johnson, W.T.K., 1989, "Radar system design for the Magellan radar mission to Venus," *Proc. Int. Soc. Photogrammetry and Remote Sensing*, Kyoto, Japan (in press).

Johnson, W.T.K., and A.T. Edgerton, 1985, "Venus Radar Mapper (VRM): Multimode radar system design," SPIE, *Instrumen. Opt. Remote Sensing Space*, v. 589, p. 158–164.

Jones, D.L., D.G. Howell, P.J. Coney, and J.W.H. Monger, 1983, "Recognition, character, and analysis of tectonostratigraphic terranes in western North America," in *Accretion Tectonics in the Circum-Pacific Regions*, M. Hashimoto and S. Uyeda, eds., Tokyo: Terra Scientific Publ. Co.

Jones, D.L., N.J. Silberling, and P.J. Coney, 1986, "Collision tectonics in the Cordillera of western North America: Examples from Alaska," in *Collision Tectonics*, M.P. Coward and A.C. Ries, eds., Geological Society of London, Special Pub. 19, p. 367–387.

Jones, D.L., N.J. Silberling, P.J. Coney, and G. Pflaker, 1987, *Lithotectonic Terrane Map of Alaska (West of the 141st Meridian)*, U.S. Geological Survey Misc. Field Studies Map MF-1874-A, scale 1:2,500,000.

Jurgens, R.F., M.A. Slade, and R.S. Saunders, 1988, "Evidence for highly reflecting materials on the surface and subsurface of Venus," *Science*, v. 240, p. 1021–1023.

Keldysh, M.V., 1977, "Venus exploration with Venera 9 and Venera 10 spacecraft," *Icarus*, v. 30, p. 605–625.

Kilburn, C.R.J., 1981, "Pahoehoe and aa lavas: A discussion and continuation of the model of Peterson and Tilling," *J. Volcanol. Geotherm. Res.*, v. 11, p. 373–382.

Kjartansson, G., 1965, *Geological Map of Iceland, Sheet 5, Central Iceland*, Reykjavik, Iceland: Museum of Natural History, Dept. Geol. Geogr., scale 1:250,000.

Kotelnikov, V.A., E.L. Akim, Yu.N. Alexandrov, N.A. Armand, A.T. Basilevsky, A.F. Bogomolov, V.M. Dubrovin, B. Feldman, V.I. Kaevitser, and V.M. Kovtunenko, 1984, "The Maxwell Montes Region surveyed by the Venera 15 and 16 Orbiters," (translation), *Soviet Astron. Lett.*, v. 10, p. 369–373.

Kozak, R.C., and G.G. Schaber, 1989, "New evidence for global tectonic zones on Venus," *Geophys. Res. Lett.*, v. 16, p. 175–178.

Kuntz, M.A., D.E. Champion, R.H. Lefebvre, and H.R. Covington, 1988, *Geologic Map of the Craters of the Moon, Kings Bowl, and Wapi Lava Fields, and the Great Rift Volcanic Rift Zone, South-Central Idaho*, U.S. Geological Survey Misc. Inv. Map I-1632, scale 1:100,000.

Kuntz, M.A., D.E. Champion, E.C. Spiker, and R.H. Lefebvre, 1986a, "Contrasting magma types and steady-state, volume-predictable, basaltic volcanism along the Great Rift, Idaho," *Geol. Soc. Amer. Bulletin*, v. 97, p. 579–594.

Kuntz, M.A., R.H. Lefebvre, D.E. Champion, J.S. King, and H.R. Covington, 1983, "Holocene basaltic volcanism along the Great Rift, central and eastern Snake River Plain, Idaho," in *Guidebook, Part 3, Geological Soc. Amer. Rocky Mountain and Cordilleran Sections Meeting*, Utah Geological and Mineral Survey Special Studies, v. 61, p. 1–34.

Kuntz, M.A., E.C. Spiker, M. Rubin, D.E. Champion, and R.H. Lefebvre, 1986b, "Radiocarbon studies of latest Pleistocene and Holocene lava flows of the Snake River Plain, Idaho: Data, lessons, interpretations," *Quat. Res.*, v. 25, p. 163–176.

Kupfer, D.H., and A.M. Bassett, 1962, *Geologic Reconnaissance Map of Part of the Southeastern Mojave Desert, California*, U.S. Geological Survey Mineral Inv. Field Studies Map MF-205, scale 1:125,000.

Kussmaul, S., L. Jordan, and E. Ploskonka, 1975, "Isotopic ages of Tertiary volcanic rocks of SW Bolivia," *Geol. Jahrb. Reihe*, v. B.14, p. 111–120.

Kwok, R., J. Curlander, and S. Pang, 1987, "Rectification of terrain induced distortions in radar imagery," *Photogrammetric Engineering and Remote Sensing*, v. 53, no. 5, p. 507–513.

Lambert, P., J.F. McHone, Jr., R.S. Dietz, and M. Houfani, 1980, "Impact and impact-like structures in Algeria, Part I. Four bowl-shaped depressions," *Meteoritics*, v. 15, p. 157–178.

Lawrence, R.D., S.H. Khan, K.A. DeJong, A. Farah, and R.S. Yeats, 1981, "Thrust and strike slip fault interaction along the Chaman transform zone, Pakistan," in *Thrust and Nappe Tectonics*, K. McClay and J.J. Price, eds., Geological Society of London, Special Pub. 9, p. 363–370.

Leberl, F.W., G. Domik, J. Raggam, and M. Kobrick, 1986, "Radar stereomapping techniques and application to SIR-B images of Mt. Shasta," *I.E.E.E. Trans. Geoscience and Remote Sensing*, v. GE-24, p. 473–481.

Lefebvre, R.H., 1975, "Mapping in Craters of the Moon Volcanic Field, Idaho, with Landsat (ERTS) imagery," *Proc. Tenth Int. Symp. on Remote Sensing of Environment,* Ann Arbor, Michigan: Environmental Research Institute of Michigan, p. 951–963.

Macdonald, G.A., 1953, "Pahoehoe, aa, and block lava," *Amer. J. Science,* v. 251, p. 169–191.

MacDonald, H.C., 1980, "Techniques and applications of imaging radars," in *Remote Sensing in Geology*, p. 297–336, B. Siegal and A. Gillespie, eds., New York: John Wiley & Sons.

MacDonald, H.C., and W.P. Waite, 1973, "Imaging radars provide terrain texture and roughness parameters in semi-arid environments," *Modern Geology,* v. 4, p. 145–158.

Mackenzie, J.S., and P.S. Ringrose, 1986, "Use of Seasat SAR imagery for geological mapping in a volcanic terrain: Askja Caldera, Iceland," *Int. J. Remote Sensing,* v. 7, p. 181–194.

Magellan Mission Plan, 1988, Document 630-50, Revision B, Jet Propulsion Laboratory, Pasadena, California (JPL internal document D-0651).

Magellan Science Requirements Document, 1987, Publication 630-6, Jet Propulsion Laboratory, Pasadena, California (JPL internal document D-1814).

Magellan Software Interface Specification, Full-Resolution Basic Image Data Record and Full-Resolution Temporary Basic Image Data Record, 1988, Report RDPS-101, Jet Propulsion Laboratory, Pasadena, California (JPL internal document).

Malin, M.C., 1980, "Lengths of Hawaiian lava flows," *Geology,* v. 8, p. 306–308.

Malin, M.C., D. Dzurisin, and R.P. Sharp, 1983, "Stripping of Keanakakoi tephra on Kilauea Volcano, Hawaii," *Geol. Soc. Amer. Bulletin,* v. 94, p. 1148–1158.

Malin, M.C., D. Evans, and C. Elachi, 1978, "Imaging radar observations of Askja Caldera, Iceland," *Geophys. Res. Lett.,* v. 5, p. 931–934.

Mann, P., M.R. Hempton, D.C. Bradley, and K. Burke, 1983, "Development of pull-apart basins," *J. Geol.,* v. 91, p. 529–554.

Martin-Kaye, P.H., and G.M. Lawrence, 1983, "The application of satellite imaging radars over land to the assessment, mapping and monitoring of resources," *Phil. Trans. Royal Soc. London,* v. A309, p. 295–314.

Masursky, H., E. Eliason, P.G. Ford, G.E. McGill, G.H. Pettengill, G.G. Schaber, and G. Schubert, 1980, "Pioneer Venus radar results: Geology from images and altimetry," *J. Geophys. Res.,* v. 85, p. 8232–8260.

McCauley, J.F., C.S. Breed, G.G. Schaber, W.P. McHugh, B. Issawi, C.V. Haynes, M.J. Grolier, and A. El Kilani, 1986, "Paleodrainages of the eastern Sahara—The radar rivers revisited (SIR-A/B implications for a mid-Tertiary trans-African drainage system)," *I.E.E.E. Trans. Geoscience and Remote Sensing,* v. 24, p. 624–648.

McCauley, J.F., G.G. Schaber, C.S. Breed, M.J. Grolier, C.V. Haynes, B. Issawi, C. Elachi, and R. Blom, 1982, "Subsurface valleys and geoarchaeology of eastern Sahara revealed by shuttle radar," *Science,* v. 218, p. 1044–1019.

McDonough, M., and P.H.A. Martin-Kaye, 1984, "Radargeologic interpretation of Seasat imagery of Iceland," *Int. J. Remote Sensing,* v. 5, p. 433–450.

McGill, G.E., S.J. Steenstrup, C. Barton, and P.G. Ford, 1981, "Continental rifting and the origin of Beta Regio, Venus," *Geophys. Res. Lett.,* v. 8, p. 737–740.

McGill, G.E., J.L. Warner, M.C. Malin, R.E. Arvidson, E. Eliason, S. Nozette, and R.D. Reasenberg, 1983, "The interior of Venus and tectonic implications," in *Venus*, D.M. Hunten, L. Colin, T.M. Donahue, and V.I. Moroz, eds., Tucson: The University of Arizona Press, p. 69–130.

McHone, J.F., and R. Greeley, 1987, "Talemzane: Algerian impact crater detected on SIR-A orbital imaging radar," *Meteoritics*, v. 22, p. 253–264.

McKee, E.D., ed., 1979, *A Study of Global Sand Seas*, U. S. Geological Survey Prof. Paper 1052, Washington, D.C.: U.S. Government Printing Office, 429 pp.

Molnar, P., and P. Tapponnier, 1975, "Cenozoic tectonics of Asia: Effects of continental collision," *Science*, v. 189, p. 419-425.

Molnar, P., and P. Tapponnier, 1977, "The collision between India and Eurasia," *Scientific Amer.*, v. 236, no. 4, p. 30-41.

Moore, H.J., D.W.G. Arthur, and G.G. Schaber, 1978, "Yield strengths of flows on the Earth, Mars, and Moon," *Proc. Lunar Planet. Science Conf. 9th*, p. 3351–3378.

Moore, H.J., and G.G. Schaber, 1975, "An estimate of the yield strength of the imbrium flows," *Proc. Lunar Science Conf. 6th*, p. 101–118.

Moore, R.K., W.P. Waite, J.R. Lundien, and H.W. Masenthin, 1968, "Radar scatterometer data analysis techniques," *Proc. Fifth Int. Symp. on Remote Sensing of Environment*, Ann Arbor, Michigan: Environmental Research Institute of Michigan, p. 765–780.

Nikolaeva, O.V., L.B. Ronca, and A.T. Basilevsky, 1986, "Circular features on the plains of Venus as an indication of their geologic history," (in Russian), *Geokhimiya*, no. 5, p. 579–589.

Nozette, S., and J.S. Lewis, 1982, "Venus: Chemical weathering of igneous rocks and buffering of atmospheric composition," *Science*, v. 216, p. 181–183.

Papson, R.P., 1977, "Geological guide to Craters of the Moon National Monument," in *Volcanism of the Eastern Snake River Plain, Idaho: A Comparative Planetary Geology Guidebook*, R. Greeley and J.S. King, eds., NASA CR-154621, Washington, D.C.: National Aeronautics and Space Administration, p. 216–232.

Peake, W.H., and Oliver, T.L., 1971, *The Response of Terrestrial Surfaces at Microwave Frequencies*, U.S. Air Force Avionics Laboratory Technical Report, AFAL-TR-70-301, Columbus, Ohio: Ohio State University, 255 pp.

Peltzer, G., and P. Tapponnier, 1988, "Formation and evolution of strike-slip faults, rifts, and basins during the India-Asia collision: An experimental approach," *J. Geophys. Res.*, v. 93, no. B12, p. 15,085–15,117.

Peterson, D.W., and R.I. Tilling, 1980, "Transition of basaltic lava from pahoehoe to aa, Kilauea Volcano, Hawaii: Field observations and key factors," *J. Volcanol. Geotherm. Res.*, v. 7, p. 271–293.

Pettengill, G.H., E. Eliason, P.G. Ford, G.B. Loriot, H. Masursky, and G.E. McGill, 1980, "Pioneer-Venus radar results: Altimetry and surface properties," *J. Geophys. Res.*, v. 85, p. 8261–8270.

Pettengill, G.H., P.G. Ford, and B.D. Chapman, 1988, "Venus: Surface electromagnetic properties," *J. Geophys. Res.*, v. 93, p. 14,881–14,892.

Pike, R.J., 1974, "Craters on Earth, Moon, and Mars—Multivariate classification and mode of origin," *Earth and Planet. Science Lett.*, v. 22, no. 3, p. 245–255.

Powers, H.A., 1948, "A chronology of explosive eruptions of Kilauea," *Pacific Science,* v. 2, p. 278–292.

Preusser, H., 1976, *The Landscapes of Iceland: Types and Regions,* The Hague: Dr. W. Junk B.V.

Prinz, M., 1970, "Idaho rift system, Snake River Plain, Idaho," *Geol. Soc. Amer. Bulletin,* v. 81, p. 941–948.

Projeto Radambrasil, 1975, *Folha NA. 20 Boa Vista e parte das folhas NA. 21 Tumucumaque, NB. 20 Roraima e NB. 21,* Rio de Janeiro, v. 8, geological map, scale 1:1,000,000.

Projeto Radambrasil, 1976, *Folha NA. 19 Pico da Neblina,* Rio de Janeiro, v. 11, geological map, scale 1:1,000,000.

Reidel, S.P., K.R. Fecht, and R.W. Cross, 1982, "Constraints on tectonic models for the Columbia Plateau from age and growth rates of Yakima folds," in *Proc. 33rd Alaska Science Conf.,* Arctic Division, Washington, D.C.: Amer. Assoc. for the Advancement of Science, p. 131.

Reidel, S.P., G.R. Scott, D.R. Bazard, R.W. Cross, and B. Dick, 1984, "Post-12 million year clockwise rotation in the central Columbia Plateau, Washington," *Tectonics,* v. 3, p. 251–273.

Rittmann, A., 1962, *Volcanoes and Their Activity,* Interscience Publ., New York: John Wiley & Sons, 305 pp.

Robinson, P.T., W.A. Elders, and L.P.J. Muffler, 1976, "Quaternary volcanism in the Salton Sea geothermal field, Imperial Valley, California," *Geol. Soc. Amer. Bulletin,* v. 87, p. 347–360.

Ross, C.S., R.L. Smith, and R.A. Bailey, 1961, "Outline of the geology of the Jemez Mountains, New Mexico," in *New Mexico Geological Soc. Guidebook 12th Field Conf.,* p. 138–143.

Roth L.E., and C. Elachi, 1975, "Coherent electromagnetic losses by scattering from volume inhomogeneities," *I.E.E.E. Trans. Antennas and Propagation,* v. AP-23, p. 674–675.

Rothery, D.A., and R.H. Lefebvre, 1985, "The causes of age dependent changes in the spectral response of lavas, Craters of the Moon, Idaho, USA," *Int. J. Remote Sensing,* v. 6, no. 8, p. 1483–1489.

Sabins, F.F., Jr., 1987, *Remote Sensing: Principles and Interpretation,* 2nd ed., New York: W. H. Freeman and Co., 449 pp.

Sabins, F.F., Jr., R. Blom, and C. Elachi, 1980, "Seasat radar image of San Andreas Fault, California," *Amer. Assoc. Petroleum Geologists Bulletin,* v. 64, p. 619–628.

Saemundsson, K., 1977, *Geological Map of Iceland, Sheet 7, North East Iceland,* Reykjavik, Iceland: Museum of Natural History, Iceland Geodetic Survey, scale 1:250,000.

Saunders, R.S., and M.C. Malin, 1976, "Venus: Geologic analysis of radar images," *Geologica Romana,* Proc. Int. Colloq. of Planet. Geol., v. 15, p. 507–515.

Saunders, R.S., and M.C. Malin, 1977, "Geologic interpretation of new observations of the surface of Venus," *Geophys. Res. Lett.,* v. 4, p. 547–550.

Schaber, G.G., 1982, "Venus: Limited extension and volcanism along zones of lithospheric weakness," *Geophys. Res. Lett.,* v. 9, p. 499–502.

Schaber, G.G., G.L. Berlin, and W.E. Brown, 1976, "Variations in surface roughness within Death Valley, California: Geologic evaluation of 25-cm-wavelength radar images," *Geol. Soc. Amer. Bulletin,* v. 87, p. 29–41.

Schaber, G.C., C. Elachi, and T.G. Farr, 1980, "Remote sensing data of SP Mountain and SP lava flow in north-central Arizona," *Remote Sensing of Environment*, v. 9, p. 149–170.

Schaber, G.G., E.M. Shoemaker, and R.C. Kozak, 1987, "The surface age of Venus: Use of terrestrial cratering record," *Solar Sys. Res.*, v. 21, p. 89–94.

Schwab, K., and H. Lippolt, 1976, "K-Ar mineral ages and late Cenozoic history of the Salar de Cauchari area (Argentine Puna)," in *Proc. Symp. Andean Antarct. Volcanol. Probl.*, O. Gonzalez Ferran, ed., Int. Assoc. Volcan. Chem. Earth's Interior, Special Ser., p. 698–714.

Self, S., F. Goff, J.N. Gardner, J.V. Wright, and W.M. Kite, 1986, "Explosive rhyolitic volcanism in the Jemez Mountains: Vent locations, caldera development and relation to regional structure," *J. Geophys. Res.*, v. 91, p. 1779–1798.

Self, S., D.E. Kircher, and J.A. Wolff, 1988, "The El Cajete series, Valles Caldera, New Mexico," *J. Geophys. Res.*, v. 93, p. 6113–6127.

Serpa, L., 1987, "The three-dimensional geometry of the Garlock Fault Zone," *Geol. Soc. Amer. Abstracts with Programs*, v. 19, p. 838.

Sharp, R.P., 1954, "Physiographic features of faulting in Southern California: Chapter V—Geomorphology," *Geology of Southern California*, Jahns, R.H., ed., California Division of Mines and Geology Bulletin, v. 170, p. 21–28.

Shoemaker, E.M., and S.W. Kieffer, 1974, *Guidebook to the Geology of Meteor Crater, Arizona*, 37th Ann. Meet. Meteor. Soc., 66 pp. including geologic map.

Sigurdsson, H., and R.S.J. Sparks, 1978, "Rifting episode in north Iceland in 1874-1875 and the eruptions of Askja and Sveinagja," *Bulletin Volcanol.*, v. 41, p. 149–167.

Smith, R. L., and R. Bailey, 1966, "The Bandelier Tuff: A study of ash-flow eruption cycles from zoned magma chambers," *Bulletin Volcanol.*, v. 29, p. 83–104.

Smith, R.L., and R.A. Bailey, 1968, "Resurgent cauldrons," *Geol. Soc. Amer. Memoir*, v. 116, p. 613–661.

Solomon, S.C., and J.W. Head, 1982, "Mechanisms for lithospheric heat transport on Venus: Implications for tectonic style and volcanism," *J. Geophys. Res.*, v. 87, p. 9236–9246.

Sparks, R.S.J., L. Wilson, and H. Sigurdsson, 1981, "The pyroclastic deposits of the 1875 eruption of Askja, Iceland," *Phil. Trans. Royal Soc. London*, v. A299, p. 241–273.

Stofan, E.R., J.W. Head, and D.B. Campbell, 1987, "Geology of the southern Ishtar Terra/ Guinevere and Sedna Planitae Region on Venus," *Earth, Moon, and Planets*, v. 38, p. 183–207.

Sugiura, R., and F. Sabins, 1980, "The evaluation of 3-cm-wavelength radar mapping for surface deposits in the Bristol Lake/Granite Mountain area, Mojave Desert, California," in *Radar Geology: An Assessment*, JPL Publication 80-61, Pasadena, California: Jet Propulsion Laboratory, p. 439–456.

Surkov, Yu.A., V.L. Barsukov, L.P. Moskalyova, V.P. Kharyukova, and A.L. Kemurdzhian, 1984, "New data on the composition, structure and properties of Venus rock obtained by Venera 13 and 14," *Proc. Lunar Planet. Science Conf. 14th*, in *J. Geophys. Res.*, v. 89, supp., p. B393–B402.

Surkov, Yu.A., F.F. Kirnozov, V.N. Glazov, A.G. Dunchenko, L.P. Tatsy, and O.P. Sobornov, 1987, "Uranium, thorium, and potassium in the Venusian rocks at the landing sites of Vega 1 and 2," *Proc. Lunar Planet. Science Conf. 17th*, in *J. Geophys. Res.*, v. 92, supp., p. E537–E540.

Surkov, Yu.A., L.P. Moskalyova, V.P. Karyukova, A.D. Dudin, G.G. Smirnov, and S.Ye. Zaitseva, 1986, "Venus rock composition at the Vega 2 landing site," *Proc. Lunar Planet. Science Conf. 17th,* in *J. Geophys. Res.,* v. 91, no. B13, supp., p. E215–E218.

Surkov, Yu.A., L.P. Moskalyova, O.P. Shcheglov, V.P. Kharyukova, O.S. Manvelyan, V.S. Kirichenko, and A.D. Dudin, 1983, "Determination of the elemental composition of rocks on Venus by Venera 13 and Venera 14 (preliminary results)," *Proc. Lunar Planet. Science Conf. 13th,* in *J. Geophys. Res.,* v. 88, supp., p. A481–A493.

Swanson, D.A., 1973, "Pahoehoe flows from the 1969-1971 Mauna Ulu eruption, Kilauea Volcano, Hawaii," *Geol. Soc. Amer. Bulletin,* v. 84, p. 615–626.

Swingle, G.D., 1973, "Structural geology of Knox County, Tennessee," *Geology of Knox County, Tennessee,* Tennessee Division of Geology Bulletin 70, p. 63–73.

Sylvester, A.G., 1988, "Strike-slip faults," *Geol. Soc. Amer. Bulletin,* v. 100, p. 1666–1703.

Theilig, E., and R. Greeley, 1986, "Lava flows on Mars: Analysis of small surface features and comparisons with terrestrial analogs," *J. Geophys. Res.,* v. 91, p. E193–E206.

Theilig, E., S. Wall, and R.S. Saunders, 1988, "Radar backscatter as a function of incidence angle for Pisgah and Craters of the Moon Lava Fields: Implications for interpretation of Magellan SAR data of Venus," *Proc. Lunar Planet. Science Conf. 19th.,* p. 323–333.

Thorarinsson, S., 1953, "The crater groups in Iceland," *Bulletin Volcanol.,* v. 14, p. 3–44.

Thorarinsson, S., 1960, "The postglacial volcanism and the postglacial history of the Myvatn area and the area between Myvatn a Fjollum," in *On the Geology and Geophysics of Iceland,* S. Thorarinsson, ed., Excursion Guide A2, 21st Int. Geol. Congress, p. 33–45.

Thorarinsson, S., 1967, "Some problems of volcanism in Iceland," *Geologische Rundschau,* v. 57, p. 1–20.

Ulaby, F.T., R.K. Moore, and A.K. Fung, 1982, "Microwave remote sensing: Active and passive," *Radar Remote Sensing and Surface Scattering and Emission Theory,* v. 2, Reading, Massachusetts: Addison-Wesley Publ. Co.

Wagner, D.L., and G.J. Saucedo, 1987, *Geologic Map of the Weed Quadrangle,* California Division of Mines and Geology, Regional Geologic Map Series, Map 4A, scale 1:250,000.

Walker, G.P.L., 1970, "Compound and simple lava flows and flood basalts," *Bulletin Volcanol.,* v. 35, p. 579–590.

Watkins, J.S., 1963, *Simple Bouger Gravity Map of Kentucky,* U.S. Geological Survey Geophys. Inv. Map GP-421, scale 1:500,000.

Watkins, J.S., 1964, *Regional Geologic Implications of the Gravity and Magnetic Fields of a Part of Eastern Tennessee and Southern Kentucky,* U.S. Geological Survey Prof. Paper 516-A, p. A1–A17.

Watters, T.R., 1988, "Wrinkle ridge assemblages on the terrestrial planets," *J. Geophys. Res.,* v. 93, p. 10,236–10,254.

Wells, S.G., J.C. Dohrenwend, L.D. McFadden, B.D. Turrin, and K.D. Mahrer, 1985, "Late Cenozoic landscape evolution on lava flow surfaces of the Cima Volcanic Field, Mojave Desert, California," *Geol. Soc. Amer. Bulletin,* v. 96, p. 1518–1529.

Wentworth, C.K., 1938, "Ash formations of the island Hawaii," *3rd Spec. Rept. Hawaiian Volcano Observatory,* 183 pp.

Wesson, R.L., E.J. Helley, K.R. Lajoie, and C.M. Wentworth, 1975, "Faults and future earthquakes," *Studies for Seismic Zonation of the San Francisco Bay Region,* R.D. Borchardt, ed., U.S. Geological Survey Prof. Paper 941A, p. 5–30.

White, B.R., 1981, "Venusian saltation," *Icarus*, v. 46, p. 226–232.

Williams, S., and R. Greeley, 1982, "Saltation flux on Venus: Laboratory results," *EOS*, v. 63, p. 1021.

Wilson, J.T., 1966, "Did the Atlantic close and then reopen?" *Nature*, v. 211, p. 676–681.

Wilson, L., and J.W. Head, 1983, "A comparison of volcanic eruption processes on Earth, Moon, Mars, Io and Venus," *Nature*, v. 302, p. 663–669.

Wise, W.S., 1966, *Geologic Map of the Pisgah and Sunshine Cone Lava Fields*, NASA TL-11, Washington, D.C.: National Aeronautics and Space Administration.

Woodward, L.A., 1977, "Rate of crustal extension across the Rio Grande Rift near Albuquerque, New Mexico," *Geology*, v. 5, p. 269–272.

Zebker, H.A., and R.M. Goldstein, 1986, "Topographic mapping from interferometric synthetic aperture radar observations," *J. Geophys. Res.*, v. 91, no. B5, p. 4993–4999.

Zisk, S.H., and P.J. Mouginis-Mark, 1980, "Anomalous region of Mars: Implications for near surface liquid water," *Nature*, v. 288, p. 735–738.

Zotkin, I.T., and V.I. Tsvetkov, 1970, "Searches for meteorite craters on Earth," *Astron. Vestnik.*, v. 4, p. 55–65.

Glossary

aa	basaltic lava flow with rough jagged surfaces
agglutinate	welded pyroclastic fragments characterized by vitric bonding material
alluvial fan	fan-shaped deposit of loose rock debris formed where a stream drains from mountains onto lowlands
altimetry	measurement of altitude
andesite	fine-grained extrusive igneous rock composed mostly of plagioclase and one or more mafic minerals
angle of repose	slope at which unconsolidated material remains stable
anticline	folded rock structure having stratigraphically older rocks in the core and limbs that dip away from the fold axis
antidip	slope inclined across the strike of layered rocks in a direction opposite to the dip
antiform	folded rock structure where the relative age of rocks in the core is not known and the limbs dip away from the fold axis
apoapsis	the greatest distance between a planet and an orbiting object (e.g., space-craft)
arachnoids (Venus)	spiderlike features
arenite	general term for sedimentary rocks composed of sand-sized fragments regardless of their mineral composition or origin
azimuth (imaging)	along-track direction of image acquisition
azimuth resolution	separation of points in the along-track direction
backscatter	portion of microwave energy returned to the radar antenna to create a radar image
band	interval in the electromagnetic spectrum whose boundaries are marked by a lower and an upper limiting wavelength or frequency.

band	range of wavelengths, cm	frequencies, GHz
L	30 – 15	1 – 2
S	15 – 7.5	2 – 4
C	7.5 – 3.75	4 – 8
X	3.75 – 2.4	8 – 12
Ka	1.18 – 0.75	26.5 – 40

basalt	fine-grained extrusive igneous rock rich in mafic minerals
block lava	lava with angular blocklike surfaces
bolide	exploding meteorite
breccia	coarse-grained clastic rock composed of angular rock fragments
butte	conspicuous isolated flattop hill with steep slopes (see *mesa*)
caldera	large volcanic depression caused by collapse or explosion at the summit of a volcano
cinder cone	conical hill formed of volcanic cinders
clastic	refers to rock composed of fragments from the erosion of preexisting rocks
composite volcano	volcano composed of interbedded lava and pyroclastic material commonly with steep slopes
dacite	fine-grained extrusive igneous rock similar to andesite but having less plagioclase and more quartz
décollement	detachment structure associated with folding and overthrusting that results in independent styles of deformation above and below
dielectric constant	ratio of electric flux density to electric field
dip	angle that a structural surface makes with the horizontal, measured perpendicular to strike
discontinuity	physical interruption in the sequence or distribution of strata
dome (volcanic)	rounded formation of viscous lava extruded from a volcano
Doppler shift	change in the observed frequency of electromagnetic waves caused by relative motion between source and detector
en echelon	steplike arrangement of features
endogenic	refers to geologic processes originating within the Earth
eolian	related to wind deposits and associated effects
fault	fracture or zone of fractures in Earth's crust accompanied by displacement of the opposing sides. Faults are classified according to the direction of relative movement:

fault (continued):
(a) normal—where the hanging wall moved down relative to the footwall
(b) reverse—where the hanging wall moved up relative to the footwall
(c) thrust—low-angle reverse fault where the dip of the fault plane is mostly below 45 deg
(d) strike-slip—where movement is parallel to the strike of the fault
(e) transform—variety of strike-slip fault where displacement abruptly terminates and crustal structure changes

flatiron	on remotely sensed images, a triangular pattern from which dip and strike of layered rocks may be inferred
flood basalt	extensive high-volume basaltic lava flow erupted from fissures
fold	product of the deformation of tabular rock bodies (e.g., *anticline*, *antiform*, *homocline*, and *syncline*)
foldover	(see *layover*)
geometric rectification	removal of geometric distortions from an image
geosyncline	downwarping of Earth's crust measured in lengths of hundreds of kilometers, where layered rocks have accumulated in thicknesses of tens of kilometers
graben	depressed elongate crustal block bounded by faults along its sides
granite	coarse-grained plutonic igneous rock composed mostly of quartz and feldspar
granite gneiss	coarse-grained banded metamorphic rock having the mineral composition of granite
grus	fragmented products of in-situ granular disintegration of granite and granitic rocks
hawaiite	type of olivine-rich basalt
homocline	general term for a series of strata that have the same dip
horst	uplifted elongate crustal block bounded by faults along its sides
hot spot	center of persistent volcanism, thought to be the surface expression of a rising hot plume in Earth's mantle
ignimbrite	igneous rock formed by widespread deposition and welding of ash flows
inselberg	prominent erosional hill or mountain rising abruptly above an extensive lowland surface
lahar	mudflow composed mostly of volcaniclastic debris on the flank of a volcano
lapilli	pyroclastic fragments with diameters between 2 and 64 mm
lava	general term for extrusive igneous material and rocks that form from it
lava tube	tunnel formed underneath the surface of a solidifying lava flow
layover	extreme case of foreshortening, where mountain tops are projected nearer the radar ground track than their bases (syn., *foldover*)

lineament	linear topographic feature that may depict crustal structure
lithosphere	rigid outer layer of Earth that includes the crust and part of the upper mantle, about 100 km thick
loess	deposit of wind-blown silt and clay
looks	number of independent radar observations summed for each resolution element
mafic	refers to rock or magma comparatively rich in magnesium and iron silicates
magma	molten rock material, including gases and liquids
mesa	broad flattop erosional hill or mountain, commonly bounded by steep slopes (see *butte*)
migmatite	composite rock of igneous and metamorphic materials
morphotectonic	refers to a tectonic interpretation of Earth's topographic features
orogeny	process of mountain building
pahoehoe	basaltic lava flow with smooth undulating surfaces
palagonite	altered volcanic glass
periapsis	the least distance between a planet and an orbiting object (e.g., spacecraft)
phenocryst	large crystal in a porphyritic igneous rock
pit crater (volcanic)	small circular or elliptical collapse depression on or adjacent to a volcano
pluton	massive igneous intrusion
porphyritic	refers to an igneous rock texture with two distinct sizes of crystals
phreatic	refers to a volcanic explosion of nonincandescent steam
pressure ridge (volcanic)	ridge formed by the uplift of a lava flow crust due to pressure of the flowing lava
pseudocrater	crater formed probably by a steam explosion as lava is emplaced over water-saturated sediments
pyroclast	fragmental material ejected by volcanic eruption
pumice	a light vesicular form of volcanic glass
range (imaging)	cross-track direction of image acquisition
range resolution	separation of points in the cross-track direction

118

rheology	study of the physical properties that govern the flow characteristics of solid material over time
rhyodacite	group of porphyritic extrusive igneous rocks intermediate in composition between dacite and rhyolite
rhyolite	fine-grained extrusive igneous rock, commonly with phenocrysts of quartz and feldspar in a glassy groundmass
rms (root mean square)	statistical measure of magnitude (e.g., small-scale roughness of a surface)
sag pond	small body of water in an enclosed depression where faulting has impounded the drainage
scarp	cliff or steep slope of some extent that may form a marked topographic boundary
shatter cone	striated conical fragment of rock with fractures
shield volcano	broad volcanic cone with gentle slopes constructed of successive nonviscous, mostly basaltic lava flows
shutterridge	ridge formed by displacement on a fault that transects ridge-and-valley topography
silicic	refers to rock or magma comparatively rich in aluminum and potassium silicates
spatter cone	low steep-sided cone built up from fluid pyroclasts coating the surface around a vent
speckle noise	scintillation of return from individual scattering elements caused by coherent illumination
specular reflection	mirrorlike reflections of a radar signal
strike	horizontal direction of a structural surface
subduction	process of one lithospheric plate descending beneath another
syncline	folded rock structure having stratigraphically younger rocks in the core and limbs that dip toward the fold axis
synthetic-aperture radar	side-looking imaging system that uses the Doppler effect to sharpen the effective resolution in the cross-track direction
tectonic	refers to structural and deformational features in Earth's crust and to forces that produce such features
tephra	general term for pyroclasts
terrain	physical region or feature of Earth's surface

terrane	region where a particular rock or rock group predominates
tholeiite	subalkaline type of basalt
tuff	general term for consolidated pyroclastic debris
tumuli	(plural of tumulus) domes or small mounds on the crust of a lava flow
vent	opening in Earth's crust through which volcanic material erupts
volcanic rock	igneous rock formed by eruption at Earth's surface

Appendix A

Orbital and Physical Properties of Venus and Earth[a]

Property	Venus	Earth
Mean distance from sun, AU	0.723	1
Mean distance from sun, 10^6 km	108.2	149.6
Orbital period, days	224.7	365.25
Mean orbital velocity, km/s	35.05	29.79
Eccentricity	0.0067	0.0167
Inclination to ecliptic, deg	3.39	—
Reciprocal mass	408,523.9	328,900.0
Mass (Earth = 1)	0.815	1.0
Mass, kg	4.871×10^{24}	5.976×10^{24}
Equatorial radius, km	6051.3[b]	6378
Equatorial radius (Earth = 1)	0.949	1.0
Ellipticity (oblateness)	0.0	0.0034
Mean density, g/cm^3	5.24	5.52
Equatorial surface gravity, m s^{-2}	8.87	9.78
Equatorial escape velocity, km s^{-1}	10.4	11.2
Sidereal rotation period	243.01 days	23.9345 hours
Obliquity, inclination of equator to orbit, deg	-2.6	23.45

[a]Data from Beatty et al., 1981; and Hunt and Moore, 1981.
[b]Revised research indicates that the mean radius value for Venus is 6051.92 (Ford, 1986).

Appendix B

Magellan Standard Data Products

AEDR   Archive Engineering Data Record: all spacecraft engineering data, Deep Space Network monitor data, conversion tables, and decommutation maps. For archive only.

ALT-EDR   Altimeter Experiment Data Record: altimeter pulse echo data, radiometer data, and ancillary data.

ATDFDR   Archival Tracking Data File Data Record: raw Doppler count and residuals edited and in time-ordered sequence. For archive only.

BADR   Basic Altimeter Data Record: a compilation of the backscatter coefficient, range measurements to the planet surface, and terrain elevation measurements from each altimeter burst.

BRDR   Basic Radiometer Data Record: contains brightness temperature and effective blackbody source temperature information derived from the radiometer data samples contained in the radar data stream, along with ancillary, calibration, ephemeris, and spacecraft engineering data corresponding to radiometer data.

C-BIDR   Compressed Basic Image Data Record: all F-BIDR data compressed from 75-m pixel spacing to 225-m pixel spacing by taking the average of 3 × 3 F-BIDR pixel arrays.

C1-MIDR   Compressed-Once Mosaicked Image Data Record: unfiltered and seam-corrected rendition of C-BIDR data. Pixel spacing is 225 m. Seam registration error not to exceed 600 m.

C1-MIDRP   Compressed-Once Mosaicked Image Data Record Photoproduct.

C2-MIDR   Compressed-Twice Mosaicked Image Data Record: unfiltered and seam-corrected C1-MIDR data that have been compressed by averaging 3 × 3 C1-MIDR pixel arrays into a single pixel. Pixel spacing is 675 m. Seam registration error not to exceed 800 m.

C2-MIDRP   Compressed-Twice Mosaicked Image Data Record Photoproduct.

C3-MIDR   Compressed-Thrice Mosaicked Image Data Record: unfiltered and seam-corrected C2-MIDR data compressed by averaging 3 × 3 C2-MIDR pixel arrays into a single pixel. Pixel spacing is 2025 m. Seam registration error not to exceed 1500 m.

C3-MIDRP   Compressed-Thrice Mosaicked Image Data Record Photoproduct.

F-BIDR   Full-Resolution Basic Image Data Record: processed SAR image swath containing 75-m pixel spacing with map projection dependent on latitude. Also includes ancillary data.

F-MIDR	Full-Resolution Mosaicked Image Data Record: mosaics of SAR image strips at full resolution, produced from F-BIDRs. Seam registration error shall not exceed 500 m.
F-MIDRP	Full-Resolution Mosaicked Image Data Record Photoproduct.
F-PIDR	Full-Resolution Polar Image Data Record: full-resolution SAR image strips from several orbits assembled side by side and not mosaicked.
F-PIDRP	Full-Resolution Polar Image Data Record Photoproduct.
GADR	Global Altimeter Data Record: a global map of topographic and backscatter information derived from altimetry data.
GADRP	Global Altimeter Data Record Photoproduct.
GRDR	Global Radiometer Data Record: BRDR data compiled into global maps of brightness temperatures with 10-km pixel spacing. A quarter of the planet per tape.
GRDRP	Global Radiometer Data Record Photoproduct.
MCDR	Media Calibration File Data Record: corrections for the effects of transmission media (tropospheric, ionospheric, and solar plasma) on the Doppler and very-long-baseline-interferometry (VLBI) data.
MPL	Maneuver Profile Listing: maneuver delta-Vs, timing, and associated information for midcourse and trim maneuvers.
NCDR	Navigation Constants Data Record: navigation constants file, station/quasar locations, and solar pressure parameters.
ODFDR	Orbit Data File Data Record: time-compressed Doppler and VLBI observations.
ODR	Original Data Record: contains all raw Magellan data transmitted to Earth.
PADR	Preprocessed Altimeter Data Record: produced from each ALT-EDR input; the input consists of pulse-compressed altimeter pulse echo.
RDR	Residuals without Spherical Harmonic Data Record.
SAR-EDR	SAR Experiment Data Record: a complete nonredundant set of radar, radiometry, and ancillary data.
SFDFSL	Small Forces Data File Summary Listing: impulses applied to the spacecraft during reaction wheel unloading.
TPMFDR	Timing and Polar Motion File Data Record.

Appendix C

Magellan Special Data Products[a]

JET PROPULSION LABORATORY

BOUGDR   Bouguer Map Data Record: digital data necessary to contour a Bouguer map on a plotting system.

BOUMAP   Bouguer Map: hardcopy of Bouguer map overlaid on Pioneer Venus Orbiter (PVO) topography.

GEOIDR   Geoid Map Data Record: digital data necessary to contour a geoid map on a plotting system.

GEOIMAP   Geoid Map: hardcopy of geoid map overlaid on PVO topography.

GRAVMAP   Gravity Map: hard copy of vertical gravity from spherical harmonic fits.

ISOMAP   Isostatic Map: hardcopy of variations in depth of compensation from an isostatic model.

LOSAPDR   Line-of-Sight Acceleration Data Record: digital data of line-of-sight acceleration on an orbit-by-orbit basis.

P-MIDR   Polar Mosaicked Image Data Record: a 16-frame data set that covers the area north of 80°N latitude. Mosaicking is by cut and paste, with no pixel averaging. Pixel spacing is 75 m at 80°N.

P-MIDRP   Polar Mosaicked Image Data Record Photomosaic.

RSHDR   Residuals with Spherical Harmonics Data Record.

SHDR   Spherical Harmonics Data Record: digital tabulation of the spherical harmonic coefficients estimated from the Doppler data.

MASSACHUSETTS INSTITUTE OF TECHNOLOGY

ARCDR   Altimeter/Radiometer Composite Data Record: altimeter and radiometer data in time sequence, orbit by orbit.

GEDR   Global Emissivity Data Record: resampled emissivity data from the ARCDR. 5-km pixel spacing. Also, digital version of GEDRP on same medium.

GEDRP   Global Emissivity Data Record Photomosaic: cartographic reprojection of GEDR in Mercator and polar stereographic coordinate systems.

---

[a] Listed by producing institution.

GREDR   Global Reflectivity Experiment Data Record: resampled reflectivity data from the
               ARCDR. 5-km pixel spacing. Also, digital version of GREDRP on same medium.

GREDRP   Global Reflectivity Experiment Data Record Photomosaic: cartographic reprojection
               of GREDR in Mercator and polar stereographic coordinate systems.

GSDR   Global Slope Data Record: resampled slope data from the ARCDR. 5-km pixel
               spacing. Also, digital version of GSDRP on same medium.

GSDRP   Global Slope Data Record Photomosaic: cartographic reprojection of GSDR in
               Mercator and polar stereographic coordinate systems.

GTDR   Global Topographic Data Record: resampled topography data from the ARCDR.
               5-km pixel spacing. Also, digital version of GTDRP on same medium.

GTDRP   Global Topographic Data Record Photomosaic: cartographic reprojection of GTDR
               in Mercator and polar stereographic coordinate systems.

STANFORD

SCVDR   Surface Characteristics Vector Data Record: sorted scattering function segments
               from altimetry and SAR analysis, electrical properties estimates from same, and
               radiometer and confidence estimates. Represents averages over surface elements of
               approximately 20 × 20 km.

UNITED STATES GEOLOGICAL SURVEY

CARTDR   Cartographic Maps Data Record: digital record of CARTMAP.

CARTMAP   Cartographic Maps: 62 map sheets, scale 1:5,000,000.

126

1. Report No. JPL Publication 89-41	2. Government Accession No.	3. Recipient's Catalog No.

4. Title and Subtitle	5. Report Date
Spaceborne Radar Observations: A Guide for Magellan Radar-Image Analysis	December 1989
	6. Performing Organization Code

7. Author(s) J.P. Ford, R.G. Blom, J.A. Crisp, C. Elachi, T.G. Farr, R.S. Saunders, E.E. Theilig, S.D. Wall	8. Performing Organization Report No.

9. Performing Organization Name and Address	10. Work Unit No.
JET PROPULSION LABORATORY California Institute of Technology 4800 Oak Grove Drive Pasadena, California 91109	11. Contract or Grant No. NAS7-918
	13. Type of Report and Period Covered
12. Sponsoring Agency Name and Address	JPL Publication
NATIONAL AERONAUTICS AND SPACE ADMINISTRATION Washington, D.C. 20546	14. Sponsoring Agency Code RE215 BP-844-20-00-30-02

15. Supplementary Notes

16. Abstract

Geologic analyses of spaceborne radar images of Earth are reviewed and summarized with respect to detecting, mapping, and interpreting impact craters, volcanic landforms, eolian and subsurface features, and tectonic landforms. Interpretations are illustrated mostly with Seasat Synthetic-Aperture-Radar and shuttle-imaging-radar images. Analogies are drawn for the potential interpretation of radar images of Venus, with emphasis on the effects of variation in Magellan look angle with Venusian latitude. In each landform category, differences in feature perception and interpretive capability are related to variations in imaging geometry, spatial resolution, and wavelength of the imaging radar systems.

Impact craters and other radially symmetrical features may show apparent bilateral symmetry parallel to the illumination vector at low look angles. The styles of eruption and the emplacement of major and minor volcanic constructs can be interpreted from morphologic features observed in images. Radar responses that are governed by small-scale surface roughness may serve to distinguish flow types, but do no provide unambiguous information. Imaging of sand dunes is rigorously constrained by specific angular relations between the illumination vector and the orientation and angle of repose of the dune faces, but is independent of radar wavelength. With a single look angle, conditions that enable shallow subsurface imaging to occur do not provide the information necessary to determine whether the radar has recorded surface or subsurface features. The topographic linearity of many tectonic landforms is enchanced on images as regional and local scales, but the detection of strutural detail is a strong

17. Key Words (Selected by Author(s))	18. Distribution Statement
Geosciences and Oceanography (General) Geology and Mineralogy Geophysics	Unclassified - Unlimited

19. Security Classif. (of this report)	20. Security Classif. (of this page)	21. No. of Pages	22. Price
Unclassified	Unclassified	126	

NASA

National Aeronautics and
Space Administration

Jet Propulsion Laboratory
California Institute of Technology
Pasadena, California